Mechanical property and meso-structure assessment of Ti6Al4V parts as a function of high-speed selective laser melting practice (Additive Manufacturing)

Prepared by:

Chenesai Nyakunu

NYKCHE002

Department of Mechanical Engineering

University of Cape Town

Supervisor:

Robert Knutsen

February 2022

Submitted to the Department of Mechanical Engineering at the University of Cape Town in partial fulfilment of the academic requirements for a Master of Science degree in Engineering

Plagiarism declaration

I know the meaning of plagiarism and declare that all the work in the document, save for that which is properly acknowledged, is my own. This thesis/dissertation has been submitted to the Turnitin module and I confirm that my supervisor has seen my report and any concerns revealed by such have been resolved with my supervisor.

This plagiarism declaration was signed by Chenesai Nyakunu, (student number – NYKCHE002), on the 11/02/2022 for the submission of a dissertation for the degree of Master of Science in Materials Engineering, at the University of Cape Town

Signed by candidate

Abstract

The use of titanium and titanium alloys, particularly titanium-6-aluminium-4-vanadium (Ti6Al4V), manufactured by 3D printing, also known as additive manufacturing, is fast evolving in several industries including the aerospace industry, medical industry, and the automotive industry. At present, titanium parts fabricated by additive manufacturing techniques such as the selective laser melting practice are built at conventional laser scan speeds typically between 0.1 m/s and 1 m/s. This project is focused on investigating the influence of high laser scan speeds on the microstructure and mechanical properties of Ti6Al4V fabricated by the selective laser melting technique. Building material at much higher scan speeds allows for a higher rate of productivity and efficiency as more parts can be built in a shorter space of time. The aim of this project is to ensure that the integrity and mechanical behaviour of the Ti6Al4V parts at the high scan speeds is still maintained by investigating whether acceptable mechanical properties are still achieved when material is built at higher scan speeds.

The material tested in this project was built by the selective laser melting (SLM) technique at four different high scan speeds namely 5.75 m/s, 6.0 m/s, 6.25 m/s and 6.5 m/s. The material for mechanical testing consisted of tensile specimens and compact-tension (CT) specimens for fracture toughness (FT) testing and fatigue crack growth rate (FCGR) testing respectively. The same material was used for microstructure analysis. Furthermore, the tensile specimens were fabricated in different build orientations namely X-TA, Y-TA, and Z-TA to investigate the effect of build orientation on tensile properties. During the SLM process, considerable thermal related stresses develop in the material being built. After fabrication, a heat treatment protocol was therefore applied to the material for stress relief. The material was heated at 600°C for two hours then cooled in air.

Tensile testing was performed on the SLM Ti6Al4V built tensile bars according to the ASTM E8/E8M standard on the Zwick machine at a strain rate of 10^{-3}/s in conjunction with a video extensometer for more accurate results. Specimens were loaded in tension with force of approximately 20 000N. The results indicated that there is no significant influence of high scan speed on the tensile properties of the material tested as there was no difference observed in tensile properties of the material built at the four different high scan speeds. The same phenomenon was observed with build orientation. The tensile properties of the specimens built

in the horizontal direction (X-TA and Y-TA) and the specimens built in the vertical direction (Z-TA) were within the same range.

The FCGR and FT tests were performed on the ESH servo hydraulic fatigue machine at room temperature according to the ASTM E647-15 and E399 standards, respectively. The FCGR tests were conducted at a load range of 1.3kN and stress ratio of 0.1. The results indicated that there is no difference in FCGR behaviour with respect to scan speed between the 5.75 m/s and 6.0 m/s specimens as one set and no difference between the 6.25 m/s and 6.5 m/s specimens as the other set, but a difference is observed between the two sets of speeds. All specimens however, displayed reasonable resistance to crack growth. The FT tests were performed at a crosshead speed of 1 mm/min. The results indicated that high scan speed has no significant influence on the fracture toughness of SLM Ti6Al4V material as there was no difference observed in fracture toughness of the materials with increase in scan speed.

The techniques used for microstructure analysis were light microscopy and scanning electron microscopy (SEM). Light microscopy was performed to reveal the microstructure and surface topography of the material built at the four different high scan speeds and three different build orientations. The results indicated that high scan speed has no significant influence on the microstructure of the material investigated. The results also indicated that build orientation influences the microstructure of the material tested. A difference in microstructure, particularly the orientation of β-grains, was observed with build orientation. The X-TA and Y-TA specimens have β-grains aligned more perpendicular to the tensile axis whilst the Z-TA specimens have the β-grains aligned more parallel to the tensile axis. However, this difference in β-grain orientation did not influence the tensile properties of these specimens to a greater extent. SEM was performed to obtain quantitative information on microstructure, particularly porosity, and for β-grain reconstruction by electron backscatter diffraction (EBSD) for the material at a much higher magnification and depth of field. The results indicated that high scan speed has no influence on porosity of the material tested as no difference was observed in the number and size of pores amongst the samples built at the four high scan speeds. However, average relative density of 97-99% was reported for these specimens which is lower in comparison with average relative density of >99% reported for the majority of the specimens built at conventional scan speeds. EBSD analysis shows that there is no difference in the size and morphology of reconstructed β-grains across the material built at the high scan speed.

It is concluded that there is no significant influence of high scan speed on the microstructure and mechanical properties of SLM Ti6Al4V within the scan speed range of 5.75 m/s to 6.5 m/s investigated in this project. The specimens built at the specified scan speeds have similar energy density input which attributes to the similar microstructure and mechanical behaviour of the specimens observed.

Acknowledgements

I would like to appreciate all individuals and departments that assisted me during the course of my research project, with special thanks to the following:

- My supervisor, Professor Robert Knutsen. His guidance, wisdom, approachability and support throughout the duration of my research made the journey much easier. He was always available to help and give advice whenever I needed it. He nurtured my critical thinking skills and helped me broaden my knowledge of materials science. I managed to get through this research mainly because of him.

- The National Laser Centre (CSIR) providing all the material for testing.

- The UCT workshop staff. Their hard work to machine my specimens and make grips for me is highly appreciated.

- The staff at the Centre for Materials Engineering at UCT, particularly Penny Louw and Soraya Von Willingh. Their assistance with equipment and laboratory procedures helped my experimental work experience much smoother.

- The staff at the Electron Microscope Unit with special thanks to Nasheeta Hanief and Miranda Waldron for teaching me how to use the MIRA3 microscope.

- My family with special thanks to my parents, Nyasha and Anne Nyakunu. Their emotional support pushed me to achieve my goals and I am forever grateful.

- My friends and colleagues. I am grateful for the constant support throughout my research from the late nights to the ups and downs and the laughs we shared.

- To the University of Cape Town , the engineering faculty and the Centre for Materials Engineering for providing me with funding to support me during the course of my degree as well as the necessary equipment, environment and personnel to complete this project.

Table of Contents

List of figures

List of tables

List of Equations

1. Introduction

1.1 Subject and motivation of research

The subject of this thesis is to research the effect of using higher laser scan rates on the microstructure and mechanical properties of titanium-6-aluminium-4-vanadium (Ti6Al4V). The samples were built by the selective laser melting (SLM) process. The aim of this project is to compare the results thereof with those obtained by SLM Ti6Al4V manufactured at the conventional scan speeds, which are typically between 0.1 m/s and 1m/s, and to identify the high laser scan rate at which the best properties are achieved using the properties of the conventionally scanned specimens as the reference.

1.2 Background to research

Titanium is a common and widely used metal in several industries. It has ideal mechanical properties such as high specific strength, excellent corrosion resistance high temperature strength and good fracture resistance. Titanium's high strength to weight ratio sets it apart from the other high-strength metals due to its low density. However, the process of extracting titanium from its mineral form is expensive and energy intensive, which is why titanium alloys have a high cost. In addition, the machining process for titanium costs 10 times more than that of aluminium[1]. Engineers are looking into cheaper novel manufacturing processes like additive manufacturing. Titanium products produced by these methods have near full density greater than 99% in most cases and near net shape and so further machining to acquire a fine finish is not required. A derivative of additive manufacturing is selective laser melting (SLM) amongst others. According to literature, SLM Ti6Al4V has comparable strength to wrought Ti6Al4V but with lower ductility[2].

The SLM process is an additive manufacturing method in which a product is formed by selectively melting powders layer by layer. The process is characterized by localized high heat inputs during very short interaction times which subsequently affects the microstructure. The integrity of the part relies on adequate localised melting to avoid porosity development. The occurrence of pores will result in a decrease in density of the SLM processed parts[2]. These pores stem from process-induced defects originating from initial powder contaminations, evaporation, or local voids after powder-layer deposition. Eventually, these pores act as strong stress raisers and finally lead to failure, especially under fatigue loading. SLM processing parameters including scanning speed affect the localised solidification events and hence microstructure and properties of the Ti6Al4V. A set of processing parameters which does not result in a too low or too high energy density input is considered conventional. Excessive or insufficient energy density results in the formation of voids therefore a systematic optimization strategy for the processing via selecting laser melting of Ti6Al4V must be implemented aiming at obtaining a minimum porosity density fraction.

SLM Ti6Al4V was noted to have lower ductility compared to wrought Ti6Al4V in several studies. This is due to the α martensitic non-equilibrium microstructure of SLM Ti6Al4V which arises due to the SLM process being characterized by high temperature gradients and fast cooling[4][5]. This fine microstructure results in a brittle (low ductility) product with high strength. In the SLM process, processing parameters like laser scanning speed, laser power, scanning direction and build orientation can be altered and varied to meet microstructure and mechanical property requirements.

This research intends to investigate the microstructure and mechanical properties at higher laser scan speeds (5.75 m/s, 6.0 m/s, 6.25 m/s and 6.5 m/s) whilst all other parameters are held constant. The aim of using higher laser scan speeds is to build bigger parts with more powerful lasers in a much less amount of time. Building parts at these higher scan speeds ensures efficiency but there is critical need to ensure good mechanical properties are still achieved.

1.3 Aims and objectives of research

This project aims to determine the effect of using high laser scan speeds on the microstructure and mechanical properties of SLM Ti6Al4V.

The targets of this research are therefore to:

- Analyse and compare the microstructures of SLM Ti6Al4V produced at laser scan speeds 5.75 m/s, 6.0 m/s, 6.25 m/s and 6.5 m/s.

- Measure the tensile properties, fracture toughness and fatigue crack growth rate for a set of specimens built at laser scan speeds 5.75 m/s, 6.0 m/s, 6.25 m/s and 6.5 m/s.

- Compare the microstructure and mechanical properties to measurements obtained on equivalent specimens built under conventional SLM conditions.

1.4 Scope and limitations of research

This project focuses on investigating the microstructure and mechanical behaviour of Ti6Al4V built by the SLM additive manufacturing technique at varying high scan speeds. The mechanical behaviour is explored by tensile testing, fatigue crack growth rate (FCGR) testing and fracture toughness (FT) testing of the SLM Ti6Al4V.

The tensile specimens, dog-bone shaped with round threaded ends, were built at varying orientations in addition to the varying scan speed. The FCGR and FT tests were conducted on compact-tension (CT) specimens built in the same orientation. The tensile, FCGR and FT tests were carried out according to the ASTM E8, E647 and E399 standards, respectively. Density tests were employed to measure the density of the material and porosity. The density tests were performed according to the ASTM B311. The tests were first performed on dummy samples to get a good sense of the load and specific parameters required. All tests were conducted at room temperature. The results obtained were used to compare the differences in mechanical properties between the material built at the different high scan speeds therefore analysing the effect of high scan speed on the mechanical behaviour of SLM Ti6Al4V as well as the effect of build orientation.

The microstructure of the material is investigated by light microscopy and scanning electron microscopy (SEM). The samples are prepared following the grinding and polishing protocols with the help of the Struers Metalog Guide. Light microscopy is used to examine the topography and grain structure of the material. SEM is used to further analyse the surface features including any defects and for the reconstruction of prior β-grains using the secondary electron (SE) detector and the electron backscatter detector (EBSD) respectively for each material condition. The fracture surfaces of the material built at each scan speed are also analysed by SEM. The results obtained were used to analyse any differences in microstructure and fracture surfaces between the material built at the different high scan speeds therefore investigating the effect of high scan speed on the microstructure of SLM Ti6Al4V.

This research was limited by the range of scan speed at which the testing material was built. The difference between each scan speed was 0.25. The 0.25 m/s difference proved to be too small as the material built at the different scan speeds had similar energy densities. The results of the material built at the different scan speeds were similar, but it is not evident whether this is due to the high scan speeds having no effect on the mechanical and microstructure of SLM Ti6Al4V or if it is due to the materials having too small a difference in scan speed. The effect of scan speed was therefore not adequately explored.

The testing material was built at the National Laser Centre which is part of the Council for Scientific and Industrial Research (CSIR) in South Africa. Not all the build parameters were disclosed by CSIR which made it difficult to ensure that all comparisons with studies from literature and conclusions drawn were solely based on the effect of scan speed thus limiting the research.

In the literature reviewed for material built at conventional scan speeds, some of the studies did not provide qualitative values of the scan speeds used. Instead, qualitative values of energy density and only two other scanning parameters were provided. In these studies, the change in energy density with varied scan speed was attributed to the effect of scan speed. This led to the effect of scan speed and that of energy density not being fully reviewed independently.

1.5 Plan of development.

The following chapter in this thesis is a review of the relevant literature, chapter 2. It briefly outlines an introduction to titanium and its alloys, additive manufacturing, and previous studies on SLM Ti6Al4V specific to laser scan speed. After which comes chapter 3 with the detailed experimental methodology and apparatus used to obtain results. This includes methods used to obtain density, microscopy work, tensile properties, fracture toughness and fatigue crack growth rate. The results of the mechanical properties and microstructural evolution of the samples built at high scan speeds (5.75 m/s, 6.0 m/s, 6.25 m/s and 6.5 m/s) is presented in chapter 4 and the discussion in chapter 5. In chapter 6, conclusions from the results and discussion are drawn, followed by recommendations in chapter 7, a list of references in chapter 8 and 9 and lastly the appendices in chapter 10.

2 Literature Review

In this chapter, relevant information on the applications of titanium alloys in different industries produced by additive manufacturing is presented. An introduction to titanium and Ti6Al4V is given with regards to its microstructure and mechanical properties. Additive manufacturing, particularly Selective Laser Melting, is introduced and discussed in relation to conventional production methods. Relevant topics which have a direct influence on this research are discussed. An introduction to linear elastic fracture mechanics (LEFM) is given with the basics of fatigue crack growth rate and fracture toughness explained.

2.1 Additive manufacturing

2.1.1 Introduction to powder metallurgy and additive manufacturing

Additive manufacturing (AM) processes are based on layer-by-layer production in which the raw material feedstock is powder which is melted by a focused heat source which subsequently cools to form a part[3]. AM has become popular due to numerous advantages associated with the process over conventional production methods. These include reduced cost of production, high flexibility of design and efficient use of material. Parts formed by additive manufacturing have near net shape and so only machining to achieve a fine surface finish is required. This means the number of production steps is reduced and hence the reduced cost of production.

The general cost of production with titanium at various stages is shown in Figure 1. The foil and castings stages of titanium production by conventional methods are the most expensive stages.

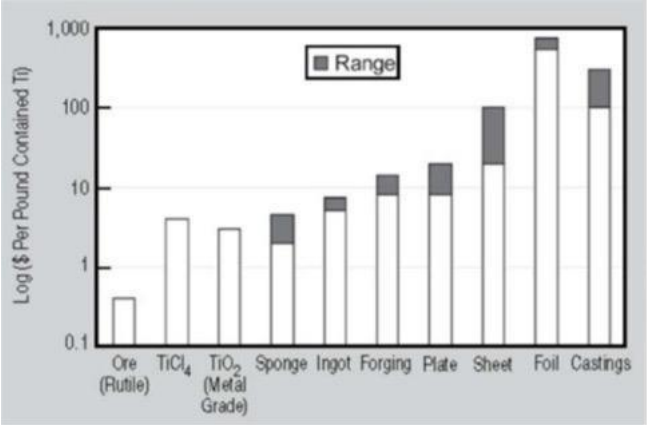

Figure 1: The general cost of Titanium at the various component production stages[2]

An example of the manufacturing cost breakdown of a Boeing 787 aircraft part is shown in the image on the right in Figure 2. The cost breakdown of the Boeing 787 shows that machining is the most incurred cost. Curbing the machining cost would significantly decrease the total manufacturing costs of the Boeing 787 which is possible with manufacturing using AM techniques.

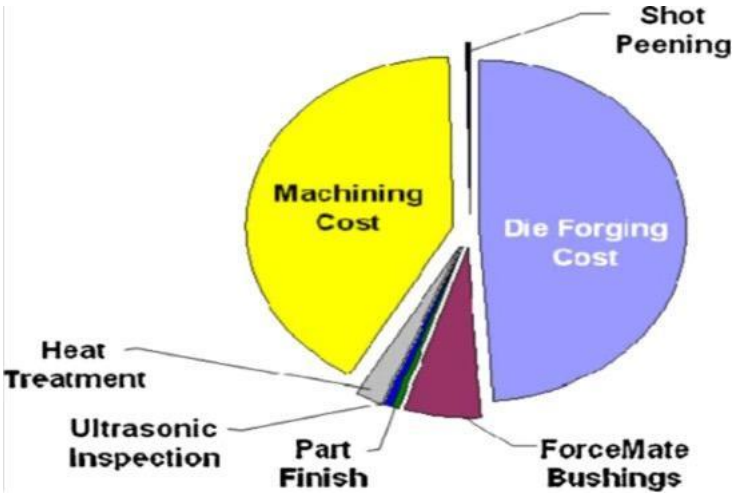

Figure 2: The manufacturing cost breakdown of Boeing 787[4]

Additionally, parts with complex geometries can be manufactured by AM techniques with ease unlike with conventional manufacturing processes which do not allow design freedom. There is minimal material waste with AM as the powder that would have remained from one-layer step of the process is carried over to the next and the remaining unmolten powder left after the whole process is reintroduced into a subsequent additive manufacturing process. AM could therefore potentially replace all conventional production methods but there is need to ensure that the integrity of the components is maintained and that production speeds are realistic to support economical production.

2.1.2 Technology Overview

A 3D-printing machine is employed for building parts using AM. A typical 3D-printing machine is shown in Figure 3.

Figure 3: 3D printing machine SLM 500[(a)]

All AM methods rely on the principle of slicing a solid model into multiple layers to create a toolpath for the computer. The computer-aided design (CAD) model and simulated toolpath illustrating the principle of the AM technology is displayed in Figure 4. The machine uses this toolpath as a source of instructions to build the part layer by layer using a heat source (electric arc, laser, or electron beam) and feedstock (metal powder). This is the 3D printing process. Typically, 3D printing technologies use Standard Tessellation Language (STL) files as input.

However, STL is not compatible with complex geometries as it does not contain any scale information which is why many AM technologies use solid models as input instead[4].

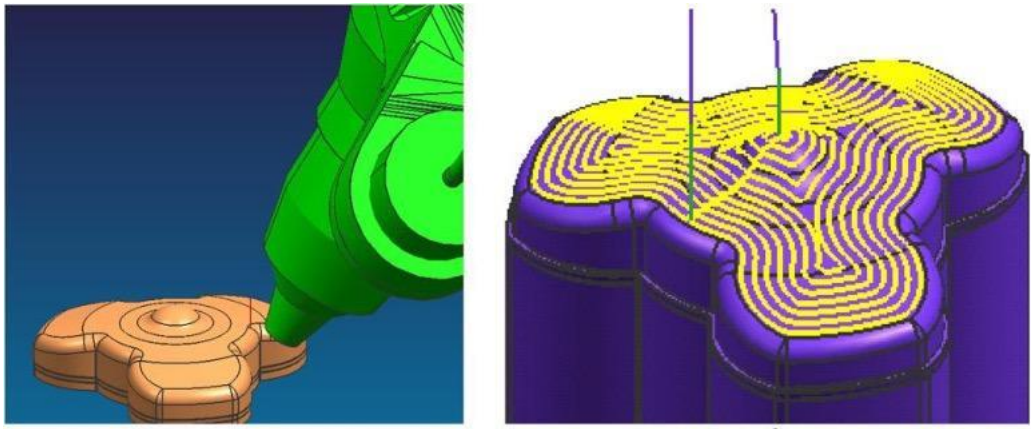

Figure 4: CAD model of the part and process head. (b) simulated toolpath for 5-axis deposition using DMSSCAM software

2.1.3 Part building technologies

According to ASTM classification standards, AM technologies for metals can be classified into two broad categories namely Powder Bed Fusion (PBF) and Direct Energy Deposition (DED). There is a trade-off within each of the two categories. PBF technologies can build products with complex geometry and hollow cooling passages, but they do not exhibit build direction flexibility as they can only build along the horizontal axis and only single material can be used per build at a time. While DED technologies exhibit build direction flexibility and offer the ability to deposit multiple materials per build at a time, their ability to build complex features and hollow cooling passages is limited[4]. The comparison of the two categories based on surface roughness and deposition rate is shown in Figure 5 where the layer thickness was used to measure surface roughness. This comparison was made in an investigation for AM of titanium alloys by Dutta et al[4].

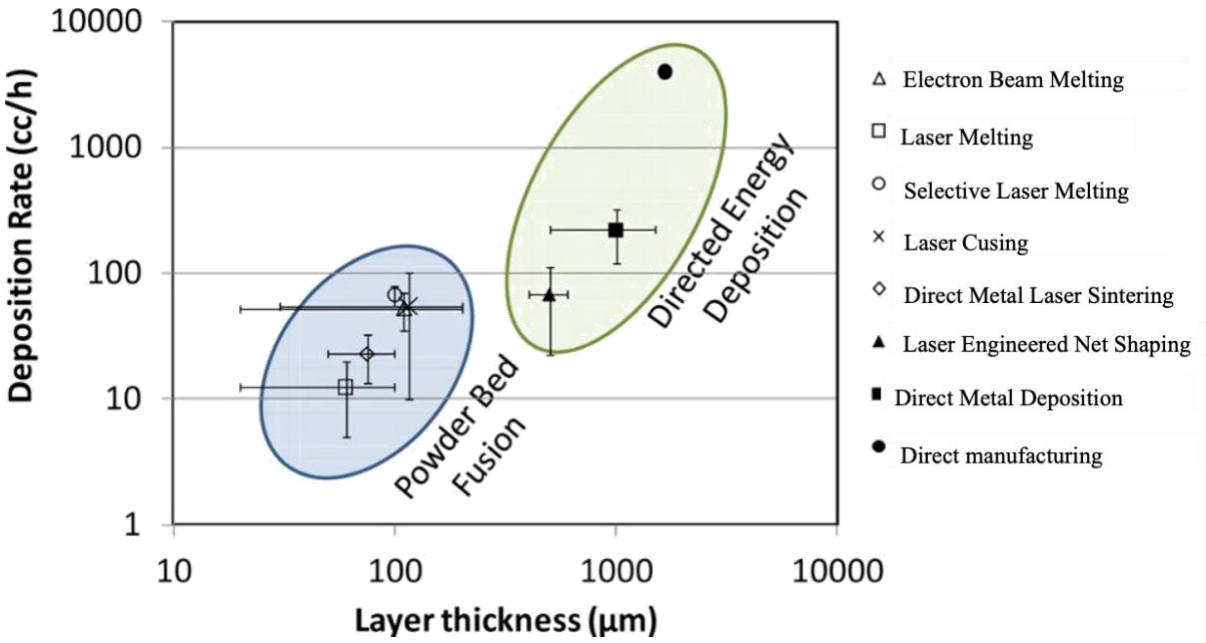

Figure 5: Comparison of powder bed fusion and direct energy deposition technologies in terms of layer thickness and deposition rate[4]

The layer thickness was used to measure surface roughness as it determined the roughness of the vertical walls of the structure being built. It was noted that the PBF technologies offer a better surface finish based on the low layer thickness (surface roughness) as they use small beam size but deposit material at much lower rates. Therefore, PBF technologies are more suitable for building smaller complex parts at low processing rates but with fine surface finish whilst DED technologies are more suitable for building larger parts at higher processing rate but with a coarse surface finish.

The several types of additive manufacturing methods are shown in Table 1: Various AM technologies for processing of titanium and its alloys[4]. All processes either fall under the powder bed fusion technology or the direct energy deposition technology. Popular processes are Electron Beam Melting (EBM), Laser Beam Melting (LBM) and Laser Metal Deposition (LMD). The process of LBM is also known as Selective Laser Melting (SLM) which is highlighted in bold as it is of the most important interest for this research project.

Table 1: Various AM technologies for processing of titanium and its alloys[4]

AM category	Process Label	Company	Description
Directed Energy Deposition (DED)	Direct Metal Deposition (DMD)	DM3D Technology LLC (Formerly POM Group)	Uses laser and metal powder for melting an depositing using a patented close loop process.
	Laser Engineered Net Shaping (LENS)	Optomec, Inc	Uses laser and metal powder for melting and depositing
	Direct Manufacturing (DM)	Sciaky, Inc.	Uses electron beam and metal wire for melting and depositing.
	Shaped Metal Deposition or Wire and Arc Additive Manufacturing (WAAM)	Not commercialized yet (patented by Rolls Royce Plc.)	Uses electric arc and metal wire for melting and depositing
Powder Bed Fusion (PBF)	Selective Laser Sintering (SLS)	3D Systems Corp. (Acquired Phenix Systems)	Uses laser and metal powder for sintering and bonding
	Direct Metal Laser Sintering (DMLS)	EOS GmbH Renishaw Inc.	Uses laser and metal powder for melting and bonding
	Laser Melting (LM)		
	Selective Laser Melting (SLM)	**SLM Solutions GmbH**	**Uses laser and metal powder for melting and bonding**
	LaserCUSING	Concept Laser GmbH	Uses laser and metal powder for melting and bonding
	Electron Beam Melting (EBM)	Arcam AB	Uses electron beam and metal powder for melting and bonding

The approach used in these processes is basically the same. An imaging method of reverse engineering is used to design a 3D CAD model on a computer, or a new design is developed as a CAD model. The model created is sliced into layers which are typically 20microns to 1 millimetre thick. The number of layers depends on the size of the component being built. The powder is then deposited layer by layer based on the data of the model and the part is built. The layers are locally melted by a heat source which will be a laser beam[3].

2.1.4 Comparison between AM and conventional methods of production

Common conventional methods of production include casting, injection moulding and forging amongst others. Manufacturing industries are always looking into improved production methods to reduce cost and expand their capability. AM, which started in the 1960s has brought to light novel techniques to expand production capacity. AM has rapidly and continuously grown and more research is directed at identifying manufacturing processes that can be replaced by AM[5].

With conventional manufacturing techniques, material is removed either by drilling, machining, or grinding techniques. However, as mentioned earlier, AM technologies use revolutionary technology to build materials with complex shapes layer by layer which allows AM technologies to have a higher level of design freedom.

AM technologies are more capable of building parts with complex geometries, and this enables these technologies to print complete parts on one process cycle thus eliminating forging and joining processes. An industrial example of this is the production of a metal acetabular cup used in hip replacement surgeries mentioned in a study by AS Unger et al[6].

Notwithstanding the distinct advantages offered by AM in terms of complex geometry possibilities, net-shape manufacturing, and conservation of material, there are several barriers to successful implementation of AM. For example, conventional production methods such as injection moulding still dominate in manufacturing industries[7]. Hopkinson and Dickens et al[8] devised a cost model to demonstrate the breakeven point of AM versus SM for high volume production. The study was based on the cost of manufacturing a small plastic lever using AM PBF vs conventional injection moulding. In this study, Hopkinson and Dickens[8] concluded that AM has a reduced unit cost compared to injection moulding for a production volume less than 10,000[9].

While SM technologies are better suited for mass manufacturing economically, AM technologies are better suited to manufacture tooling and fixtures required for traditional mass manufacturing moulds[10]. Furthermore, advances in the rapid improvement of AM technologies are due to focussed research on low cost machines, application of the complex geometry advantage to more industries and increased material variability[5]. Nevertheless, improvement in the speed of component manufacture by AM will open new opportunities to improve the economic viability of producing higher volume output. Of course, there are other factors to consider when scaling up because AM can also be prone to development of defects during the additive process[12]. AM makes up for the lack of geometry complexity in manufacturing processes that involve cutting, drilling and or grinding from larger blocks of solid to build materials (subtractive manufacturing technologies) but there is often a trade-off for poor tolerance and relative quality[13].

2.1.5 Density of Additive Manufacturing products

Parts built by additive manufacturing have relative densities from 97% - 99% which is typically lower than that of parts built by conventional methods[5]. Therefore, there is critical need to ensure the right build parameters are used for the AM process to reach optimal relative density. Build parameters vary depending on the material of interest. If the wrong parameters are used, there is a high risk of getting a lower relative density of the finished product. Low relative density can arise due to defects such as voids or pores from partially melted powders.

2.1.6 Selective Laser Melting (SLM)

SLM is a powder-based process in which layers of about 20microns to a millimetre are spread on a powder bed[14]. A schematic diagram of the SLM process is shown in Figure 6.

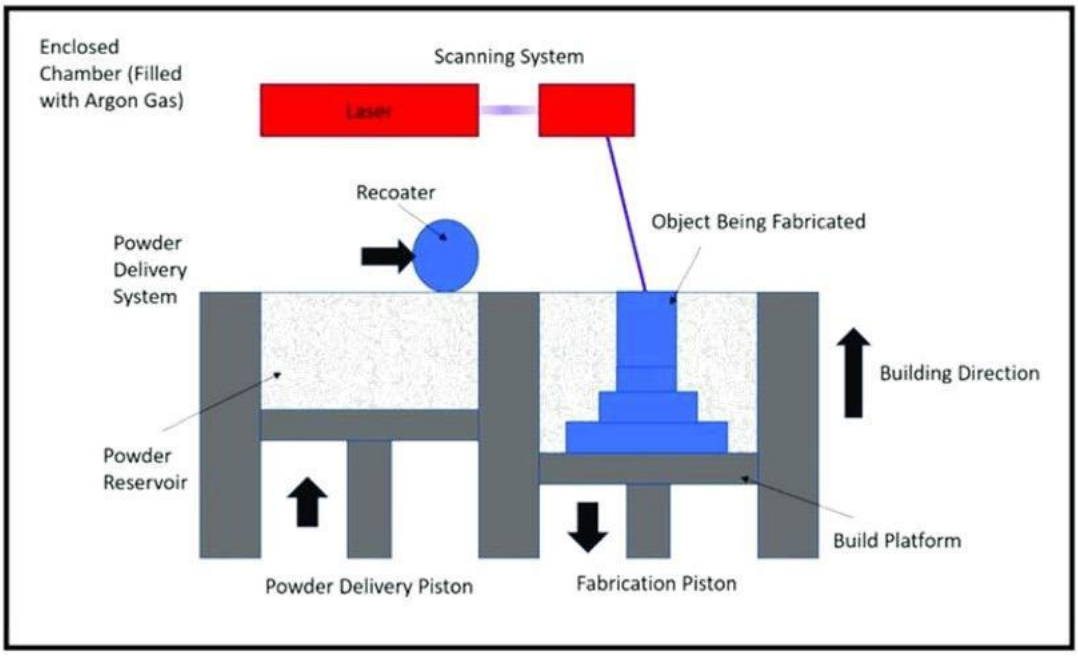

Figure 6: Schematic diagram of the SLM process[14]

Metal powder is fed onto the bed and a levelling system is incorporated to ensure uniform distribution of the powder. A laser beam with a specific laser power typically between 20W and 1KW is focused onto the powder with the aid of a galvanometer scanner. The laser beam moves with a specific scanning speed across the powder layer. The laser beam moves in the x-y plane on the metal powder based on the cross section of the part being built. The individual melt tracks follow a pattern known as the scan strategy, in which they overlap with a hatch spacing. The energy density applied to the powder layer causes the exposed powder to melt as well as the areas adjacent to the melt pool because of heat conduction. When the melt solidifies, the melt tracks and the layer below that would have solidified earlier are fused together. After a layer is selectively melted and solidified, the powder bed is lowered, and another layer of powder is fed. These steps are repeated throughout the SLM process until the part is completely built[3]. The SLM process is associated with very high temperature gradients due to the rapid heating and cooling rates as the laser beam moves along the added powder layers.

During the SLM building process, support structures are used to fix the part being built onto the build plate especially for supporting its overhanging and horizontally oriented surfaces. These support structures (lattice-like) are also important for heat dissipation. They are to be removed when the part needs to be finished. The SLM process is carried out in an inert gas environment to minimise the oxygen content (less than 0.1%) and avoid oxidation of the metal powder. Argon or nitrogen are added to the closed chamber to prevent interaction of the metal powder with the environment and to protect the melt[3].

The parameters associated with SLM are laser scan speed, layer thickness, hatch spacing, laser power and build orientation. Energy density is another parameter which is derived from laser power, hatch spacing, scan speed and layer thickness. Several studies have been done to investigate the effect of each of the parameters on the microstructure and mechanical properties of SLM products. A few of the studies are reviewed in section 2.6.

The build plate can be pre-heated to minimize residual stresses by lowering thermal gradients. Pre-heating temperatures of about 200ºC to 500ºC are commonly used. Residual stresses are stresses that remain within a material after it has reached equilibrium with the environment. They can be induced by thermal factors or plastic deformation. Production processes induce residual stresses, and the extent of the residual stresses varies from one production method to another. In most cases, residual stresses are unfavourable, were they result in deformations from the intended shape. Laser based processes introduce large amounts of residual stresses due to the high thermal gradients induced in the processes during the rapid melting and cooling stages. Therefore, all properties were measured in stress relieved conditions in this project.

2.1.6.1 SLM Ti-6Al-4V

The high temperature gradients associated with the SLM process due to high heating and cooling rates result in a non-equilibrium phase present in Ti6Al4V parts built by the SLM process[15]. The phase is a very fine acicular martensite. In comparison to the microstructure of Ti6Al4V parts manufactured by conventional production methods, the SLM Ti6Al4V martensitic microstructure results in high strength properties but very low ductility. The layer-by-layer mechanism of the SLM process results in the formation of columnar grains due to epitaxial growth of the grains from the previously molten powder layers as scanning progresses. The columnar grains are usually in the direction of the build direction[16]. A side view of columnar grains perpendicular to the scan direction in SLM Ti6Al4V is shown in Figure 7.

Figure 7: Side view of columnar grains in SLM built Ti-6Al-4V[15]

The orientation of the columnar grains depends on the direction of the local conductive heat transfer which is influenced by the scan direction[15]. The as built SLM Ti6Al4V only consists of the HCP structure as observed by XRD analysis[17]. The orientation of the columnar grains plays an important role in the microstructure and mechanical behaviour of SLM Ti6Al4V and this is further discussed in section 2.6.

2.2 Introduction to Titanium

Titanium is ranked as the 4th most abundant structural metal and the 9th most abundant element in the earth's crust with a concentration of about 0.67%[18], ranked after aluminium, magnesium and iron. However, it is hardly extracted purely which makes its processing difficult. Due to this, titanium has a high production cost[19] .

The properties of titanium which make it popular with a wide diversity of use across different industries include:

- Low density (light weight) which gives it a high strength-to-weight ratio[18]
- High specific strength
- Biocompatibility
- High temperature performance
- Excellent corrosion resistance
- Good flexibility
- Alloying of metal to improve tensile strength
- Comparable cost to super alloys
- Availability in different types and forms

Titanium and titanium alloys are mainly used in fields such as aerospace, biomedical, marine, petrochemical and automobile industries. The aerospace industry has benefited from the introduction of titanium for structures like the airframes and the engine components. Benefits have been on steam-turbine blades, superconductors, hydrogen storage media, and nuclear and fossil fuel power condenser tubing in other fields. Marine submergible vessels and ocean thermal-energy conversion components are some applications and uses of titanium and its alloys due to the excellent corrosion resistance[18].

The Biocompatibility of titanium allows it to be used in the biomedical industry as implants and prosthetics. Due to its inflated cost of extraction and desirable properties, titanium is limited to use in which high performance is required[20]. Most of the titanium that is produced is used in the aerospace industry[21].

2.2.1 The metallurgy of titanium

Titanium is allotropic, which means that it can exist as two or more crystal structures. The two crystal forms of titanium are Hexagonal Close Packed structure, HCP, also known as α titanium which is stable at low temperatures and Body Centred Cubic structure, BCC, also known as β titanium which is stable at elevated temperatures (above 882ºC)[19]. The schematic diagrams of HCP α titanium and BCC β titanium are shown in Figure 8.

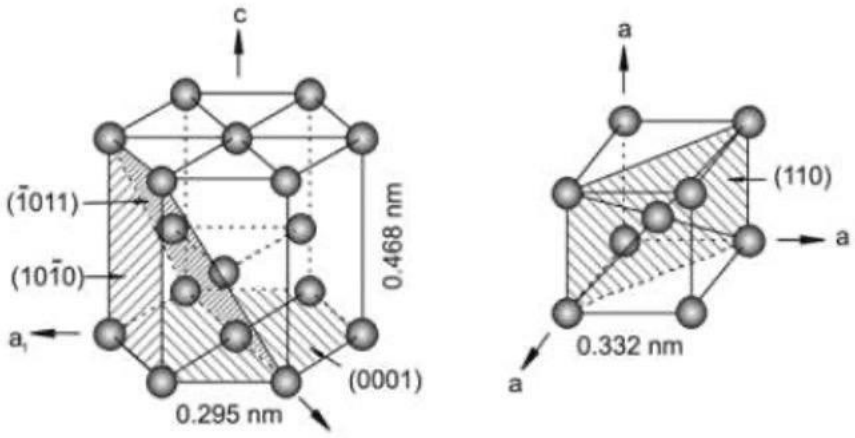

Figure 8: The crystal structures of bcc (left) and hcp (right)[19]

Allotropic transformation occurs when one crystal structure completely changes to the other at a transformation temperature known as the transus temperature. It is the basis of the large variety in properties of titanium alloys. Commercially pure titanium (CP Ti) is used in applications that require excellent corrosion resistance such as in heat exchangers, pumps, and piping. Pure Titanium can be strengthened by impurities like oxygen although this decreases the corrosion resistance.

2.2.2 Classification of titanium alloys

Addition of alloying elements either results in solid solution strengthening, a change in the transus temperature or no change at all depending on the elements. A schematic showing the effect of alloying elements on the phase constitution of titanium alloys is shown in Figure 9.

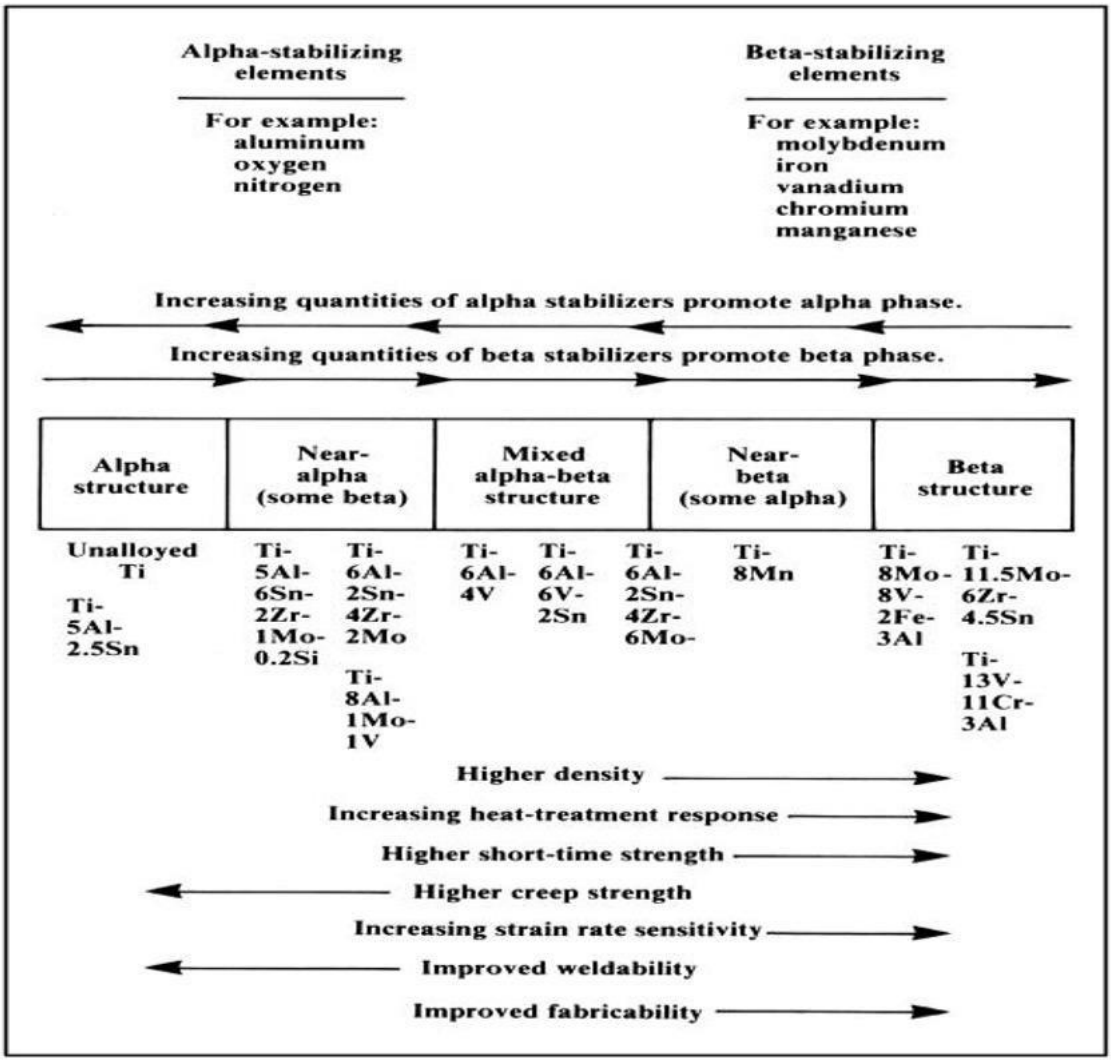

Figure 9: The effects of alloying elements on the structure of titanium and some selected properties[22]

Alloying elements that increase the transus temperature are called α stabilizers. Examples of α stabilizers are aluminium, oxygen, nitrogen, and carbon. Alloying elements that lower the transus temperature are called β stabilizers[19]. Examples of β stabilizers are niobium, tantalum, vanadium, and molybdenum. Manganese, iron, and chromium also lower the transus temperature, but a eutectoid reaction is produced which results in a two-phase structure at room temperature. Zirconium and tin have no effect on the transus temperature and are therefore considered neutral elements.

Titanium alloys are therefore classified as Alpha (α), Beta (β), and Alpha + beta (α + β) depending on the alloying elements. The commonly used group of Ti alloys is the alpha + beta group. At equilibrium, both the alpha and beta phases are stable at room temperature. The beta fraction in alpha + beta group ranges from about 5 to 40%[19]. The properties of alpha-beta alloys can be controlled by heat treatments. This is due to these alloys having two states. In these heat treatments, the precipitation and microstructural states of the beta component are adjusted[18]. The most common alpha-beta alloy is Titanium-6Aluminium-4Vanadium and it accounts for more than 50% of all the titanium usage worldwide[19].

2.3 Titanium-6Aluminium-4Vanadium (Ti6Al4V)

Ti6Al4V is an alpha-beta alloy which consists of 6% aluminium and 4% vanadium by weight. The composition varies slightly depending on the manufacturing process and this is shown in Table 2. Ti6Al4V is commonly used due to good creep resistance, biocompatibility, high specific strength and good corrosion resistance[23].

Table 2: Chemical composition of Ti-6Al-4V[23]

Elements	Ti	Al	V	C	Fe	O	N	H
Typical wt.%	Balance	6	4	0.03	0.1	0.15	0.01	0.003
Cast wt. %	Balance	5.5-6.75	3.5-4.5	<0.1	<0.3	<0.2	<0.05	<0.015
Wrought wt. %	Balance	5.5-6.75	3.5-4.5	<0.08	<0.3	<0.2	<0.05	<0.015

The tensile strength and ductility of Ti6Al4V manufactured by conventional ingot metallurgy processing methods are shown in Table 3. The remarkably low density of Ti6Al4V is of great advantage in the aerospace and automobile industries as it results in significant reduction in the aircraft weight and automobile components whilst still exhibiting high strength, lowering the costs and improving fuel efficiency[24]. It is for these reasons that this research was done on Ti6Al4V. Titanium has in many instances replaced heavier materials such as steel in many engineering applications.

Table 3: Mechanical properties of Ti-6Al-4V[23]

Property	Ti-6Al-4V (Typical)	Ti-6Al-4V (Cast)	Ti-6Al-4V (Wrought)
Yield Strength	950 MPa	758 MPa	860 MPa
Ultimate Tensile Strength	1020 MPa	860 MPa	930 MPa
Elongation	14%	>8%	>10%
Reduction of Area	40%	>14%	>25%

Ti6Al4V can be manufactured with different methods such as casting, forging and powder metallurgy. However, titanium has hard machinability and therefore the extraction cost is only a small fraction of the total cost of the component when manufactured using conventional methods[23] which are most often subtractive manufacturing (SM).

2.3.1 Phase transformations in Ti6Al4V

Ti6Al4V exists as β phase when heated to above the β -transus from room temperature as it would have gone through the α + β region. Cooling from above the β-transus under equilibrium results in the reverse transformation occurring, β phase to α phase. The β-transus for commercial Ti6Al4V is close to 1000°C[25]. If the rate of cooling from high temperatures above the β-transus is high, equilibrium will not be maintained and non-equilibrium phases are formed[19].

2.3.1.1 Phase Transformation upon heating of Ti6Al4V

The pseudo binary phase diagram of Ti6Al4V based on the effect of vanadium content is shown in Figure 10. The vertical line on the diagram indicates the composition of the alloy being investigated, which has approximately the same vanadium content as Ti6Al4V. “The vertical line indicates that the amount of β increases with increase in temperature during heating, with a full transformation to β at a temperature of 956°C. Above this temperature, the solid β is stable only up until 1693°C after which complete melting occurs. Since equilibrium is not always attained the microstructures formed might be different from those expected based on the phase diagram[26].

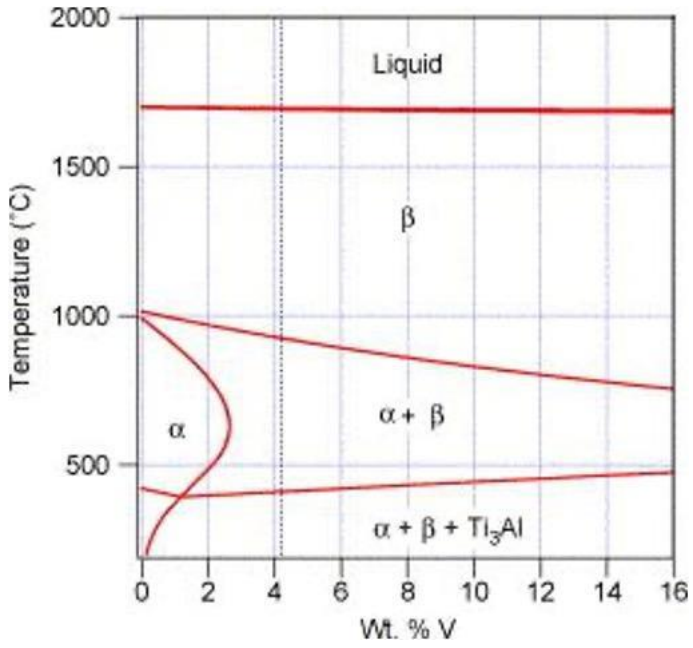

Figure 10: Calculated pseudo binary phase equilibrium showing the influence of vanadium content on the α-Ti and β-Ti phase. The vertical dashed line represents the nominal alloy composition[26]

The transformation from α to β phase is considered as a diffusion-controlled growth of the β phase[26]. It occurs upon heating and the amount of β phase formed depends on the heating rate. Elmer et al[26] conducted a study to observe the changes in the crystal structure of Ti6Al4V by measuring the amounts of α and β respectively under specific heating conditions using x-ray diffraction (XRD) techniques. In the first experiment, nine different samples were heated to different peak temperatures between 600°C and 1000°C respectively at the same heating rate of 30°C/s and the amount of β phase was measured as the fraction of BCC in each case. The results of this experiment are shown in Figure 11.

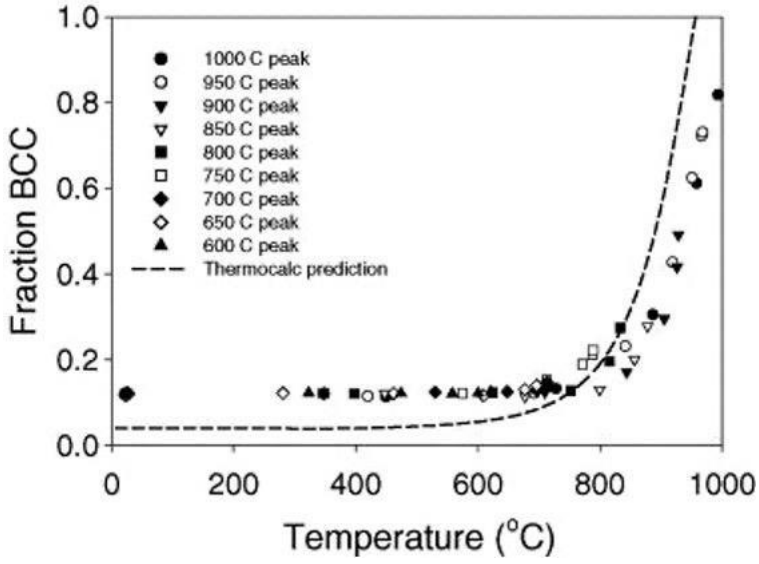

Figure 11: The measured fraction of Ti6Al4V BCC phase in the heat affected zone during continuous heating by XRD. The dashed line shows the thermodynamic prediction[26].

"In this experiment, the amount of β (shown as Fraction BCC on the graph) increased with an increase in peak temperature. This illustrates that different amounts of BCC are produced depending on the temperature that Ti6Al4V is heated to. The increase in BCC observed follows a similar trend to the dotted curve plotted from thermodynamic predictions although the starting ® content in the experiment is higher than that predicted by thermodynamics. When Ti6Al4V is heated to high temperatures and rapidly cooled during manufacture, only a small amount of ® that is formed at high temperatures transforms to α upon rapid cooling since the α to β transformation is diffusion controlled. This results in a higher starting β content at room temperature than predicted by thermodynamics"[26]. This phenomenon is observed in mill annealed Ti6Al4V which is heated to about 700° and it can explain the phase transformation dynamics in SLM Ti6Al4V since it involves high heating and cooling rates.

In the second experiment, the effect of heating rate on the transformation rate was investigated. In the first instance, two samples were both heated to 500°C at a heating rate of 10°C/s. The heating rate of one of these two samples was then reduced to 2°C whilst the other sample was kept at the same heating rate of 10°C but heated to 1000°C. The fraction of BCC formed in these samples was measured and compared to that formed with the samples that were heated at 30°C/s in the first experiment. The results are shown in Figure 12.

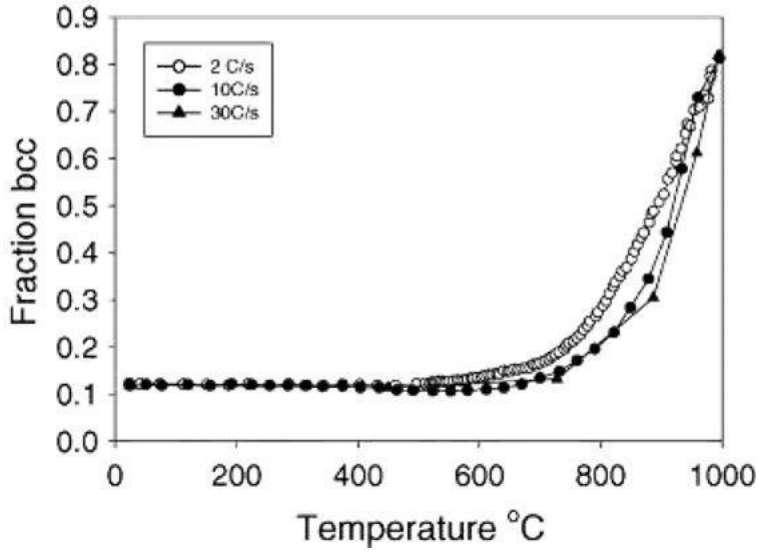

Figure 12: Measured BCC phase fraction vs temperature of the samples heated at different heating rates[26]

From the graph in Figure 12, it is shown that the Ti6Al4V samples heated at the lowest rate (2°C/s) yield the highest volume fraction of the beta phase at temperatures below approximately 925°C. At 925°C the measured amounts of BCC become of the samples heated at 2°C/s and 10°C/s become equal. Looking at the graph, the transformation rate of the sample heated at 10°C/s seems to be limited below this temperature. It is only when this temperature is reached that diffusion is rapid enough to recoup for the high heating rate. The same is observed with the samples heated at 30°C/s whereby a temperature of 1000°C is required for the diffusion to make up for the high heating rate[26].

This experiment leads to the conclusion that if Ti6Al4V samples are heated at high heating rates, transformation kinetics are limited therefore a higher β transus temperature will have to be reached for equilibrium diffusional rate to be achieved. For the sample heated at 30°C/s, a temperature of 1000°C is required for the diffusional rate to reach that of the sample heated at 2°C[26].”

2.3.1.2 Phase Transformation upon cooling of Ti6Al4V

The transformation of the β phase upon cooling is of essential importance in the microstructural revolution of titanium since different types of microstructures are yielded depending on the cooling rate. Rapid cooling results in the β phase undergoing a martensitic transformation whilst slow cooling allows for diffusional transformation. Diffusional transformation is the nucleation and growth of the α phase from the β phase, usually on the β-phase grain boundaries. A schematic diagram illustrating this transformation process is displayed in Figure 13.

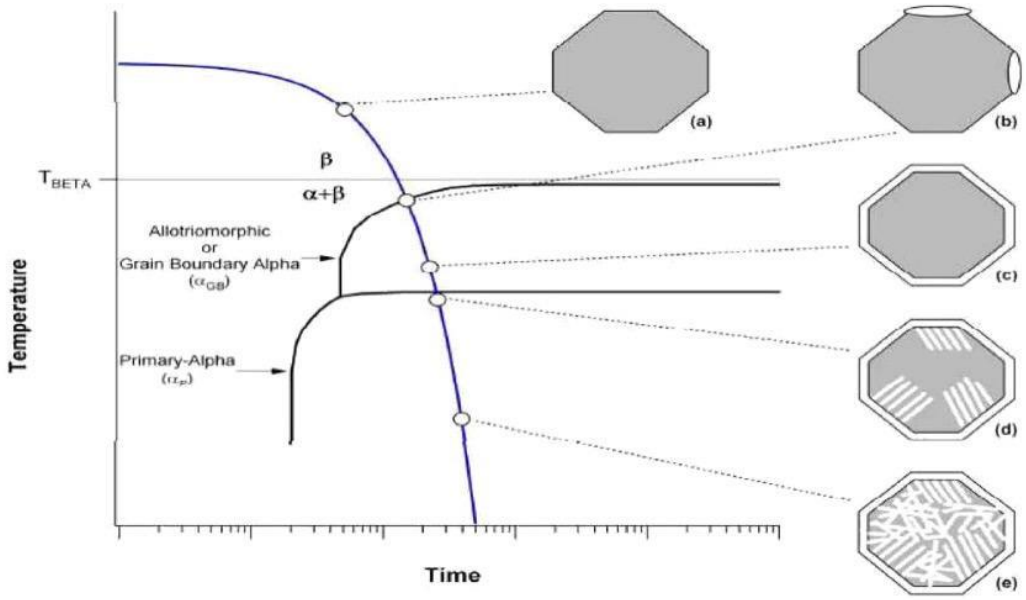

Figure 13: The process of nucleation and growth of α to form an equilibrium α/β microstructure when cooling slowly from above the β-transus temperature[27]

From the graph in Figure 13, (a) shows a single β grain that exists above the β-transus temperature, (b) shows the nucleation of grain-boundary α allotriomorphs at temperatures just beneath the β-transus, (c) shows the completion of this grain-boundary α, (d) shows the growth of α lamellae colonies into the parent βgrain from the α allotriomorphs, and (e) shows the nucleation and growth of basket-weave α lamellae in the interior of the parent β grain as cooling continues[27].

When the α phase starts growing after cooling, vanadium is required to diffuse out of the growing α phase into the remaining β phase. However, the rate at which vanadium diffuses out is slower than that of aluminium diffusing into the α phase. As a result, the interface between the two phases becomes rich in vanadium and even richer than the fraction of vanadium in the ® phase. The growth of α precipitates continues from the α precipitate grain boundaries into the vanadium rich β grains (high aspect ratio lamellae). The growing α phase has a fixed orientation relationship with that of the parent β phase based on the Burgers orientation relationship. The growing alpha phase can only assume 12 orientation variants[27].

Multiple lamellae of α phase emerge with some retained β phase between them of the same orientation as the parent beta grain. These lamellae pockets are called colonies. Lamellae can form either as colonies or as single lamellae. When lamellae nucleate and form as single lamellae, a Widmanstätten (basket-weave) structure is formed. This structure is most prevalent when cooling from above the β-transus temperature since it mostly occurs within the parent β grains. It also prevails when samples are soaked in the β phase region for a long period of time resulting in large β grains forming before the cooling process[27]. Larger beta grains exaggerate the occurrence of intragranular nucleation and growth and hence promote Widmanstätten growth.

Research on the effect of cooling rates on microstructure and the diffusion process has been performed by several scientists. In one study by Ahmed and Rack[28] they investigated the effect of cooling rates on microstructure evolution in Ti6Al4V that had been heated to 1050°C. The end quench Jominy procedure was performed, and the cooling rates were determined as a function of location and temperature being derived from the sample temperature-time history during cooling which was observed by monitoring the thermocouples continuously. The results of this research are shown in Figure 14.

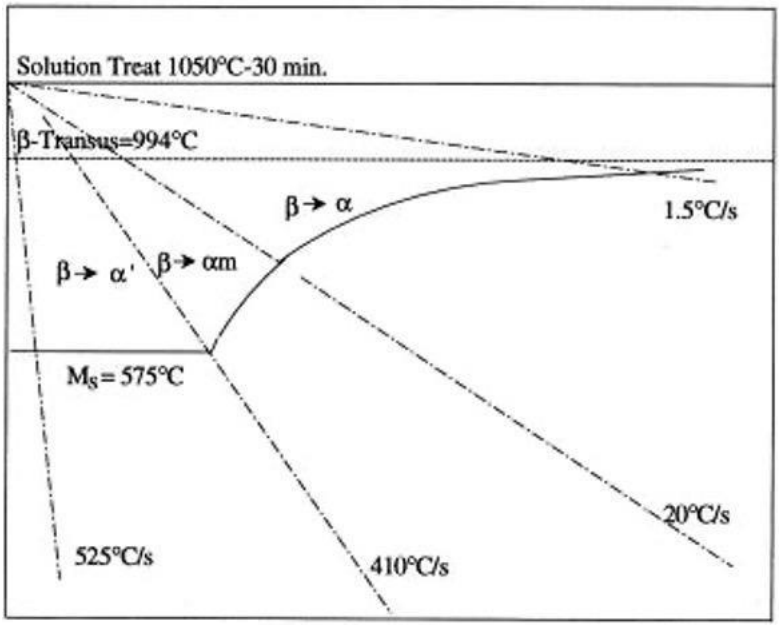

Figure 14: The cooling diagram for Ti-6-Al-4V Beta solution treated at 1050°C for 30 mins[28]

Cooling rates higher than 410°C/s were required for Ti6Al4V to fully transform into a martensitic microstructure. Lower cooling rates resulted in mixed microstructures of α' martensitic, massive α and various other forms of diffusion controlled α[28]. The critical cooling rate was identified to be 20°C/s. At rates below 20°C/s, diffusional transformation into an equilibrium structure of α and β took place.

2.3.1.3 Martensitic transformations

As mentioned earlier, when Ti6Al4V is rapidly cooled from above the Ms temperature, no time is allowed for diffusion to take place and martensitic transformation occurs. The transformation involves the movement of atoms resulting in the change of the bcc into the hcp crystal lattice and the products obey the Burgers orientation relationship in just the same way as for the diffusion products. The results of martensitic transformation can either be α' martensite which can further be split into acicular martensite and massive/lath martensite, or orthorhombic martensite commonly denoted as α''[29].

In Ti6Al4V, α' is the most common martensite (α'' is mostly common in alloys with high β-stabiliser elements). An increase in the abundance of orthorhombic α'' martensite was noted in a study by Lee and Welsh[30] when Ti6Al4V was quenched from temperatures between 800ºC and 900ºC which was due to the increased vanadium content of the β phase present at that temperature. The lath martensite exists as packets of small laths belonging to the same Burgers relationship variant. The acicular α' martensite exists as a mixture of α plates each with different variants of the Burgers relationship[29].

The β phase exhibits different compositional changes at different temperatures within the α+β region due to the change in vanadium concentration when the α phase starts growing[27]. These compositional changes must be considered. Acicular and lath martensite cannot be distinguished as they both have an HCP crystal structure. Consequently, electron backscatter diffraction will index both structures as titanium α HCP phase. Transmission electron microscopy can be used to distinguish the two structures.

2.3.2 Microstructure of Ti-6Al-4V

In this section, the microstructural features of Ti6Al4V particularly the prior-β grain boundaries, porosity, existing phases, and crystallographic texture will be described as they influence mechanical behaviour of the alloy.

The α+β alloys (Ti6Al4V) generally exhibit three different microstructures depending on the heat treatments involved. The three microstructures are fully lamellar, fully equiaxed and bimodal. These microstructures are illustrated in Figure 15.

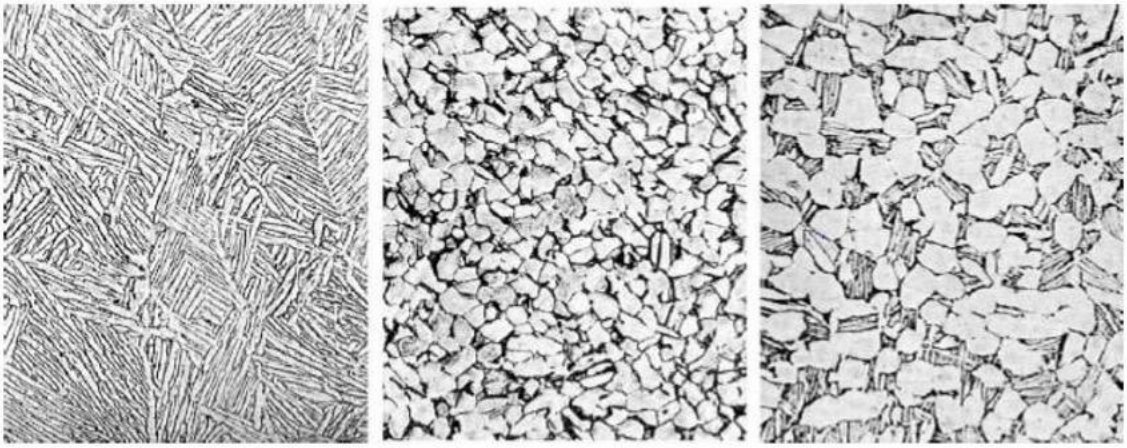

Figure 15: The three distinct microstructures of Ti-6Al-4V from left to right: fully lamellar, equiaxed and bi-modal[31]

2.3.2.1 Fully Lamellar microstructure

The processing route for obtaining a fully lamellar structure and an image of the microstructure is demonstrated in Figure 16. The lamellar microstructure is obtained when the alloy is heated into the β phase region usually just 30-50ºC above the β-transus to control grain size, followed by continuous cooling and aging between 700ºC and 800ºC[31]. Ti6Al4V can age harden by the precipitation of Ti_3Al. Aging increases strength of the alloy.

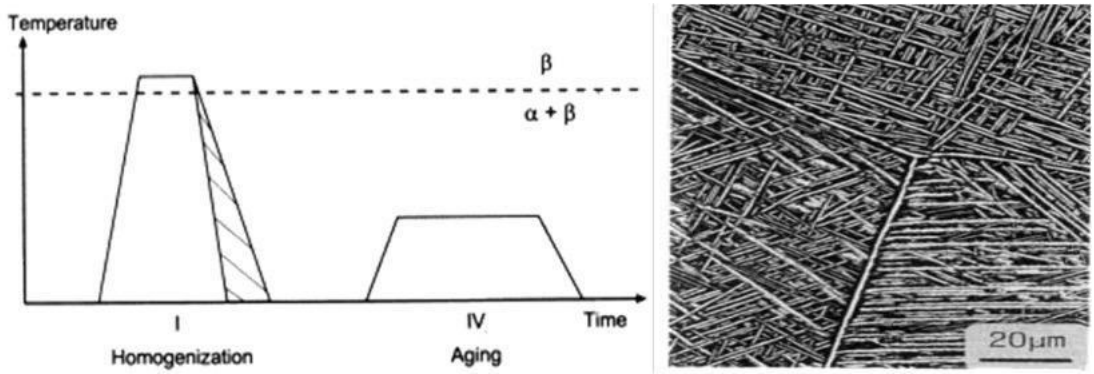

Figure 16: From left to right: Processing route for fully lamellar microstructure[32] and the achieved lamellar microstructure of Ti6Al4V showing the basket-weave pattern[21]

The lamellae are either fine or coarse depending on the cooling rate[21]. The microstructures obtained by slow cooling (furnace cooling) and fast cooling (quenching) are displayed in Figure 17. Slow cooling rates from the β phase result in pure lamellar microstructure (shown by the microstructure obtained after furnace cooling) and the slower the cooling rates, the course the lamellae. Fully lamellar structures (shown by the microstructure obtained after water quenching) have excellent stress corrosion resistance and high fracture toughness. However, they have low ductility[22].

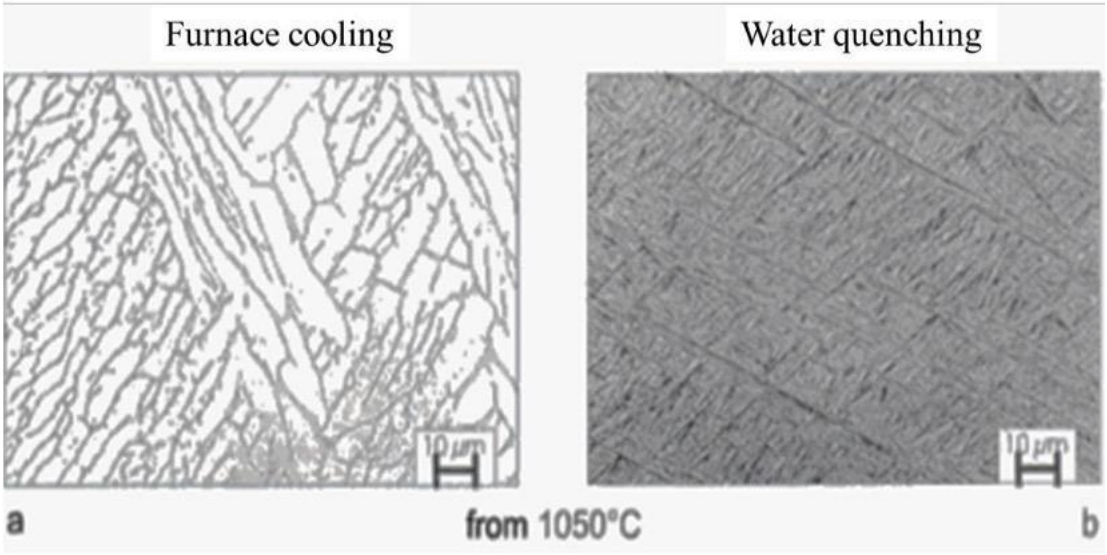

Figure 17: Microstructures of Ti-6Al-4V after (a) furnace cooling (b) water quenching[19]

2.3.2.2 Bi-modal microstructures

Bi-modal structures are comprised of both equiaxed and lamellar structures. An image showing the bi-modal structure is shown in Figure 18. The equiaxed structure is formed within the matrix of the transformed β lamellar structure during the recrystallization process. A deformation step is therefore required to create a bi-modal structure[33].

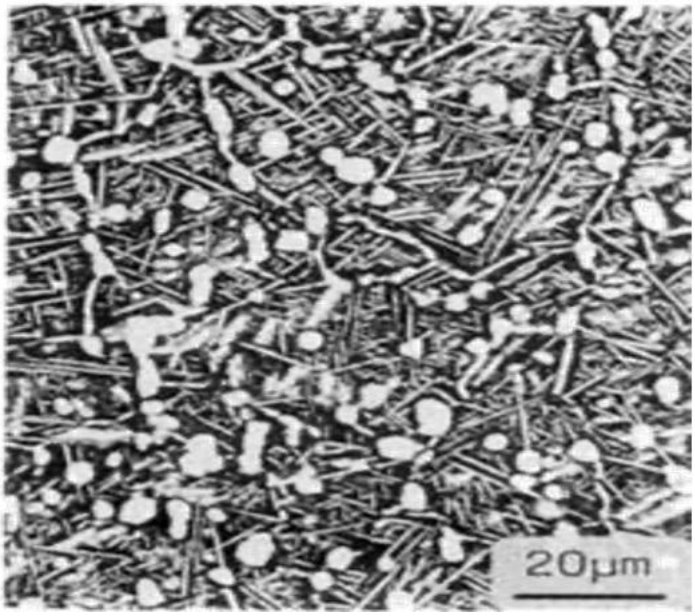

Figure 18: Bi-modal microstructure of Ti6Al4V[21]

The process route for obtaining a bi-modal structure is shown in Figure 19. The first step is homogenization in the β phase region wherein the lamellar structure is formed upon cooling. The structure is then deformed at an elevated temperature. The recrystallisation process then follows which results in the structure now being comprised of equiaxed α grains. It is done at a temperature in the α+β region. The equiaxed α is retained and the β decomposes into a lamellar structure upon cooling[32].

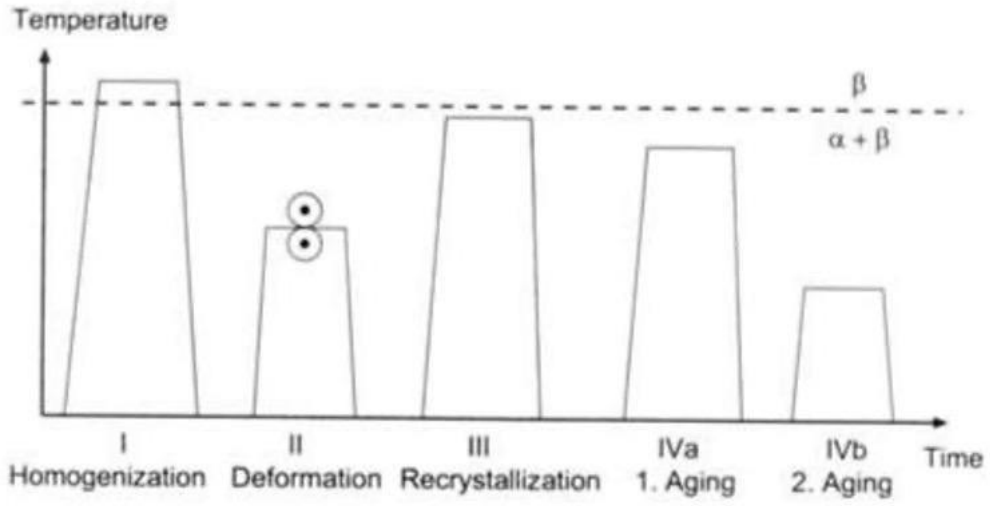

Figure 19: Processing route for bi-modal microstructures in Ti-6Al-4V[32]

2.3.2.3 Fully Equiaxed microstructure

Equiaxed structures have globular α grains surrounded by β phase at grain boundary "triple points." [21]. An image of an equiaxed structure is reproduced in Figure 20. The process route for obtaining equiaxed microstructure is the same as that shown in for bi-modal structures but with a much lower recrystallization temperature. The most important step in this process is the recrystallization process below the β-transus. The volume fraction of equiaxed alpha surrounded by retained beta phase is determined by the recrystallization step. The temperature of the recrystallization step is low to ensure no β grains are formed[32]. Heating temperatures and cooling rates also affect the equiaxed structures. Fully equiaxed microstructures result in high strength, high ductility but relatively low fracture toughness.

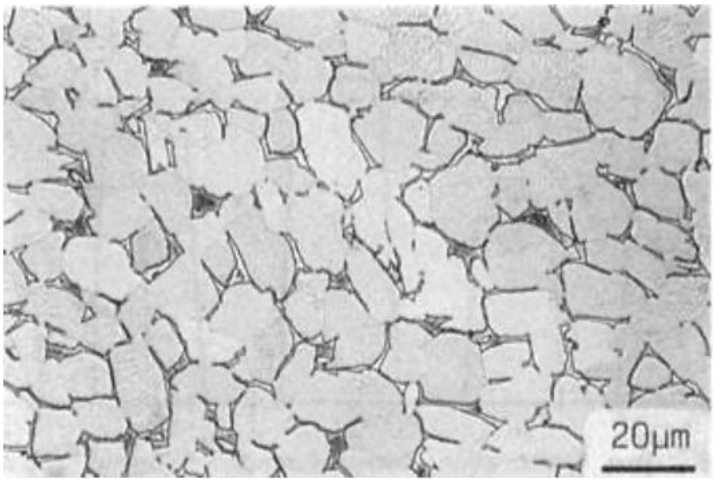

Figure 20: Equiaxed microstructure of Ti6Al4V with α grains appears light and β phase appearing dark at grain boundaries and triple points[29]

2.4 Illustration of industrial application of SLM Ti6Al4V

2.4.1 Brake callipers

Brake callipers are a component of the disk-brake system of a vehicle which aid to the function of the brakes. They are located on each wheel. Their function is to get the vehicle to reduce its speed. Brake callipers squeeze the brake pads against the rotors which slows down the spin of the wheel therefore slowing down the vehicle. Brake callipers achieve this function by acting as a bracket to support the brake pads on either side of the rotor and by using pistons to convert pressure exerted on the brake fluid by the master cylinder into the friction on the rotor[b]. An image of a brake calliper incorporated into the disc brake system is shown in Figure 21.

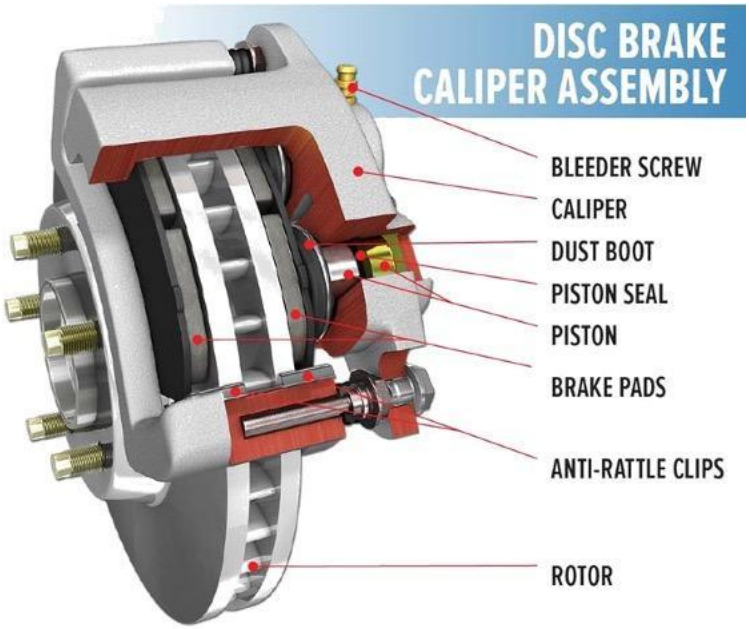

Figure 21: Brake calliper and disc-brake system[c)]

Over the past few decades, the automotive industry has established new technical developments and innovations for extreme performance. Bugatti, which is a French luxury automotive brand has succeeded in designing a brake calliper that can be produced by 3D printing. An image showing the new 3D printed brake calliper from Bugatti is shown in Figure 22.

Figure 22: 3D printed brake calliper, Bugatti[d)]

Brake callipers have been manufactured with aluminium as the main material to date, but the new brake has titanium (Ti6Al4V) as its main material. The new choice of material combines minimum weight with maximum stiffness. The Ti6Al4V alloy offers considerably higher performance than aluminium. For example, a 3D printed Ti6Al4V component has a tensile strength of 1250 MPa. The new titanium brake calliper is 41 cm long, 21 cm wide and 13.6 cm high with a weight of only 2.9 kg. An aluminium 3D printed component with the same dimensions weighs 4.9 kg. Bugatti could therefore reduce the density of the component by 40% and ensure even higher strength as the same time by using titanium[d)].

2.5 Mechanical testing

2.5.1 Linear Elastic Fracture Mechanics

The behaviour of cracked material under specific load is investigated by a mechanics framework which is referred to as fracture mechanics. Fracture mechanics gives an insight to a materials toughness, crack growth processes and their application to real life engineering problems. Materials which are homogenous and isotropic have small strains and displacements and they behave in a linear elastic manner. The applied mechanics framework used on these materials is therefore referred to as linear elastic fracture mechanics (LEFM)[34]. For materials that are have higher plasticity, where the size of the crack tip plastic zone is similar to that of the crack length, the applied mechanics framework would be elastic plastic fracture mechanics (EPFM).

2.5.1.1 Stress Intensity Factor

The stress intensity factor (SIF) is used to analyse properties of a material in the presence of a crack. When a notch is machined into a specimen the tip of the notch becomes an area of high stress concentration as the crack grows from it. The radius of the crack growing from the notch tip is significantly smaller and it approaches zero. There will therefore be much higher local stresses and higher stress concentration at the crack tip. Stress intensity factor is defined as the amount of stress at the crack-tip and is defined by Equation 1.

$$K_I = Y\sigma\sqrt{\pi a}$$

Equation 1: Stress intensity factor

In Equation 1, K_I is the stress intensity factor in mode I fracture condition (in which stress is orthogonal to the local plane of the crack surface), Y is a geometrical modification factor, σ is applied stress and 'a' is the crack length of a surface crack of half the length of an internal crack[35]. The relationship between K_I and σ shown by this equation is known as the "triangle of integrity." The SIF is measured in MPa√m.

2.5.1.2 Fatigue Crack Growth Rate

Fatigue Crack Growth Rate (FCGR) is used to test fatigue failure of a material by a process of crack propagation and subsequent growth which is driven by applied cyclic loads[36]. Fracture by fatigue occurs when an object is subjected to repeated stresses well below the yield stress which induce damage over some time. This is primarily the reason why over 80% of mechanical failures are due to fatigue and it is the cause of turbine-engine failures in aircrafts. Repeated cycles of stresses can be noted in machined parts such as springs, aircraft wings, axles, connecting rods and turbine engines which are subjected to alternating loads.

Fatigue failure starts off with either a small crack which may develop, an already existing surface crack or from surface imperfections. These act as stress raisers and will prompt crack initiation. Notches also act as stress raisers. Cracks can still initiate in the absence of flaws due to the formation of slip planes[37]. When a material is subjected to fluctuating stresses, intrusions and extrusions form along the slip planes which resemble crack initiation at approximately 45° to the applied stress on planes of easy shear. This is depicted in Figure 23. Fracture is considered to be either ductile or brittle depending on the specimen geometry, the loading conditions and the properties of the material[38]. Ductile materials are more prone to fatigue failure as they remain elastic when the load is low enough with only the tip of the crack being the plastic zone, and then undergo fast fracture when the critical crack length is reached[39].

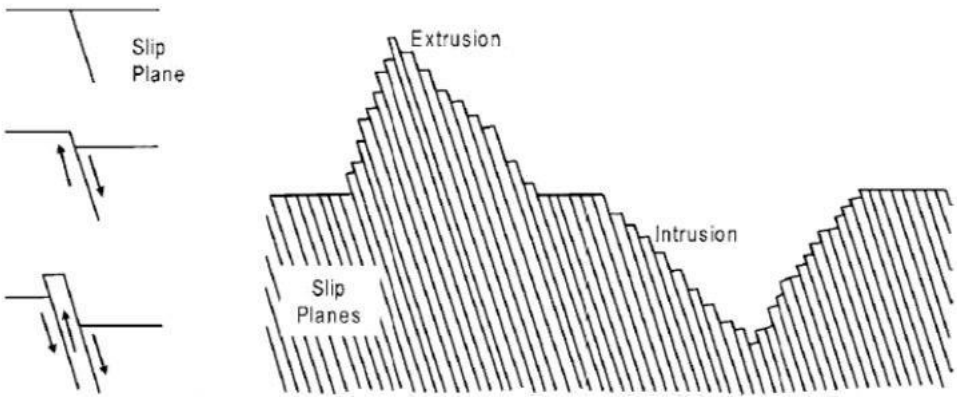

Figure 23: Development of intrusions and extrusions during fatigue[37]

Crack growth involves three stages. Stage I is crack initiation which is influenced by microstructural features like grain boundaries. If a material has fine grain structure, the crack comes across more impediments as it finds direction. Grain refinement therefore increases fatigue strength[38]. As crack length increases the stress intensity becomes dominant and the crack direction becomes perpendicular to the applied stress[37].

Stage II and III are part of the crack propagation phase which begins when the crack direction becomes perpendicular to the applied stress. Stages I and II of crack propagation are shown in Figure 24.

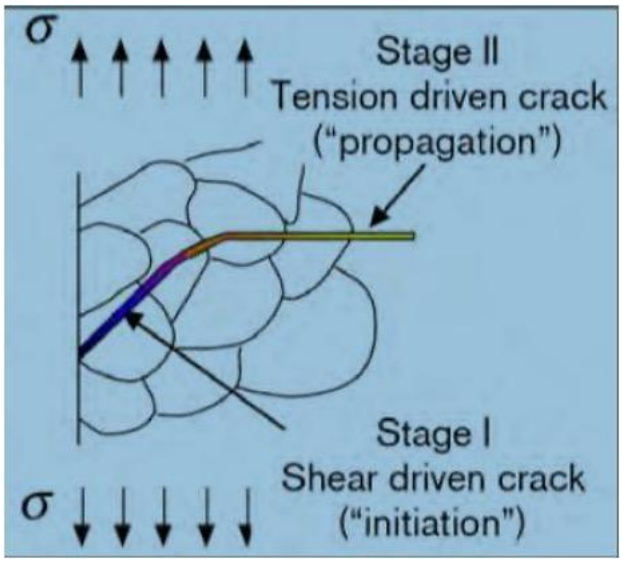

Figure 24: Stages I and II of fatigue crack propagation[37]

In Stage II crack growth is due to the tensile stress. Crack growth in stage II is stable and this is where striations are formed. Striation formation is based on the continuous opening and closing of the crack tip during fatigue loading and can be examined by SEM. Each striation represents a fatigue cycle[37]. When the crack length reaches a critical length, stage III crack propagation begins. At this stage, the material cannot withstand the stress intensity and fast fracture occurs instantly[37]. The three stages of crack growth can be represented on what is known as the Paris curve. A Paris curve illustrating the three stages of crack growth is shown in Figure 25.

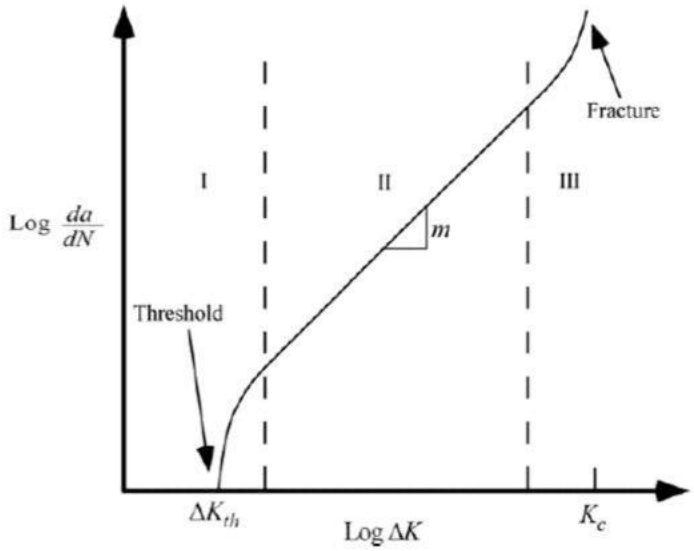

Figure 25: Paris curve showing crack growth behaviour[40]

The Paris curve is plotted on a log-log scale where the cyclic stress intensity amplitude (ΔK) is the x-axis and the crack growth rate per cycle (da/dN) is the y-axis. The Paris curve is divided into three regions which correspond to the three stages of crack growth discussed above. The first region represents crack initiation whereby the limiting value is the fatigue threshold stress intensity (ΔKth). In this region, no fatigue cracking occurs below ΔKth. The second region is where stable crack growth occurs and a linear relationship between cyclic stress intensity amplitude and crack growth rate. This region is quantified by LEFM with a law known as the Paris law defined by Equation 2.

$$\frac{da}{dN} = C(\Delta K)^m$$

Equation 2: Paris law

In Equation 2, *C* and *m* are both material parameters which are obtained experimentally based on the properties of the material and the environment. When the crack growth reaches region III, the crack growth rate increases rapidly, and the stress intensity reaches a critical value. At this critical value, the material does not have the ability to resist fracture anymore, and so fast fracture occurs. Both *C* and *m* parameters determine the crack growth rate according to the Paris equation.

The smaller the two parameters, the lower the crack growth rate. A finding by Ohta and Sasaki[41] suggests that crack closure depends on ΔK and that as ΔK approaches to the threshold level, the crack tip becomes closer and thus the value of ΔKeff decreases. With smaller m values, the crack opening level remains constant with an increase in ΔK whereas with higher m values, it increases linearly with increase in ΔK. Therefore, the exponent *m* parameter mainly reflects the dependency of crack growth on ΔK. The parameter *C* depends on *m* and the calculated crack growth rate and ΔK at each point as illustrated by the Paris equation. The effect of the two parameters suggests that the cyclic straining at the crack tip primarily affects the crack closure behaviour rather than the damage accumulation process in the plastic zone as it varies with ΔK[42].

2.5.1.3 Fracture Toughness

The ability to resist fracture at the critical stress intensity is known as the material's fracture toughness. Fracture toughness is defined by Equation 3 shown below.

$$K_{IC} = \sigma_f Y \sqrt{\pi a_c}$$

Equation 3: Calculation for Fracture toughness K_{IC}

In Equation 3, σ_f is the stress at fracture, Y is a dimensionless geometrical factor and ac is the critical crack length of a surface crack or half the length of an internal crack. As thickness of a material increases, fracture toughness approaches an asymptotic value known as plane strain fracture toughness which is considered to be the true fracture toughness of the specimen as it is independent of the materials thickness[43]. The thickness parameter for a plane strain fracture toughness specimen must be selected such that the fracture toughness measurement is valid. The thickness parameter, B is calculated based on Equation 4.

$$B \geq 2.5 \left(\frac{K_{IC}}{\sigma_y}\right)^2$$

Equation 4: Criteria for determining the test specimen thickness parameter, B, for a valid fracture toughness measurement

In Equation 4, B is the specimen's thickness. The relationship between the specimen's thickness and fracture toughness is shown in Figure 26. The smaller the thickness, the higher the fracture toughness. In the diagram, the specimens are displayed to show plane stress and plane strain. Plane stress is a stress state in which the normal stress and the shear stress applied perpendicular to the x-y plane are assumed to be zero. Plane strain is a state of strain in which the strain normal to the x-y plane and the shear strain are assumed to be zero. Thinner specimens will be in plane stress condition in which shear lips are seen on the fracture surface[43].

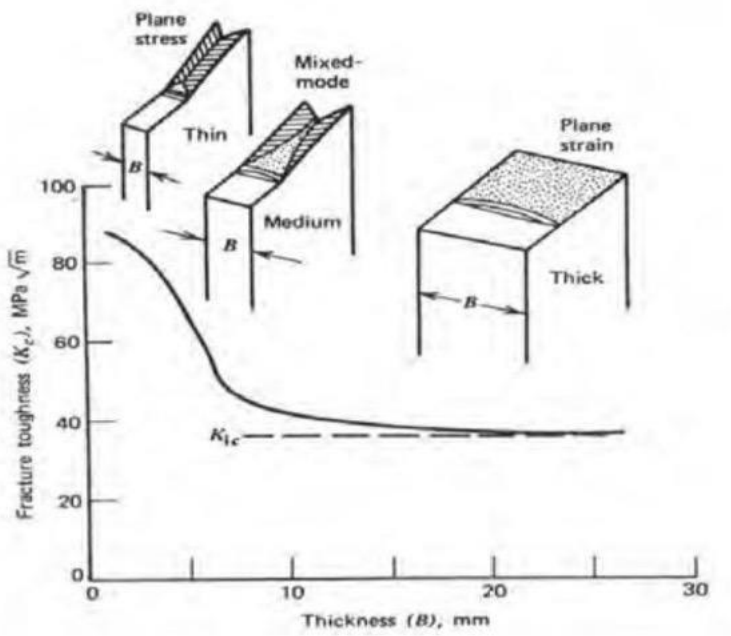

Figure 26: Relationship between specimen thickness and fracture toughness[43]

Fatigue and fracture toughness testing can be used to investigate the structural integrity of engineering systems when inherent flaws are subjected to operational stresses. The integrity of engineering systems is determined based on the fitness of the system to carry out its function. Fracture mechanics provides a relationship between flaw size, stress and toughness which is known as the “Triangle of integrity” which is shown in Figure 27.

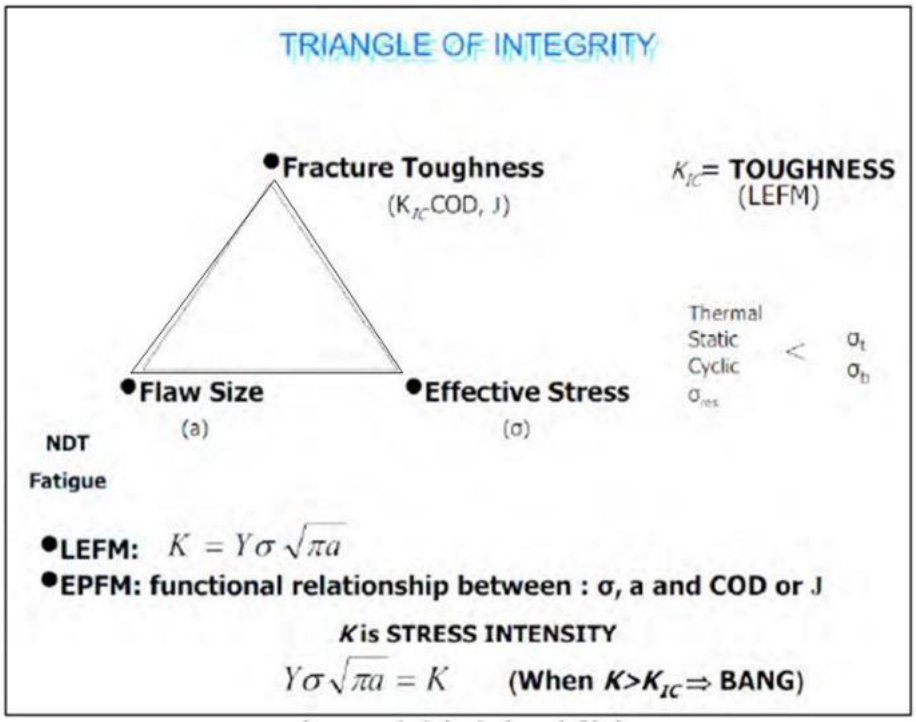

Figure 27: The Triangle of Integrity[44].

If one of the components of the "Triangle of Integrity" is known, the other two can be calculated. The Paris equation can also be used to calculate the remaining components by substituting Equation 1 into Equation 2. This new equation is shown in Equation 5.

$$\frac{da}{dN} = C\left(\Delta\sigma Y\sqrt{\pi a}\right)^m$$

Equation 5: Stress intensity factor equation inserted into Paris equation

Equation 5 can be rearranged to calculate the number of cycles to failure. The rearranged equation is displayed in Equation 6.

$$dN = \frac{da}{C\left(\Delta\sigma Y\sqrt{\pi a}\right)^m}$$

Equation 6: Rearranged Equation 2.5

Equation 6 can then be integrated between the ai determined from the NDT testing and the critical crack, a_f, determined from the "Triangle of Integrity" for the number of cycles to failure to be solved. The integration expression is shown in Equation 7.

$$N_f = N \int_0^{N_f} dN = \int_{a_i}^{a_f} \frac{da}{C\left(\Delta\sigma Y\sqrt{\pi a}\right)^m}$$

Equation 7: Integration expression for number of cycles to failure

When the "Triangle of Integrity" and the Paris equation are combined, some important fracture mechanics parameters or conditions can be answered, such as:

- The safety of the specimen in the presence of a crack
- The critical crack size at service loads
- The probability of the time it would take for a crack to grow from initial to critical size

2.6 Relevant case studies

In this section, microstructure and mechanical properties were assessed in several studies to test the operational performance of the SLM Ti6Al4V parts with special interest in the influence of scan speed. The authors in these studies used different terminologies to define the specimen build orientations investigated. In Pal's work, the specimens built with the tensile axis in the vertical direction are defined as "lengthwise vertical." The same type of orientation is defined as "XZ" in Cain's work and "ZX" in the work of Simonelli et al. The specimens built with the tensile axis in the horizonal direction are defined as "width-wise vertical" in Pal's work. The same orientation is defined as "XY" in Cain's work an "XY (flat)" in the work of Simonelli et al. Other orientations mentioned in Pal's work are the lengthwise and width-wise specimens built at an inclination of 30° on the build plate. The four case studies are important to this research as they help understand current findings and the gap in literature.

2.6.1 Pal et al (2019)

Pal et al[45] investigated the effect of energy density and build orientation on the microstructure and mechanical properties of Ti6Al4V manufactured by selective laser melting. The aim of this case study is to emphasise the role of energy density (and how it is impacted by scan speed) on the microstructure and properties of SLM built parts. In addition, build orientation is included as a variable. Energy density is the energy input on which the melting process of the powder, fusion and solidification depend. The effect of energy density was analysed by varying the laser scan speed as it is one of the build parameters expected to directly influence energy density according to the energy density equation shown in Equation 8.

$$E = \frac{P}{v * h * H}$$

Equation 8: Energy density

In Equation 8, E is the energy density, P is the laser power, v is the scan speed, h is the hatch spacing and H is the layer thickness. According to this equation, energy density and scan speed are inversely proportional, therefore an increase in scan speed is expected to result in a decrease in energy density.

Four build orientations were investigated. The specimens were built either lengthwise vertical, lengthwise inclined, width-wise vertical and width-wise inclined. Seven different energy densities were achieved by varying the scan speed from 150 mm/s to 1000 mm/s. The rest of the build parameters used were kept constant. The energy densities, relative densities and tensile properties of the specimens are shown in Table 2.4 and an image showing the build orientations of the tensile specimens after fabrication is displayed in Figure 28.

Table 4: Energy Densities used in the work performed by Pal

Sample set number	**Scanning speed (mm/s)**	**Energy Density (J/mm^3)**	**Average Relative Density (g/mm^3)**	**Ultimate Tensile strength (MPa)**	**Yield strength (MPa)**	**Elongation at break (%)**
1	1000	39	4.38	1162	980	5.3
2	800	49	4.39	1275	1088	5.4
3	600	65	4.38	1290	1113	5.4
4	400	97	4.38	1308	1148	4.1
5	300	130	4.33	1012	980	3.0
6	200	30	4.30	530	535	2.4
7	150	30	4.32	413	378	1.8

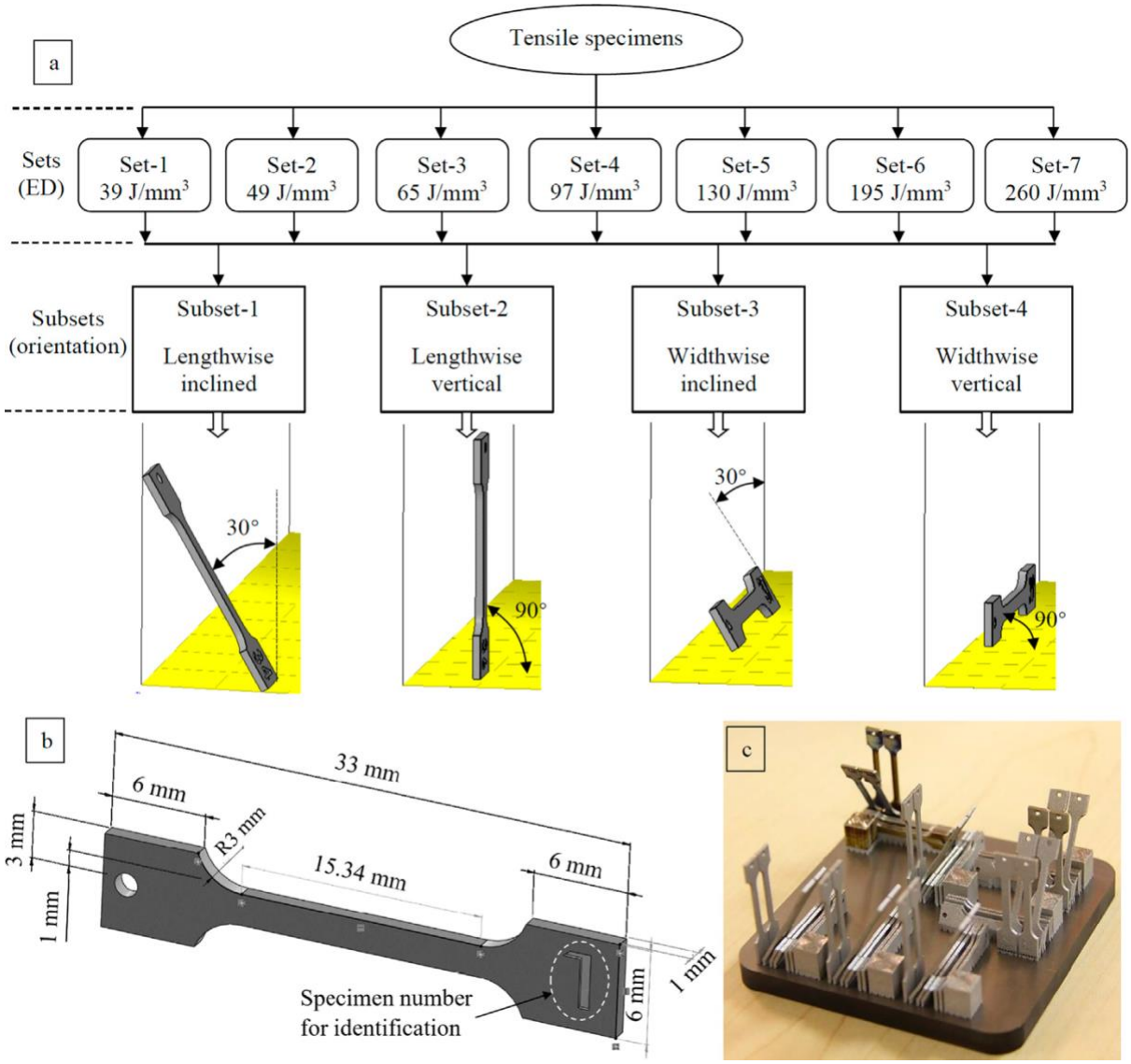

Figure 28: Tensile specimens fabricated by the Selective Laser Melting with different EDs and building orientations (a) fabrication setup of the tensile specimens; (b) dimensions of the tensile specimens; (c) photograph of fabricated tensile specimens

The density of the samples was measured using the Archimedes principle. The density results obtained displayed a dependency of relative density on energy density. The samples built vertical in both the lengthwise and width-wise sets have higher density compared to their pair inclined specimens. Furthermore, the specimens built lengthwise vertical had higher density than those built width-wise vertical, but this phenomenon is not observed in the set of specimens built with the highest energy density. Another perspective revealed that set 3 fabricated with energy density of 65 J/mm had the highest density of 4.3979 g/cm^3 which translates to 99.3% relative density. It was observed that the average relative densities increase from set 1 fabricated with the lowest energy density of 39 J/mm^3 to set 3 (energy density of 65 J/mm^3) and then decrease from set 4 (energy density of 97 J/mm^3) to set 7 (energy density of 260 J/mm^3).

The mechanical behaviour of the samples built with different energy densities and build orientation was investigated by tensile testing. The ultimate tensile strength and elongation results obtained showed that the tensile properties varied with energy density and build orientation. When the energy density is increased from 39 J/mm^3 to 49 J/mm^3, an increase in tensile strength is observed. The same phenomenon is observed when the energy density is further increased to 65 J/mm^3 and 97 J/mm^3 . However, when the energy density is further increased to 130 J/mm^3 and above, a decrease in tensile strength and ductility is observed. The tensile specimens built with the highest energy density (260 J/mm^3) had poor tensile strength and ductility. The lengthwise vertical and width-wise vertical specimens both had better tensile properties compared to their inclined counterparts. The lengthwise vertical specimens had the best tensile properties compared to the width-wise vertical specimens in all the sets of different energy densities except for the set of specimens built with an energy density of 39 J/mm^3.

Pore morphology, void defects and the microstructural properties of the material built in different energy densities were explored using SEM. Tensile properties are affected by relative density and hence it is important to analyse the presence of pores and how it varies with energy density. The microstructure was analysed in the vertical and horizontal planes. The results of the SEM images showing the presence of pores is shown in Figure 29.

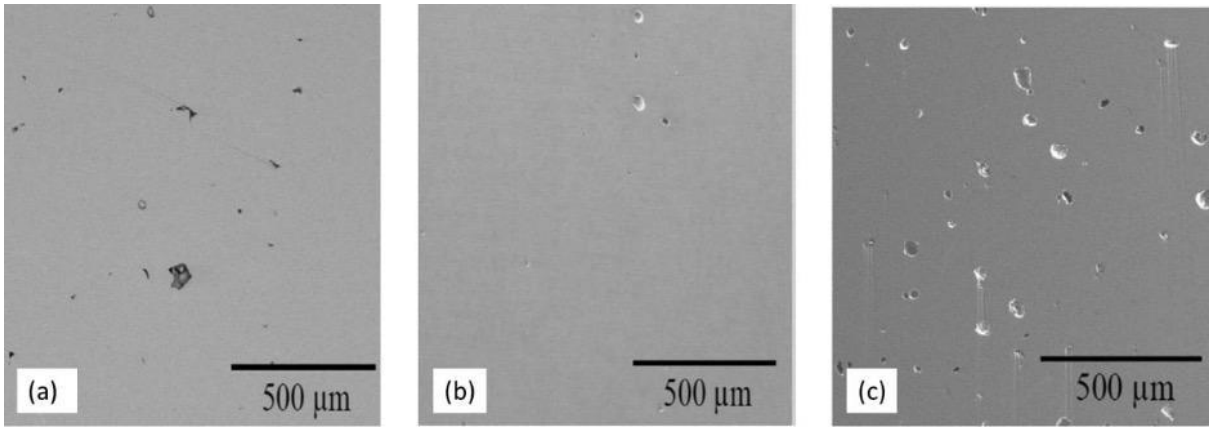

Figure 29: SEM images of the vertical cross-sections of the pores on the specimens fabricated with different energy densities of (a) 39 J/mm^3, (b)65 J/mmm^3 and (c) 260 J/mm^3

The porosity observed had an influence on the tensile properties of the material. The specimens built with different energy densities had different shaped pores. The specimens from sets 1, 5, 6 and 7 were observed to have pores with many angular points whilst sets 2, 3 and 4 had spherical pores. The pores with many angular points initiate microcracks which affects the strength of the material. The difference in the shape of pores observed is due to the change in scan speed which influences energy density. The SEM images of the type of pores observed in the material built with different energy densities are displayed in Figure 30.

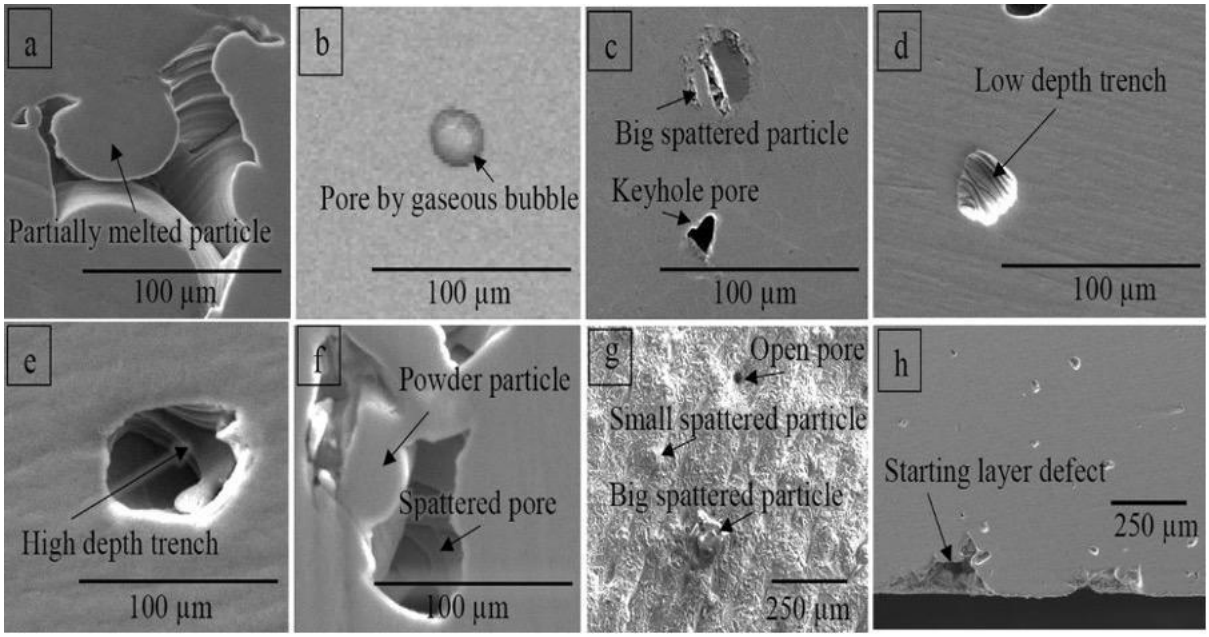

Figure 30: SEM images showing the type of pores observed in the material, (a) A pore due to insufficient of ED of 39 J/mm^3 (scan speed = 1000 mm/s), (b) A pore occurred by entrapment of gaseous bubble in a specimen having manufactured with ED of 49 J/mm^3 (scan speed = 800 mm/s), (c) A defect happened by a big spattered particle and a pore happened by keyhole effect observed across all scan speeds (d) A pore with low wavy wall in a specimen having ED of 65 J/mm^3 (scan speed = 600 mm/s), (e) A pore with big wavy wall in a specimen having ED of 130 J/mm^3 (scan speed = 300 mm/s), (f) A big pore happed by massive spattering in a specimen having ED of 195 J/mm^3 (scan speed not provided), (g) An example of the top surface of any specimen which is included open pore and small and big spattered particles, and (h) an example of void formation in bottom layers

The type of pore observed in Figure 30(a) is believed to be due to the insufficient energy density of 39 J/mm^3. Low energy density results in improper melting of powder particles which then obstruct the flow of molten material. The molten material cannot reach the destined spaces, and this results in voids. The type of pores formed due to this consequence have partially molten powder particles, inert gas, highly irregular inner surface, and critical corner points at which microcracks initiate. Moreover, high scan speed causes rapid cooling of the molten material due to the fast movement of the laser focal point across the powder particles. The rapid cooling does now allow enough time for the molten material to move and fill the space which results in improper pool formation.

High scan speed is also responsible for less viscous molten pools and pore formation by the keyhole effect in the molten pool which is shown in Figure 30(c). The pore formed by gaseous bubble entrapment shown in Figure 30(b) is a type of pore usually observed because of the SLM process. When the scan speed is reduced to 600 mm/s, less pores by the keyhole effect are seen. The lower scan speed used resulted in a lower cooling rate which led to less spattering of the material. The specimens built at this scan speed with energy density of 65 J/mm^3 (set 3) therefore have the best tensile properties. With higher energy density however, there are higher temperature gradients and more spattering of the material as shown in Figure 30(f) and (g). High temperature gradients cause the Marangoni effect and bending of the built parts during cooling and solidification. High spattering of the material at the bottom of the part being built in the starting layer (known as the starting layers defect) during the SLM process can result in the formation of pores. The molten pool in the starting layer does not get enough support to be stable as it is built on support structures with gaps among the support units. This defect results in low density and reduced surface quality of the product.

The tensile properties of the material were influenced by microstructure, particularly the orientation of the prior β-grains. The vertical and horizontal cross-sections of the microstructure of the material are illustrated in Figure 31.

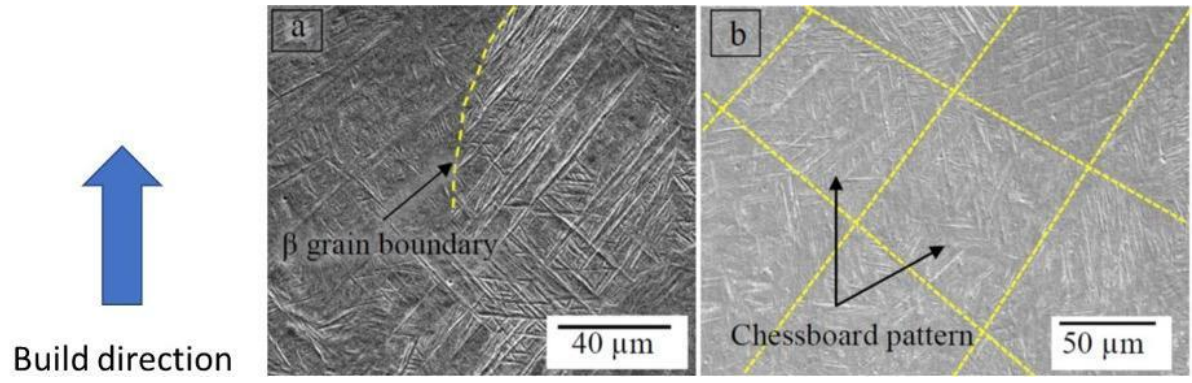

Figure 31: The microstructure of the Ti-6Al-4V alloy product manufactured by SLM process, (a) vertical plane, which is across the layers; (b) horizontal plane, which is along a layer

The acicular martensitic microstructure that is observed in the micrographs can be seen in both micrographs. The horizontal cross-section shows a chessboard pattern texture. The vertical cross-section illustrates the direction of the β-grain boundaries which is the same as the build direction. The prior β-grains grow across the layers, parallel to the build direction. In the lengthwise built specimens, the β-grains grow in the direction of the tensile axis whereas in the width-wise built specimens, the β-grains grow in the direction perpendicular to the tensile axis. Due to this phenomenon, the specimens built in the two orientations yield different tensile properties. Pal et al hypothesized that the probability of crack initiation and propagation is higher in the width-wise built specimens due to the tensile stress being perpendicular to the β-grain boundaries. Consequently, the width-wise built specimens have lower tensile strength compared to the lengthwise built specimens.

2.6.2 Cain et al (2015)

Cain[46] investigated the crack propagation and fracture toughness of SLM fabricated Ti6Al4V. The aim of this case study is to emphasise the role of build orientation on the properties of SLM built parts. In a study by Van Hooreweder[47], the SLM Ti6Al4V samples produced had near full density (>99%) with fracture toughness and FCGR properties like those of the mill-annealed vacuum arc melted Ti6Al4V parts. The effect of build orientation and post build treatments was analysed by Leuders[48]. In the latter, residual stress was noted to have an influence of crack growth ergo on fatigue properties. The two studies influenced the study of crack propagation and fracture toughness of SLM Ti6Al4V by Cain et al[46]. Post SLM processing heat treatments were considered in this study to reduce residual stress and transforming the as built martensitic microstructure. A third building orientation was introduced to investigate the anisotropy effect ion mechanical properties in a more extensive way.

The fracture toughness and fatigue crack growth rate tests were performed on standard compact-tension (CT) specimens built at the same conventional scan speed (between 0.1 m/s and 1 m/s) but in different build orientations. The actual scan speed used was not provided. The dimensions of the specimens were defined and labelled according to the ASTM E-399 standard: the first letter is the axis direction perpendicular to the notch plane and the second letter is the axis direction in which the crack is expected to propagate. Consequently, three specimen geometries arise. The dimensions of the tensile specimens were adopted whereby the thickness of the specimens was built up in the Z-direction in the XZ specimens and the height the specimens was built up in the Z-direction in the XY specimens. The specimen geometries and build orientations are shown in Figure 32.

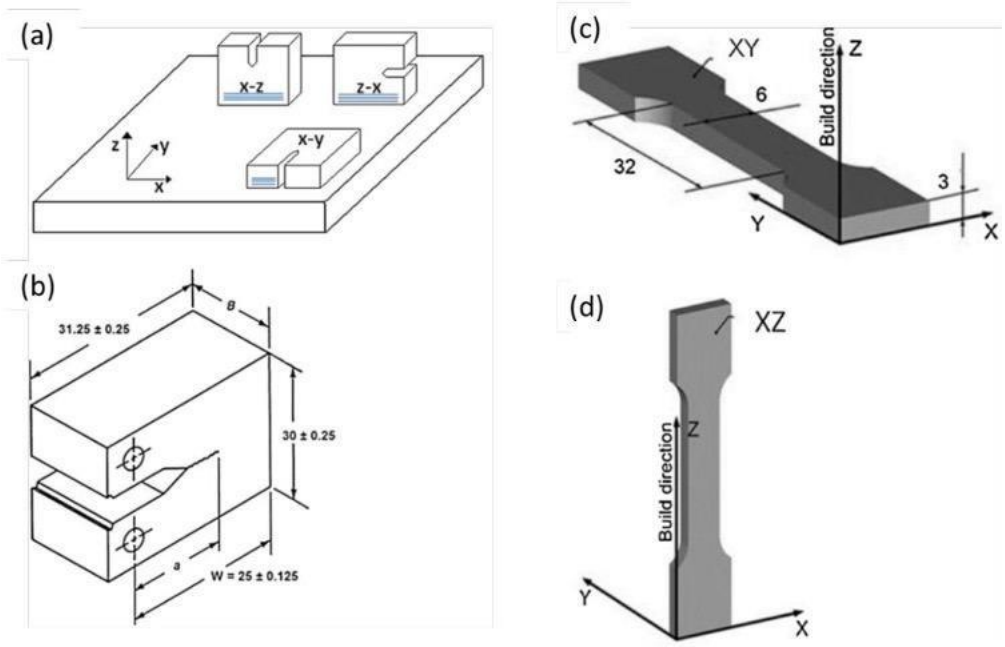

Figure 32: (a) CT specimen orientations as they appear on the build platform. (b) CT specimen geometry (c) and (d) tensile specimen geometry and orientation

Density was measured and reported to be >99% for all specimens. In this research, two heat treatment conditions were investigated. One set was stress relieved at 650°C for 4 hours and the other set was annealed at 850°C for 8 hours. Tensile testing, fatigue crack growth testing and fracture toughness testing were carried out on all as-built (AB), stress relieved (SR) and heat-treated (HT) specimens according to the ASTM E8/E8M, E647 and E399 standards, respectively. Three tests were performed for each condition. A summary of the tensile tests results obtained is presented in Table 5.

Table 5: Summary of the tensile properties for the AB, SR, and HT specimens

	Yield strength [MPa]	Ultimate tensile strength [MPa]	Elongation at break [%]
AB (XY)	1093± 64	1279 ± 13	6±0.7
AB (XZ)	1125± 22	1216 ± 8	6±0.4
SR (XY)	1145± 17	1187 ± 10	7±2.7
SR (XZ)	1132± 13	1156 ± 13	8±0.4
HT (XY)	973± 8	996 ± 10	3±0.4
HT (XZ)	964± 7	998 ± 14	6 ± 2

In the work performed by Cain et al, no significant difference in tensile strength is observed with build orientation. There was very little necking observed in all specimens. With the SR specimens, the ultimate tensile strength is lower but with a slight increase in elongation at failure. With the HT specimens, the ultimate tensile strength is further decreased whilst the elongation at failure also decreased.

A summary of the K_{IC} fracture toughness results obtained are shown in Table 6. The HT specimens have the highest fracture toughness compared to the SR and AB specimens. The AB specimens have the lowest fracture toughness. There is no difference in fracture toughness between the XY and XZ specimens across all build orientations. The results illustrate that post heat-treatment processes increase fracture toughness of SLM Ti6Al4V with the biggest difference seen in the ZX specimens.

Table 6: Summary of the fracture toughness results for the AB, SR, and HT specimens

K_{IC} (MPa $m^{1/2}$)	**XY**	**XZ**	**ZX**
AB	28±2	23±1	16±1
SR	28±2	28±1	31±2
HT	41±2	41±2	49±1

A summary of the FCGR results obtained is displayed in Table 7. The Paris exponents *m*, the Paris crack growth rate constants *C*, and the correlation factor *R*2 between data and linear fit are tabulated for all the specimens. The *C* and *m* parameters reflect the dependency of crack growth on ΔK therefore any differences in these parameters result in different crack growth rates. The smaller the two parameters, the slower the crack growth rate.

The specimens that were post-treated had better R2 value, deducing that there is more scatter in the AB specimens relative to the SR and HT specimens. The greater scatter for the AB specimens could be a result of the variable residual stress distributions introduced by the SLM process.

Table 7: Summary of the Paris parameters and relevant correlation factors

	m	***C* (m/cycle)**	R^2
XY-AB	3.37	5.79E−12	0.74
XY-HT	3.83	2.04E−12	0.91
XY-SR	5.84	9.93E-15	0.91
XZ-AB	4.17	7.51E-12	0.84
XZ-HT	3.11	1.71E-11	0.95
XZ-SR	3.24	1.16E-11	0.93
ZX-AB	4.41	2.08E-12	0.78
ZX-HT	2.94	2.58E-11	0.87
ZX-SR	3.35	8.85E-12	0.90

For the XY specimen orientation, the AB specimen has the smallest *m* whilst the SR specimen has the highest *m* parameter. This suggests that the AB specimen has the slowest crack propagation rate, and the SR specimen has the fastest crack propagation rate. In the XZ and ZX orientations however, AB condition displays the highest crack propagation rate (highest *m* parameter) whilst the slowest propagation rate is observed in the SR condition (lowest *m* parameter). There is no noticeable difference between the FCGR behaviour of the HT and SR conditions. Overall, it is shown that the AB condition of the XZ and ZX specimens display the highest crack growth rates whilst it has the slowest crack propagation rate in the XY specimens.

The microstructure of the XY plane (perpendicular to the build direction) of the SLM Ti6Al4V shown in Figure 33(a) displays a chequerboard pattern, which is characteristic of the bi-directional scanning strategy. The microstructure parallel to the build direction is shown in Figure 33(b). The columnar grain structure typical of SLM produced parts is a result of epitaxial growth from the layer-by-layer deposition during the SLM process. The metal powder solidifies into the β phase. When it cools it transforms into different microstructures depending on the post treatment processes and temperature. The AB specimens exhibit the martensitic morphology with fine α' plates, Figure 34(a). When the AB specimens are heated to 650°C for the stress relief process, the α' plates of the martensitic microstructure become coarser and transform into acicular α, Figure 34(b). When the specimens are heated to a much higher temperature of 890°C for the HT condition, the β phase from the cooling phase forms the Widmanstätten α/β structure shown in Figure 34(c).

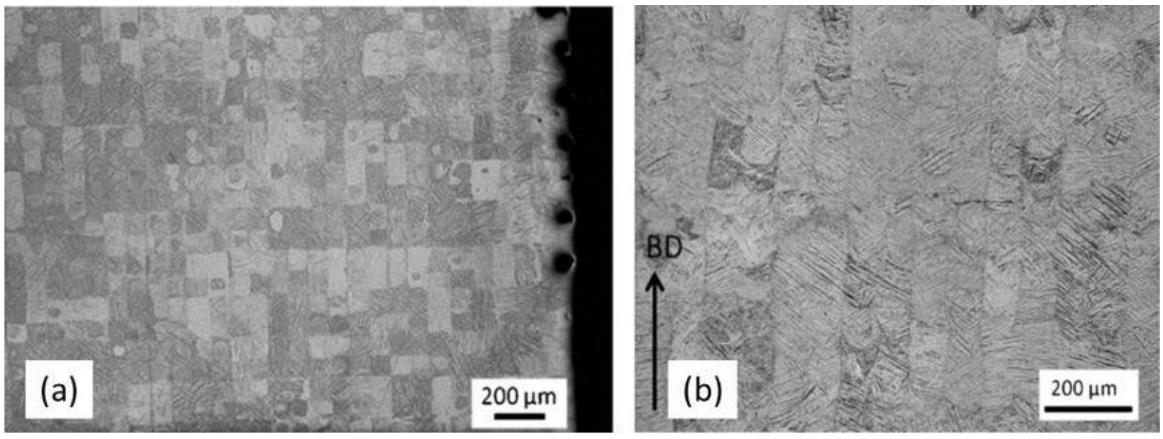

Figure 33: Microstructure of the XY plane (a) perpendicular to the build direction displaying the chequerboard pattern and (b) The microstructure section parallel to the build direction showing the columnar prior β grains

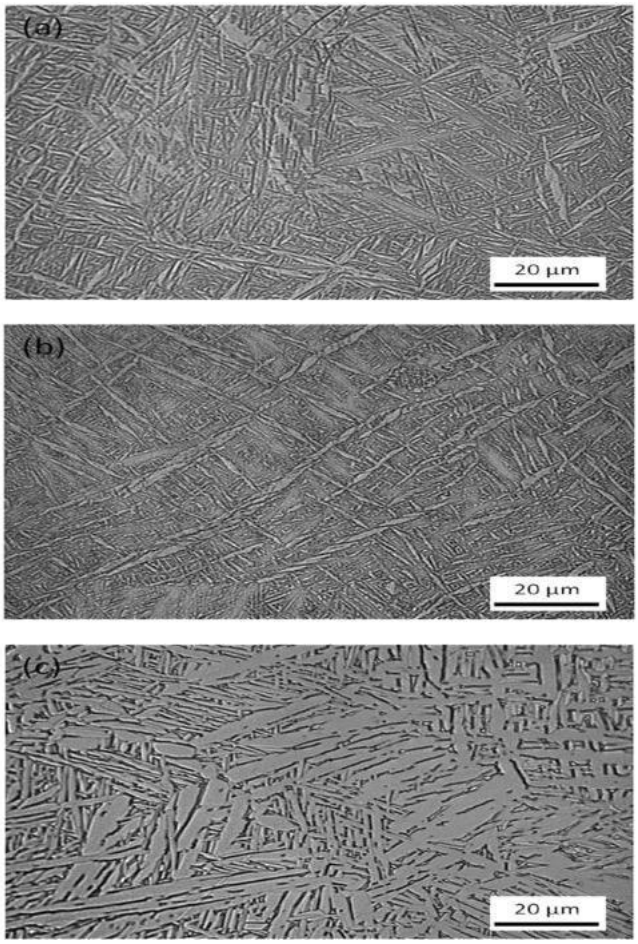

Figure 34: The microstructure perpendicular to the build direction in the (a) AB condition, (b) SR condition and (c) HT condition

The SR and HT specimens have much lower yield strength and ultimate tensile strength compared to the AB specimens. This shows that the yield strength and ultimate tensile strength values decrease upon heat treatment. This phenomenon coincides with the microstructure morphologies of the specific specimens. The coarser the microstructure, the lower the strength.

The importance of microstructure and residual stress anisotropy is seen in the fracture toughness results. In the AB condition, the XY specimens had the highest K_{1C} value of 28 Mpa.$m^{0.5}$ followed by the XZ specimens with 23 MPa.$m^{0.5}$. The ZX specimens had the lowest K_{1C} value of 16 MPa.$m^{0.5}$. All specimens had the same microstructure constituents, but they still yielded different K_{1C} values, and this is due to anisotropy within the specimens from the difference in orientation. If anisotropy had not been considered, the XZ specimen would have been expected to have the lowest fracture toughness since the crack path is in the same direction as the columnar grains. The ZX specimen would have been expected to have the highest fracture toughness since the crack path is perpendicular to the columnar grain structure and the XY specimen would have been intermediate.

The FCGR behaviour closely mimics that of fracture toughness for all the orientations and conditions. The AB XY specimen has the lowest FCGR whilst the AB ZX and XZ specimens have similar yet higher FCGR. There is noticeable improvement in FCGR resistance in the XZ and ZX specimens after heat treatment but not so much with the XY specimen which implies lowest FCGR resistance in the XY specimen after heat treatment.

The FCGR results from the study by Cain et al[46] and other studies were compared and are illustrated in Figure 35. In the study by Leuders[48] it is reported that the AB-ZX specimens have the lowest FCGR resistance and there is a noticeable improvement with heat treatment. The inclusion of FCGR data for conventional wrought Ti6Al4V shows that the FCGR trend lines reported for SLM Ti6Al4V are not significantly different to the conventional wrought Ti6Al4V alloy. Therefore, there is a close correlation between the respective trend lines.

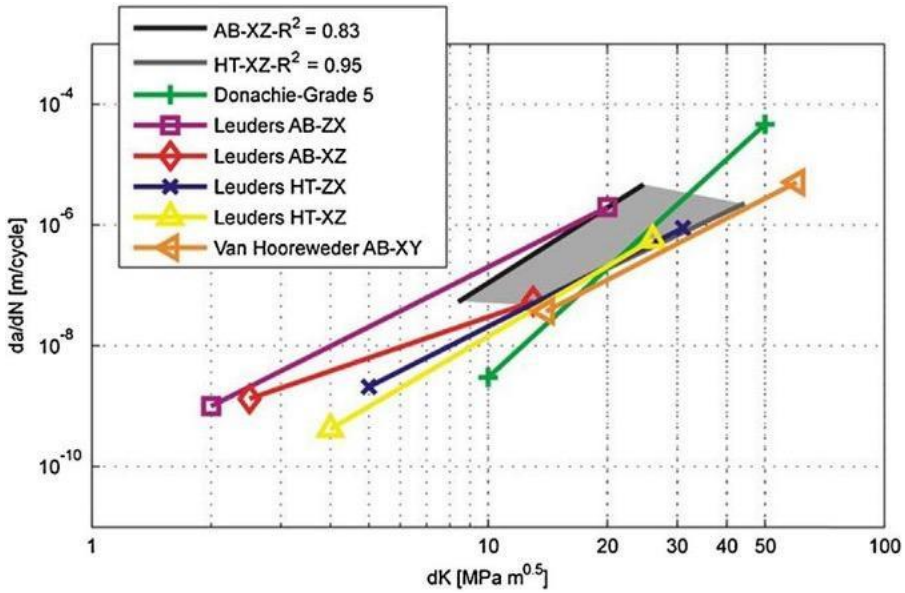

Figure 35: Comparison of slowest and fastest crack growth data of several studies.

2.6.3 Do Dang Khoa et al

In the work performed by Do Khoa et al[49] to study the effect of laser energy input on the microstructure and mechanical properties of SLM Ti6Al4V alloys, specimens were built at varying scan speeds with all other process parameters kept constant as shown in Table 8. The three energy inputs that arise due to the different scan speeds are listed as 0.5E0 , E0 and 2E0 respectively. The aim of this case study is to emphasize the effect of varying scan speed on the energy density and properties of SLM Ti6Al4V parts. Optical microscopy and SEM were performed to analyse the microstructural features and porosity of the specimens. This was performed on two of the surfaces of the 5 x 5 x 5 mm^3 cubic specimens shown in Figure 36. The top surface is perpendicular to the build direction and the side surface is parallel to the build direction. The relative densities of all the specimens were determined using the Archimedes principle.

Table 8: Processing parameters for the three different energy inputs for the SLM Ti6Al4V parts

Parameter	**$0.5E_0$**	**E_0**	**$2E_0$**
Laser power, P (W)	120	120	120
Hatch spacing, h (µm)	80	80	80
Layer thickness, t (µm)	50	50	50
Scanning speed (mm/s)	800	400	200
Energy Density (J/mm^3)	37.5	75	150

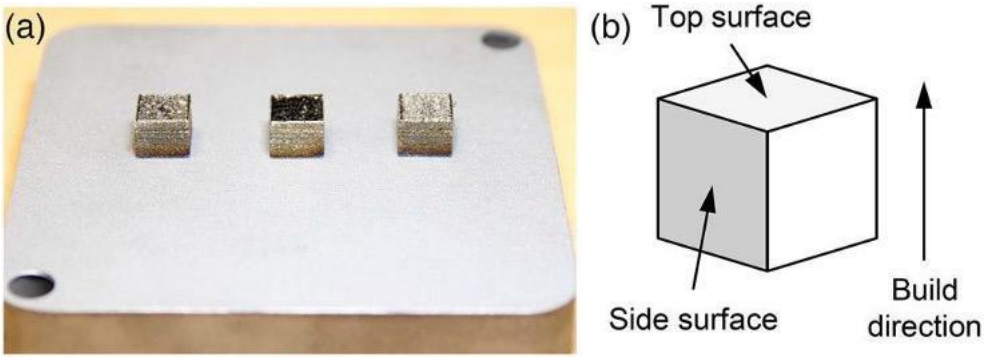

Figure 36: (a) The 10 × 10 × 10 mm^3 Ti-6Al-6V specimens as manufactured by SLM, and (b) the schematic showing the definition of the top and side surfaces in a 5 × 5 × 5 mm^3 cube machined from the specimen

The measured relative densities for the $0.5E_0$, E_0 , and $2E_0$ specimens were 93.5% 99.0% and 99.2% respectively. The distribution of pores in the top and side views of the specimens are shown in the SEM images in Figure 37. The volume porosity can be related to the relative density of the specimens measured by Archimedes method. Porosity plays an important role in determining the mechanical properties of SLM parts as it is already of concern in conventionally manufactured parts. Achieving fully dense products has been a challenge for additive manufacturing as porosity and relative density are influenced by process parameters and powder characteristics[50]. Campanelli[51] and Kruth[52] suggested that gaseous entrapment during solidification in SLM may result in the formation of pores in the built specimens.

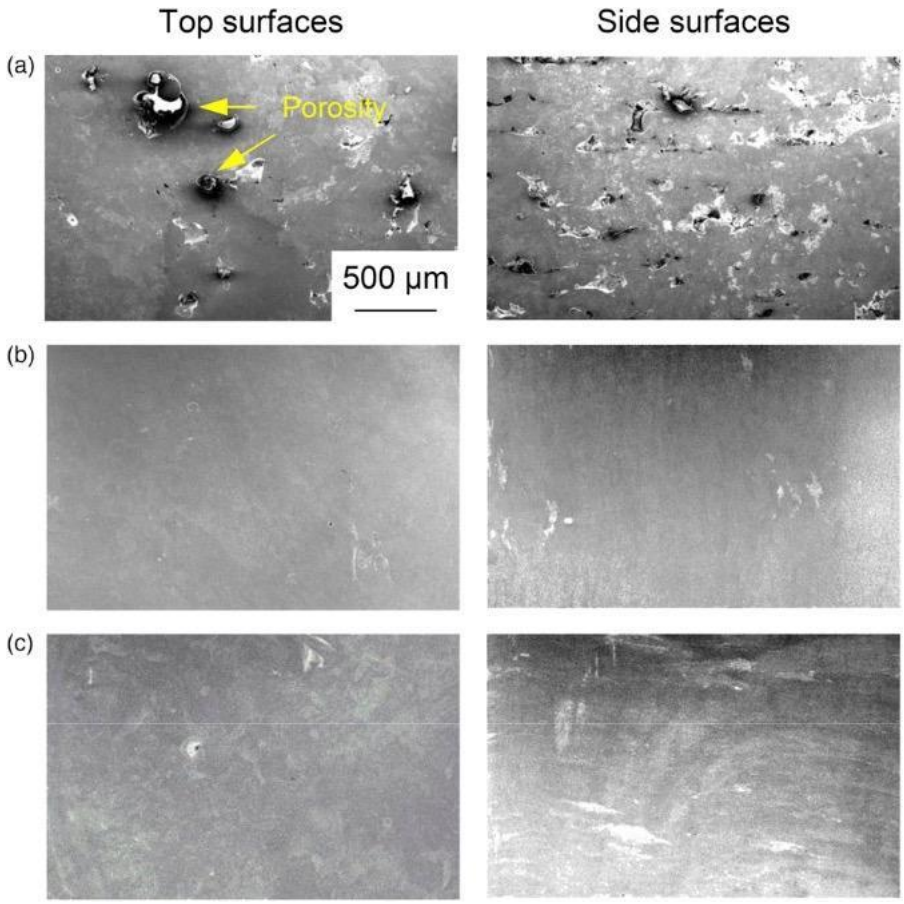

Figure 37: SEM images showing the top and side views of the SLM Ti6Al4V specimens built at different energy inputs a) 0.5E0 b) E0 c)2E0

The Ti6Al4V powders used in the work performed by Do Khoa et al[49] were spherical with a size within the range of the layer thickness and low carbon percentage of about 0.007 wt.%. The porosity in the specimens were therefore thought to be only due to the SLM processing parameters. The specimens built at the low $0.5E_0$ energy input had the highest porosity of 6.5% with convoluted pores (Figure 37(a)). The low energy input results in partial melting of the powders shown. Most of the pores are in the layer boundaries and this illustrates that low energy input results in horizontal cracks and delamination in the SLM specimens. As the energy input is increased to E_0 and to $2E_0$, the percentage porosity decreases to 1% and 0.8% respectively. More energy input results in more heat being transferred to the molten powders which then move to fill up the pores[50].

The SEM top and side view microstructures of the specimens are shown in Figure 38. The microstructure consists of the expected martensitic α' laths which were measured in the SEM images and analysed. When the energy input was increased from 0.5E0 to E0 and to 2E0, the average lath size increased from 23.6 42.9 and to 53.6µm, respectively. It was therefore noted that energy input influences lath size. According to Semiatin[53], the martensitic lath sizes in Ti6Al4V decreases with an increase in cooling rate. This is explained by the partial differential equation which can be expressed for the SLM solidification process with the laser power P and scanning speed v shown in Equation 9.

$$T - T_0 = \frac{\eta P}{2\pi k R}\, x\, exp\, exp\, ((-v(x + R)\, /2\alpha$$

Equation 9: SLM solidification process equation

In Equation 9, T is temperature, η is the absorptivity parameter, k is the thermal conductivity, ⟨ is the thermal diffusivity and $R = \sqrt{x^2 + y^2 + z^2}$ with x, y and z being the orthogonal coordinates. Therefore, the high energy input (2E0) due to the low scan speed and fixed laser power, deceases the cooling rate which results in larger martensitic lath sizes in the specimen. The low energy input (0.5E0) due to the high scan speed and fixed laser power increases the cooling rate which results in smaller martensitic lath sizes.

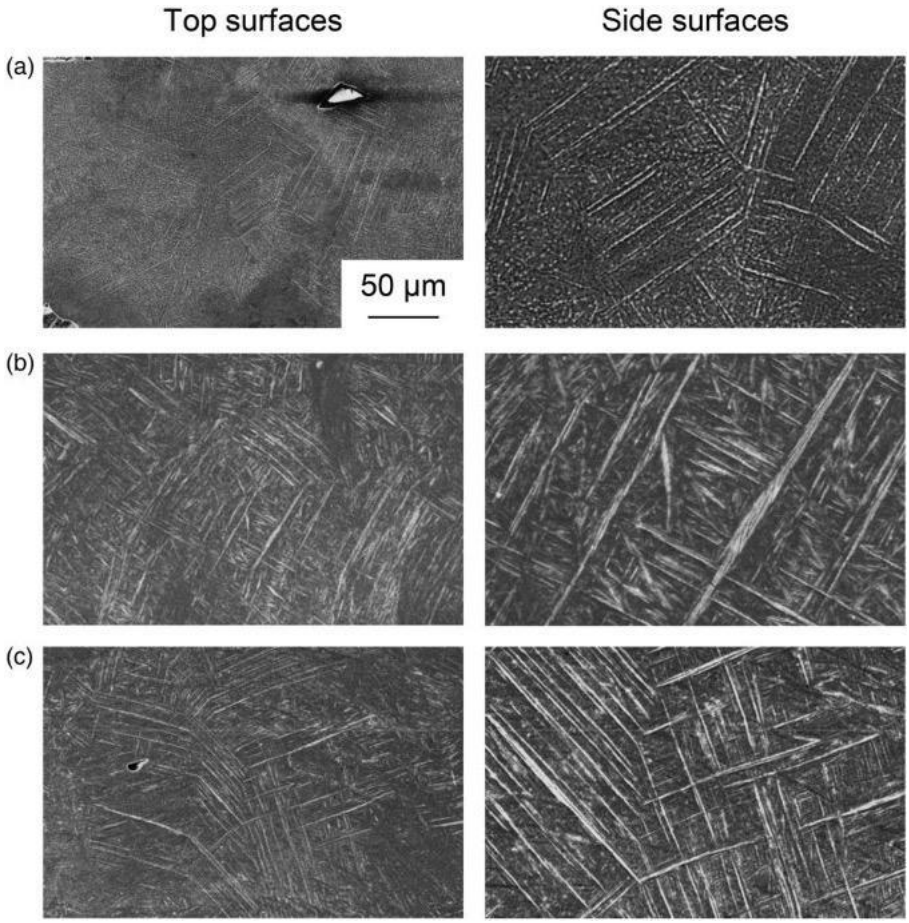

Figure 38: SEM images showing the acicular martensitic microstructure in the top and side

Based on the results of this study, it was concluded that when the laser energy input is increased due to a decrease in scan speed, the specimens become denser. The increase of laser energy density causes the reduced cooling rate which results in an increase in martensitic lath size.

2.6.4 Simonelli et al (2014)

The effect of build orientation on SLM Ti6Al4V was also investigated by Simonelli et al[54]. The tests were performed on tensile specimens built with the processing parameters shown in Table 9.

Table 9: Processing parameters used for the SLM Ti6Al4V parts in a study by Simonelli et al

Processing parameters	
Laser power [w]	15
Layer thickness [µm]	50
Point distance [µm]	45
Exposure time [µs]	200
Hath spacing [µm]	100
Scan speed [mm/s]	225
Oxygen concentration [%]	0.3
Laser spot size [µm]	70

The orientations in which the tensile bars were built are shown in Figure 39. The specimens were built with gauge thickness, length and width of 3 mm, 35 mm, and 6 mm respectively. The specimens were examined in both the as built and stress relieved conditions but only the results of the stress relieved specimens will be discussed for the purposes of this project.

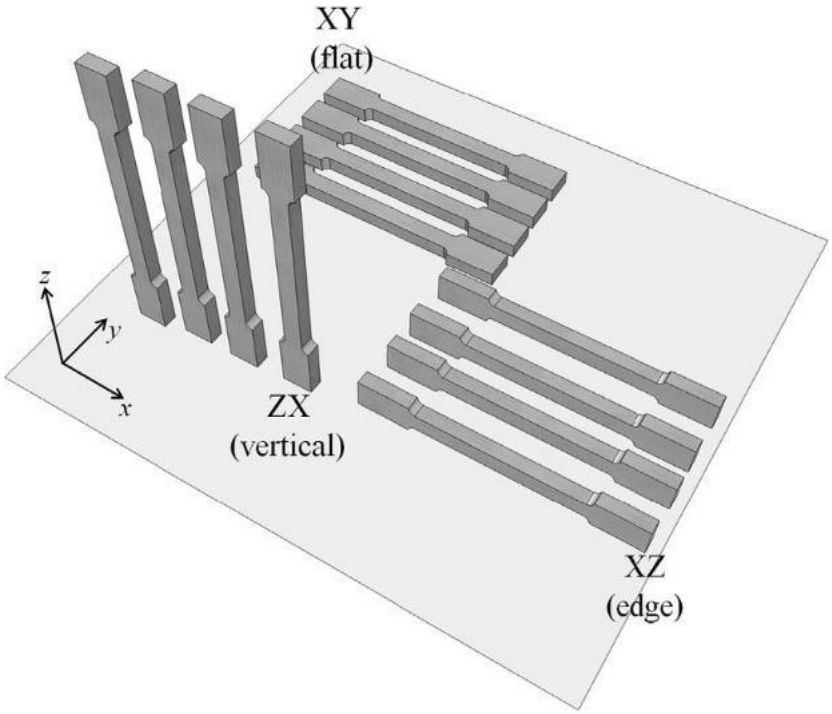

Figure 39: The three orientations for the tensile specimens in the work performed by Simonelli et al

The microstructures of the specimens in the frontal plane (XZ), lateral plane (YZ) and horizontal plane (XY) are illustrated in Figure 40. The microstructure observed in the frontal and lateral planes differs significantly from the microstructure observed in the horizontal plane. This is due to the typical layer-wise mechanism of the SLM process which results in the prior β-grains growing in a columnar fashion almost parallel to the build direction. The frontal and lateral planes align.

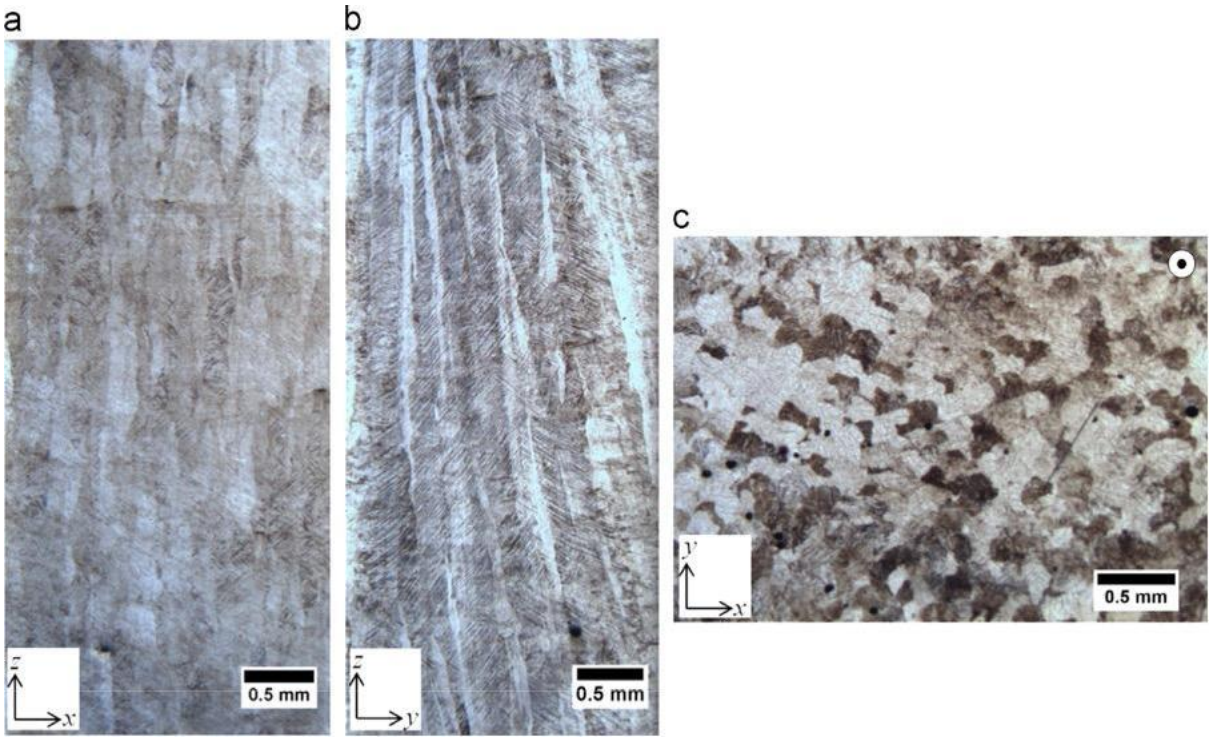

Figure 40: Optical micrographs showing the microstructure of the stress relieved SLM TI6Al4V samples investigated in the work performed by Simonelli et al in (a) the frontal plane. (b) the lateral plane and (c) the horizontal plane

The tensile tests results obtained in this study are shown in Table 10. The results illustrate that build orientation has no effect on elastic modulus, minimal effect on the yield strength and ultimate tensile strength of the specimens and significant effect on the ductility measured by elongation at fracture. The XZ specimens have the highest elongation at fracture whilst the XY specimens have the lowest elongation at fracture.

Table 10: Tensile properties of the stress relieved SLM Ti6Al4V specimens investigated in the work performed by Simonelli et al

	Elastic Modulus [GPa]	**Yield Strength [MPa]**	**Ultimate Tensile Strength [MPa]**	**Elongation at fracture [%]**
XZ (edge)	113 ± 9	958 ± 6	1057 ± 8	12.4 ± 0.7
ZX (vertical)	117 ± 6	937 ± 9	1052 ± 11	9.6 ± 0.9
XY (flat)	112 ± 6	974 ± 7	1065 ± 21	7.0 ± 0.5

The anisotropy associated with the difference in the orientation of β-grains based on build orientation explains the tensile results obtained. The orientation of the prior β-grains is observed to have no effect on the elastic modulus. This is due to the weak α texture exhibited by SLM Ti6Al4V specimens. The edge and the flat specimens have similar microstructures but different ductility. The flat specimens have the lowest elongation at fracture. This is explained by the possibility of uneven deposition of the powders in the successive layers during the SLM process caused by the curling of the flat-oriented bars. This may result in defects which undercut the ductility of the flat specimens. The relatively lower yield strength and UTS observed in the ZX specimens is possibly due to interlayer porosity. The ZX specimens which are vertically built have the highest number of layers and can therefore have higher interlayer porosity thus diminishing the yield strength and UTS.

The fracture surface profiles of the tensile bars after testing are shown in Figure 41. The images primarily show that the predominant mode of fracture in intergranular, which is showed by the cracks growing along the grain boundaries. Research on the fatigue crack propagation of Ti alloys reports that crack propagation depends on the crystallographic orientation of the α grains containing the crack tip and on the number of grain boundaries in the microstructure. This is due to the phenomenon of the crack tip deflecting upon reaching grain boundaries in materials with fine microstructures, which generates intergranular fracture.

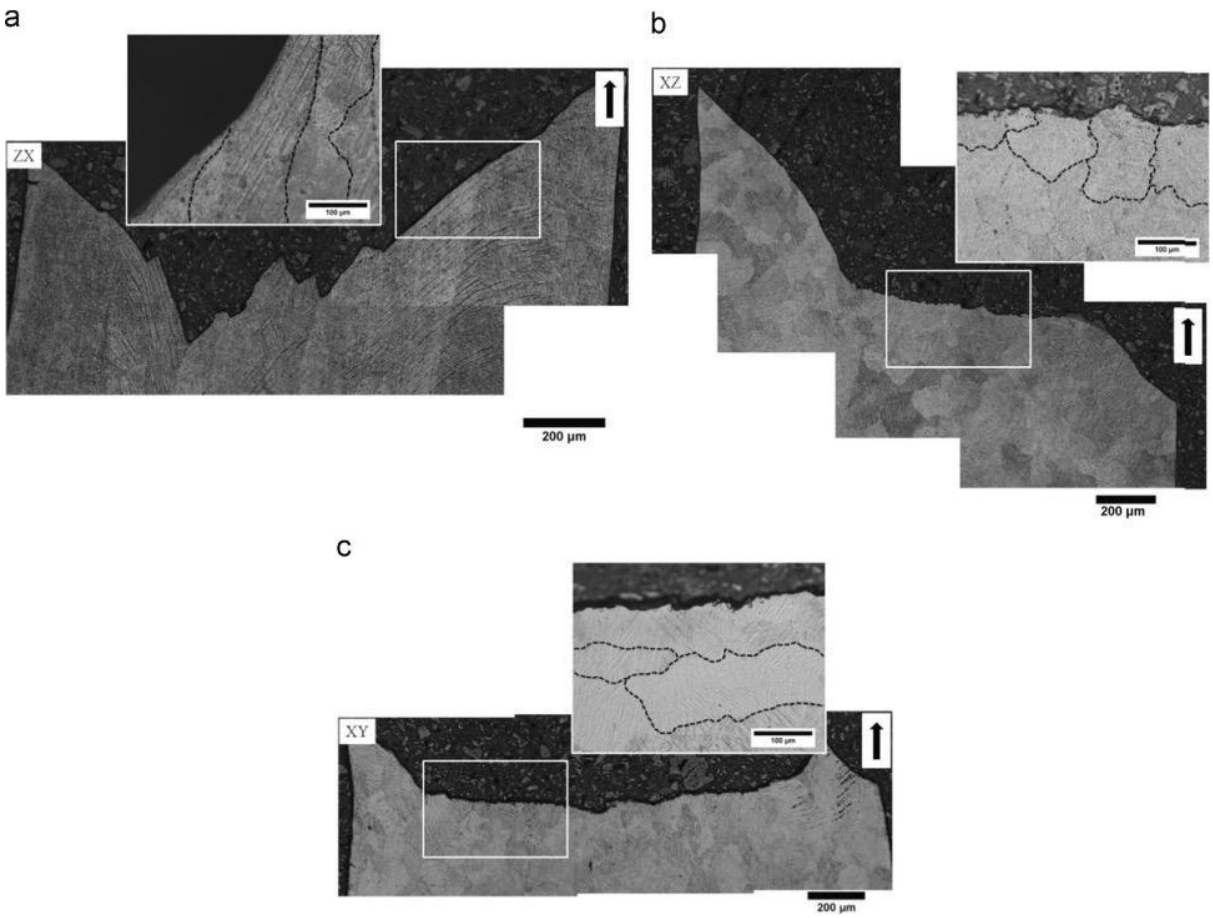

Figure 41: Fracture surface profiles of the tensile specimens built in the (a) vertical ZX-orientation, (b) flat XY-orientation. The insets show the intergranular fracture mechanism along both α and β grain boundaries shown by the dotted lines

From the fracture surface profiles, a difference in the surface roughness of the central portion of the fracture profiles was observed in the specimens built in the different orientations. Surface roughness was higher in the ZX vertical specimens. This is explained by the anisotropy which resulted in the vertical specimens fracturing along the α grain boundaries within the width of an entire prior β-grain boundaries parallel to the build direction.

It was therefore concluded that ductility of SLM Ti6Al4V is dependent on build orientation, with the XZ edge specimens having the best ductility and tensile properties. Build orientation also influences fracture surface profiles due to the orientation of the prior β-grains in relation to the axial loading direction. The dominant fracture mode observed for all the specimens is intergranular which is owed to the lack of strong texture in SLM Ti6Al4V and absence of α colonies.

2.6.5 Summary of case studies

From the relevant studies, it has been commonly concluded that scan speed influences the energy density input for SLM manufactured parts with a >20% variation in scan speed. An increase in scan speed results in a decrease in energy density input. Changes in energy density input influence microstructure, particularly lath size, relative density, and mechanical properties of SLM Ti6Al4V. In most of these studies, different energy densities used by different researchers have ended up imparting similar relative densities, greater than 99%. This is because all the other parameters (eg hatch spacing and laser power) were adjusted by a magnitude to make up for the change in scan speed based on the energy density equation. Build orientation also influences the microstructure of SLM Ti6Al4V parts, particularly the orientation of the β-grain boundaries, which in turn influences mechanical properties. In the study by Cain et al, no significant differences in tensile strength were observed with change in build orientation. It was concluded that tensile properties are much less influenced by build orientation. For fracture toughness and crack propagation, the effect of build orientation was only observed in the as built specimens, with the ZX specimens having the most inferior properties. It was concluded that heat treatments like stress relief and annealing lessen the anisotropy effect as fracture toughness and crack growth rate improves regardless of build orientation. The studies by Pal et al and Simonelli et al report different findings with regards to which orientation yield the best tensile properties. Pal et al suggests that lengthwise built tensile bars, which are like the ZX vertical specimens from the work of Simonelli et al, have the best tensile properties whilst Simonelli et al suggests otherwise. For the purposes of this research, it is therefore important to investigate whether similar effects of high scan speeds are observed with the higher range of scan speed employed in the current study and to further investigate the effect of build orientation on tensile properties.

3 Experimental Apparatus and Procedure

This chapter provides full detail of the Ti6Al4V samples analysed, the apparatus used, the standards observed and the experiments and tests that were performed. The experimental procedure gives an insight of what the aim and objectives of this research for the SLM built Ti6Al4V samples entail.

3.1 Materials selection

Ti6Al4V samples were built by SLM at the CSIR National Laser Centre. The 3D printing machine used to build the samples is shown in Figure 42.

Figure 42: The Aeroswift machine used to build the SLM samples at the CSIR National Laser Centre.

The ADC Aeroswift machine is the world's fastest and largest powder bed metal 3D printer. It was developed by a Pretoria based company in collaboration with the CSIR in South Africa in 2017. The 3D printing technology of the Aeroswift machine uses the PBF process described in section 2.1.3. The focus of the machine was particularly on titanium in the beginning with the hope of expanding to a wider range of alloys. The machine allows for fabrication of materials with highly complex geometries whilst providing cost effective solutions to industries with minimal material wastage.

The Aeroswift machine is believed to have potential to revolutionise manufacturing with increased production rates which is made possible using a high-power 5kW fibre laser. The high-power laser technology increases the melting efficiency and maximum part size. The production of larger parts is facilitated by the combination of the distinct scanning strategy and vapour extraction system of the Aeroswift machine. The distinct vapour extraction system ensures uniform distribution of the laser power throughout the part being built resulting in consistency for parts up to 2m high. The distinct scanning strategy involves a pre-heating process up to 500°C which reduces residual stresses therefore allowing for the fabrication of larger parts.

The built samples consisted of near shape round tensile specimens and orthorhombic blocks for microstructure analysis, fatigue crack growth rate (FCGR) and fracture toughness tests shown in Figure 43. The dimensions of the specimens are shown in Table 11. The sets of samples received were as follows:

- 3x12 tensile specimens
- 3x4 orthorhombic blocks for FCGR testing
- 3x4 orthorhombic blocks for fracture toughness testing

Table 11: Sample dimensions as built and received

Material	dimensions
Rods	70mm x 6mm
FCGR blocks	45mm x 35mm x 8mm
Fracture toughness blocks	45mm x 35mm x 14mm

Figure 43: Specimens built for microstructure analysis and mechanical testing at the CSIR National Laser Centre

The samples were grouped based on the scan speed and tensile axis orientation used during the SLM process in building the samples. The number and orientation of the samples received for testing are shown in Table 12. Four scan speeds were used. The tensile specimens were built in the X-TA, Y-TA, and Z-TA orientations. The specimens were named based on the direction in which the tensile axis was built. The X-TA specimens were fabricated with the tensile axis built along the x-axis, the Y-TA specimens with the tensile axis built in along the y-axis and the Z-TA specimens with the tensile axis in the z-axis parallel to the build direction.

The orthorhombic blocks for FCGR and fracture toughness testing were all built in the XZ orientation. The notation of the FCGR and fracture toughness specimens is defined according to the ASTM E399 standard using the two-letter code whereby the first letter designates the direction normal to the crack plane, and the second letter the expected direction of crack propagation.

Table 12: Samples received for testing

Scan speed [m/s]	**Rods for tensile testing**	**Blocks for FCGR**	**Blocks for fracture toughness**
5.75	3x X-TA 3x Y-TA 3x Z-TA	3 XZ	3 XZ
6.0	3x X-TA 3x Y-TA 3x Z-TA	3 XZ	3 XZ
6.25	3x X-TA 3x Y-TA 3x Z-TA	3 XZ	3 XZ
6.5	3x X-TA 3x Y-TA 3x Z-TA	3 XZ	3 XZ

The testing specimens were stress relieved at 600°C for two hours before final machining. During the SLM process, the scanned layers are subjected to rapid thermal cycles. High temperature gradients generate residual stresses which can be detrimental to the proper functioning and the structural integrity of built parts thus the need for a stress relief heat treatment.

3.2 Specimen configuration

The tensile specimens were further machined at the University of Cape Town (UCT) workshop to meet the requirements for tensile testing according to the ASTM E8/E8M standard drawing shown in Figure 44.

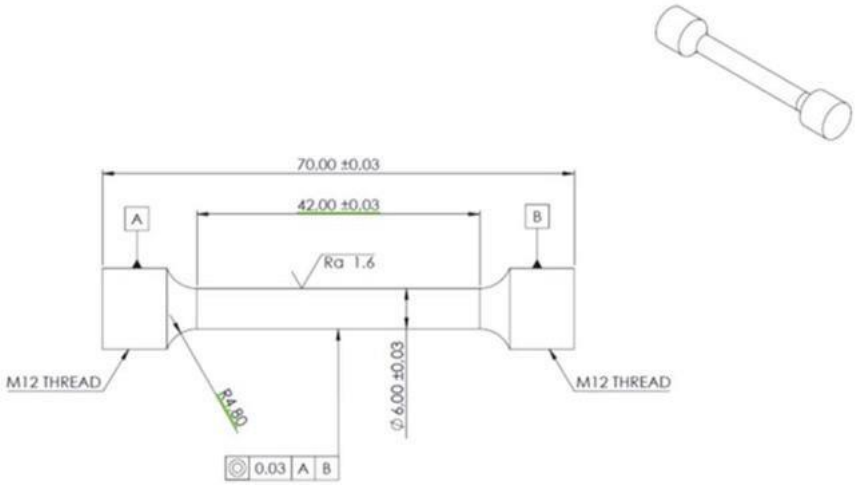

Figure 44: Drawing of the tensile testing specimens

The dimensions of the compact specimens for FCGR and fracture toughness testing were defined as a function of the width (W). The FCGR specimen drawing is shown in Figure 45a). The specimen had dimensions of width 32 mm and thickness of 6.25mm. The fracture toughness specimen drawing is shown in Figure 45b). The specimens had the same width but with a thickness of 12.5 mm. These dimensions were chosen in compliance with the specimen ligament size specifications mentioned in section 7.1 of the ASTM E399 standard. The specimens were machined at the UCT workshop according to the ASTM E647 and E399 standards respectively for final dimensions and a notch of 15 mm was machined into the specimens. Figure 46 shows the schematics of the FCGR and fracture toughness specimens after final machining.

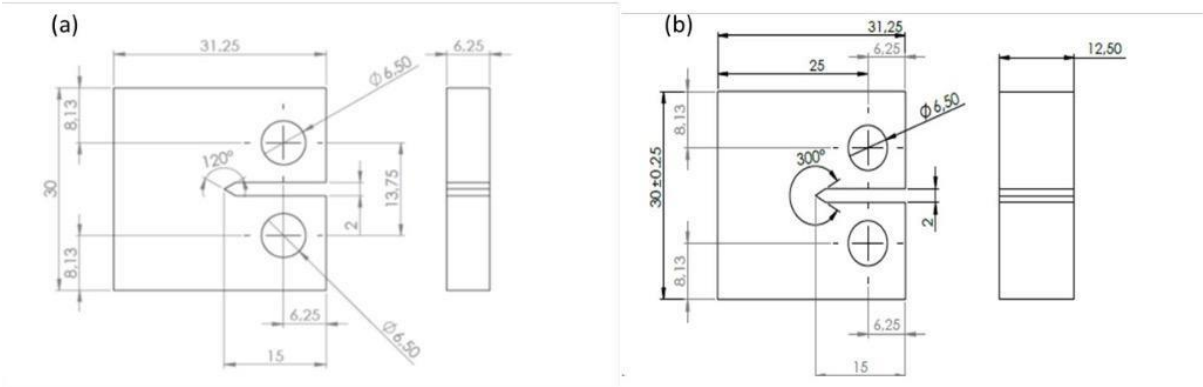

Figure 45: Drawings of the (a) FCGR and (b) fracture toughness compact test specimens machined at the UCT workshop

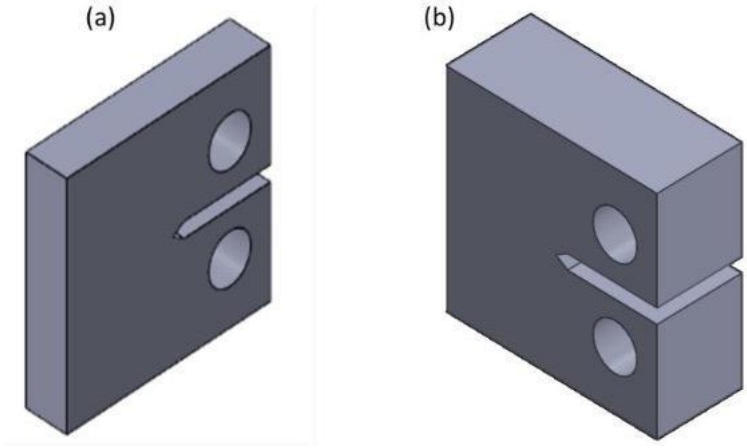

Figure 46: Schematics of the (a) FCGR and (b) fracture toughness specimens after machining

3.3 Tensile testing

Tensile tests were performed to analyse the strength and ductility of the SLM Ti6Al4V specimens. Tensile tests were done according to the ASTM E8/E8M standard on the Zwick machine at a strain rate of 5×10^{-4}/s in conjunction with a video extensometer for more accurate results. Samples were displaced until fracture.

Testing machines are either hydraulic or sturgeon depending on how the load is applied[55]. In this research, the tensile tests were performed on the sturgeon Zwick testing machine shown in Figure 47. The advantage of using the video extensometer is that it eliminates contact with the specimen which improves accuracy by eliminating errors caused by moving parts. The tensile specimens were ground to a fine surface finish and spray painted in white all the way round. The gauge length was marked with two black bands on each end, which was in contrast with the white spray paint. The distance between these bands was automatically measured by the video extensometer for a more accurate gauge length reading. Strain is measured in the vertical direction and the video extensometer keeps track of the strain until the sample is broken.

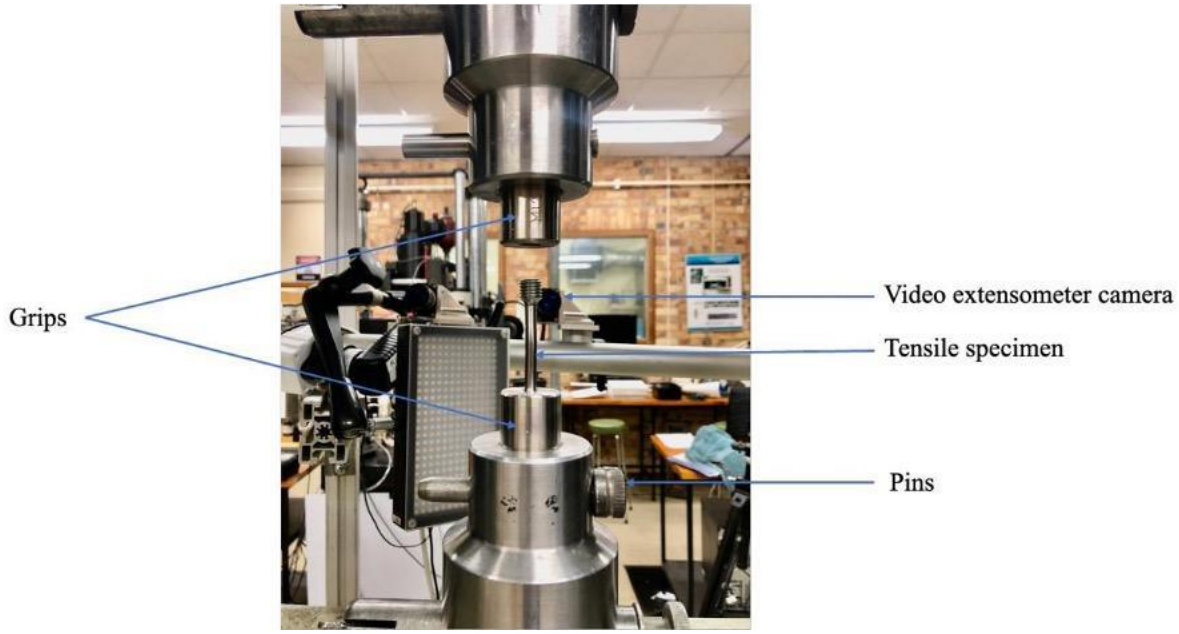

Figure 47: The Zwick universal testing machine at the UCT Centre for Materials Engineering, Department of Mechanical Engineering

The Zwick universal machine consists of a mobile crosshead and a stationary load cell, and the crosshead was set to move at 1 mm/min in accordance with the ASTM E8/E8M standard. The gauge length of the specimens was approximately 36 mm. The specimens were placed between the grips and displaced. The specimens' resistance to displacement is recorded as tension. For each scan speed and build orientation, triplicate tests were performed resulting in a total of 36 tests. After running the tests, the load and extension data was collected and used to calculate the stress and strain values which were used to plot stress-strain curves from which the YS, UTS and percentage elongation values were estimated.

3.4 FCGR testing

The tests were conducted on the ESH servo hydraulic fatigue machine at room temperature following the procedure outlined in the ASTM E647 -15 standard. The ESH servo hydraulic fatigue machine is a 50KN Instron software operated machine which uses a feedback system which allows comparison between input information and performance. An error is given off which is then corrected by the servo-valve to adjust the actuator movement accordingly[56]. The machine can be controlled via load, strain, or position control. An image of the machine is shown in Figure 48.

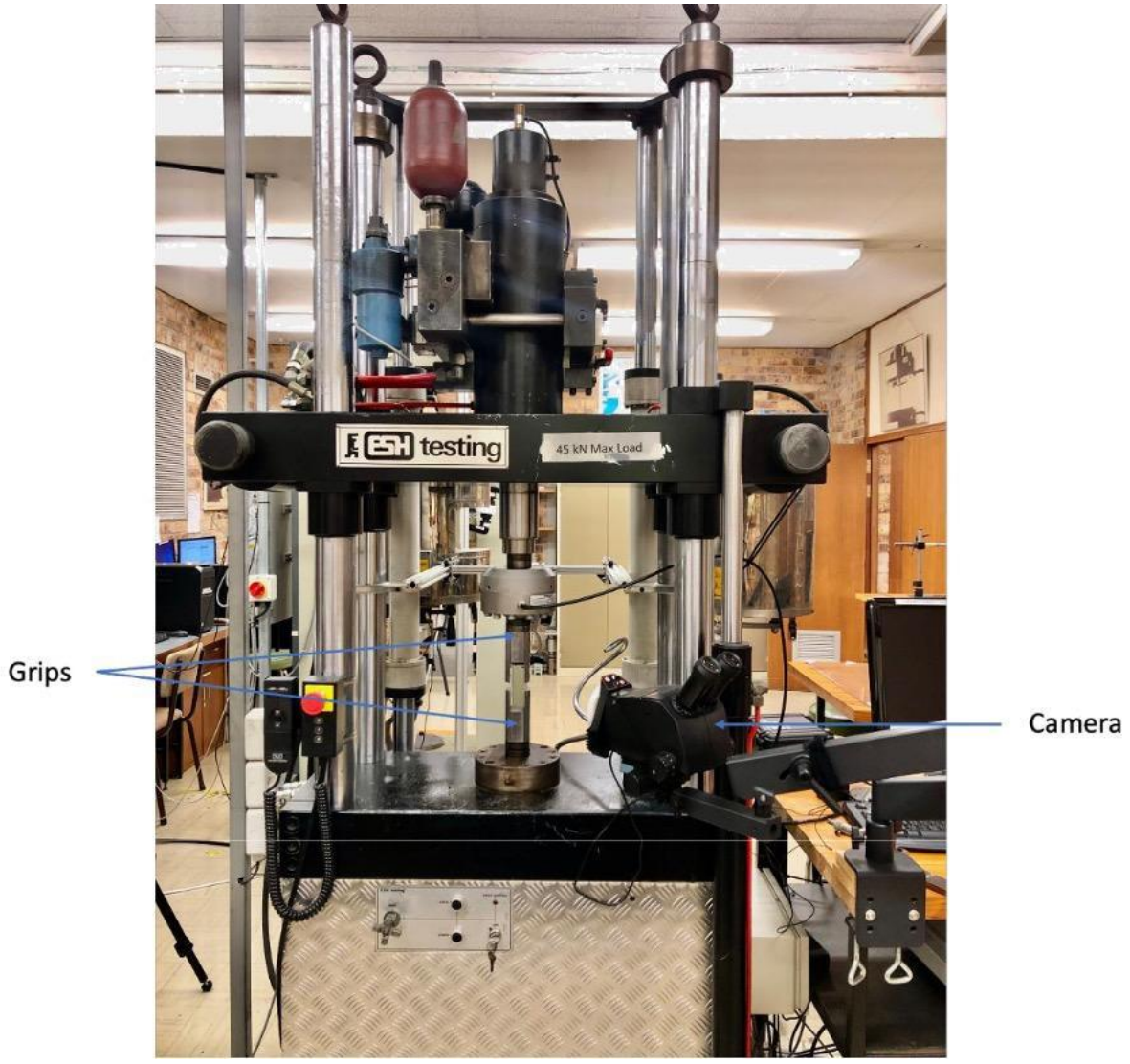

Figure 48: ESH servo-hydraulic testing machine the UCT Centre for Materials Engineering, Department of Mechanical Engineering

For each of the four scan speeds, three fatigue crack growth tests were performed resulting in a total of twelve tests. All specimens were built in the XZ build orientation. Crack extension was measured at intervals of 1mm. An image of the specimens after being polished in preparation for testing is shown in Figure 49. Horizontal lines approximately 1 mm apart were drawn onto the specimens from the notch (right image in Figure 49) to note the distance travelled by the crack as it propagates during the test. The exact length between the lines was measured by a microscope system linked to a computer with measurement tools to improve accuracy. The crack length in between the horizontal lines was estimated at about three points between a set of horizontal lines to get more data points for plotting to get as much information as possible from the results.

Figure 49: Fatigue crack growth rate specimen before testing. image on the right is the same specimen with scribes about 1 mm apart to monitor crack propagation

Several trials at different loads with dummy specimens were performed before deciding on the P_{max} to be used for the actual testing and to determine whether the specimens were suitable for testing with the process outlined in the ASTM E647 standard. During the testing with the dummy specimens, the crack propagated at a steady pace at a load of 2 kN. Initial fatigue pre-cracking was therefore performed at a P_{max} of 2kN, and the pre-cracks were grown to 1mm before any data was collected. The purpose of pre-cracking is to remove the effect of the machined starter notch on the K-calibration of the specimen and the effect of changes in the crack front shape on the crack growth rate data to be collected. In the final stages of pre-cracking, P_{max} was reduced to ensure that the value of K_{max} used towards the end of the pre-cracking did not exceed the initial K_{max} as prescribed in the ASTM E647 standard. The load was therefore reduced to 1.3 kN in the final stages of pre-cracking and for the rest of the FCGR testing. The R ratio (P_{min}/P_{max}) used was 0.1 and frequency of 7Hz.

The details of importance to fatigue crack growth rate tests are as follows:

- The width of the specimen W, which is 25 mm

- The thickness of the specimen B, which is 6.25 mm

The dimensions of the CT specimens are important because they are selected with considerations of specimen buckling and through-thickness crack-curvature. With these considerations in mind, the ASTM E647 and E399 standards recommend that the thickness, B of the CT specimens be within the range W/20 ≤ B ≤W/4, after selecting a value for the width of the specimen, W.

The crack length and number of cycles passed were recorded and the results were used to plot two graphs: a crack length (a) versus number of cycles (N) graph and a crack growth rate (da/dN) versus stress intensity factor range (ΔK). The stress intensity factor range and the crack growth rate values were calculated according to the procedure outlined in the ASTM E647 standard. The stress intensity factor range (ΔK) at each increase in crack length that was noted was calculated according to Equation 10 below:

$$\Delta K = \frac{\Delta P}{B\sqrt{W}} \frac{2 + \alpha}{(1 - \alpha)^{\frac{3}{2}}} (0.886 + 4.64\alpha + 13.32\alpha^2 + 14.72\alpha^3 - 5.6\alpha^4$$

Equation 10: Calculation of ΔK

Where:

a = crack length from bearing points of the specimen
α = a/W
$\Delta P = P_{max} - P_{min}$

The crack growth rate at each point was calculated according to the equation below:

$$\frac{da}{dN} = \frac{a_2 - a_1}{N_2 - N_1}$$

Equation 11: Calculation of crack growth rate at each point of measured crack length

Where:

a1 = the crack length at the first point

a2 = the crack length at the second point

N1 = the number of cycles at a1

N2 = the number of cycles at a2

The calculated values of ΔK and da/dN at each point per specimen were plotted against each other on a da/dN versus ΔK graph to form a Paris curve from which the crack growth rates of the different specimens could be evaluated and compared. A worked example of how the crack growth rate was against the stress intensity factor range from calculations at each point is displayed in Figure 50.

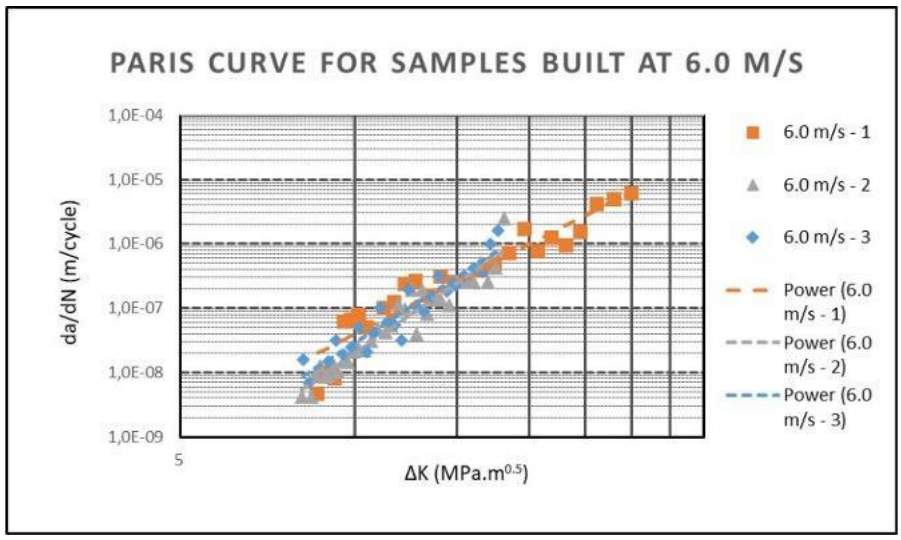

Figure 50: A worked example of da/dN plotted against ΔK to form a Paris curve

3.5 Fracture Toughness testing

The fracture toughness tests were performed following the procedure outlined in the ASTM E399 standard on the ESH servo hydraulic fatigue machine shown in Figure 48 at a crosshead speed of 1 mm/min. For each scan speed, three fracture toughness tests were performed resulting in a total of twelve tests. Results were plotted on a force versus displacement graph.

The details of importance to fracture toughness tests are as follows:

- The width of the specimen W, which is 25 mm
- The thickness of the specimen B, which is 12.5 mm
- The cyclic rate of crack initiation SIF, 15MPa.m$^{0.5}$
- Pre-crack extension, 0.5 a/W
- Force ratio R of 0.1
- Frequency at 7 Hz
- Loading rate until fracture = 2MPa.m$^{0.5}$/s

The width of the specimen was selected to ensure that the FT results obtained from the test method outlined in the ASTM E99 standard are valid. For the test to be valid, the specimen ligament size (W-a) must not be less than 2.5(KIC/σYS) where σ*YS* is the 0.2 % offset yield strength of the material under the testing conditions. The selected value of W satisfies this requirement.

The thickness of the specimen was calculated based on the recommendation stated in the ASTM E399 for the thickness of the specimen to be one-half of the width of the specimen. It is recommended in the standard for the force ratio to be between -1 and +0.1. The more negative the force ratio, the faster the crack propagation. A force ratio of 0.1 was therefore selected to ensure steady crack growth rate for accurate testing. The length of the pre-crack was calculated according to the equation in the standard which states that the ratio of the crack length to the width of the specimen shall be 0.5 (0.5 a/W). The loading rate and frequency was selected based on the capacity of the ESH machine and the typical behaviour of Ti6Al4V.

3.6 Density measurements

Density measurements were performed according to the procedure for density measurement for powder metallurgy materials described in the ASTM B311 standard. The method is based on Archimedes principle which states that a body submerged in a fluid at rest is acted on by a buoyant force which has the same magnitude as the weight of the fluid that is displaced by the body[57]. The specimens were weighed in air and weighed when immersed in distilled water with a scale having an accuracy of ±0.0001 g. Figure 51 shows an illustration of the set up for the density measurements. The scale and set up used for density measurements in this research project is displayed in Figure 52. The measurement of each specimen was repeated 3 times and the specimens were completely dried before each consecutive measurement. Thereafter, the relative densities of the specimens were calculated according to the equation below:

$$\rho = \frac{m_a}{m_a - m_w} * \rho_w$$

where ρ is the density of the sample, m_a is the mass of the sample in air, m_w is the mass of the sample immersed in water and ρ_w is the density of water.

The percentage relative density of the SLM samples is calculated by comparing the full density value to the standard density value of Ti6Al4V, 4.429 gcm^{-3} [22].

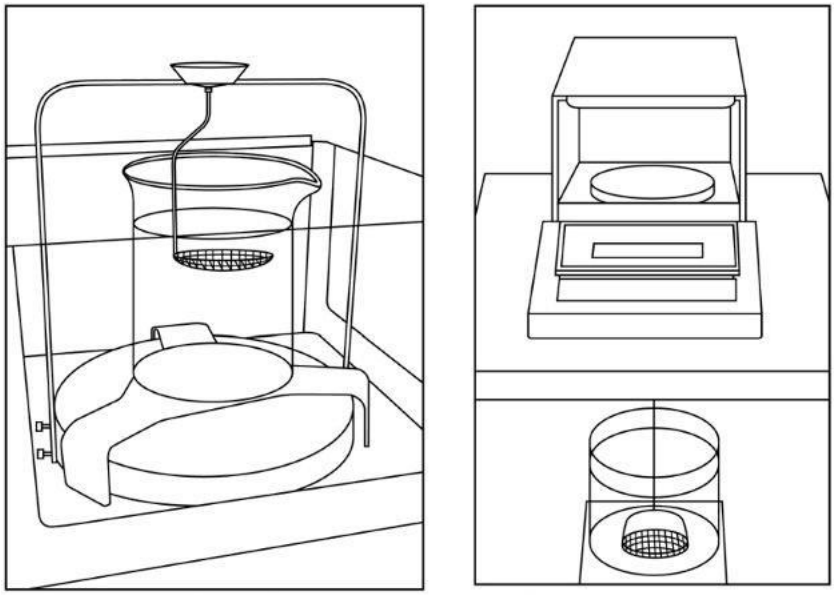

Figure 51: Illustration of method used to weigh the samples in water

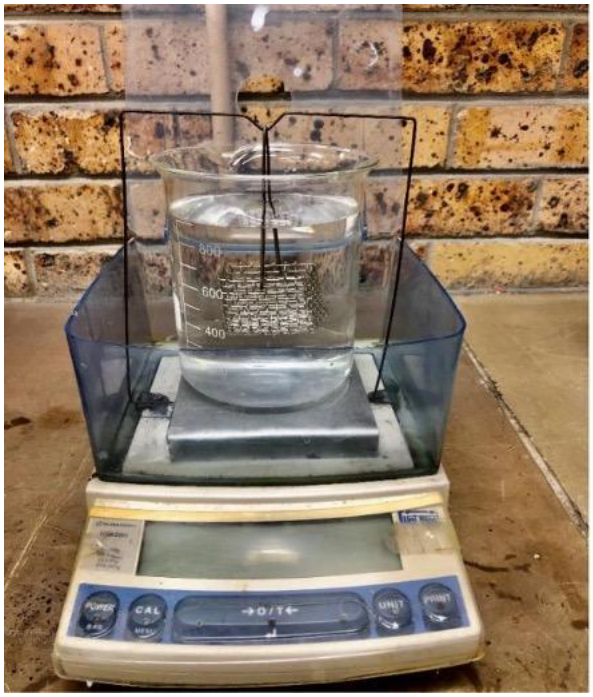

Figure 52: Beaker and support set up for the density measurements

3.7 Microscopy

The SLM Ti6Al4V samples were prepared for microstructure analysis following the protocol in the Struers Metalog guide. The steps involved are cutting, hot mounting, grinding, polishing, and etching.

3.7.1 Sample preparation

3.7.1.1 Cutting

The Abrasive wet cutting method was used to section samples as it gives off minimal damage to the samples being cut. An Al2O3 cutting wheel consisting of an abrasive and a binder was used. A coolant constantly flushed the wheel as the samples were being cut to minimize frictional heat and remove debris from the cutting area. After sectioning, a microslice was used to cut the samples into smaller mountable sizes.

3.7.1.2 Mounting

Hot mounting was the selected mounting process for the SLM Ti6Al4V samples. Hot mounting was performed on a Struers Labopress-3 at 180°C for 16 minutes; 8 minutes heating time and 8 minutes to cool at a force of 20KN to get good adhesion between the resin and the sample. An acrylic conducting thermosetting resin, PolyFast was used for the hot mounting.

3.7.1.3 Grinding and Polishing

The grinding and polishing steps were done on a Struers Tegrapol-11 polishing machine linked to a Tegradoser-5 supplied by IMP solutions. The samples for light microscopy and SE imaging were ground from 500grit up until the last polishing step with attack solution. The attack solution consisted of hydrogen peroxide and colloidal silica OP suspension in the ratio 1:5. The polishing protocol is shown in Table 13. The best surface quality of the samples for light microscopy and SEM imaging was achieved with this polishing protocol which was selected after thorough research on the polishing protocols used in other studies on titanium. Some of the protocols from the research involved the 6µm and 3µm polishing steps after the 9µm step. However, these protocols did not yield the best results for the specimens investigated in this

project. When the extra polishing steps were omitted as observed in a study by Clinning[58], a better surface quality was achieved with no visible scratches.

Table 13: Grinding and polishing protocol for light microscopy and SEM imaging

Step	**Grit/Pad**	**Speed**	**Force**	**Lubricant**	**Time [min]**
1	800 SiC	150 rpm	30N	Water	2
2	1200 SiC	150 rpm	30N	Water	2
3	MD Dac	150 rpm	30N	9µm diamond suspension	10
4	MD Chem	150 rpm	30N	OP-Nap colloidal silica	10
5	MD Chem	150 rpm	30N	Water	5

The surface quality of the samples polished using the protocol outlined in Table 13 was adequate for light microscopy and SEM imaging but it proved to be poor for EBSD analysis. The indexing was quite poor and in some instances no Electron Backscatter Diffraction Patterns (EBSP) could be seen. This meant that the surface quality of the samples had to be further improved foe EBSD hence a new polishing protocol was devised. The process involved several trial-and-error steps of all the grinding and polishing steps until better EBSD indexing was achieved. The grinding and polishing protocol used for EBSD analysis is displayed in Table 14. The samples were plasma cleaned after polishing to ensure non-contaminated surfaces before the analysis.

Table 14: Grinding and polishing protocol for EBSD analysis

Step	Grit/Pad	Speed	Force	Lubricant	Time [min]
1	800 SiC	150 rpm	30N	Water	2
2	1200 SiC	150 rpm	30N	Water	2
3	2400 SiC	150 rpm	30N	Water	2
4	MD Nap	150 rpm	30N	3µm	10
5	MD Chem	150 rpm	30N	OP-Nap colloidal	10
6	MD Chem	150 rpm	30N	Water	5

3.7.1.4 Etching

Samples were etched for light microscopy and SEM imaging using Kroll's reagent which is typically used for titanium samples. Etching was done to reveal the microstructure of the samples by removing the near surface of the material and preferentially attacking the grain boundaries which give microtopographic relief to the sample. The microstructure can then be seen by the light being dispersed in the light microscope. The composition of Kroll's reagent is shown in Table 15. samples were etched till a cloudy surface appeared which was for about 6 seconds, and they were quickly rinsed with ethanol and dried in hot air.

Table 15: Components of Kroll's reagent

Components	Volume (ml)
60% HNO_3	7.2
60%HF	3.6
Distilled water	89.2

3.7.2 Microscopy Techniques

Microscopy is used to examine microstructures of materials that are not visible with the naked eye. There are several types of microscopy techniques, and each can be used depending on the required magnification and depth of field. In this project, light microscopy and scanning electron microscopy were used.

3.7.2.1 Light microscopy

Light microscopy was performed using a Nikon Eclipse MA200 microscope to examine the surface topography and to reveal the microstructure of Ti6Al4V samples by showing the contrast between different grains. Images were taken at a magnification of 100x at which the elongated grains could be clearly seen. The Nikon Eclipse Ma200 microscope was ideal as it is equipped with the Normaski prism which assists in distinguishing grain boundaries and other microstructural features. Samples for light microscopy were prepared as outlined in section 3.7.1. The images obtained were compared from one scan speed and build orientation to the other, respectively. An image of the Nikon MA200 microscope is shown in Figure 53.

Figure 53: The Nikon MA200 microscope

3.7.2.2 Scanning Electron Microscopy

Scanning electron microscopy (SEM) was used to obtain quantitative information on microstructure and crystallography of the material at a much higher magnification and depth of field. SEM was performed using a Tescan MIRA3 Rise SEM shown in Figure 54. The secondary electron (SE) detector was used for basic imaging of the topography of the surfaces of the samples. The electron backscattered diffraction (EBSD) detector was employed to study the β → α transformation in the Ti6Al4V material and the reconstruction of the parent β-grains by post-processing of the EBSD data obtained on the α-grains.

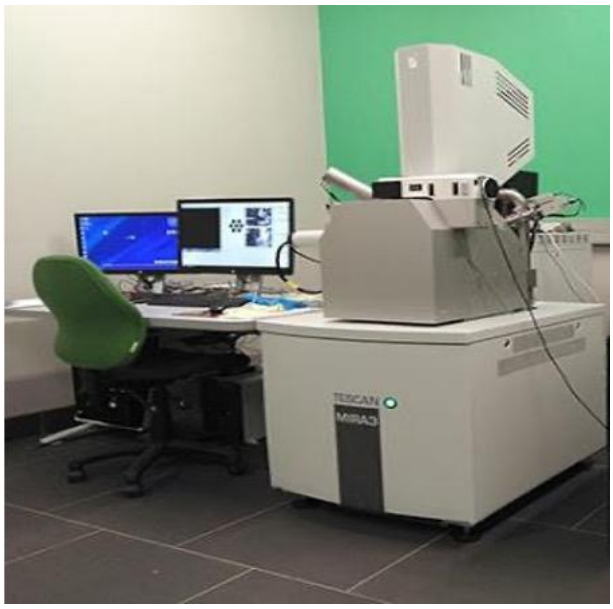

Figure 54: The Tescan MIRA3 Rise SEM at the UCT Electron Microscope Unit

The polished un-etched samples were used to investigate qualitative topography at high resolution using SEM imaging and the fractured CT specimens were used for fractography. The SE detector was selected because it gave more detailed surface information on the porosity as opposed to the Back-scattered Electron (BSE) detector. The fractured surface of one-half of the CT specimens per scan speed was examined for fractography at a working distance of 36mm with no sample preparation. Both SE imaging and fractography were performed at an accelerating voltage of 20kV, beam intensity of 15 and spot size of 5 (0.9 nano Amps).

The same polished un-etched samples were used to analyse quantitative grain size and the reconstruction of the β-grains using the EBSD technique. The EBSD detector was employed to obtain information on the crystallographic orientation at each scan point within a selected region. The samples were mounted directly onto a stub such that they were at a 70° angle to the detector. EBSD was carried out at a working distance of 12mm, an accelerating voltage of 20kV, beam intensity of 15 and spot size of 3.5. The size range of the scanned images was 330µm - 350µm. A step size of 0.2µm and a binning mode of 8x8 was used for the EBSD scans. These parameters were selected for final analysis after several trials with varying parameters because they yielded the best imaging and indexing for the samples. To get a good number of elongated grains in one map, a montage setting on the Aztec software was employed. With the montage setting, multiple maps can be scanned across the sample in one go forming one continuous map with a wider view. The size of each small map was kept at 400µm x 400µm. Each montage consisted of 15 maps, 5 maps in the horizontal direction and 3 maps in the vertical direction.

The scanned points on the maps were each colour coded depending on the orientation relative to the Euler angle positions on the Cartesian axis. Scanned point with similar orientations were assigned the same colour. The indexing achieved was between 40% and 60%, which is not substantial. The Tango mapping program on the Oxford Instruments HKL Channel 5 software was used for post-processing the maps. The first processing performed was a "clean-up." In this process, wild spikes were removed first then noise-reduction was executed whereby the non-indexed points were replaced with more reliable orientations which are determined by the orientations of at least four of the neighbouring indexed points. The sample preparation for EBSD analysis was thorough, involving a lot of trial-and-error steps to achieve the best surface quality and mapping so the non-indexed points are believed to be random and a consequence of the overlapping patterns especially at grain boundaries which cause the indexing algorithm to fail. The non -indexed point will be assigned the same orientation as the neighbouring indexed points if the pixel of the non-indexed point is below a particular angular deviation.

There are different levels of cleaning and the higher the cleaning level, the higher the percentage indexing of the map. The clean-up process improves the indexing rate of the maps. However, there are risks associated with filling up the non-indexed points depending on the objective of the analysis. For purposes of quantitative analysis of grain size and orientation distributions, too much cleaning may be risky to the integrity of the data. On the other hand, analysing orientation prevalence, grain size and shape is not likely to be affected by high levels of cleaning. For the purposes of this project, the EBSD technique was used for reconstruction of the parent β-grains as mentioned earlier and no quantitative information was investigated. The EBSD maps were therefore 100% cleaned with no risk of distorting data integrity.

After the "clean-up" process, further post-processing for the reconstruction of the parent β-grains from the α phase formed upon cooling. The reconstruction is based on the principle of the Burgers orientation relation between the α/β lattices which states that the β-grain can transform into 12 α variants upon cooling. The 12 α variants can therefore be used to extrapolate the orientation off the parent β. Reconstruction of the β-grain sis important because it provides information about the microstructure of the Ti6Al4V prior to cooling during the SLM process which can potentially explain the mechanical behaviour observed.

Summary

This chapter has described the types, dimensions and orientation of the materials involved in the research project as well as the techniques and procedures undertaken to investigate the objectives of the research with the relevant the ASTM standards. The procedures and microscopy techniques to be conducted and the measurements of relative density have been discussed. The following chapter entails the results obtained from these experimental procedures.

4 Results

This chapter presents the outcome of the experiments and tests done to compare the porosity, relative densities, microstructure, tensile properties, FCGR and fracture toughness of the SLM Ti6Al4V at the different scan speeds. The results are further discussed in section 5.1.

4.1 Tensile test results

The results from the tensile tests were obtained from stress-strain curves which were calculated from the tensile load versus extension data. The stress-strain curves were used to plot true-stress versus true-strain curves for more accurate readings.

Microsoft tools for shapes were used to accurately read off the tensile values from the derived curves and this is illustrated in Figure 55. Three specimens of each of the build orientations were tested for repeatability purposes. They were labelled as X-TA 1, X -TA 2 X-TA 3 and the same for the specimens built in the Y-TA and Z-TA orientations. Little necking was observed in the tensile tests.

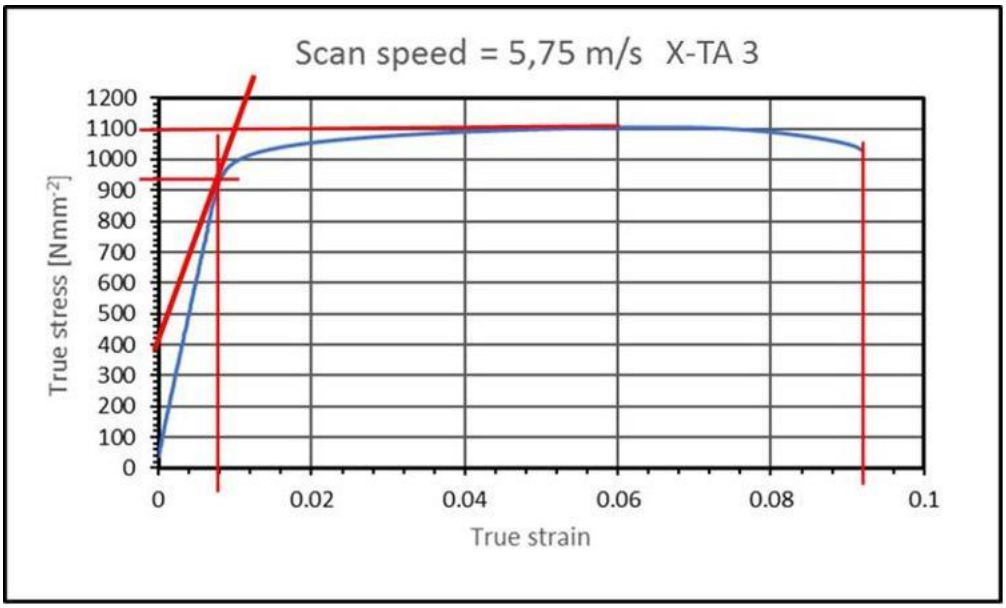

Figure 55: An Illustration of how the tensile properties were obtained from the true-stress true-strain curves. This was implemented on all curves obtained

From the tensile results, the yield strength, UTS and elongation at failure were the parameters of interest. The elastic modulus of the specimens is not calculated as it has been reported that elastic modulus does not vary with build orientation in SLM Ti6Al4V.

4.1.1 The effect of scan speed on the tensile properties

The results showing the relationship between scan speed and tensile properties are shown in this section. The yield strength, UTS and ductility is later compared for each scan speed to analyse the correlation between scan speed and tensile behaviour.

4.1.1.1 5.75 m/s

The tensile test results for the specimens built at 5.75 m/s are shown in this section. The tensile properties obtained are shown in Table 16. Three specimens were tested but specimen Y-TA 3 was compressed during the tensile tests and therefore discarded. The elongation at break for the Y-TA 2 specimen is significantly lower than the other Y-TA specimen and therefore can be regarded as an outlier. The true-stress true-strain curves of the specimens built at 5.75 m/s are shown in Figure 56.

Table 16: Tensile properties of specimens built at 5.75 m/s

Scan speed [m/s]	**Specimen**	**Yield Strength [MPa]**	**UTS [MPa]**	**Percentage Elongation at Failure [%]**	**Energy density [J/mm^3]**
5.75	X-TA 1 X-TA 2 X-TA 3 **Average for X-TA**	900 910 910 **907± 6**	1130 1100 1100 **1110± 17**	9 8 10 **9.0± 1.0**	**65.2**
	Y-TA 1 Y-TA 2 **Average for Y-TA**	960 1080 **1020 ± 85**	1100 1090 **1095± 7**	10 5 **7.5±3.5**	
	Z-TA 1 Z-TA 2 Z-TA 3 **Average for Z-TA**	840 900 860 **867± 31**	1078 1080 1050 **1069± 17**	8 7 7 **7.3± 0.6**	
Averages For each scan speed		**920± 74**	**1091± 23**	**8± 1.7**	

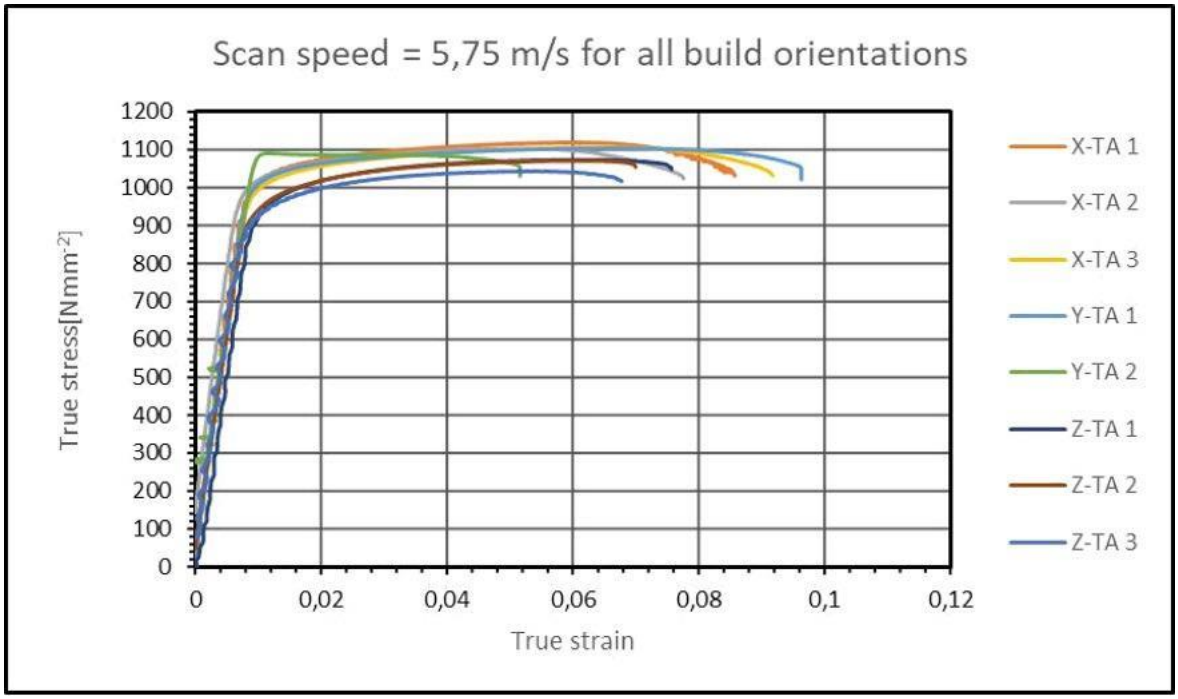

Figure 56: True stress true strain curves for all specimens built at a scan speed of 5.75 m/s

4.1.1.2 6.0 m/s

The tensile test results for the specimens built at 6.0 m/s are shown in this section. The tensile properties of the specimens are shown in Table 17. The yield strength, UTS and elongation at failure values are comparable to the values obtained from the results of the specimens built at 5.75 m/s. The true-stress true-strain curves of the specimens built at 6.0 m/s are shown in Figure 57.

Table 17: Tensile properties of the specimens built at 6.0 m/s

Scan speed [m/s]	Specimen	YS [MPa]	UTS [MPa]	Percentage Elongation at Failure [%]	Energy density [J/mm^3]
6.0	X-TA 1 X-TA 2 X-TA 3 **Average for X-TA**	978 982 1010 **990 ±17**	1060 1110 1050 **1107 ±45**	10 6 10 **8.7±2.3**	62.5
	Y-TA 1 Y-TA 2 Y-TA 3 **Average for Y-TA**	1000 1000 978 **993 ±13**	1150 1120 1102 **1124 ±24**	9 10 8 **9.0±1.0**	
	Z-TA 1 Z-TA 2 Z-TA 3 **Average for Z-TA**	920 939 900 **920 ±20**	1039 1062 1182 **1094 ±77**	7 8 8 **7.7±0.6**	
Averages For each scan speed		**967±39**	**1108±48**	**8±1.4**	

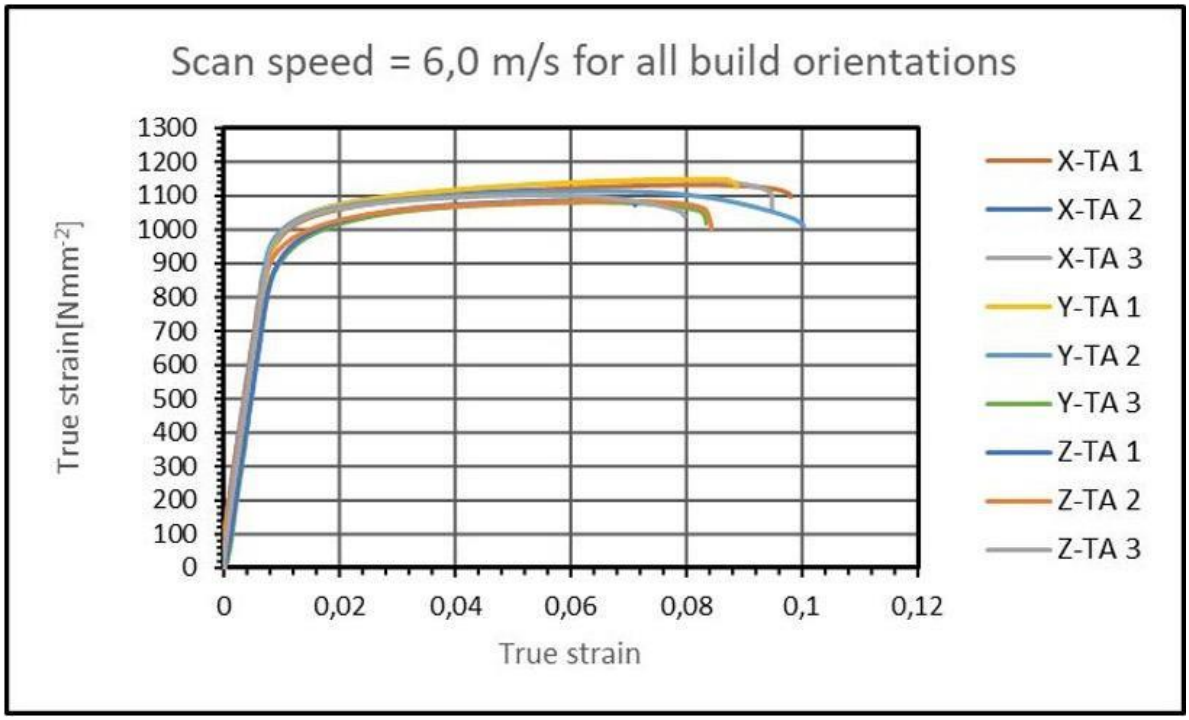

Figure 57: True stress true strain curves for all specimens built at a scan speed of 6.0 m/s

4.1.1.3 6.25 m/s

The tensile test results for the specimens built at 6.25 m/s are shown in this section. The specimens built at 6.25 m/s have comparable yield strength and UTS to the specimens built at 5.75 m/s as is illustrated in Table 18. However, the specimens have significantly inferior ductility. The true-stress true-strain curves of the specimens built at 6.25 m/s are shown in Figure 58.

Table 18: Tensile properties of the specimens built at 6.25 m/s

Scan speed [m/s]	Specimen	YS [MPa]	UTS [MPa]	Percentage Elongation at Failure [%]	Energy density [J/mm^3]
6.25	X-TA 1	880	1000	1	60
	X-TA 2	900	1100	4	
	X-TA 3	950	1060	3	
	Average for X-TA	**910 ± 36**	**1053 ± 50**	**2.7±1.5**	
	Y-TA 1	930	1100	7	
	Y-TA 2	950	1110	5	
	Y-TA 3	930	1020	1	
	Average for Y-TA	**937 ± 12**	**1077 ± 49**	**4.3±3.1**	
	Z-TA 1	880	1098	5	
	Z-TA 2	910	1080	4	
	Z-TA 3	920	1020	1	
	Average for Z-TA	**903 ± 21**	**1067 ± 41**	**3.3± 2.1**	
Average per scan speed		**917 ± 26**	**1065 ± 42**	**3.4±2.1**	

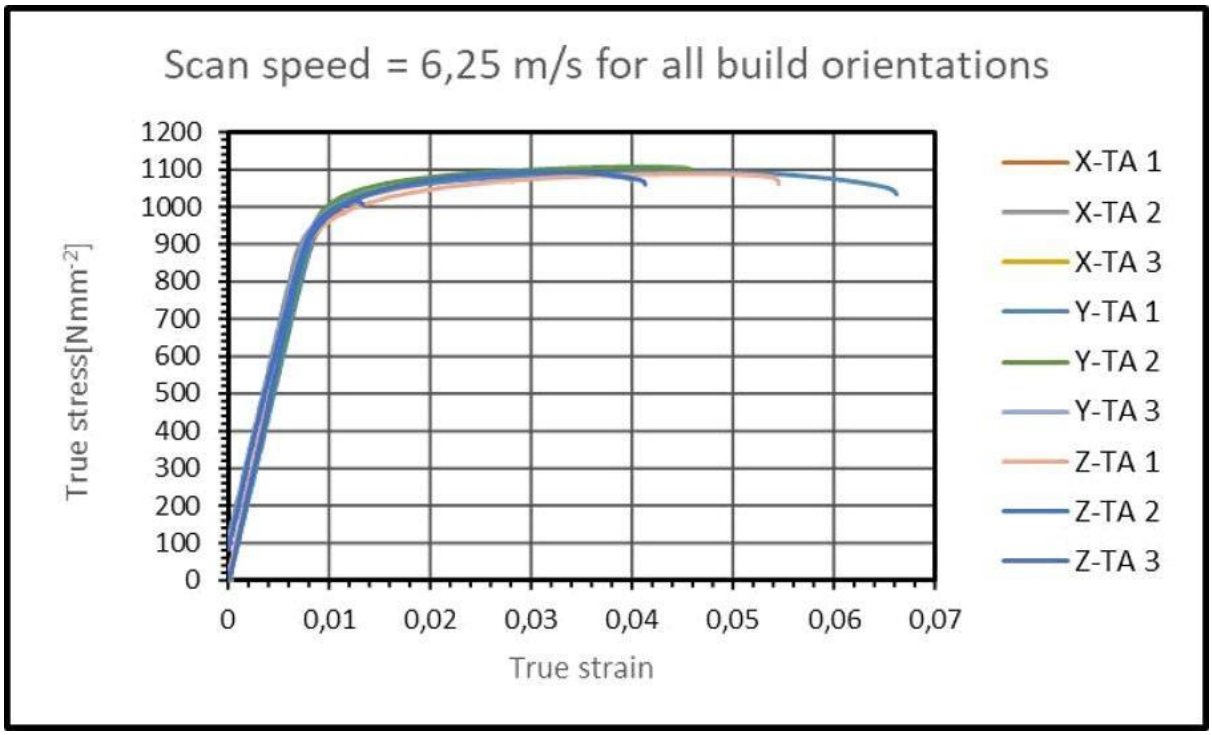

Figure 58: True stress true strain curves for all specimens built at a scan speed of 6.25 m/s

4.1.1.4 6.5 m/s

The tensile test results for the specimens built at 6.25 m/s are shown in this section. The results obtained from the tests for the 6.5 m/s specimens compare to the results obtained from the rest of the scan speeds and no significant difference is observed. A summary of the results obtained from the tensile testing of specimens built at 6.5 m/s is illustrated in Table 19. The true-stress true-strain curves of the specimens built at 6.5 m/s are shown in Figure 59.

Table 19: Tensile properties of the specimens built at 6.5 m/s

Scan speed [m/s]	**Specimen**	**YS [MPa]**	**UTS [MPa]**	**Energy density [J/mm^3]**	
6.5	X-TA 1 X-TA 2 X-TA 3 **Average for X-TA**	980 990 970 **980 ± 10**	1020 1120 1010 **1117 ± 6**	9 9 9 **9.0±0.0**	**57.7**
	Y-TA 1 Y-TA 2 Y-TA 3 **Average for Y-TA**	1060 1040 970 **1023 ± 47**	1090 1080 1100 **1090 ± 10**	7 7 9 **7.6±1.6**	
	Z-TA 1 Z-TA 2 Z-TA 3 **Average for Z-TA**	880 870 880 **877 ± 6**	1060 1080 1060 **1067 ± 12**	6 7 6 **6.3± 0.6**	
Average per scan speed		**960 ± 70**	**1091 ± 23**	**7.6±1.3**	

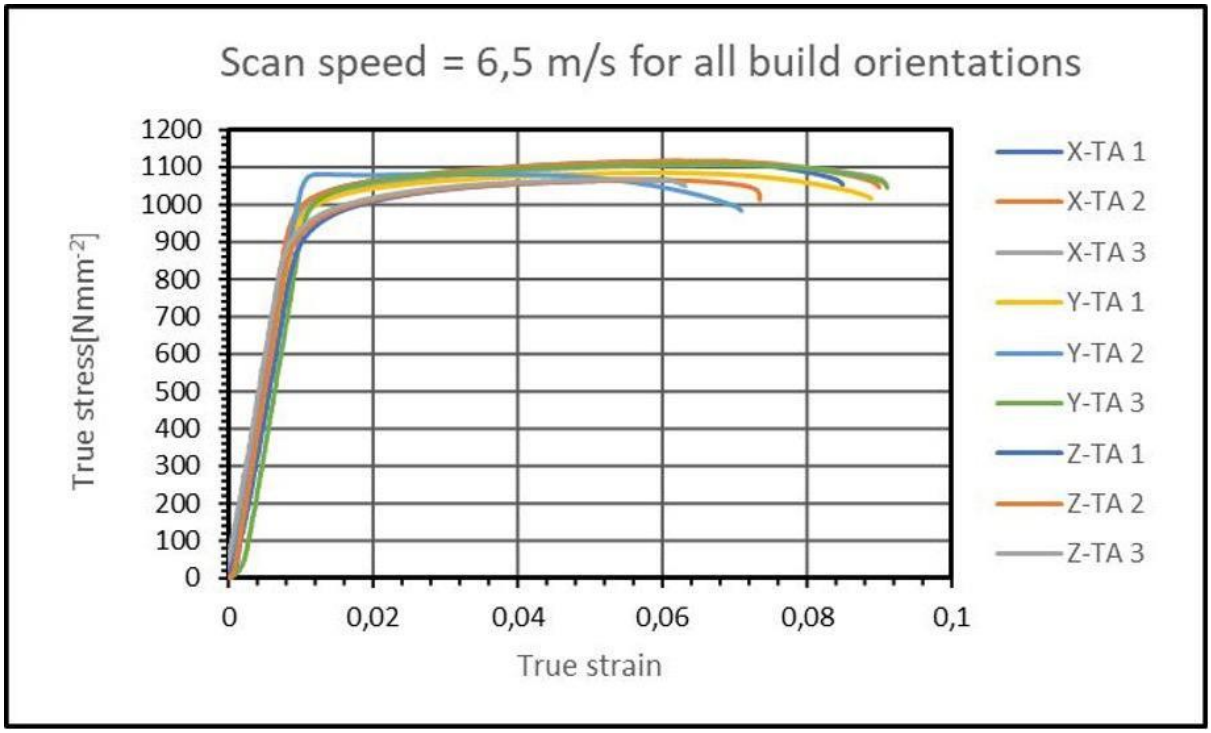

Figure 59: True stress true strain curves for all specimens built at a scan speed of 6.5 m/s

4.1.1.5 Comparison between 5.75 m/s, 6.0 m/s, 6.25 m/s and 6.5 m/s

The true-stress versus true-strain curves for the specimens built at 5.75 m/s, 6.0 m/s and 6.5 m/s show that the X-TA and Y-TA curves tend to cluster together whilst the Z-TA curves cluster together separately from the Y-TA and Z-TA curves. The 6.25 m/s specimens however, show inconsistent behaviour with regards to this phenomenon.

The UTS, yield strength and elongation at break results were analysed separately against scan speed for better comparison. The average values of each of the three properties from the tables above were plotted.

The relationship between scan speed and UTS is shown in Figure 60. The standard deviation error bars were added to the graphs to display the range of UTS for each scan speed. The error bars for all of the scan speeds overlap which illustrates that the samples across all four scan speeds have UTS values within the same range.

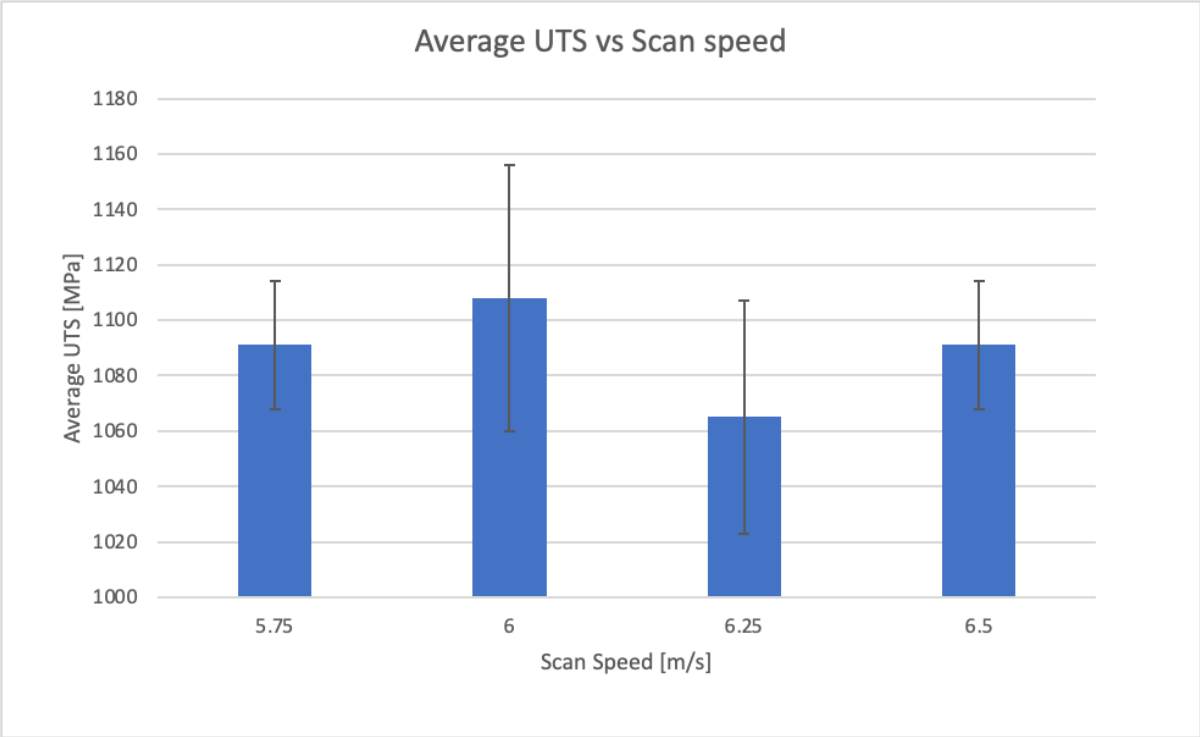

Figure 60: Average UTS from each scan speed vs scan speed

The relationship between scan speed and yield strength is shown in Figure 61. From the graph, it is observed that the specimens built at 5.75 and 6.25 m/s have a lower average yield strength value compared to the rest of the scan speeds. However, the values are still within the same range as observed with the UTS and they overlap with those of the samples built at 5.75, 6.0 and 6.5 m/s. The samples across all four scan speeds therefore have yield strength within the same range.

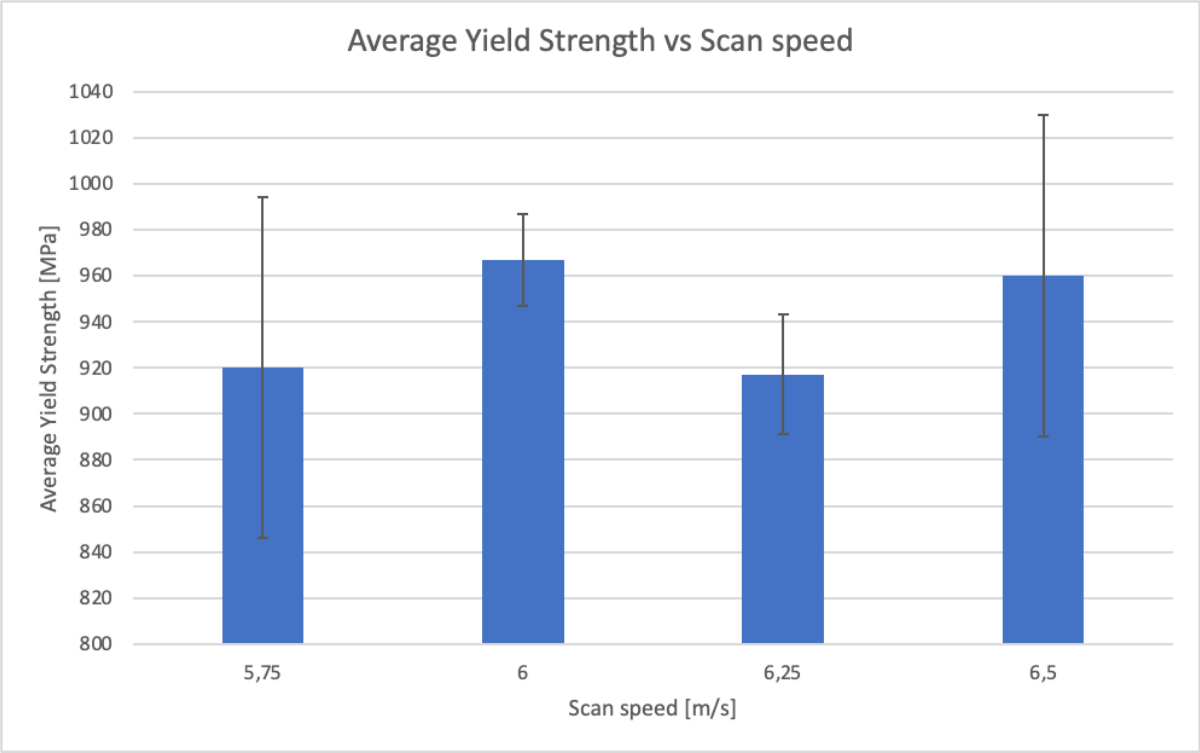

Figure 61: Average yield strength from each scan speed vs scan speed

The relationship between scan speed and elongation at break is shown in Figure 62. The average elongation at break of the 5.75 6.0 and 6.5 m/s specimens is within the same range. The 6.25 m/s specimens, however, have lower elongation at break thus having the lowest ductility which is not within the same range as other specimens built in the other three scan speeds.

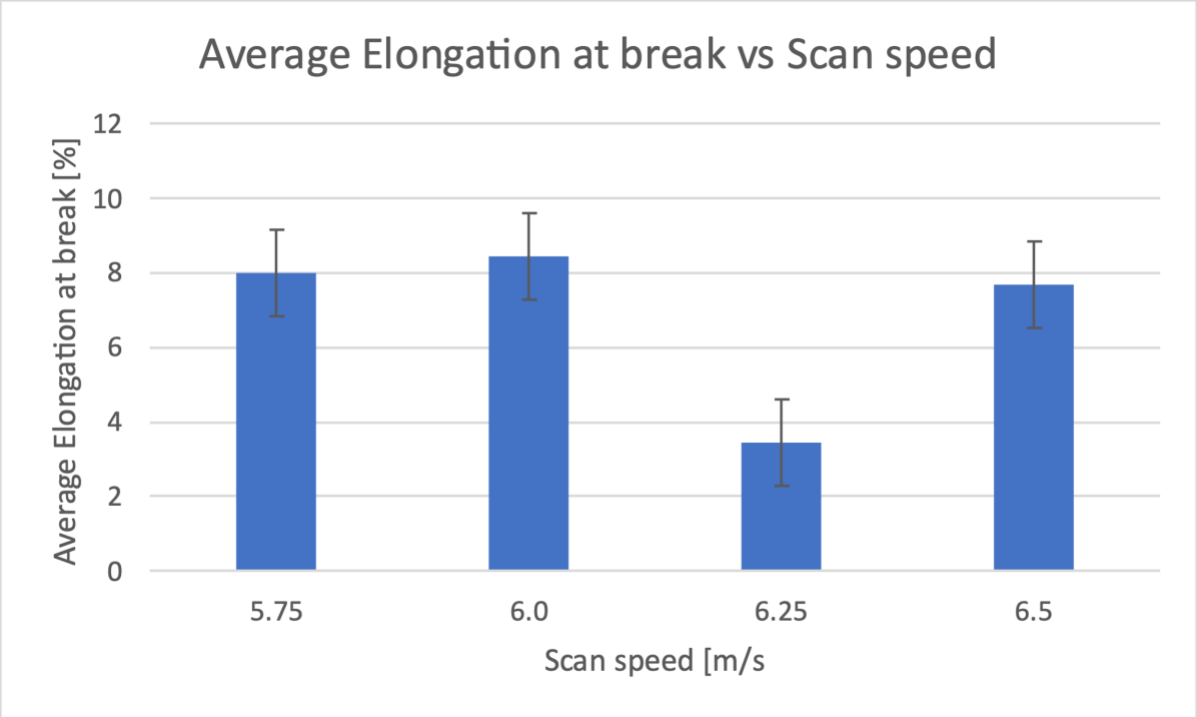

Figure 62: Average elongation at break from each scan speed vs scan speed

4.1.2 The effect of build orientation on the tensile properties

The results showing the relationship between build orientation and tensile properties are shown in this section. The yield strength, UTS and ductility is later compared for each build orientation to analyse the correlation between build orientation and tensile behaviour.

4.1.2.1 X-TA

The tensile test results for the specimens built in the X-TA orientation are shown in this section. A summary of the tensile properties obtained is shown in Table 20. The true stress true strain curves of these specimens are illustrated in Figure 63.

Table 20: Tensile properties of all specimens built in the X-TA orientation

Build Orientation	**Scan speed [m/s]**	**Yield strength [MPa]**	**UTS [MPa]**	**Elongation at failure [%]**	**Energy density [Jmm^3]**
X-TA	5.75 1 5.75 2 5.75 3	900 910 910	1130 1100 1100	9 8 10	65.2
	6.0 1 6.0 2 6.0 3	978 982 1010	1060 1110 1150	10 6 10	62.5
	6.25 1 6.25 2 6.25 3	880 900 950	1000 1100 1060	1 4 3	60
	6.5 1 6.5 2 6.5 3	980 990 970	1120 1120 1110	9 9 9	57.7
Average		**947 ± 44**	**1097 ± 40**	**7.3±3.1**	

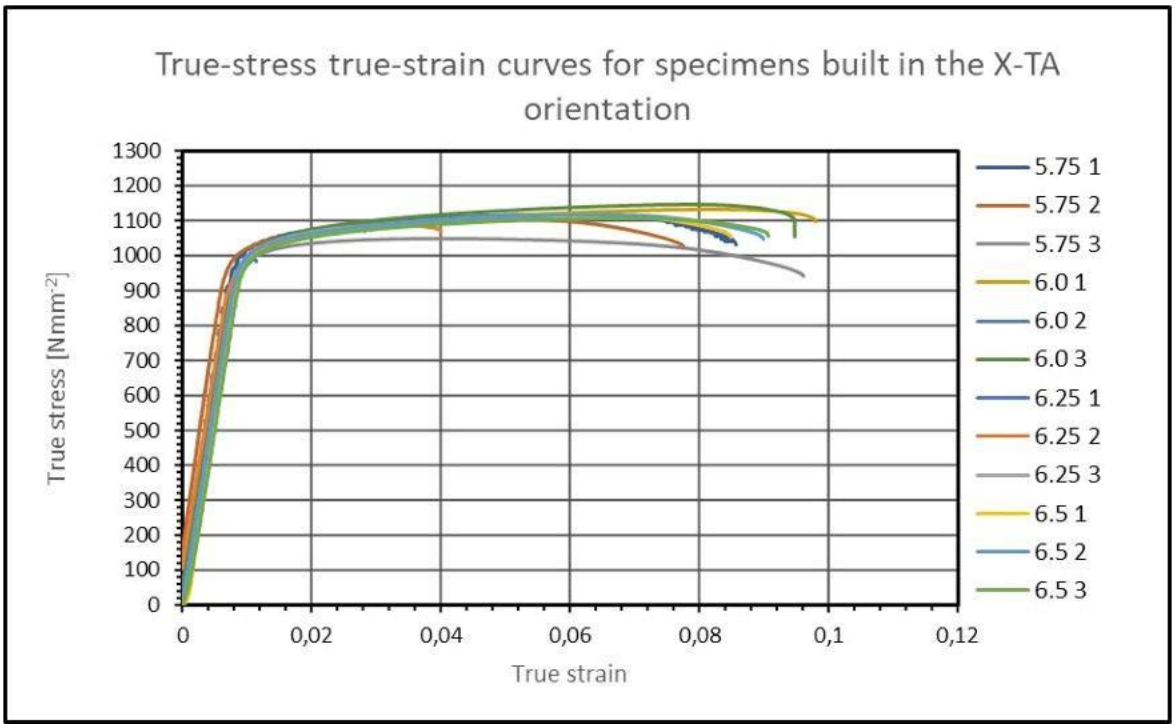

Figure 63: True stress true strain curves for all specimens built in the X-TA orientation

4.1.2.2 Y-TA

The tensile test results for the specimens built in the Y-TA orientation are shown in this section. A summary of the tensile properties obtained is shown in Table 21. The true stress true strain curves of these specimens are illustrated in Figure 64.

Table 21: Tensile properties for all specimens built in the Y-TA orientation

Build Orientation	Scan speed [m/s]	Yield strength [MPa]	UTS [MPa]	Elongation at failure [%]	Energy density [Jmm^3]
Y-TA	5.75 1 5.75 2	960 1080	1100 1090	10 5	65.2
	6.0 1 6.0 2 6.0 3	1000 1000 978	1150 1120 1102	9 10 8	62.5
	6.25 1 6.25 2 6.25 3	930 950 930	1100 1110 1020	7 5 1	60
	6.5 1 6.5 2 6.5 3	1060 1040 970	1090 1080 1100	7 7 9	57.7
Average		**991 ± 51**	**1097 ± 31**	**7.1±2.7**	

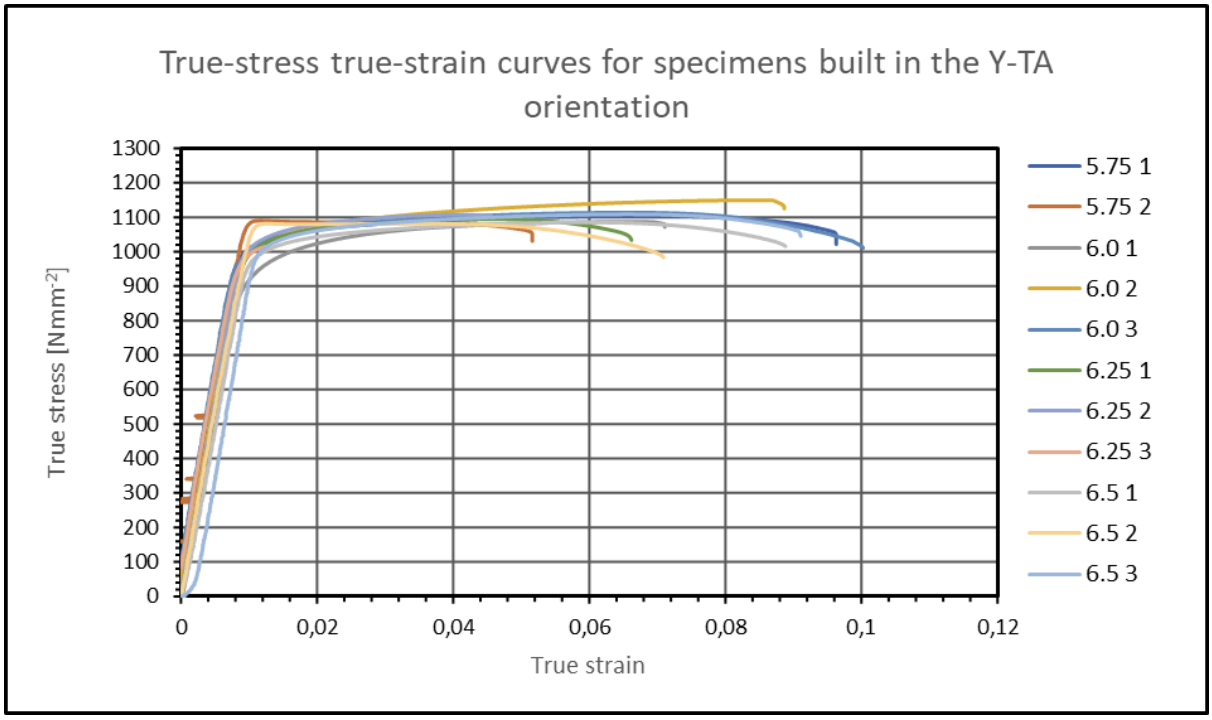

Figure 64: True stress true strain curves for all specimens built in the Y-TA orientation

4.1.2.3 Z-TA

The tensile test results for the specimens built in the Z-TA orientation are shown in this section. A summary of the tensile properties obtained is shown in Table 22. The true stress true strain curves of these specimens are illustrated in Figure 65.

Table 22: Tensile properties of all specimens built in the Z-TA orientation

Build Orientation	**Scan speed [m/s]**	**Yield strength [MPa]**	**UTS [MPa]**	**Elongation at failure [%]**	**Energy density [Jmm^3]**
Z-TA	5.75 1	840	1078	8	65.2
	5.75 2	900	1080	7	
	5.75 3	860	1050	7	
	6.0 1	920	1039	7	62.5
	6.0 2	939	1062	8	
	6.0 3	900	1182	8	
	6.25 1	880	1098	5	60
	6.25 2	910	1080	4	
	6.25 3	920	1020	1	
	6.5 1	880	1060	6	57.7
	6.5 2	870	1080	7	
	6.5 3	880	1060	6	
	Average	**892 ± 28**	**1074 ± 40**	**6.2±2.0**	

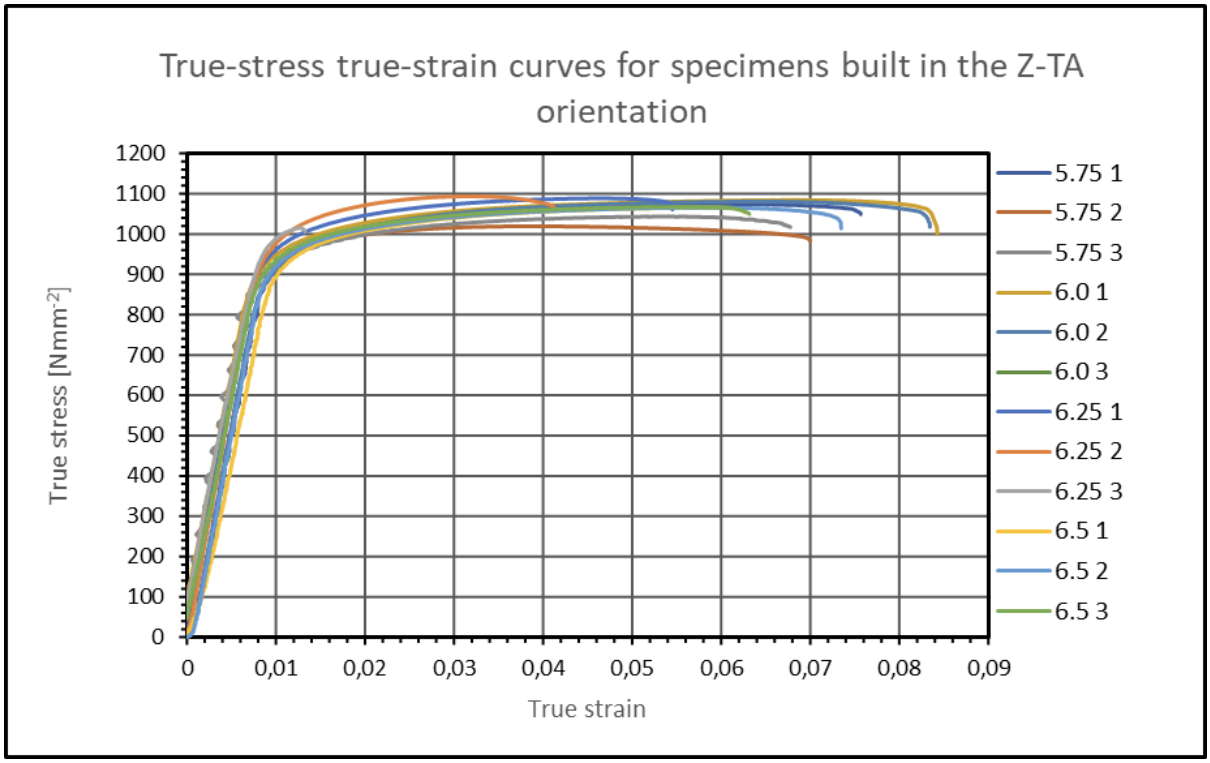

Figure 65: True stress true strain curves for all specimens built in the Z-TA orientation

4.1.2.4 Comparison between X-TA, Y-TA, and Z-TA

The UTS, yield strength and elongation at break results were analysed separately against build orientation for better comparison. The average values of each of the three properties were calculated and used as the representative value for each build orientation.

The relationship between UTS and build orientation is shown in Figure 66. The specimens built in the X-TA, Y-TA and Z-TA have UTS values within the same range.

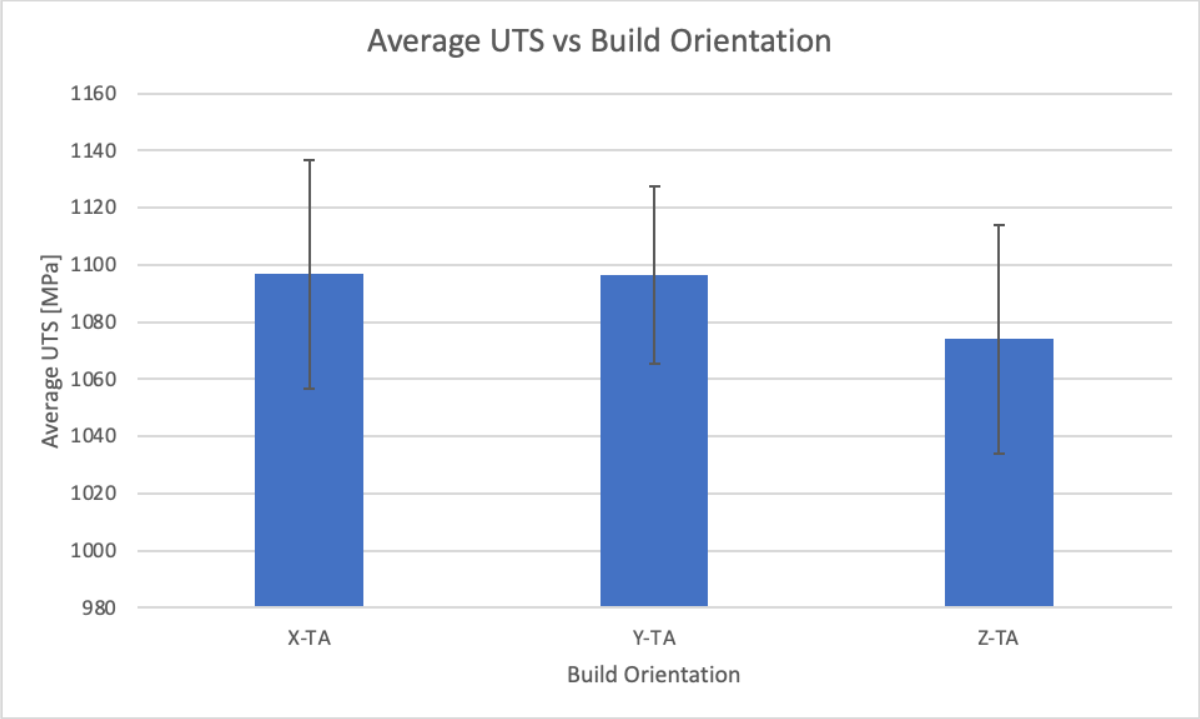

Figure 66: Average UTS from each build orientation vs build orientation

The relationship between yield strength and build orientation is shown in Figure 67. The specimens built in the Y-TA orientation have the highest average yield strength. However, all specimens built in the three orientations have UTS values within the same range.

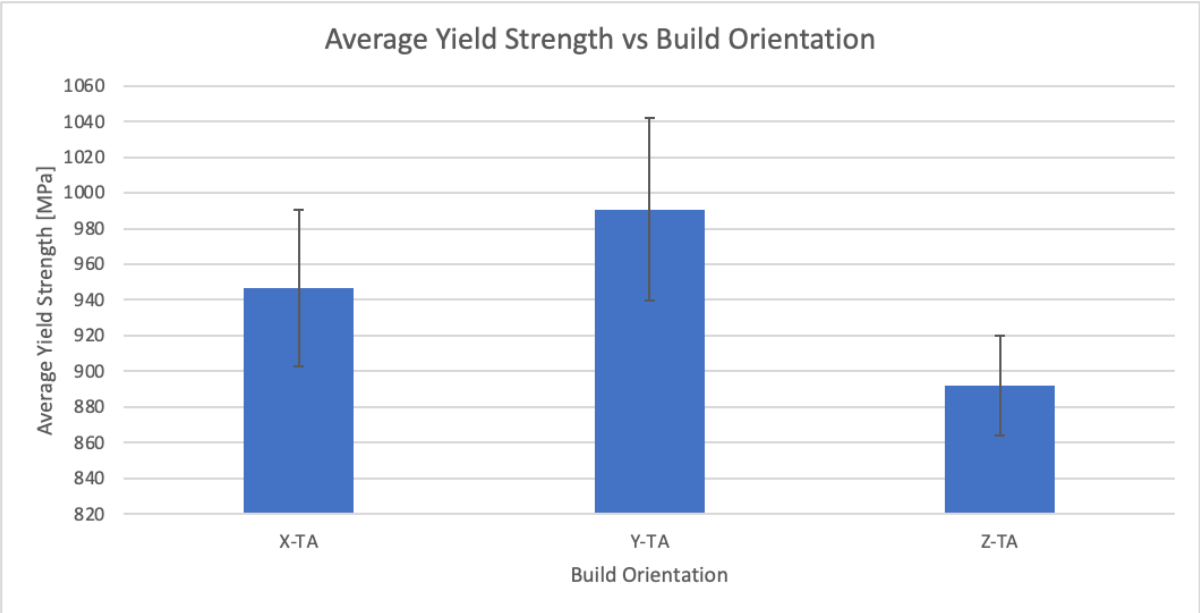

Figure 67: Average yield strength from each build orientation vs build orientation

The relationship between elongation at break and build orientation is shown in Figure 68. The X-TA, Y-TA and Z-TA specimens have comparable ductility as their average elongation at break values are within the same range. No significant difference in elongation at break with build orientation is observed.

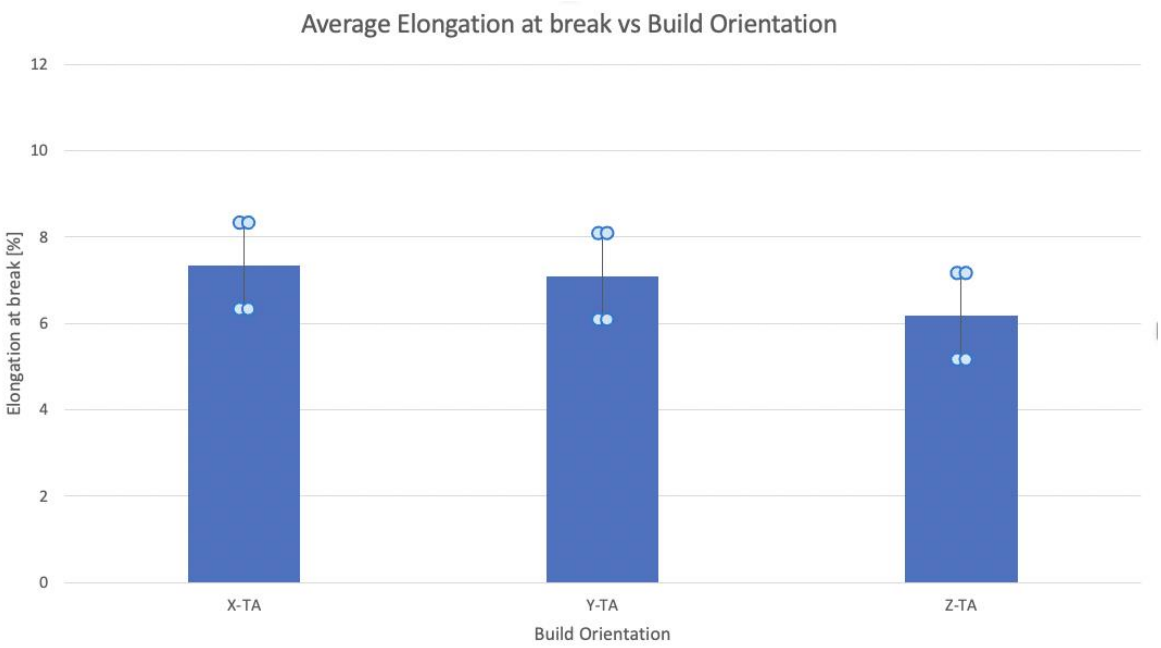

Figure 68:Average elongation at break from each build orientation vs build orientation

The tensile properties do not vary significantly with scan speed as they all lie in the same range except for the elongation at break of the 6.25 m/s which is lower. Build orientation in SLM Ti6Al4V parts has an influence on microstructure which can affect tensile strength but this is not observed in these results. Other effects on microstructure such as pores and defects also affect tensile strength. This is further investigated in section 4.5. The results are further discussed in section 5.1.

4.2 Fatigue crack growth rate test results

The results obtained from the FCGR tests will be shown in this section. The results are presented as crack length versus number of cycles to failure and Paris curves. The FCGR tests were run until fracture and all tests were performed at the same load. All FCGR specimens were built in the XZ orientation.

4.2.1 5.75 m/s

The results obtained from the FCGR tests for the specimens built at 5.75 m/s are shown in this section. The crack length versus number of cycles to failure graph for specimen 1 and specimen 2 built at 5.75 m/s are shown in Figure 69. Unfortunately, specimen 3 was spoiled during unloading from the machine and therefore could not be included in the results. The crack propagated to the same range of length for all two specimens which was between 15.75mm mm and 16.75mm.

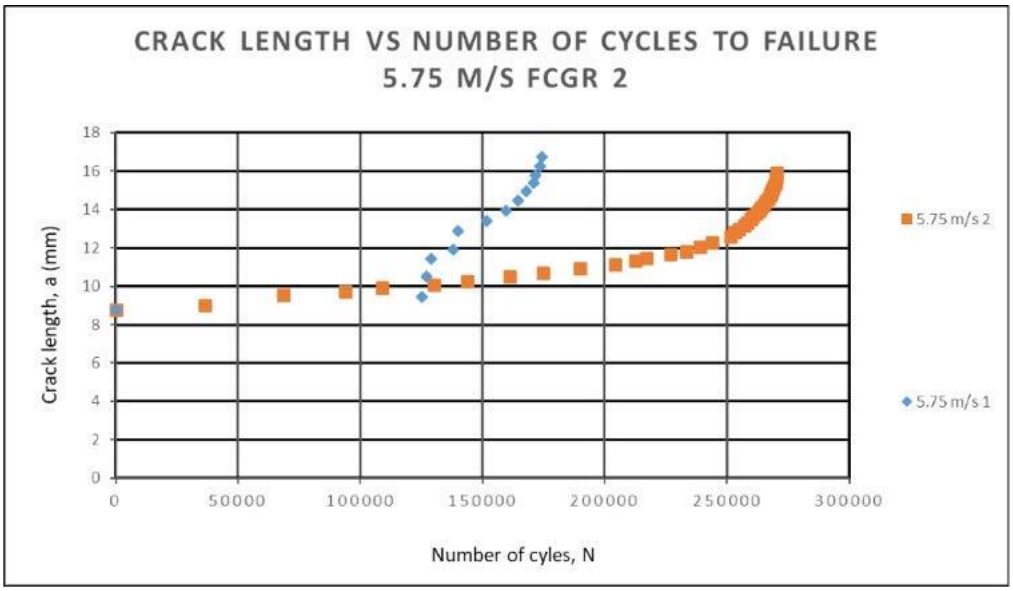

Figure 69:Crack length vs number of cycles to failure for specimen built at 5.75 m/s.

The Paris curves for the specimens built at 5.75 m/s are displayed in Figure 70. These curves were calculated to show the Paris region of the specimens which is of interest for FCGR determination. This was done for all scan speeds. Low crack growth rates were observed which is expected when testing at low cyclic stress intensity factor range. The data was plotted at a stress intensity factor range between 8 and 20 MPa.m$^{0.5}$. Paris equations for the specimens were constructed from the data obtained during the tests. The Paris equations are displayed in Table 23.

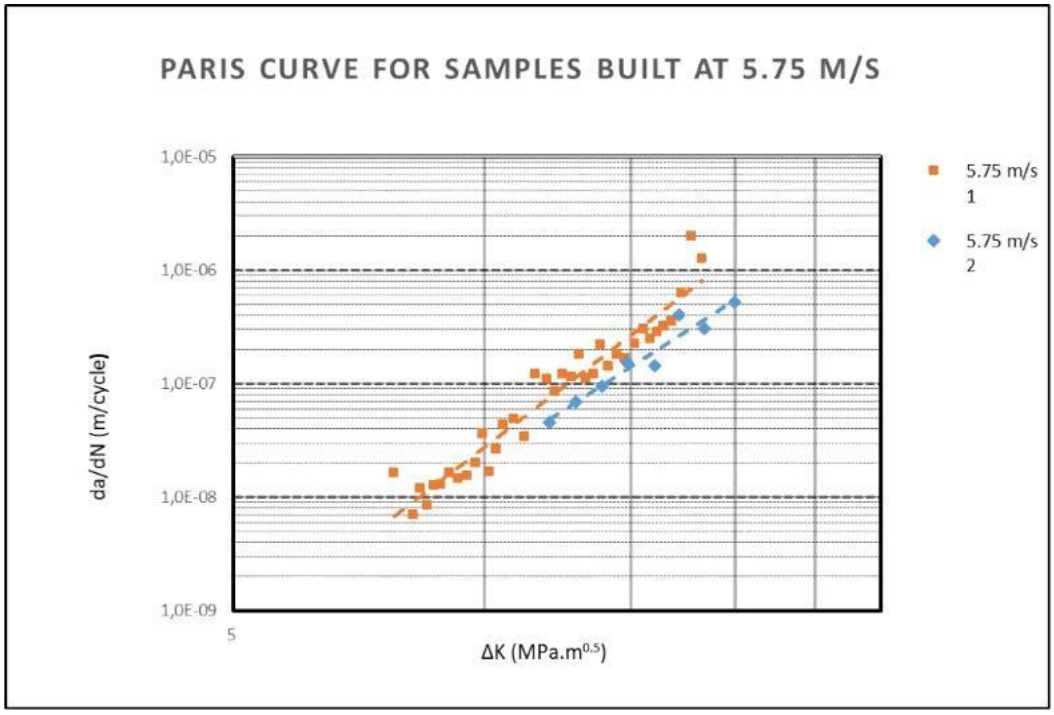

Figure 70:Fatigue crack growth rate curve for specimens built at 5.75 m/s.

Table 23: Paris equations for specimens built at 5.75 m/s, 1 and 2

Specimen	Paris Equation
1	$\frac{da}{dN} = (7.0\ x\ 10^{-14} \pm\ 2.33\ x\ 10^{-13})\Delta K^{5.61 \pm 0.64}$
2	$\frac{da}{dN} = (4.0\ x\ 10^{-13} \pm\ 2.33\ x\ 10^{-13})\Delta K^{4.71 \pm 0.64}$
Range of *C* values for specimen 1	$-1.63\ x\ 10^{-13}$ - $3.03\ x\ 10^{-13}$
Range of *C* values for specimen 2	$1.67\ x\ 10^{-13}$ - $6.33\ x\ 10^{-13}$
Range of *m* values for specimen 1	4.97 - 6.25
Range of *m* values for specimen 2	4.07 - 5.35

Both specimens built at 5.75 m/s displayed stable crack growth rate behaviour and similar levels of scatter. The C and m values of both specimens are within the same range.

4.2.2 6.0 m/s

The results obtained from the FCGR tests for the specimens built at 6.0 m/s are shown in this section. Figure 71 shows the crack length versus number of cycles to failure curve for the three specimens built at 6.0 m/s. Specimens 2 and 3 displayed stable crack growth behaviour and no anomalous behaviour. The curve for specimen 1 is quite steep and failed at the lowest number of cycles, approximately after 250 000 cycles. Specimens 2 and 3 failed after 370 000 cycles. The difference in behaviour of specimen 1 from the others is not expected since all specimens are similar. The difference is further investigated from fracture surface analysis. The crack propagated to the same range of length for all three specimens which was between 17.75mm and 18.75mm.

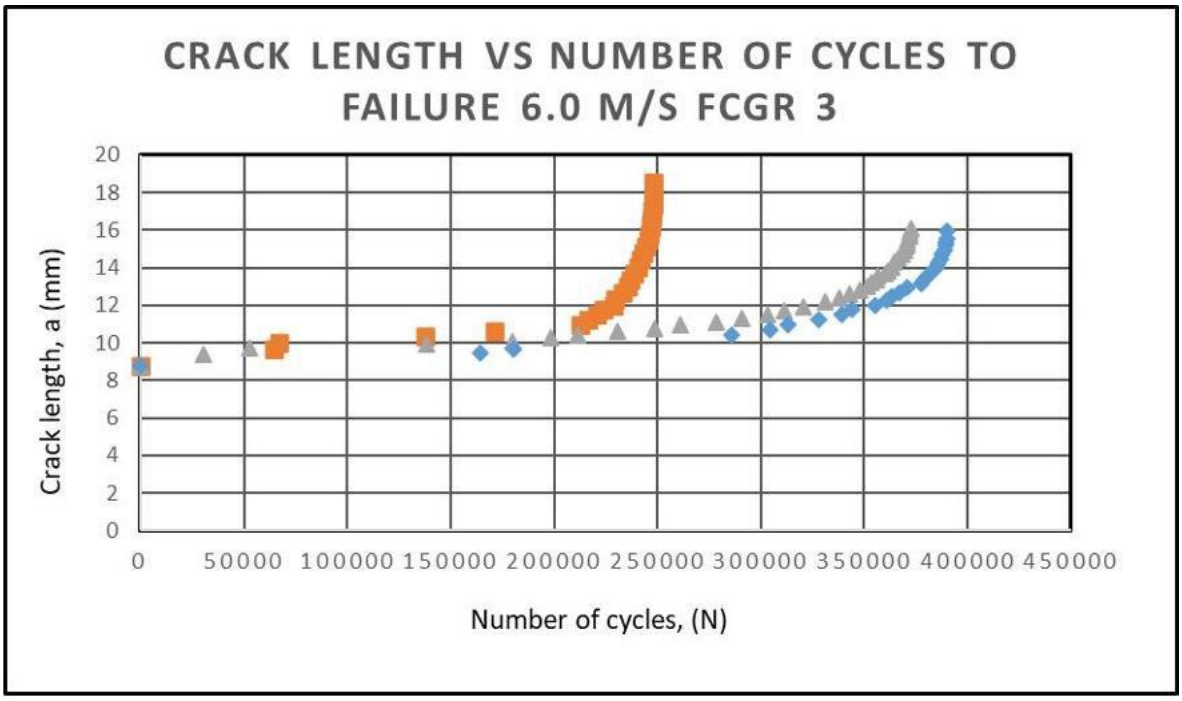

Figure 71:Crack length vs number of cycles to failure for specimen built at 6.0 m/s.

The Paris regime for the specimens built at 6.0 m/s is shown in Figure 72. The data was plotted at a stress intensity factor range between 8 and 20 MPa.m$^{0.5}$ for specimens 2 and 3. The data for specimen 1was plotted over a wider stress intensity factor range of between 8 and 30 MPa.m$^{0.5}$. These results could imply that specimen 1 displayed anomalous behaviour or that the crack in specimen 1 developed a preferred propagation path because of the alignment of the columnar grains. In all the XZ specimens, the crack propagates in the direction parallel to the columnar grains, but it is possible to notice differences in crack propagation in these specimens depending on the path taken by the crack.

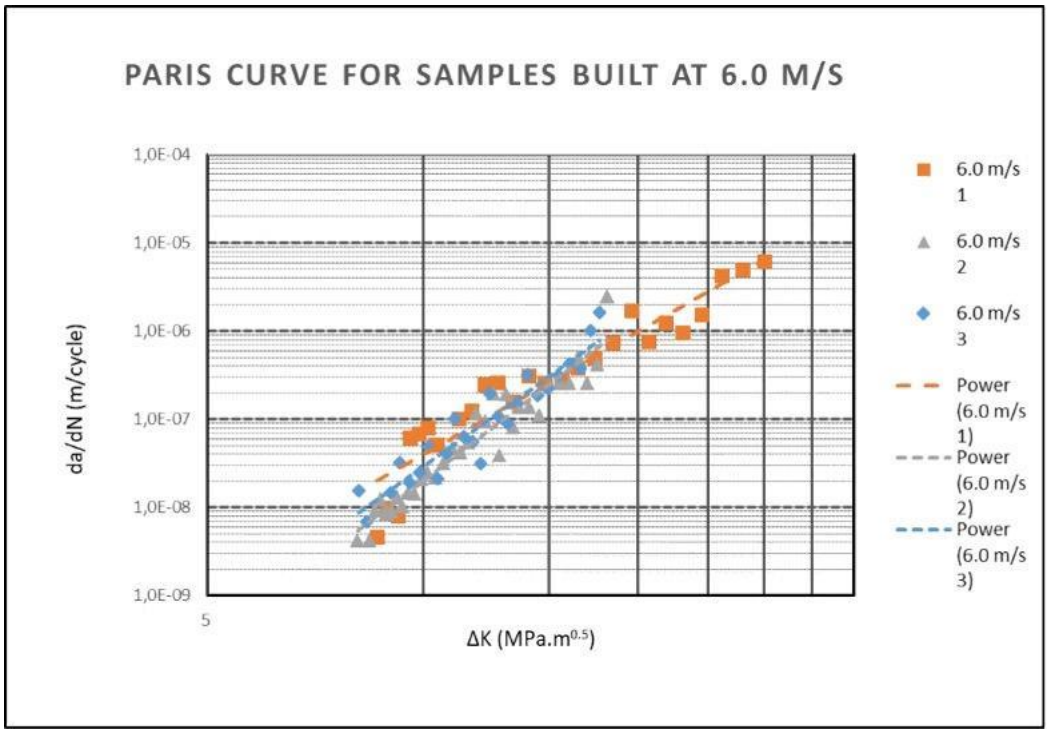

Figure 72: Fatigue crack growth rate curve for specimens built at 6.0 m/s.

The Paris equations for the specimens were constructed and are displayed in Table 24. The *m* values of specimens 2 and 3 are within the same range whilst that of specimen 1 is relatively lower. The *C* values are similar.

Table 24: Paris equations for the specimens built at 6.0 m/s

Specimen	Paris Equation
1	$\frac{da}{dN} = (9.0\ x\ 10^{-13}\ \pm\ 5.03\ x\ 10^{-13})\Delta K^{4.64 \pm 0.81}$
2	$\frac{da}{dN} = (1.0\ x\ 10^{-14}\ \pm\ 5.03\ x\ 10^{-13})\Delta K^{6.19 \pm 0.81}$
3	$\frac{da}{dN} = (5.0\ x\ 10^{-14}\ \pm\ 5.03\ x\ 10^{-13})\Delta K^{5.81 \pm 0.81}$
Range of *C* values for specimen 1	$3.97\ x\ 10^{-13}$ - $1.4\ x\ 10^{-12}$
Range of *C* values for specimen 2	$4.93.97\ x\ 10^{-13}$ - $5.13\ x\ 10^{-13}$
Range of *C* values for specimen 3	$-4.53.97\ x\ 10^{-13}$ - $5.53\ x\ 10^{-13}$
Range of *m* values for specimen 1	3.83 - 5.45
Range of *m* values for specimen 2	5.38 - 7.00
Range of *m* values for specimen 3	5.00 - 6.62

4.2.3 6.25 m/s

The results obtained from the FCGR tests for the specimens built at 6.25 m/s are shown in this section. The results shown are for two specimens. The third specimen was discarded due to human error after running for a few cycles during the pre-cracking procedure. The crack length versus number of cycles results for the two specimens built at 6.25 m/s is shown in Figure 73. Specimen 1 fractured after 590 000 cycles and had the largest number of cycles to failure for this speed. Specimen 2 fractured after 350 000 cycles. The crack propagated to the same range

of length for both specimens which was between 18.75 and 21.75mm. The Paris curves are displayed in Figure 74.

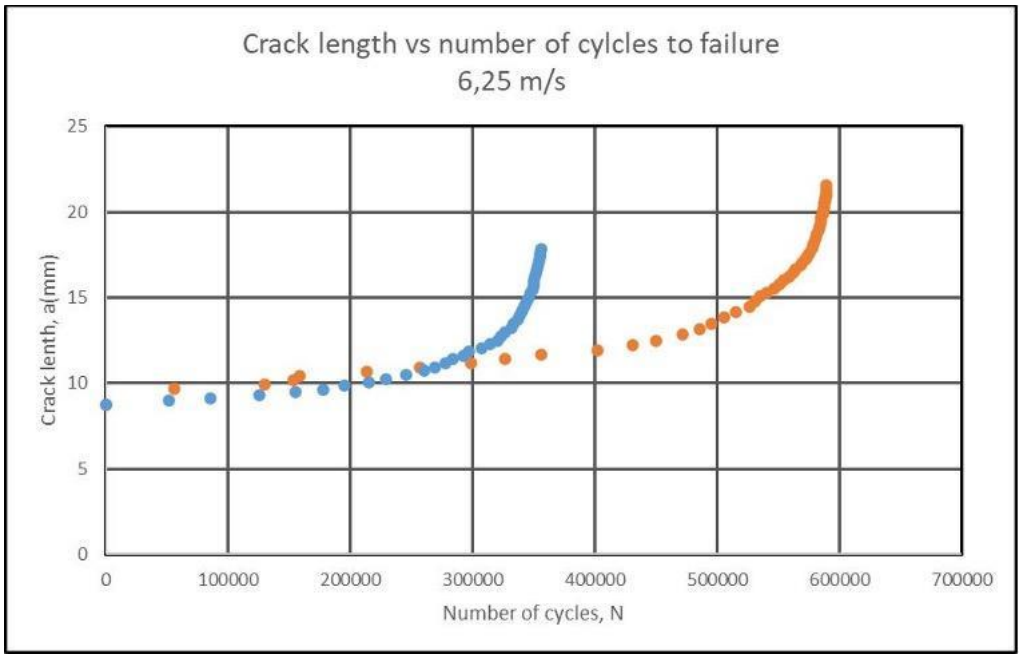

Figure 73: Crack length vs number of cycles to failure for specimen built at 6.25 m/s.

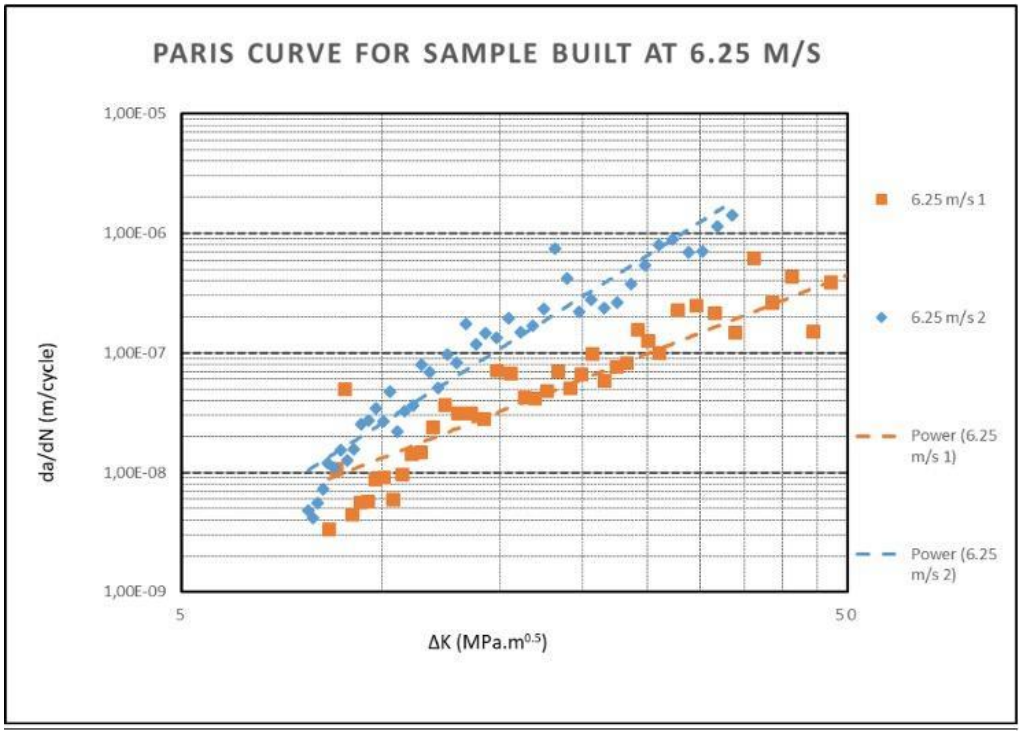

Figure 74: Fatigue crack growth rate curve for specimen built at 6.25 m/s.

The two specimens built at 6.25 m/s displayed stable crack growth rate. The data was plotted at a stress intensity factor range between 8 and 33 MPa.m$^{0.5}$ for specimen 1 and at a stress intensity factor range between 8 and 50 MPa.m$^{0.5}$ for specimen 2. A summary of the Paris equations is displayed in Table 4.10. The *C* and *m* parameters of the two specimens built at 6.25 m/s are within the same range.

Table 25: Paris equations for the specimens built at 6.25 m/s

Specimen	Paris Equation
1	$\frac{da}{dN} = (9.0\ x\ 10^{-11}\ \pm\ 5.80\ x\ 10^{-11})\Delta K^{2.19\ \pm\ 0.94}$
2	$\frac{da}{dN} = (8.0\ x\ 10^{-12}\ \pm\ 5.80\ x\ 10^{-11})\Delta K^{3.52\ \pm\ 0.94}$
Range of *C* values for specimen 1	$4.93.97\ x\ 10^{-13}$ - $5.13\ x\ 10^{-13}$
Range of *C* values for specimen 2	$8.00\ x\ 10^{-12}$ - $6.00\ x\ 10^{-11}$
Range of *m* values for specimen 1	1.25 - 3.13
Range of *m* values for specimen 2	2.58 - 4.46

4.2.4 6.5 m/s

The results obtained from the FCGR tests for the specimens built at 6.5 m/s are shown in this section. Figure 75 shows the crack length versus number of cycles for the specimens built at 6.5 m/s. Specimen 2 displayed the steepest curve and failed after the least number of cycles (150 000 cycles). Specimen 1 and 3 displayed more similar curves although specimen 1 fractured after 325 000 cycles and specimen 3 fractured after 450 000 cycles. The crack propagated to the same range of length for all three specimens which was between 19.75mm and 20.75mm.

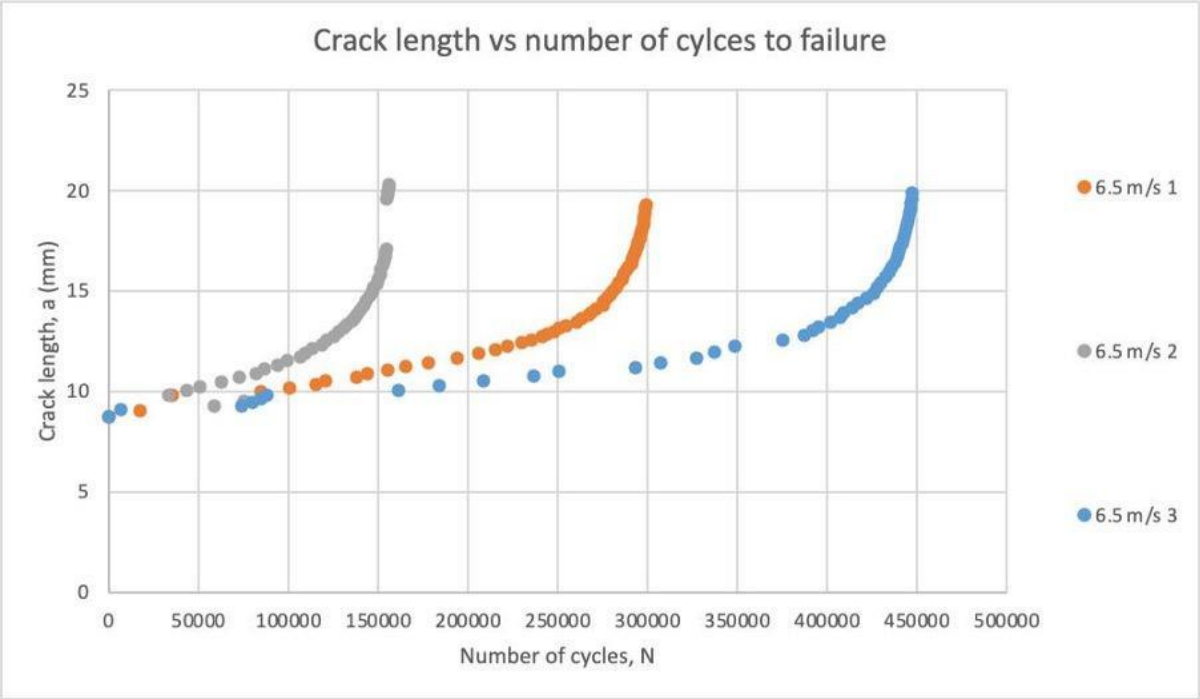

Figure 75: Crack length vs number of cycles to failure for specimen built at 6.5 m/s

The Paris curves for the specimens built at 6.5 m/s are shown in Figure 76. The data was plotted at a stress intensity factor range between 8 and 50 MPa.m$^{0.5}$ for specimen 2 and 3 and at a stress intensity factor range between 8 and 40 MPa.m$^{0.5}$ for specimen 1. All three specimens display similar levels of scatter. A summary of the Paris equation is displayed in Table 26 that follows. The *C* and *m* values are within the same range.

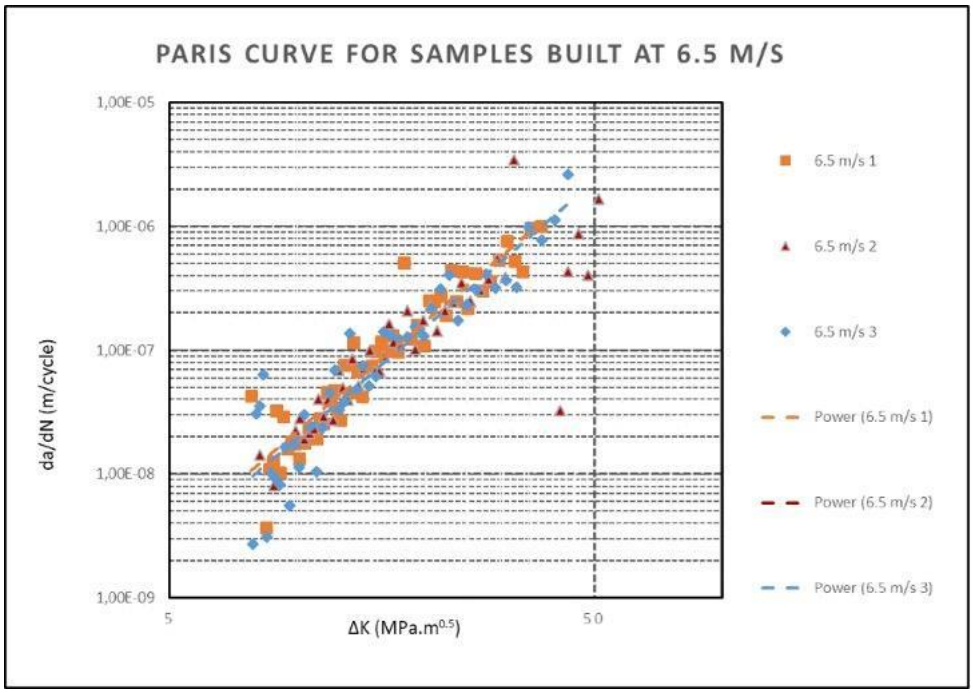

Figure 76: Fatigue crack growth rate curve for specimen built at 6.5 m/s

Table 26: Paris equations for the specimens built at 6.5 m/s

Specimen	Paris Equation
1	$\frac{da}{dN} = (3.0 \times 10^{-11} \pm 3.79 \times 10^{-11})\Delta K^{2.94 \pm 0.30}$
2	$\frac{da}{dN} = (9.0 \times 10^{-11} \pm 3.79 \times 10^{-11})\Delta K^{2.43 \pm 0.30}$
3	$\frac{da}{dN} = (2.0 \times 10^{-11} \pm 3.79 \times 10^{-11})\Delta K^{2.97 \pm 0.30}$
Range of C values for specimen 1	-7.86×10^{-12} - 6.79×10^{-11}
Range of C values for specimen 2	5.21×10^{-11} - 1.28×10^{-10}
Range of C values for specimen 3	-1.79×10^{-11} - 5.79×10^{-11}
Range of m values for specimen 1	2.64 - 3.24
Range of m values for specimen 2	2.13 - 2.73
Range of m values for specimen 3	2.67 - 3.27

4.2.5 Comparison between 5.75 m/s, 6.0 m/s, 6.25 m/s and 6.5 m/s

A summary of the average FCGR results for each scan speed is shown in Table 27. The average Paris equation for each scan speed was calculated to analyse and compare the crack growth rates and behaviour of the specimens built at the different high scan speeds.

Table 27: Average Paris equations for each scan speed

Scan speed [m/s]		Range of *C* values	Range of *m* values
5.75	Specimen 1	-1.63×10^{-13} - 3.03×10^{-13}	4.97 - 6.25
	Specimen 2	1.67×10^{-13} - 6.33×10^{-13}	4.07 - 5.35
6.0	Specimen 1	3.97×10^{-13} - 1.4×10^{-12}	3.83 - 5.45
	Specimen 2	$4.93.97 \times 10^{-13}$ - 5.13×10^{-13}	5.38 - 7.00
	Specimen 3	$-4.53.97 \times 10^{-13}$ - 5.53×10^{-13}	5.00 - 6.62
6.25	Specimen 1	$4.93.97 \times 10^{-13}$ - 5.13×10^{-13}	1.25 - 3.13
	Specimen 2	8.00×10^{-12} - 6.00×10^{-11}	2.58 - 4.46
6.5	Specimen 1	-7.86×10^{-12} - 6.79×10^{-11}	2.64 - 3.24
	Specimen 2	5.21×10^{-11} - 1.28×10^{-10}	2.13 - 2.73
	Specimen 3	-1.79×10^{-11} - 5.79×10^{-11}	2.67 - 3.27

The average Paris equations show that the specimens built at 5.75 and 6.0 m/s have similar results within the same range. There is no significant difference in FCGR behaviour between the two scan speeds. The specimens built at 6.25 m/s and 6.5 m/s have similar results and no significant difference is seen between the two. However, they show different FCGR behaviour in comparison with the specimens built at 5.75 and 6.0 m/s. This is observed in the C and m values. The results are further discussed in section 5.2.

4.3 Fracture toughness test results

The results obtained from the fracture toughness tests performed according to the method outlined in section 3.5 are shown in this section.

The fracture toughness results are presented as crack measurements and force versus displacement curves. The data obtained after each fracture toughness test is used to plot load vs displacement curves up to the point where the highest load was reached (Pmax). To determine a valid KIC value, PQ is estimated by drawing a secant line through the origin. An illustration of how the values of Pmax and PQ were estimated is shown in Figure 77. Pmax and PQ values are used to calculate KQ as instructed in the ASTM E399 standard. This was done for all the tested specimens. For all the tests done, the Pmax/PQ ratios do not exceed 1.10 and the calculated values of $2.5(KQ/\sigma YS)^2$ are less than the specimen ligament size (W-a) therefore the KQ value from each test is equal to KIC and the tests are valid fracture toughness tests.

Figure 77: An illustration of the estimation of Pmax and PQ values

The length of the fatigue pre-crack is also required for the calculation of K_Q. It is measured from the load line to the crack front. Three measurements of the fatigue pre-crack are taken from different regions, one at mid-thickness and the other two at quarter-thickness positions. The crack measurements are illustrated in Figure 78. The average of these measurements is calculated with the length of the notch added to the measurements. The total of the average of the measurements and the notch length is then used as the average crack length for calculating K_Q.

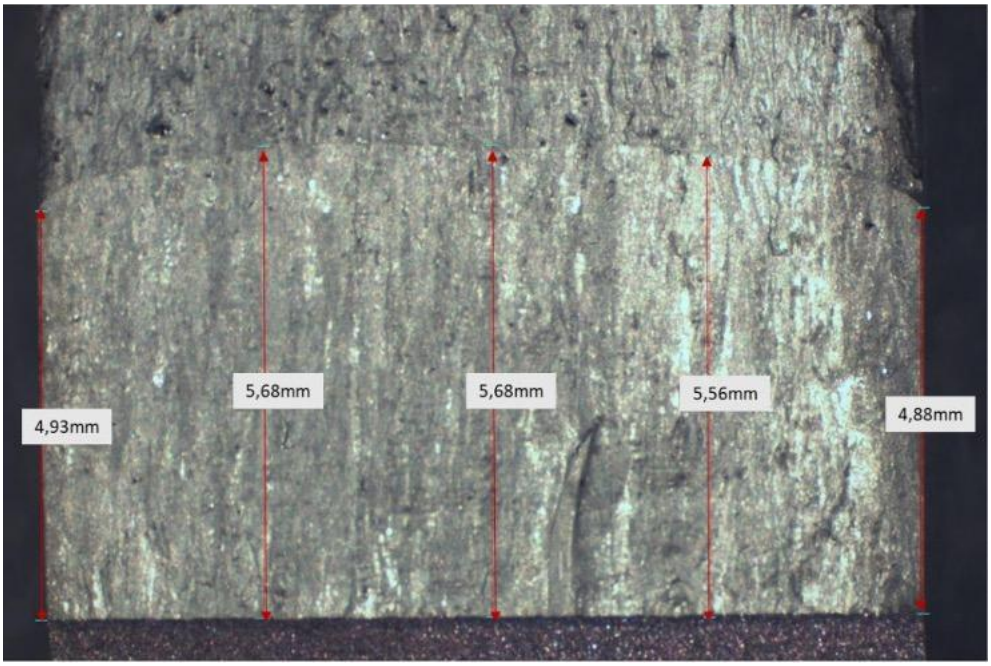

Figure 78: Measurements of crack length after fracture

4.3.1 5.75 m/s

A total of three specimens were tested for the 5.75 m/s scan speed. The important parameters used to determine KQ and the results are shown in Table 23 below.

Table 28: Fracture toughness results for specimens built at 5.75 m/s

Speed [m/s]	**Specimen**	**P_{max} [N]**	**P_Q [N]**	**Average crack length [mm]**	**K_{max} [MPa.m$^{0.5}$]**	**K_Q [MPa.m$^{0.5}$]**
5.75	**1**	8000	8000	14.38	50.33	50.33
	2	9300	9100	13.19	49.58	48.52
	3	9200	9000	13.77	53.07	51.92
					Average	**50.26 ± 1.7**

Table 23 shows some of the parameters that were used to calculate K_{max} and K_Q which are the maximum experienced load (Pmax), the force determined by the position of the drawn secant line when it meets the curve from the origin (P_Q) and the average crack length as calculated from the three measurements. The same parameters are listed in the tables to follow in this section. The K_Q values obtained from the three specimens are within the same range which shows good repeatability in the results.

4.3.2 6.0 m/s

A total of three specimens were tested for the 6.0 m/s scan speed. Table 24 below summarises the fracture toughness results for the specimens built at 6.0 m/s. The fracture toughness results of the specimens built at 6.0 m/s show lower maximum load values which correspond to the lower K_Q values in comparison with the 5.75 m/s specimens.

Table 29: Fracture toughness results for specimens built at 6.0 m/s

Speed [m/s]	**Specimen**	**P_{max} [N]**	**P_Q [N]**	**Average crack length [mm]**	**K_{max} [MPa.m$^{0.5}$]**	**K_Q [MPa.m$^{0.5}$]**
6.0	**1**	8800	8600	13.41	48.30	47.20
	2	7800	7200	14.55	50.28	46.21
	3	8200	7800	14.13	49.71	47.28
					Average	**49.96 ± 0.5**

4.3.3 6.25 m/s

A total of three specimens were tested for the 6.25 m/s scan speed. Table 25 below summarises the fracture toughness results for the specimens built at 6.25 m/s. The average K_Q value calculated for the 6.25 m/s specimens is within the same range as that of the 5.75 m/s specimens.

Table 30: Fracture toughness results for specimens built at 6.25 m/s

Speed [m/s]	**Specimen**	**P_{max} [N]**	**P_Q [N]**	**Average crack length [mm]**	**K_{max} [MPa.m$^{0.5}$]**	**K_Q [MPa.m$^{0.5}$]**
6.25	**1**	8300	8000	14.71	54.83	52.85
	2	8200	7800	14.39	51.64	49.12
	3	8800	8200	14.40	55.53	51.74
					Average	**51.24 ± 1.9**

4.3.4 6.5 m/s

A total of three specimens were tested for the 6.5 m/s scan speed. Table 26 below summarises the fracture toughness results for the specimens built at 6.5 m/s. The average K_Q value calculated for the 6.25 m/s specimens is within the same range as that of the 5.75 m/s and the 6.25 m/s specimens.

Table 31: Fracture toughness results for specimens built at 6.5 m/s

Speed [m/s]	**Specimen**	**P_{max} [N]**	**P_Q [N]**	**Average crack length [mm]**	**K_{max} [MPa.m$^{0.5}$]**	**K_Q [MPa.m$^{0.5}$]**
6.5	**1**	7800	7600	15.02	54.03	52.64
	2	7000	6800	15.54	52.80	51.29
	3	7800	7400	14.94	53.36	50.62
					Average	**51.52 ± 1.2**

4.3.5 Comparison between 5.75 m/s, 6.0 m/s, 6.25 m/s and 6.5 m/s

The fracture toughness results of the SLM Ti-6Al-4V display acceptable results and behaviour. The specimens built in the different scan speeds display similar results although the specimens built at 6.0 m/s have relatively lower K_Q values. The results are further discussed in section 5.3.

4.4 Density test results

A summary of the average density results for the tensile specimens built in the X-TA, Y-TA and Z-TA orientations at the different scan speeds are shown in Table 27.

A similar scatter plot is shown for the relationship between build orientation and density in Figure 80. More details on the density results can be found in section 10.

Table 32: Summary of average density test results for all scan speeds and orientations

Scan speed [m/s]	X-TA density [g/cm^3]	Y-TA density [g/cm^3]	Z-TA density [g/cm^3]
5.75	4.36 ± 0.02	4.32 ± 0.00	4.32 ± 0.01
6.0	4.30 ± 0.03	4.32 ± 0.03	4.32 ± 0.04
6.25	4.32 ± 0.02	4.33 ± 0.02	4.30 ± 0.02
6.5	4.34 ± 0.06	4.33 ± 0.05	4.31 ± 0.01

The average density results shown in Table 32 were consistent with the absolute density of Ti6Al4V, 4.429 g/cm^3 found in literature[22]. The density values were converted to percentage relative density according to the equation below:

$$Measured\ density\ \div Standard\ density of\ Ti6Al4V) * 100$$

Equation 12: Conversion of density values to relative density

Where, the standard density of Ti6Al4V is the absolute density of Ti6Al4V from literature. These values were then plotted on scatter plots to explicitly show the relationship between density, scan speed and build orientation, respectively. Looking at the values in Table 32, there is sufficient overlap in the density values for the specimens across all scan speeds and build orientation which suggests no variation of relative density with change in scan speed or build orientation.

The percentage relative density value for each specimen is plotted against scan speed as shown in Figure 79 displaying the relationship between scan speed and density. From the results, the specimens built across all scan speeds have similar variation in relative density and the scatter is quite substantial.

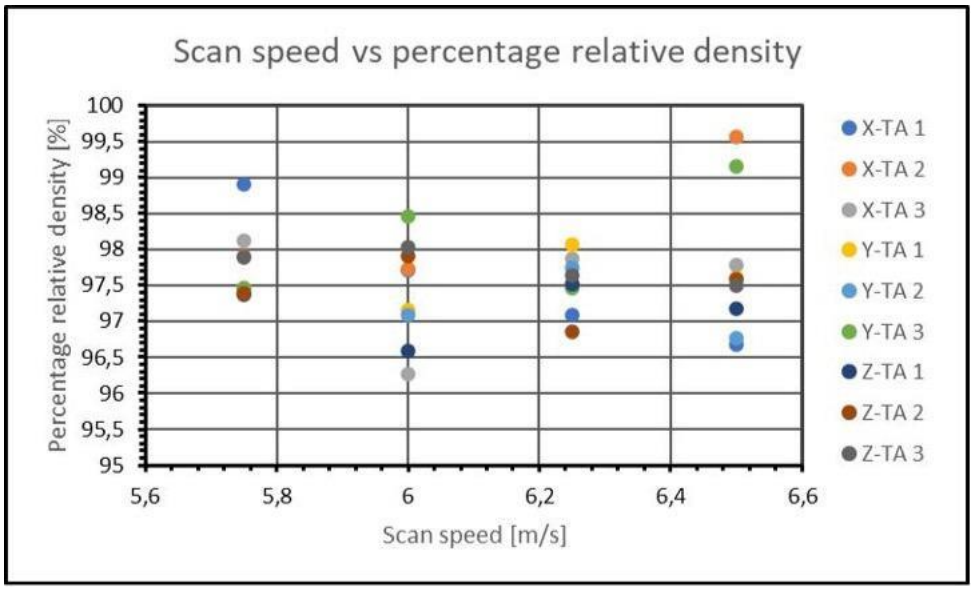

Figure 79: Scatter plot showing the relationship between scan speed and relative density of the specimens built at the higher scan speeds

The percentage relative density value for each specimen is plotted against build orientation as shown in Figure 80 displaying the relationship between build orientation and density. There is substantial range in density within each build orientation although the range is somewhat narrower for the samples built in the Z-TA orientation.

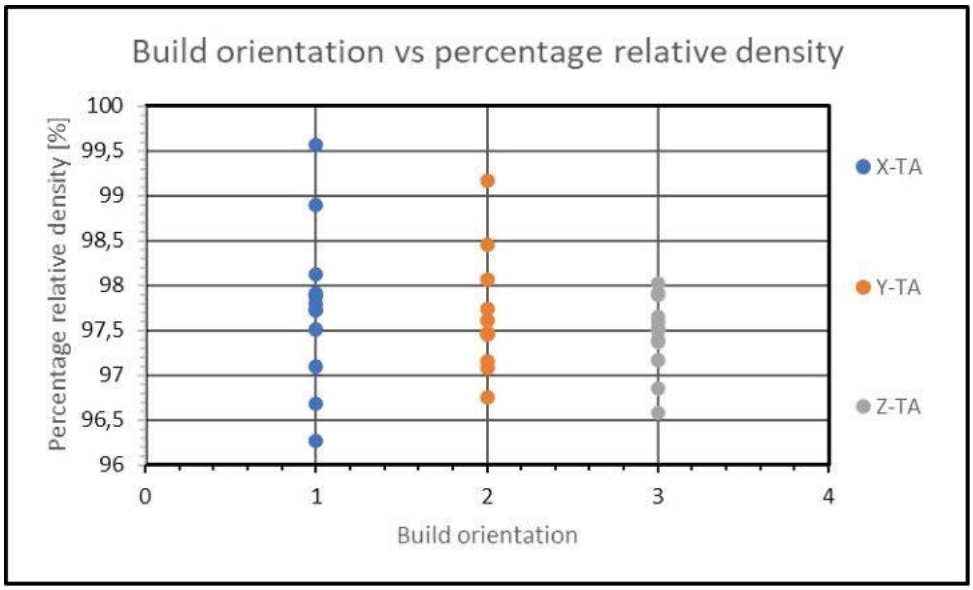

Figure 80: Scatter plot showing relationship between build orientation and relative density of the specimens built at the higher scan speeds. The build orientations are labelled as 1, 2 and 3 for the X-TA, Y-TA, and Z-TA respectively

4.5 Microstructure

Microstructure analysis was carried out on the tensile specimens to identify the different microstructural characteristics as function of build orientation. The fractured compact tension specimens were examined after toughness testing to determine aspects of fracture occurrence from the fractography analysis. The techniques used were light microscopy and SEM imaging, where the latter included the use of electron backscattered diffraction (EBSD). The results are shown in this section.

4.5.1 Light microscopy

Microstructure analysis was first investigated using light microscopy. The objectives were to highlight the type of microstructure and to provide contrast of grain boundaries in relation to other surface features of the specimens built in different orientations. The microstructure observed in all images is predominantly martensitic acicular α which is characteristic of SLM fabricated Ti6Al4V due to the high temperature gradients during the laser scanning process. The α emerges upon cooling of the β phase.

Microscopy images were taken in two views; the front view, which is along the frontal plane of the tensile specimens and the side view which is along the longitudinal plane of the tensile specimens. Due to the layer-by-layer mechanism of the SLM process, the microstructures in the side and front view will differ. Images were taken for all four scan speeds.

4.5.1.1 5.75 m/s

The microstructure of the material built at 5.75 m/s is shown in this section. The images shown represent the side (longitudinal plane) and front (frontal plane) views of the material for each of the build orientations.

4.5.1.1.1 X-TA

The two views of the microstructure of the material built in the X-TA orientation at 5.75 m/s are shown in Figure 81. The images were acquired at X10 objective lens magnification.

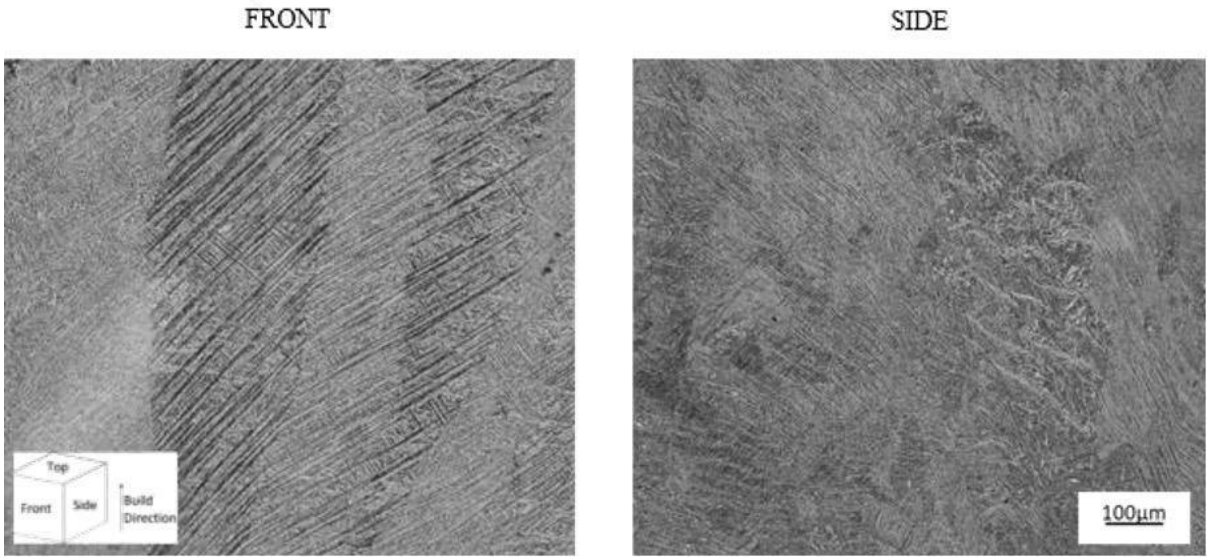

Figure 81: Light microscope images of the material built at 5.75 m/s in the X-TA orientation. Images were taken at X10 objective lens magnification

The microstructure seen in the front view shows a columnar arrangement of the martensite colonies. This columnar arrangement arises due to the martensite colonies transforming from a prior beta grain that existed as a columnar grain parallel to the build direction. These columnar grains are typical of SLM produced material. They arise due to epitaxial growth caused by layer-by-layer deposition. They are observed in the view perpendicular to the build direction in the material built in the X-TA orientation. The columnar grains are irregularly shaped and vary in size.

The side view displays a different grain structure compared to the one observed in the front view. Elongated grains are not observed in the side view of the X -TA material. The difference in grain structure is expected as the material is cut along different planes for the two views due to the layer-by-layer mechanism of the SLM process.

The images of the material taken at X100 objective lens magnification are illustrated in Figure 82.

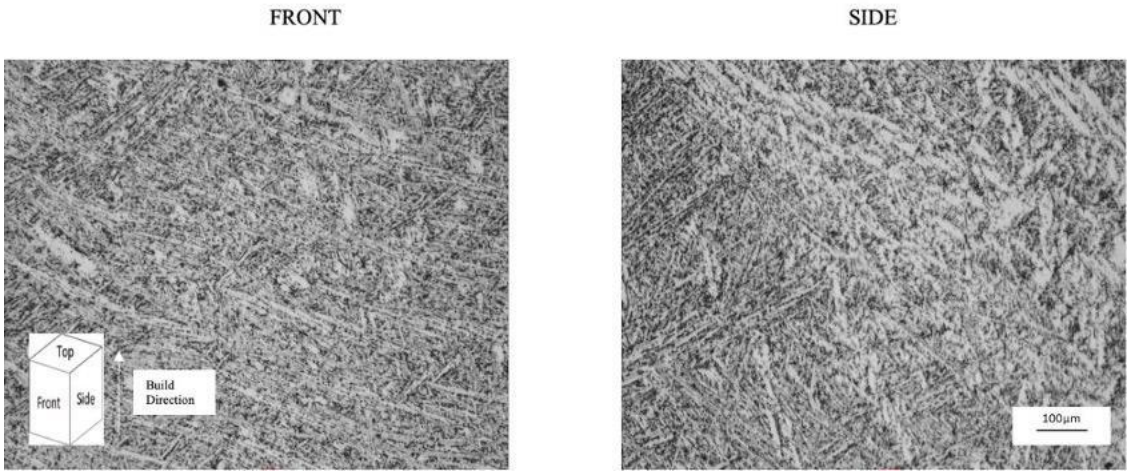

Figure 82: Light microscope images of the material built at 5.75 m/s in the X-TA orientation. Images were taken at X100 objective lens magnification

The acicular microstructure seen in the front view of Figure 4.28, is the structure enclosed by the columnar β-grains observed at low magnification. The martensitic structure is comprised of slightly course α-plates which is typical of stress relieved SLM Ti6Al4V as the martensitic structure partially decomposes to acicular α with coarser α-plates.

4.5.1.2 Y-TA

The two views of the microstructure of the material built in the Y-TA orientation at 5.75 m/s are shown in Figure 83.

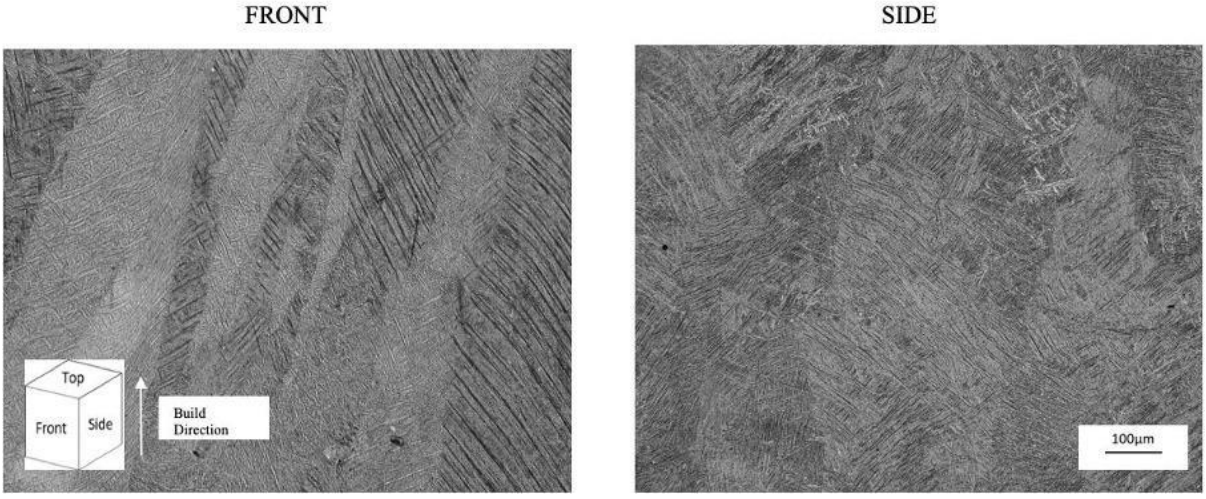

Figure 83: Light microscope images of the material built at 5.75 m/s in the Y-TA orientation. The images were taken at X10 objective lens magnification

The same martensitic microstructure is observed in the specimens built in Y-TA orientation. The columnar grains are orientated in the same direction observed in the microstructure of the X-TA material and they are observed in the front view, perpendicular to the build direction.

4.5.1.3 Z-TA

The two views of the microstructure of the material built in the Z-TA orientation at 5.75 m/s are shown in Figure 84.

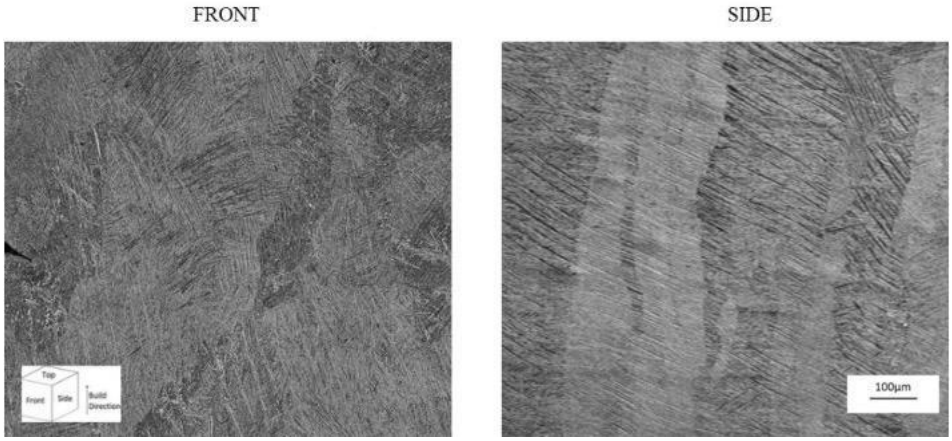

Figure 84: Light microscope images of material built at 5.75 m/s in the Z-TA orientation

The martensitic microstructure observed in the material built in Z-TA orientation is like the microstructure observed in the X-TA and Y-TA material. However, the direction of the orientation of the columnar grains is different. In The Z-TA material, the columnar grains are observed in the side view, parallel to the build direction and not in the front view as seen in the X-TA and Y-TA material.

4.5.1.4 Comparison between 5.75 m/s, 6.0 m/s, 6.25 m/s and 6.5 m/s

The microstructures of the material built at 6.0 m/s, 6.25 m/s and 6.5 m/s are shown in this section. The images shown represent the side and front views of the material for each of the build orientations. The microstructures are grouped per build orientation.

4.5.1.4.1 X-TA

The two views of the microstructures of the material built in the X-TA orientation at 6.0 m/s, 6.25 m/s and 6.5 m/s respectively are illustrated in Figure 4.31. The images display the same microstructure observed with the 5.75 m/s material, the elongated grains in the front view and the acicular martensitic structure in the side view. No difference in microstructure of the X-TA material is observed with increase in scan speed.

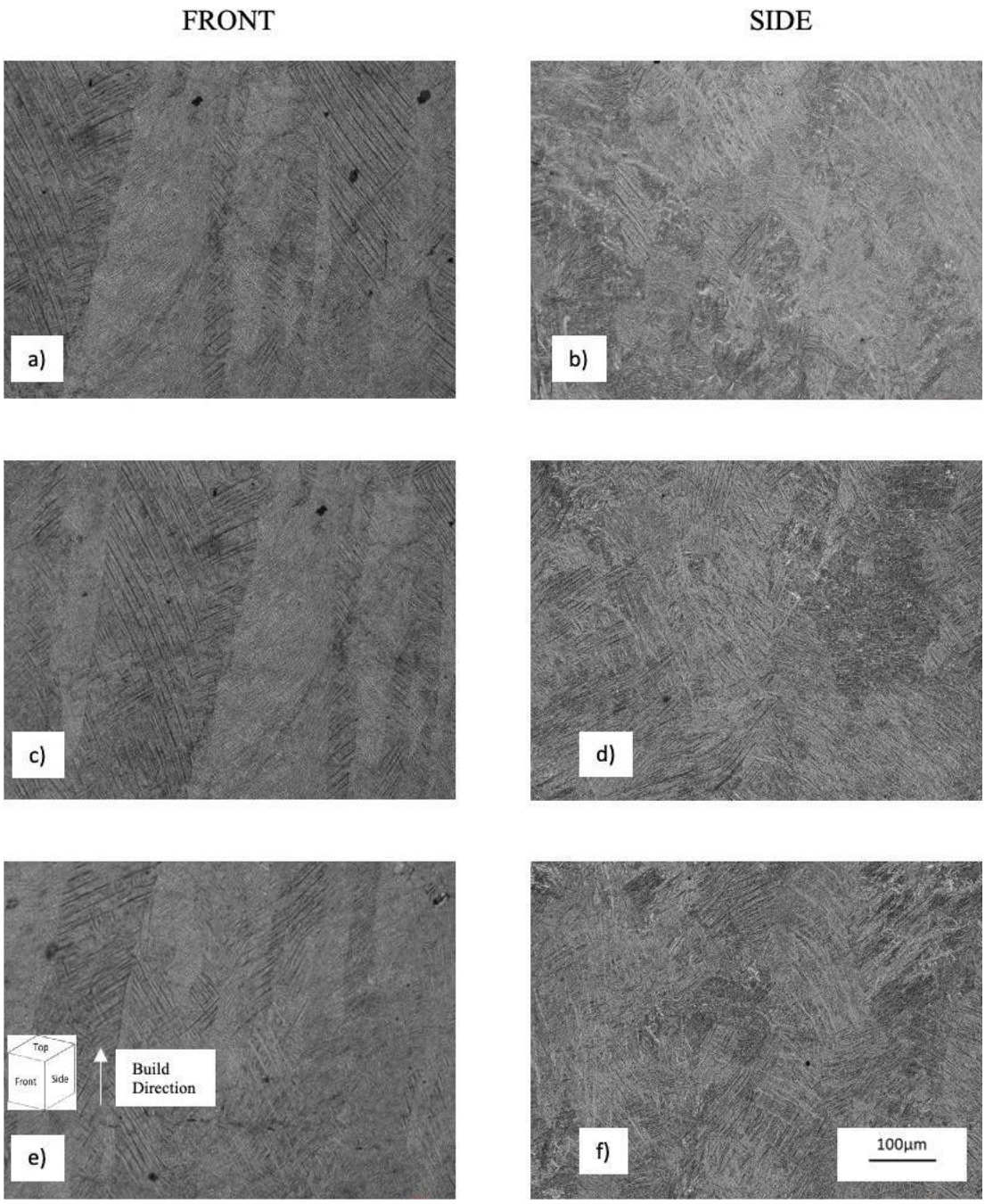

Figure 85: Light microscope images of the material built at the rest of the three scan speeds in the X-TA orientation, a) & b) 6.0 m/s, c) & d) 6.25 m/s and e) & f) 6.5 m/s. The images were taken at X10 objective lens magnification

4.5.1.4.2 Y-TA

The two views of the microstructures of the material built in the Y-TA orientation at 6.0 m/s, 6.25 m/s and 6.5 m/s respectively are illustrated in Figure 86. The images display the same microstructure observed with the X-TA material, the elongated grains in the front view and the acicular martensitic structure in the side view. No difference in microstructure of the Y-TA material is seen with increase in scan speed.

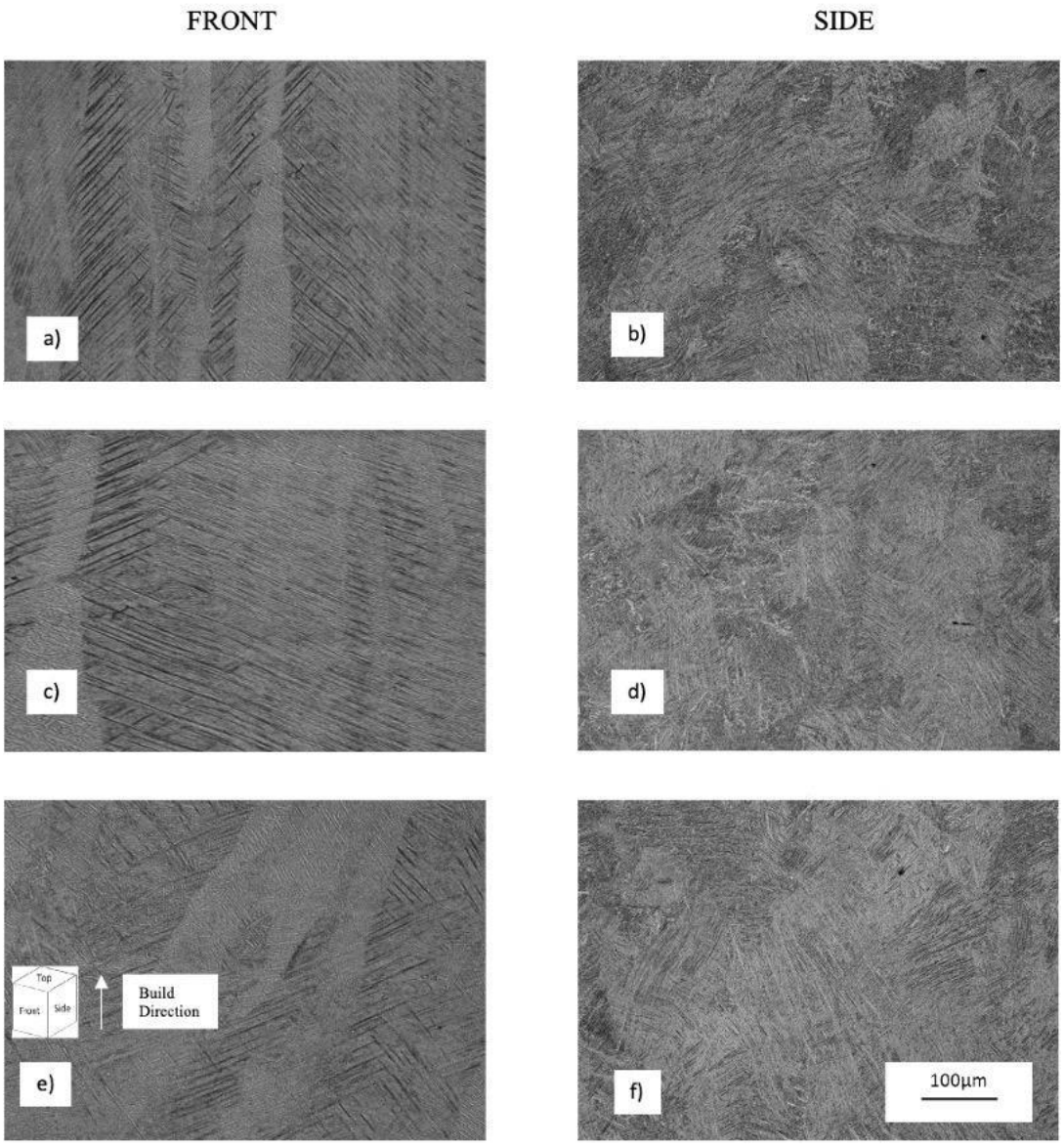

Figure 86: Light microscope images of the material built at the rest of the three scan speeds in the Y-TA orientation, a) & b) 6.0 m/s, c) & d) 6.25 m/s and e) & f) 6.5 m/s. The images were taken at X10 objective lens magnification

4.5.1.4.3 Z-TA

The two views of the microstructures of the material built in the Z-TA orientation at 6.0 m/s, 6.25 m/s and 6.5 m/s respectively are shown in Figure 4.33. The images display the same microstructure observed with the X-TA and Y-TA material. However, the elongated grains are seen in the side view and not in the front view as with the material built in the other two orientations. No difference in microstructure of the Z-TA material is observed with increase in scan speed.

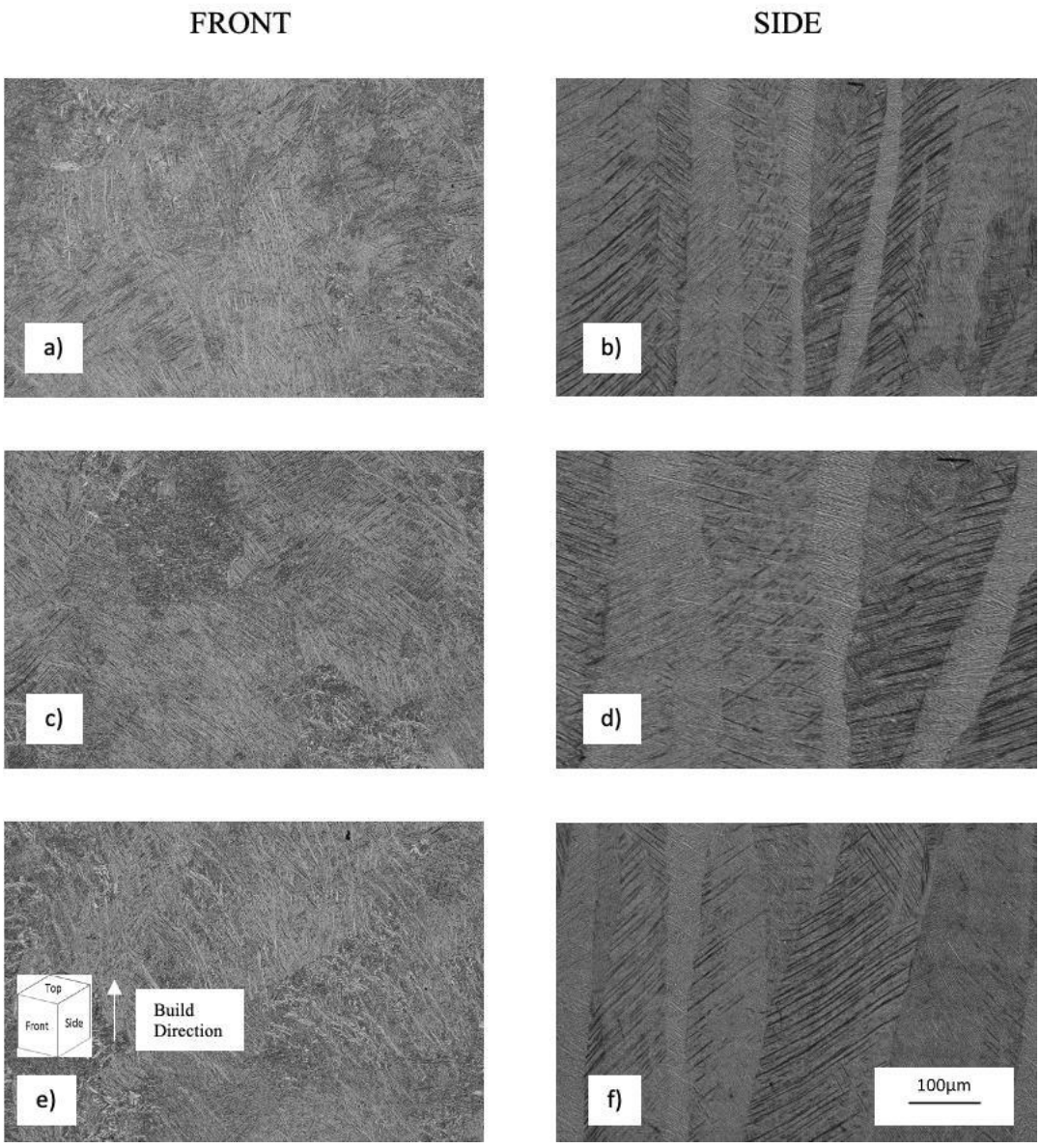

Figure 87: Light microscope images of the material built at the rest of the three scan speeds in the Z-TA orientation, a) & b) 6.0 m/s, c) & d) 6.25 m/s and e) & f) 6.5 m/s. The images were taken at X10 objective lens magnification

A similar microstructure is observed in the material built across the different scan speeds. The columnar grain size and lath size is comparable across all scan speeds.

4.5.2 Scanning electron microscopy

The morphology of pores and void defects of the material are explored using scanning electron microscopy (SEM). With the use of SEM imaging, microstructure analysis is performed at much higher magnifications coupled with better resolution.

SEM images of the pores observed in the specimens built across all scan speeds are shown in Figure 88. The pores are inevitably formed due to the SLM process. Some of the pores are spherical and some are irregularly shaped. The irregularly shaped pores are pores formed due to the keyhole effect in the molten pool which is a consequence of high scan speed. The same type of pores is observed in all the specimens built at the different scan speeds.

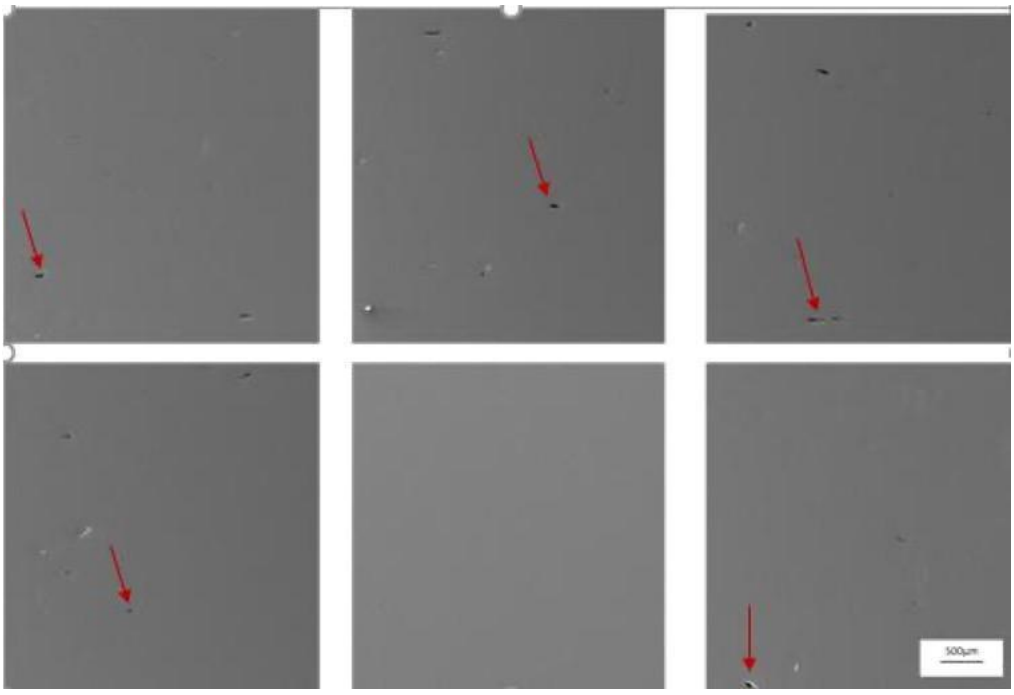

Figure 88: SEM image showing pores on the SLM Ti6Al4V specimens

Other defects observed within the microstructures of the SLM Ti6Al4V samples are shown in Figure 89. The type of pores observed are voids enclosing partially melted powder particles which are evident of improper melt pool formation. When the laser moves fast because of high scan speed, the molten zone cools rapidly which leads to improper pool formation. During the laser melting process, there is insufficient time for the molten metal to fill the space between the powder particles in the available short space of time. The voids have irregular inner surfaces and critical corner points, which have a high tendency to initiate microcracks.

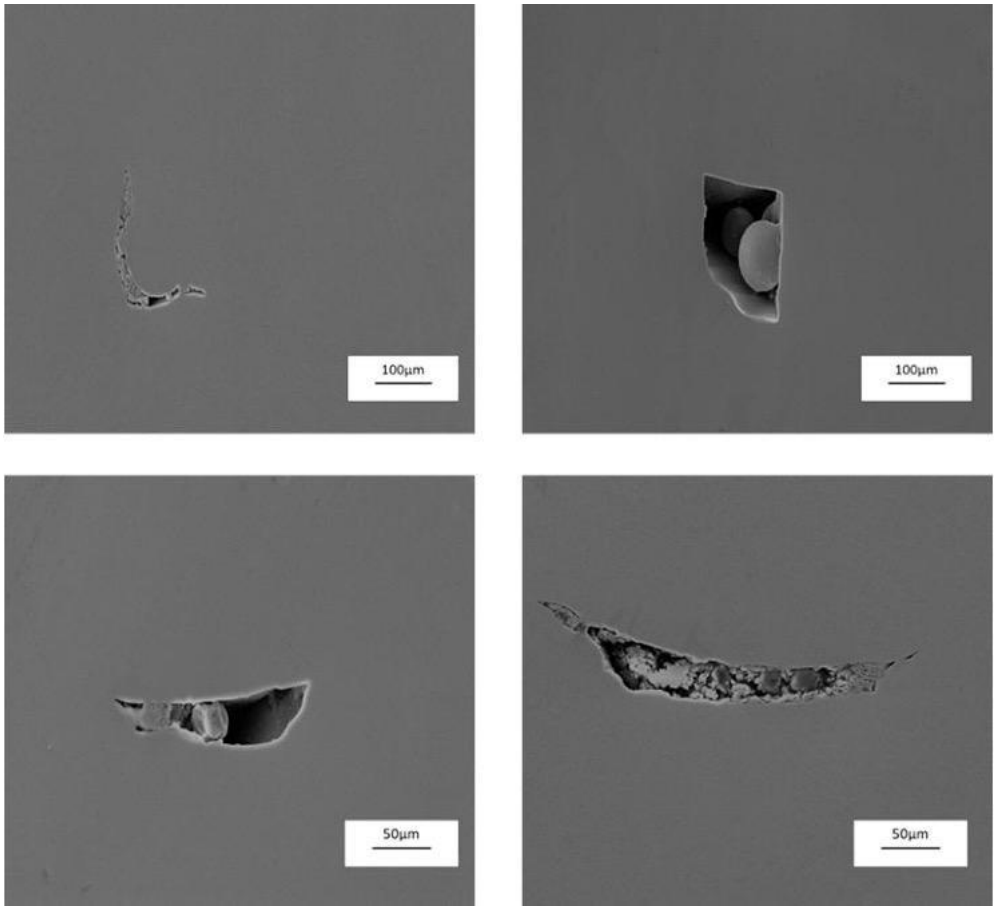

Figure 89: SEM images showing voids with improper pool formation

The defects shown can possibly compromise the integrity of the specimen's microstructure and affect the mechanical performance thereof. The defects are either a consequence thermal stresses or high scan speed.

The formation of the spherical pores and the irregularly shaped pores can be attributed to several other mechanisms including the balling effect whereby the irregular scan tracks are created as well as inter-ball porosity. To add on to that, the balling effect causes the surface of the newly added layer to be rough which impedes the homogenous distribution of fresh powder.

EBSD analysis was performed on two specimens from the extremes of the scan speed range which are the 5.75 m/s specimen and the 6.5 m/s specimen. EBSD was carried out for the reconstruction of the parent β-grains of the microstructure of the SLM Ti6Al4V material. The maps obtained are shown in Figure 90 and Figure 91for the 5.75 m/s and the 6.5 m/s specimens respectively. Both maps show a variation in grain size and shape across the material. Some grains are longer and thinner than others whilst some grains are more spherical than others. The microstructure shows columnar morphology parallel to build orientation. In overall, the reconstruction of the parent b-grains highlights the columnar morphology which represents the large prior b-grains.

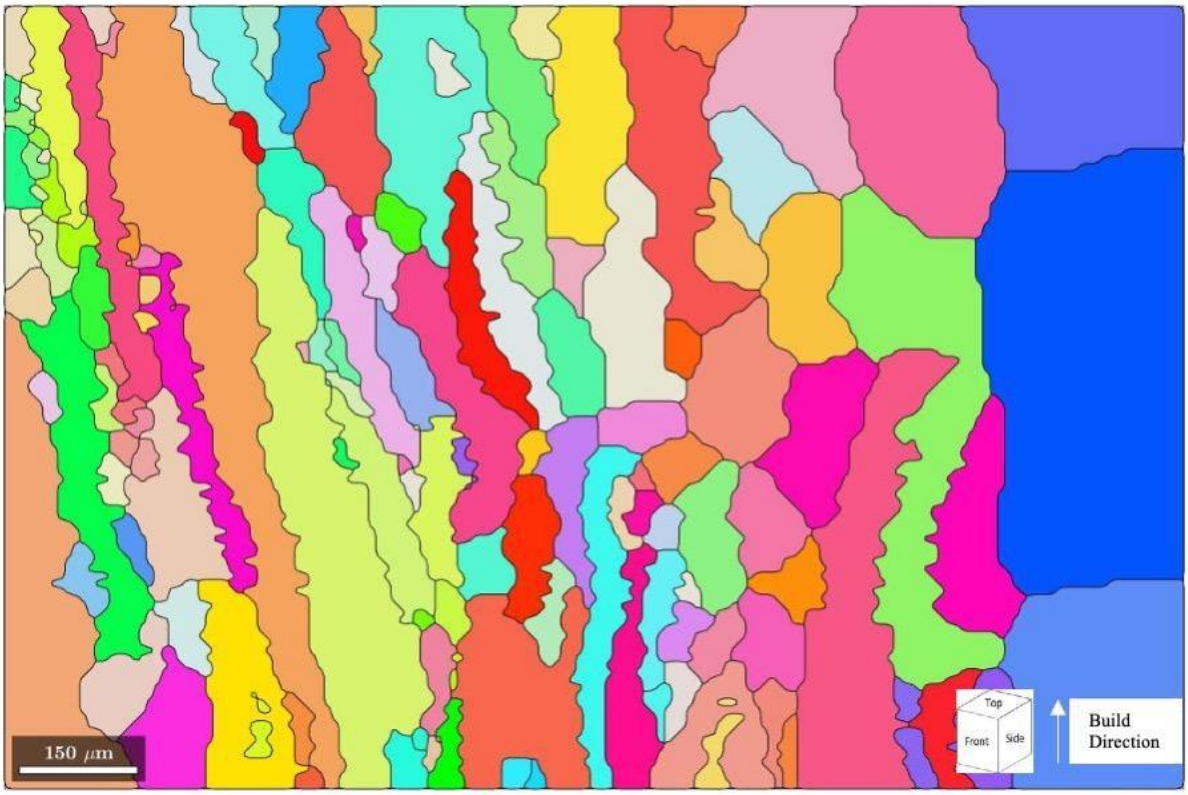

Figure 90: EBSD map showing the reconstructed β-grains for the specimen built at 5.75 m/s

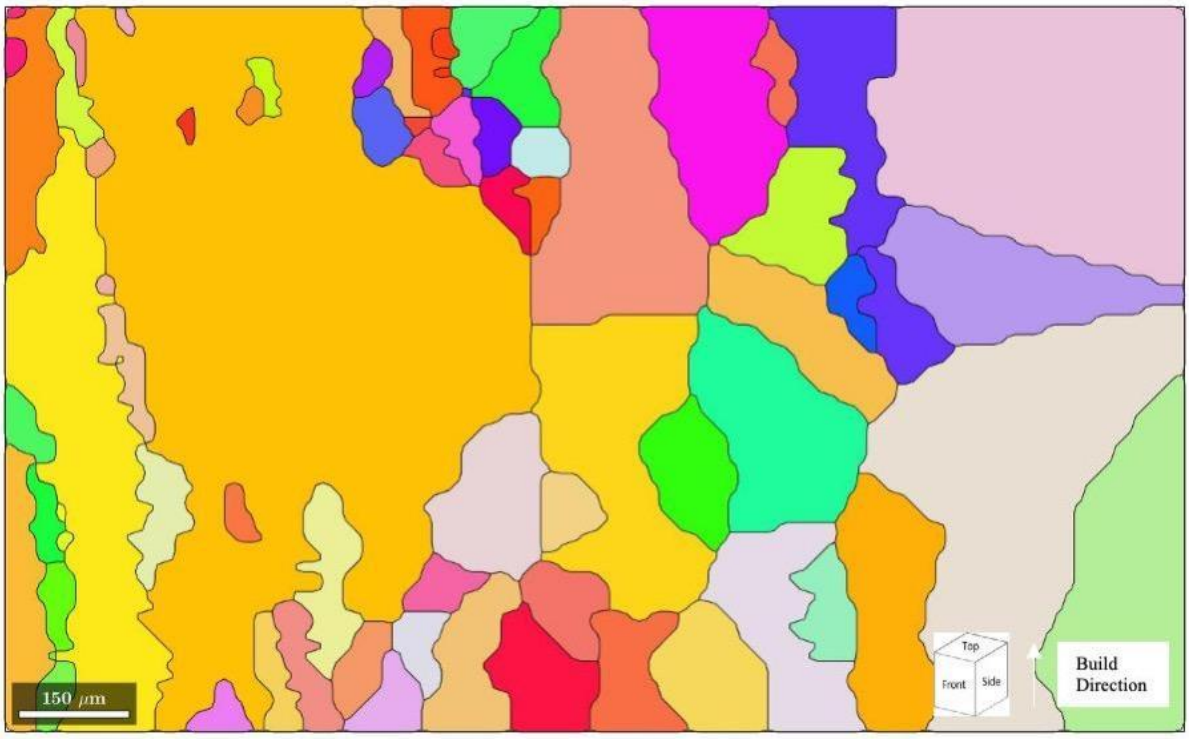

Figure 91: EBSD map showing the reconstructed β-grains for the specimen built at 6.5 m/s

4.6 Fractography

To study the crack propagation in more detail and to assess whether there is a correlation between porosity defects and fracture, the microstructure of the fracture surfaces of fracture toughness specimens for each scan speed were analysed by SEM. The general overview of the fracture surfaces of the specimens built in all scan speeds is displayed in Figure 92a) -d). The fatigue pre-crack region can be easily distinguished in all the specimens and three sections are highlighted as shown in Figure 92a). Region 1 is where the pre-crack begins, region 2 is the area of crack growth and region 3 is the area of final fracture which occurs during the actual fracture toughness test. The pre-cracks of the specimens built at all four speeds show desirable crack fronts as no uneven crack growth is observed. The specimens from all four scan speeds displayed similar fracture surfaces and pre-crack regions. The black spots on the specimens are marks left by the beam during scanning.

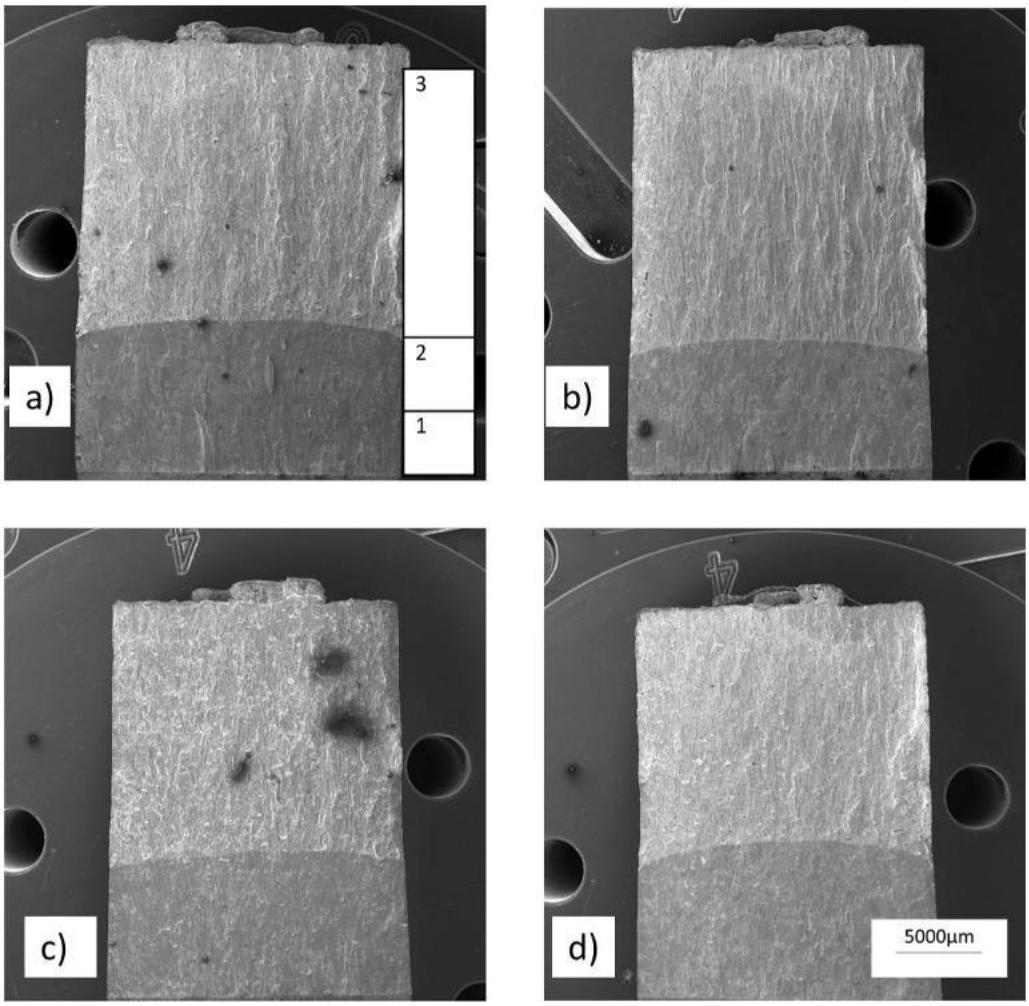

Figure 92: Fractography images of the FT specimens built at all scan speeds a) 5.75 m/s, b) 6.0 m/s, c) 6.25 m/s and 6.5 m/s

The crack growth and fast fracture regions at higher magnification are shown in Figure 93. The features seen in the crack growth surfaces of the specimens are small irregular facets shown by the black arrows and fine cracks shown by the orange arrows. It is considered that the irregular facets are micro-voids which arise because of the occurrence of pores in the microstructure. When the material is placed under mechanical stress, nucleation and growth of these micro-voids occurs resulting in the fine cracks which are microcracks. These features are typical of brittle crack growth propagation. The final fracture surfaces are characterized by dimpled appearances which are shown by the red arrows. The dimples vary in size, and they are randomly distributed. Dimples are typical of ductile trans-granular fracture, and they arise from microvoid coalescence.

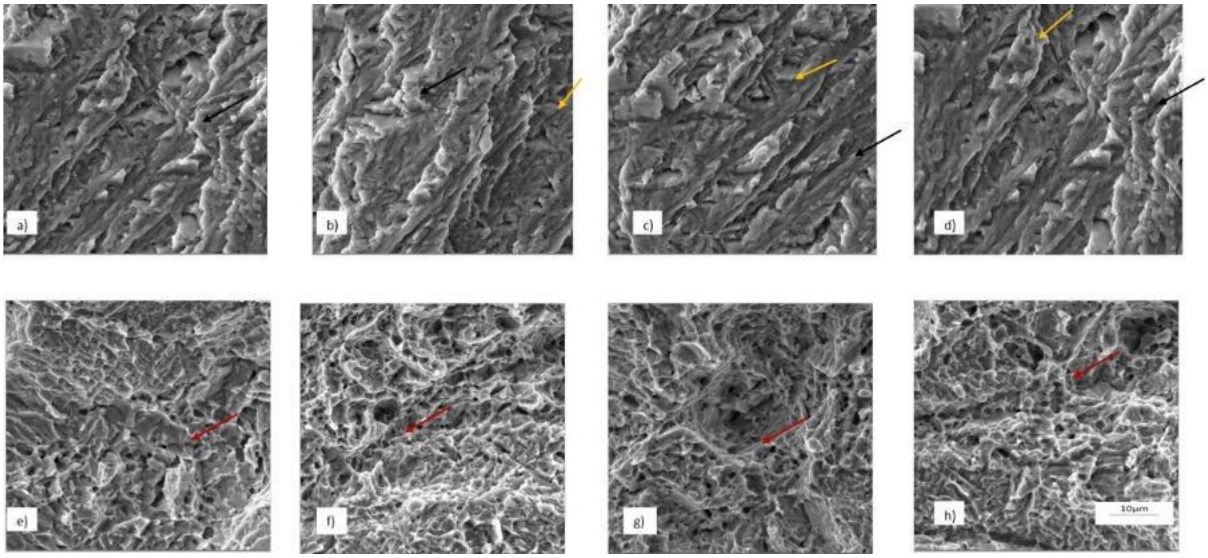

Figure 93: Crack growth and final fracture microscopy images of the fractured CT specimens for each scan speed. The SEM images in the first row a) to d) show the crack growth phases and the images in the second row e) to h) show the final failure phase. Direction of crack propagation is from bottom to top in each fractography image. a) & e) 5.75 m/s, b) & f) 6.0 m/s, c) & g) 6.25 m/s and d) & h) 6.5 m/s.

5 Discussion

The results obtained from all the mechanical testing and microstructure analysis will be discussed in this section. The results are analysed to assess the trend in behaviour of the material built at the different higher scan speeds. The scan speeds involved are 5.75, 6.0 6.25 and 6.5 m/s. The build orientations for the tensile specimens are X-TA (with the tensile length along the horizontal x-axis), Y-TA (with the tensile length along the y-axis) and the Z-TA (with the tensile length in the vertical direction). For the FCGR and FT specimens the build orientation is XZ (built horizontally along the x-axis with expected crack propagation along the z-axis). In this case the applied load direction in the x-direction.

5.1 Tensile behaviour

The tensile behaviour of the specimens built at the higher scan speeds was analysed based on the effect of scan speed and build orientation, respectively. Four scan speeds were examined to assess the effect of higher scan speeds on the tensile behaviour of the material and three build orientations were examined to assess the effect of build orientation on the tensile behaviour of the material. The results obtained are used to address the question of whether suitable tensile behaviour is still achieved in materials built at higher scan speeds.

5.1.1 Effect of scan speed

The tensile test results for the specimens fabricated at the higher scan speeds 5.75 m/s, 6.0 m/s, 6.25 m/s and 6.5 m/s generally show no significant differences in tensile properties with increase in scan speed. However, the 6.25 m/s specimens have lower elongation at break compared to the rest of the specimens. The results of the ductility of the specimens built at 6.25 m/s are therefore excluded from the general analysis of specimens built at higher scan speeds and will be discussed separately. A summary of the average yield strength, ultimate tensile strength, and elongation at break of the specimens built at the higher scan speeds in comparison with specimens built at conventional scan speeds from literature is shown in Table 33. The average percentage relative densities have been calculated from Table 32 and also inserted into this table. Energy density values have also been added.

Table 33: Summary of average tensile test results of specimens built at different scan speeds

Scan speed [m/s]	Yield strength [MPa]	UTS [MPa]	Elongation at break [%]	Average Percentage Relative density [%]	Energy density [J/mm^3]
5.75	920 ± 74	1091 ± 23	8±1.7	98.22	65.2
6.0	967 ± 39	1108 ± 48	8±1.4	97.99	62.5
6.25	917 ± 26	1065 ± 42	3.4±2.1	97.99	60
6.5	960 ± 70	1091 ± 23	7.6±1.3	98.67	57.7
SR (XZ)[46]	1132± 13	1156 ± 13	8±0.4	>99	Not provided
XZ (edge)[54]	958 ± 6	1057 ± 8	12.4 ± 0.7	>99	Not provided

From the table above, the average tensile properties of the specimens built at 5.75, 6.0, 6.25 and 6.5 m/s are comparable to the properties obtained from literature. It is also observed that there is no significant difference in the tensile behaviour of the specimens built at the higher scan speeds compared to that of specimens bult at conventional scan speeds. In a study by Shunmugavel et al[59] of SLM Ti6Al4V specimens built at a conventional scan speed (less than 1 m/s), the yield strength and ultimate tensile strength was reported to be 964 MPa and 1041 MPa respectively for the longitudinal specimens and 1058 MPa and 1114 MPa respectively for the transverse specimens. Simonelli et al[54] achieved UTS of 1117 MPa and an elongation of 8.9% with SLM Ti6Al4V specimens built at a scan speed of 0.225 m/s. The tensile properties of the specimens built at conventional scan speeds reported in these studies are similar to the tensile properties of the specimens built at the high scan speeds in this project except for the ductility of the 6.25 m/s specimens.

In a study by Cain et al however, the specimens built at a conventional scan speed are reported to have higher tensile strength compared to the specimens examined in this project. A density of > 99% for the specimens was reported. A high density ensures fewer pores in the material leading to an improved resistance against crack growth. A lower density is characterized by more pores and inferior material properties, which could explain the fast propagation in the samples built at high scan speeds as pores act as stress raisers. Higher scan speeds cause rapid cooling of the molten zone due to the laser focal spot moving faster, which leads to improper pool formation because the molten metal is unable to fill the space between the powder particles in the available time[12]. High scan speeds are also responsible for the pore formation by the keyhole effect in the molten pool and comparatively lower viscosity of the pool. The densities reported for the specimens built at the high scan speeds in this research project were ranging from 97% to 99.5% therefore they did not necessarily have lower relative density. The observed difference in tensile properties is not due to density.

Generally, specimens built at different scan speeds are built with different energy densities during the SLM process with the other processing parameters being held constant. It is therefore expected for specimens built at different scan speeds to yield different tensile properties. Pal et al[45] demonstrated that the specimens built with the lowest energy densities (39 J/mm^3) have the lowest tensile strength. When the energy density is increased to a certain degree (65 – 97 J/mm^3), the tensile properties increase. However, the specimens built with energy densities between 130 and 195 J/mm^3 have lower tensile strength and poor ductility. The same situation is observed in a study by Zhou et al[60]. An increase in ultimate tensile strength to a maximum is observed when the energy density is increased to 1000 J/mm^3. However, when the energy density is increased to 1333 J/mm^3, it results in lower tensile strength. This is because an energy density of 1333 J/mm^3 is deemed too high in this study. When this energy density is used, the molten pool temperature becomes higher which results in coarser α lamellae in the Widmanstatten structure[60] which results in the lower tensile strength[60]. Reference for the energy density values used to fabricate the specimens for this project can be seen in Table 33.

In this project, the effect of energy density on the tensile behaviour of the specimens built at the different scan speeds is not observed. This is because the different speeds used are considerably close to each other. Therefore, there is no significant variation in the energy density values of these specimens as shown in Table 33 above. This could explain why the specimens built at the different scan speeds still have similar tensile properties. A change in tensile behaviour is observed with a significant change in energy density.

5.1.2 Effect of build orientation

As mentioned earlier, three build orientations were examined for the tensile specimens. The results obtained show that tensile properties do not vary with build orientation. A summary of the results is shown in Table 34.

Table 34: Summary of the average tensile results of specimens built in different orientations

Build orientation	**Yield strength [MPa]**	**UTS [MPa]**	**Elongation at break [%]**	**Average Percentage Relative density [%]**
X-TA	947 ± 44	1097 ± 40	7±3.1	98.44
Y-TA	991 ± 51	1097 ± 31	7± 2.7	98.44
Z-TA	892 ± 28	1074± 40	6 ± 2	97.76

The tensile properties of the samples built in the X-TA, Y-TA and the Z-TA specimens are all in the same range. The variation in tensile properties with build orientation is observed in several studies although some studies are conflicting as described in section 2.6. In this research, no significant effect of build orientation on tensile properties is observed.

Cain et al also investigated the effect of build orientation on the tensile properties of the conventional scan speed-built specimens. In the work of Cain et al, the SR (XY) and SR (XZ) specimens were of interest for comparison. The XY specimens are built in the same orientation as the Y-TA specimens in this project and the XZ specimens are built in the same orientation as the Z-TA specimens tested in this project. In the study by Cain et al, no significant difference in yield strength, UTS and ductility was observed between the XY and XZ specimen orientations as observed in this research project. Looking at the average tensile results shown in Table 33, the same conclusions can be made for this project.

Porosity size, quantity and shape also influence tensile properties as pores act as stress raisers. With fewer pores, there is better resistance to crack initiation and propagation. Low density identifies with many pores which act as stress raisers thus facilitating fast crack propagation. Interlayer porosity is inevitable in SLM processed material. Materials built in different orientations may have a different number of layers. In the case of the X-TA and Y-TA specimens they are bound to have the same number of layers as they are both horizontally built. The Z-TA specimens, however, consist of the highest number of layers as they are vertically built[54]. Pores and defects usually emerge between layers which consequently results in Z-TA specimens having a larger number of pores along the tensile axis due to them having a larger number of layers. As these interlayer defects are perpendicular to the tensile axis, they are consequently pulled apart by the force in tension during the tensile testing[61]. As observed in this project however, the Z-TA specimens have similar relative density to that of the X-TA and Y-TA specimens which means there is no significant difference in porosity in these samples.

In a study by Pal et al[45], specimens built at energy densities ranging from 49 J/mm^3 to 97 J/mm^3 had almost spherically shaped pores whilst those built at energy densities of 39 J/mm^3, 130 J/mm^3 195 J/mm^3 and 260 J/mm^3 had pores with corner points. The pores having corner points can initiate microcracks which could play a vital role in strength variations and thus, the strength of the specimens can be decreased. Although no change in tensile properties is observed with the change in energy density and no difference in relative density observed in all specimens built at the high scan speeds in this project, it is important to investigate how the effect of interlayer porosity in Z-TA specimens was negated.

5.2 Fatigue crack growth rate behaviour

The FCGR results of the specimens built at the different higher scan speeds are used to address the question of whether suitable FCGR behaviour is still achieved in materials built at higher scan speeds and whether there is a difference in FCGR behaviour with change in higher scan speeds. As described in section 3.4, a practical mechanism for determining FCGR is investigating the dependence of crack growth on the cyclic stress intensity which would have resulted from crack opening displacement. This mechanism is based on the assumptions that strain is distributed evenly and that there is small scale yielding in the plastically deformed region at the advancing crack tips.

5.2.1 Comparison with specimens built at conventional scan speeds

Work done on FCGR behaviour of SLM Ti6Al4V specimens built at conventional scan speeds was studied and compared to the work done in this project to investigate any change in FCGR behaviour due to scan speed.

From the work of Cain et al, the FCGR specimen built in the XZ orientation (same orientation as in this project) and stress relieved is of interest in this section. The specimens built at 6.25 m/s and 6.5 m/s display a more similar crack growth behaviour to the XZ specimen in the work performed by Cain et al. The *m* values of the 6.25 and 6.5 m/s specimens are lower than that of the XZ specimen built at a conventional scan speed but the values are generally much closer to each other. The *C* values are the same. The 5.75 and 6.0 m/s specimens have lower crack growth rate compared to the XZ specimen built at a conventional scan speed. The *m* values of these specimens are much higher than that of the specimen in the work by Cain et al whilst the *C* values are lower. The same pattern is observed in the work performed by Xu et al[62] with the specimens labelled as 0° which are similar to the XZ specimens investigated in this project. A summary of the FCGR results from this project is shown in Table 35. The Paris equations for the specimens from the literature mentioned are also shown.

Table 35: Summary of the Paris equations from literature and from each scan speed in this project

Scan Speed [m/s]	Sample	Paris Equations
	SR-XZ[46]	$\frac{da}{dN} = (1.16\ x\ 10^{-11})\Delta K^{3.24}$
	0°[62]	$\frac{da}{dN} = (6.5\ x\ 10^{-10})\Delta K^{3.8}$
5.75	1	$\frac{da}{dN} = (7.0\ x\ 10^{-14} \pm 2.33\ x\ 10^{-13})\Delta K^{5.61 \pm 0.64}$
	2	$\frac{da}{dN} = (4.0\ x\ 10^{-13} \pm 2.33\ x\ 10^{-13})\Delta K^{4.71 \pm 0.64}$
6.0	1	$\frac{da}{dN} = (9.0\ x\ 10^{-13} \pm 5.03\ x\ 10^{-13})\Delta K^{4.64 \pm 0.81}$
	2	$\frac{da}{dN} = (1.0\ x\ 10^{-14} \pm 5.03\ x\ 10^{-13})\Delta K^{6.19 \pm 0.81}$
	3	$\frac{da}{dN} = (5.0\ x\ 10^{-14} \pm 5.03\ x\ 10^{-13})\Delta K^{5.81 \pm 0.81}$
6.25	1	$\frac{da}{dN} = (9.0\ x\ 10^{-11} \pm 5.80\ x\ 10^{-11})\Delta K^{2.19 \pm 0.94}$
	2	$\frac{da}{dN} = (8.0\ x\ 10^{-12} \pm 5.80\ x\ 10^{-11})\Delta K^{3.52 \pm 0.94}$

6.5	1	$\frac{da}{dN} = (3.0\ x\ 10^{-11} \pm\ 3.79\ x\ 10^{-11})\Delta K^{2.94 \pm 0.30}$
	2	$\frac{da}{dN} = (9.0\ x\ 10^{-11} \pm\ 3.79\ x\ 10^{-11})\Delta K^{2.43 \pm 0.30}$
	3	$\frac{da}{dN} = (2.0\ x\ 10^{-11} \pm\ 3.79\ x\ 10^{-11})\Delta K^{2.97 \pm 0.30}$

The Paris regime of the specimen built at a conventional scan speed from the work by Cain et al is shown in Figure 94. The stress relieved XZ specimen is represented by the blue Paris curve.

For each of the higher scan speeds investigated in this project, the specimen with *C* and *m* values more similar to the calculated average *C* and *m* of the respective scan speed was selected in order to visualize the Paris regions per scan speed and to note how they compare. The Paris regimes for these specimens can be seen in Figure 95.

The Paris curves shown in Figure 95 display the shape of crack growth expected of Paris curves shown in Figure 25 in section 2.5.1.2. Stage I however, which is the crack initiation stage, is not clearly shown. This is the area of the threshold stress intensity factor which is not determined in this project. Stage II of crack propagation is represented by the linear region of the Paris curves. The start of Stage III, which is when fast fracture occurs, cannot be clearly seen due to the crack growth rate of the material increasing rapidly.

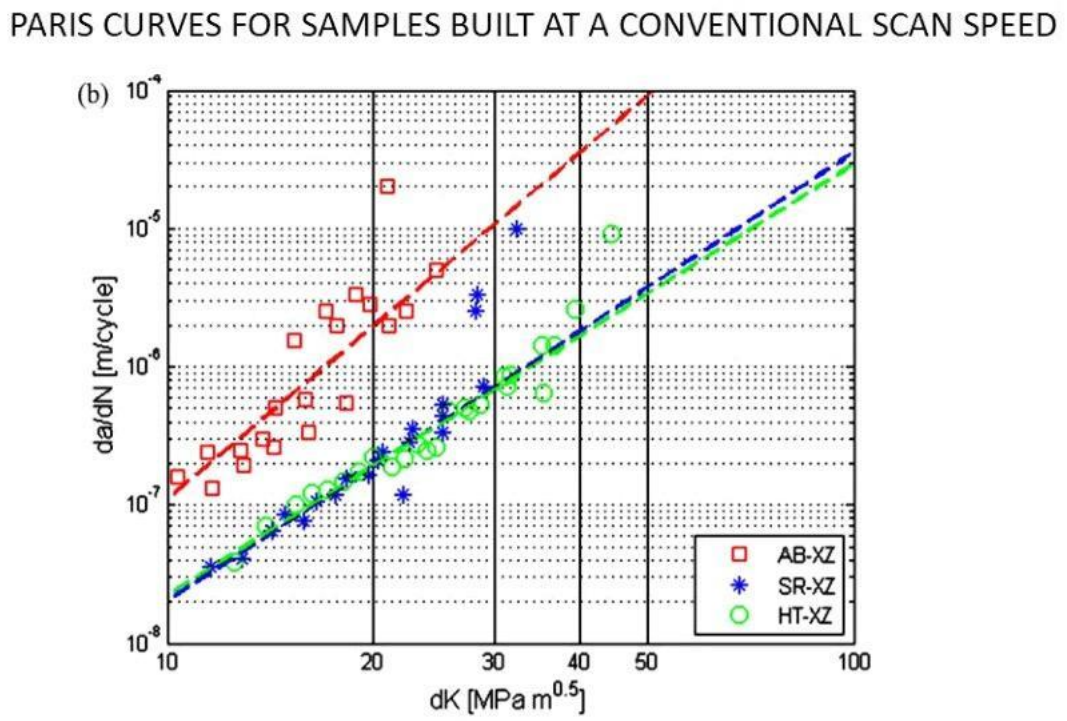

Figure 94: Crack growth da/dN versus stress intensity range dK for SLM samples built in the XZ specimen orientation at a conventional scan speed. The focus is on the SR-XZ specimen for comparison purposes

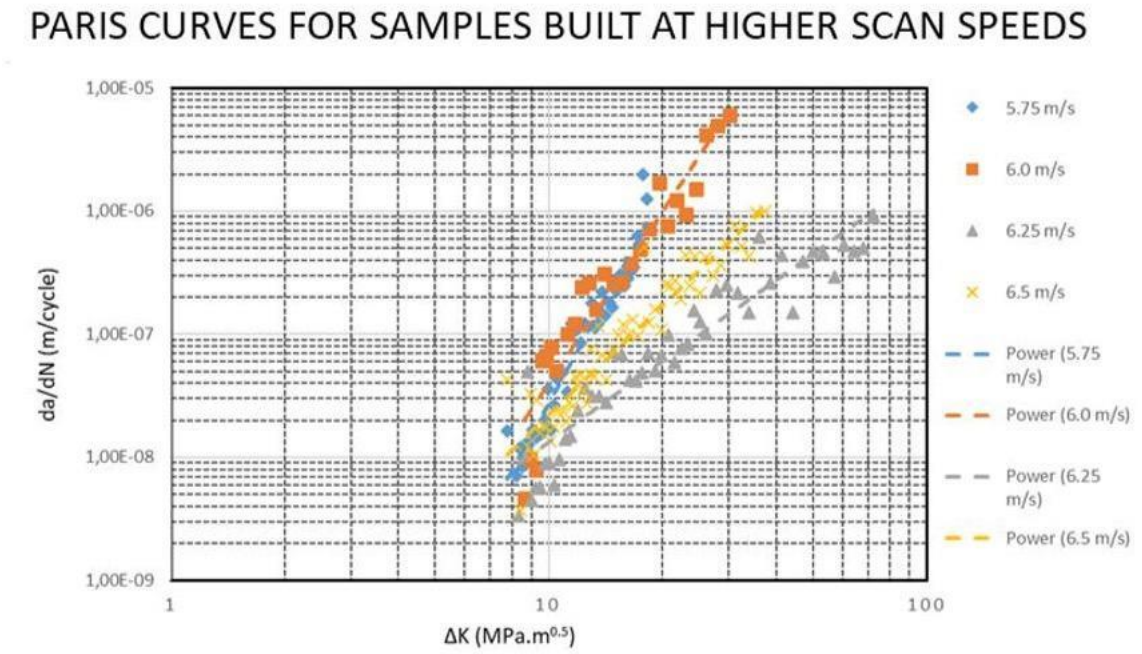

Figure 95: Paris curves for specimens built at high scan speeds

A density of > 99% for the specimens in the literature mentioned was reported. The densities reported for the specimens built at the higher scan speeds were lower, ranging from 97% to

99%. However, the 6.25 and 6.5 m/s specimens have similar crack growth behaviour to the specimens built at the conventional scan speeds with higher density. The 5.75 and 6.0 m/s specimens have higher crack growth rates, but it is not clear whether this is due to the lower density since the 6.25 and 6.5 m/s specimens do not show high crack growth rate behaviour although they also have lower density compared to the specimens built at the conventional scan speed. As observed in the tensile results, there is no clear effect of high scan speed on the tensile behaviour of the specimens as they were fabricated in the same range of energy density values. The same phenomenon is expected for the crack growth behaviour of the specimens, but it is only observed with only one set of scan speeds (6.25 and 6.5 m/s). Therefore, it can be said that there is no observed effect of high scan speed on the crack growth behaviour of the specimens but there is need to investigate the higher crack growth rates exhibited by the 5.75 and 6.0 m/s specimens.

5.2.2 Comparison between 5.75 m/s, 6.0 m/s, 6.25 m/s and 6.5 m/s

Looking at the FCGR Paris equations, the 5.75 m/s and 6.0 m/s specimens have similar Paris equations. Moving on to the 6.25 m/s and 6.5 m/s specimens, the *C* value becomes bigger, and the *m* value becomes smaller. The 6.25 m/s and 6.5 m/s specimens have similar Paris equations. The consequence of having a higher *m* value is a steeper region II of the Paris curve. The *C* and *m* values of the Paris equation define FCGR behaviour and can be used to describe any differences amongst the scan speeds.

It is therefore observed that there is no difference in FCGR behaviour with respect to scan speed between the 5.75 m/s and 6.0 m/s specimens and no difference between the 6.25 m/s and 6.5 m/s specimens, but a difference is observed between the two sets of speeds. All specimens however, displayed reasonable resistance to crack growth.

In this discussion of FCGR results, the 5.75 m/s and 6.0 m/s specimens will be referred to as belonging to one set and the 6.25 m/s and 6.5 m/s specimens will be referred to as belonging to another set. Comparing the Paris regions of the two sets of scan speeds, it can be observed that there is more scatter in the data of the 6.25 m/s specimens. Region II of the 5.75 m/s and 6.0 m/s specimens respectively is much more linear than that of the 6.25 m/s and 6.5 m/s specimens. The 5.75 m/s and 6.0 m/s specimens have much steeper Paris curves which is consistent with the higher m values. The steeper the Paris curve, the higher the fatigue crack growth rate.

An increase in scan speed from 5.75 m/s to 6.0 m/s does not result in a change in FCGR but when the scan speed is further increased to 6.25 m/s, a difference in FCGR is observed. Then again, when the scan speed is further increased to 6.5 m/s, no difference in FCGR is observed. However, there are no microstructural differences that can explain this behaviour as all specimens have similar microstructure.

As discussed in section 2.5.1.2, the *m* parameter mainly reflects the dependency of crack closure behaviour on ΔK. It is possible to assume that the difference in *m* values which translates to a difference in FCGR behaviour of the two sets of scan speeds is due to the possibility of a difference in the damage in the plastic zone. However, a finding by Ohta and Sasaki[41] suggests that crack closure depends on ΔK and that as ΔK approaches the threshold level, the crack tip becomes closer and thus the value of ΔK_{eff} decreases. With smaller m values, the crack opening level remains constant with an increase in ΔK whereas with higher m values, it increases linearly with an increase in ΔK. Therefore, this suggests that the cyclic straining at the crack tip primarily affects the crack closure behaviour rather than the damage accumulation process in the plastic zone as it varies with ΔK[42].

Both *C* and *m* parameters determine the crack growth rate according to the Paris equation. The smaller the two parameters, the lower the crack growth rate. In this project however, only the effect of *m* is clearly observed. The 5.75 and 6.0 m/s specimens have higher m values compared to the 6.25 and 6.5 m/s. However, they have much smaller *C* values. As much as the 5.75 and 6.0 m/s specimens have smaller C values, they still exhibit higher crack growth rates. This means that any change in the *m* parameter is more critical to FCGR behaviour than that of the *C* parameter.

The Paris equations suggest that the 5.75 m/s and 6.0 m/s specimens behave in the same manner and the 6.25 m/s, and 6.5 m/s specimens behave in the same manner. However, this trend is not observed in the number of cycles to failure. During the testing of the specimens built at the same scan speed, a variation in the number of cycles to failure is observed. This irregularity is observed across all scan speeds even with specimens fabricated under the same build parameters. Although specimens tend to behave differently at times, it is not expected for specimens built under the same conditions to not have a consistent number of cycles to failure as they are assumed to be uniform. The results suggest that the specimens are not uniform. This is displayed in Table 36.

Table 36: Number of cycles to failure for all specimens

Scan speed	Specimen	Number of cycles to failure ($\Delta P = 1.17$ kN)	Range of cycles
5.75	**1**	270 000	100 000
	2	170 000	
6.0	**1**	250 000	120 000
	2	370 000	
	3	370 000	
6.25	**1**	590 000	240 000
	2	350 000	
6.5	**1**	325 000	300 000
	2	150 000	
	3	450 000	

Looking at the results one scan speed at a time, specimens built at the same scan speed fail after a different number of cycles. For example, specimens 1 and 2 built at 5.75 m/s fail after 270 000 and 170 000 cycles respectively and specimens 1 and 2 built at 6.25 m/s fail after 590 000 and 350 000 cycles, respectively. The calculated cycle range values show that the difference in number of cycles to failure is quite significant, with the 6.5 m/s specimens having the highest scatter. The high levels of scatter suggest a lack of homogeneity in the microstructure of the specimens. The microstructures obtained from light microscopy do not display lack of homogeneity. However, the EBSD maps of reconstructed parent β-grains show a variation in grain size and shape within the same specimens (Figure 90 and Figure 91).

Generally, lack of homogeneity can be attributed to residual stresses, but this effect is not expected as all specimens are stress relieved.

A summary of the average number of cycles to failure vs scan speed is shown in Table 37. The 6.25 m/s specimens fracture after the highest number of cycles and the 5.75 m/s specimens fracture after the least number of cycles.

Table 37: Summary of cycles to failure for all scan speeds

Scan speed	**Average number of cycles to failure**
5.75	220 000
6.0	330 000
6.25	470 000
6.5	308 000

The fatigue crack paths of the specimens built at all scan speeds were examined to note crack growth stability during testing. A high degree of deviation in crack path from the direction perpendicular to the load direction is a reflection of unsteady crack growth behaviour. This is common in material with non-homogenous microstructure. Images of the crack paths observed after the FCGR testing are shown in Figure 96 and Figure 97. An image showing a steadier crack path along the horizontal is shown in Figure 97.

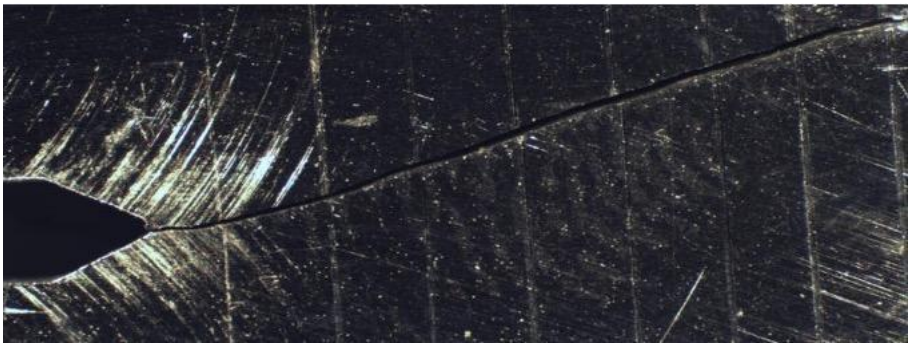

Figure 96: Fatigue crack path deviating from the horizontal

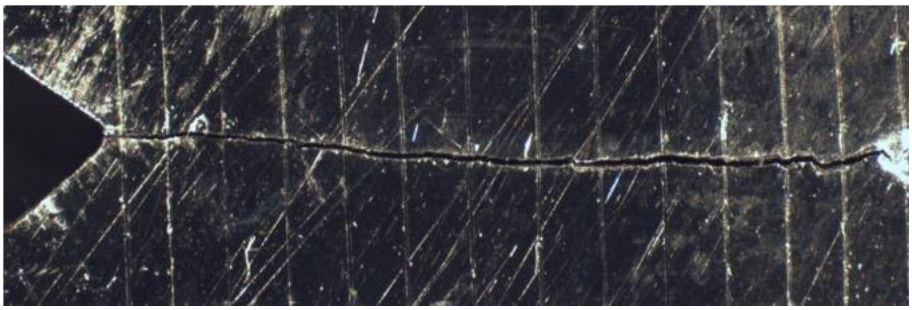

Figure 97: Fatigue crack path steady along the horizontal

Crack growth was stable and relatively steady in all the specimens tested. However, some deviations in the crack path were observed in some specimens. Out of all three specimens tested for each scan speed, the crack path is not quite parallel to the crack plane in at least one specimen. The crack path deviates from the horizontal and propagates at a slope. In the beginning, the crack struggles to maintain a steady path in the direction perpendicular to the load direction then stabilizes and becomes almost perpendicular to the load direction. A high degree of crack deviation causes the energy within the material to be shared between two cracks instead of one, which results in an invalid reduced crack growth rate result. In this case, the results of these specimens are still valid according to the ASTM E647 standard as the angle of deviation is less than 45°.

5.3 Fracture toughness behaviour

The effect of high laser scan speeds on the ability of the material to resist fast crack propagation under an applied stress resulting in fracture was investigated to address the question of whether suitable fracture toughness behaviour is still achieved in materials built at higher scan speeds and whether there is a difference in fracture toughness with change in the higher scan speeds.

5.3.1 Comparison with specimens built at conventional scan speeds

The fracture toughness results for the SLM Ti6A4V built at high scan speeds are acceptable as they compare to the fracture toughness values obtained from literature. The results have demonstrated that there is no effect of higher scan speed on the fracture toughness of the SLM Ti6Al4V specimens. There is no difference in fracture toughness between specimens built at conventional scan speeds and specimens built at higher scan speeds. The results of the specimens built at the higher scan speeds were compared to the fracture toughness of specimens built at conventional scan speeds from literature. Table 38 summarizes the average fracture toughness results for each scan speed and values from work performed by Cain et al[46] and work performed by Van Hooreweder[47] respectively. The stress relieved XZ specimen from work done by Cain et al is of interest as it is built in the same orientation as the XZ specimens investigated in this project.

Table 38: Fracture toughness comparison

Ti6Al4V condition	**Fracture toughness [MPa.m$^{0.5}$]**
SLM Ti6Al4V[47]	52.4 ± 3.48
SLM Ti6Al4V[46]	30±1
SLM Ti6Al4V – 5.75 m/s	50.26 ± 1.7
SLM Ti6Al4V - 6.0 m/s	46.96 ± 0.5
SLM Ti6Al4V - 6.25 m/s	51.24 ± 1.9
SLM Ti6Al4V - 6.5 m/s	51.52 ± 1.2

Comparing the results from a study by Cain et al[46], the fracture toughness of the materials is much lower than the fracture toughness of both the materials studied in this research and those in Van Hooreweder's[47] work. It is not clear why there is a difference in fracture toughness with Cain's[46] work but no difference with Van Hooreweder's[47] work since specimens in both studies were built at lower scan speeds. However, the difference could be due to the specimens in Cain's[46] work being built at a low scan speed that is not within the same range as the specimens studied in this research unlike Van Hooreweder's[47] specimens. In Cain's[46] work, the specimens were built at a scan speed less than 1 m/s whilst those in Van Hooreweder's[47] work were built at 1.6 m/s. It can therefore be said that the effect of scan speed on fracture toughness of specimens can only be observed when a comparison between specimens built at scan speeds in different ranges is made. No difference in fracture toughness is noticed between materials built at scan speeds within the same range.

5.3.2 Differences between the high scan speeds

From the results, no difference in fracture toughness of the materials is observed with increase in scan speed. The three specimens tested for each scan speed and the results obtained were similar and showed good repeatability. The average KQ values of the specimens built at all four scan speeds, which are equivalent to the KIC values, were within the same range. The fracture toughness values are displayed in Table 38.

As mentioned earlier, there is not much of a difference in energy density applied during the SLM process to the specimens built at the different scan speeds. Energy density influences the SLM melting process, solidification and fusion as different energy densities result in different cooling rates and number of cycles of reheating and cooling of the successively added layers. Therefore, different energy densities result in a variance in porosity and microstructure thus affecting the materials properties.

During the melting process, some powders may be improperly melted, and the molten pool may also contain metallic vapour and gaseous bubbles. All these contaminants cause improper pool formation resulting in the formation of pores and defects depending on the energy density applied[45]. Low energy density typically results in improper melting of a few powder particles which can possibly obstruct the flow of molten powders resulting in void spaces[45]. On the other hand, specimens built with the highest possible energy density do not necessarily exhibit

the best properties. In a study by Pal et al[45], the specimens built with the lowest energy density (39 J/mm^3) had the least favourable properties and an improvement in these properties was observed when the energy density was slightly improved to 49 J/mm^3 and to the range of 65 J/mm^3 to 97 J/mm^3. However, further increase in energy density to the range of 130 J/mm^3 to 195 J/mm^3 did not result in further increase in the materials performance. The specimens fabricated with the highest energy density had poor strength and ductility. The specimens built at the high scan speeds had energy densities within the range of 57.7 – 65.2 J/mm^3 as shown in Table 33. The magnitude of increase in scan speed for the specimens investigated in this project is 4%. In Pal's work, the variation in scan speed was by 33%, 25% and 50%. Consequently, the difference in energy densities of these specimens is higher (ranging from 39 – 256 J/mm^3) and more significant thus resulting in a difference in performance of the specimens. Given that the specimens built at the higher scan speeds have energy densities within the same range, it explains why no significant difference in fracture toughness due to difference in energy density is observed.

5.4 Microstructure analysis

According to Lutjering[32], the most important microstructural feature in SLM materials is the α-colony size. With an increase in temperature gradient, the α-colony size becomes smaller resulting in a microstructure that upgrades yield stress but lowers fracture toughness and crack propagation. Higher temperature gradients are expected with an increase in scan speed and the material built at the higher scan speed is expected to have a microstructure with a smaller α-colony size[45]. Be that as it may, no difference in microstructure and α-colony size was observed between the specimens built at higher scan speeds (6.5 m/s, 6.25 m/s, 6.0 m/s) and the specimens built at 5.75 m/s due to the difference between the scan speeds not being sufficient for a difference to be observed. The microstructures of the high scan speed specimens are shown in section 4.5.1.4.

Another microstructural parameter that affects mechanical performance is density. High density ensures fewer pores. With fewer pores, there is better resistance to crack propagation and greater fracture toughness. Low density identifies with many pores which act as stress raisers thus facilitating fast crack propagation and impede accurate determination of the material's mechanical behaviour as they highly influence failure mechanisms[63]. Material built at high scan speed is expected to have lower relative density due to the consequence of improper pool formation because of the fast movement of the laser which causes more rapid cooling of the molten material[45]. In this project, voids enclosing partially melted powder particles are observed in the material built at the high scan speeds(Figure 89). These voids are a consequence of improper pool formation. Irregularly shaped pores were also observed in the material built at the high scan speeds (Figure 88). These pores are formed due to the keyhole effect in the molten pool which is also a consequence of high scan speed. As such, the material built at the high scan speeds have lower density in comparison to material built at conventional scan speeds such as those in the work performed by Cain et al reported to have >99% density. However, no difference in density was observed amongst the specimens built at the high scan speeds as the scan speed was increased.

All specimens exhibited the acicular α martensitic microstructure typical of SLM Ti6Al4V parts regardless of scan speed and build orientation. The different characterization of microstructure in the different planes, perpendicular and parallel to the build direction respectively, shows anisotropic characteristics due to the layer-by-layer mechanism of the SLM process. The anisotropy explains why build orientation influences mechanical behaviour of SLM Ti6Al4V built specimens, which is described in section 5.1.2 with regards to the difference in tensile behaviour of the Z-TA specimens to the X-TA and Y-TA specimens.

EBSD analysis shows a variation in the size and morphology of the reconstructed parent β-grains in the 5.75 m/s and 6.5 m/s specimens. In both specimens, longer thinner grains and more spherical wider grains are observed. The images of the reconstructed parent b-grains can be seen in Figure 90 and Figure 91 With increase in scan speed, the width of the columnar grains is expected to decrease as the energy density input is decreased[64]. However, this is not strictly observed in the material analysed due to the variation in size and morphology that is observed. This finding explains why no differences in microstructure, tensile strength and fracture toughness are observed with scan speed amongst the specimens built within the 5.75 m/s – 6.5 m/s range in this research. It further reveals that the difference between the scan speeds within this range is not sufficient to analyse the effect of scan speed thereof. The work done to investigate the effect of scan speed in literature involved a wider range of scan speed with an increase in scan speed greater than 20%. The percentage increase in scan speed in this research work is only 4.35%. The prior β-grain boundaries are thought to be preferential paths for fracture. The fact that the specimens built at the different scan speeds have the same β-grain morphology proves why there is no difference in fracture toughness and fatigue crack growth rate observed amongst the specimens.

6 Conclusions

The results indicate that when SLM Ti6Al4V specimens are fabricated at the specified higher scan speeds there is no significant change in the microstructure and mechanical performance in comparison with specimens built at conventional scan speeds (1 m/s and below). Acceptable tensile strength, fracture toughness and crack growth rate properties are still achieved in the material built at higher scan speed. Comparing the properties of the materials built at the different high scan speeds, no significant difference in mechanical performance is observed. The results also indicate that build orientation in SLM Ti6Al4V influences the tensile properties of the material to a certain extent, with the material built in the X-TA and Y-TA orientations having more comparable properties than with the material built in the Z-TA orientation although not so significant.

To address the aims and objectives of this work individually, the following conclusions are drawn:

- The microstructure of the material was investigated using light microscopy and SEM. It can be concluded that the material built across all scan speeds exhibited acicular martensitic microstructure which is typical of SLM fabricated material due to the high temperature gradients during the laser scanning process. Columnar elongated grains (prior β-grains) which appear due to epitaxial growth are observed along the build direction which is perpendicular to the tensile axis direction in the X-TA and Y-TA specimens and parallel to the tensile axis direction in the Z-TA specimens. There is no difference in microstructure of the specimens built at high scan speeds compared to that of specimens built at conventional scan speeds and no difference in microstructure within the set of material built at the high scan speeds therefore there is no effect of high scan speed observed on the microstructure. EBSD analysis shows that there is no difference in the size and morphology of reconstructed β-grains across the material built at the high scan speed. There is a difference in orientation of the β-grains in the specimens built in different orientations. In the Z-TA tensile specimens, the prior β-grains are along the tensile axis parallel to the build direction.

- Porosity, which is an inevitable consequence of SLM fabricated parts, was observed within the microstructure of the specimens and it plays a role in the mechanical integrity of the specimens. The 97-99% average relative density reported for the specimens investigated in this work, which is lower than the >99% relative density reported in most studies performed on SLM material built at conventional scan speeds, suggests that there is more porosity in the specimens fabricated at the high scan speeds in this project. The difference in relative density is due to the high scan speed consequence of improper pool formation and pore formation by keyhole effect. However, the difference in porosity is not significant as the specimens with 97-99% relative density show similar mechanical behaviour to the specimens with >99% relative density.

- There is no effect of high scan speed observed on the tensile behaviour of the specimens. The specimens built at the high scan speeds have similar behaviour to specimens built at conventional scan speeds. Although the specimens investigated in this project were fabricated at high scan speeds, the rest of the SLM build parameters were calculated such that an acceptable range of energy density was applied during the process. Suitable tensile properties are therefore still achieved when SLM Ti6Al4V parts are fabricated at high scan speeds. There is no change in tensile strength observed with increase in high scan speed within the range of scan speeds investigated in this project. The specimens were built with energy densities within the same range and therefore no effect of the change in scan speed is observed.

- No effect of build orientation on tensile properties of SLM Ti6Al4V is observed in this project. The consequences of build orientation and orientation of β-grain boundaries suggest that the specimens built horizontally (X-TA and Y-TA specimens) yield better tensile properties. However, no significant difference in these properties is observed between the specimens built horizontally (X-TA and Y-TA) and the specimens built vertically (Z-TA) in this project.

- The crack growth rate behaviour of the material was determined by investigating the dependence of crack growth on the cyclic stress intensity which would have resulted from crack opening displacement. Fatigue crack growth rate is characterized by the *m* and *C* parameters of the Paris equation. A variation in the number of cycles to failure is observed within each scan speed. This indicates some degree of crack growth instability which is seen by the deviation of the crack paths in the crack images taken after testing. Since the specimens were stress relieved, it is not clear why there was some degree of crack deviation during testing. The 6.25 m/s and 6.5 m/s specimens have the best crack growth behaviour which is comparable to that of specimens built at conventional scan speeds. The average fatigue life of the two sets of speeds was 470 000 and 308 000 cycles, respectively at a load range of 1.3 kN. The Paris equation constants *C* and *m* for the 6.25 m/s specimens were seen to be 4.9×10^{-11} and 2.86 ± 0.94 and for the 6.5 m/s specimens they were seen to be 5.0×10^{-11} and 2.73 ± 0.30. The 5.75 m/s and 6.0 m/s specimens, however, show much higher crack growth rates. The average fatigue life of the two sets of speeds was 220 000 and 330 000 cycles, respectively at a load range of 1.3 kN. The Paris equation constants *C* and *m* for the 5.75 m/s specimens were seen to be 2.35×10^{-13} and 5.16 ± 0.64 respectively and for the 6.0 m/s specimens they were seen to be 3.2×10^{-13} and 5.55 ± 0.81, respectively.

- The fracture toughness of the material was investigated by the linear-elastic plane-strain fracture toughness test as the material was expected to fracture in a linear-elastic manner. The fracture toughness of the material built at the higher scan speeds is comparable to that of material built at conventional scan speeds. The material built at 6.0 m/s is seen to have a marginally lower KQ value although it is still within the same range of KQ as the rest of the specimens built at the other high scan speeds. The marginally lower fracture toughness is owed to experimental error. It can be concluded that no effect of high scan speed is observed on the fracture toughness of the material.

7 Recommendations

After completion of the tests, the following recommendations are proposed to fully address the objectives of this project:

- It is recommended for the high scan speed material to be built at scan speeds with a higher difference between them for better comparison. Material built at different scan speeds within a wider range will have a bigger difference in energy density applied to the material during the SLM process. Since energy density influences the microstructure and mechanical behaviour of SLM material, a bigger difference in energy density due to scan speed would be more sufficient to adequately investigate the effect thereof.

- To have a fair comparison of the material built at conventional scan speeds and material built at high scan speeds, it is recommended that both materials be built by the same party. This ensures complete certainty that the material is built under strictly the same conditions and parameters with the only difference being scan speed. This is critically important because it ensures all differences observed to be only and entirely due to difference in scan speed. Some of the studies from literature do not mention the other build parameters used and the energy densities applied which makes it difficult to conclude that the difference or similarities observed were not influenced by build parameters other than the scan speed itself.

- Several ASTM standards for mechanical testing recommend that triplicate tests be performed for each condition for adequate precision. As such, three specimens were built for each scan speed and build orientation for this project. However, some specimens were spoiled due to human error and therefore discarded. This resulted in only duplicate results being reported for some results. Therefore, since ASTM standards recommend triplicate tests which would require three specimens per condition, it is recommended to build more than three specimens per condition and for them to be at the researcher's disposal in case a specimen gets spoiled and cannot be used any further for testing.

- The porosity reported for the specimens built at the high scan speeds is 97-99%. A >99% density ensures the material better mechanical performance. No previous work has been done on material built at the scan speeds investigated in this project so it is not clear whether a consistent >99% density can be achieved at these scan speeds, but it is recommended that the processing parameters be further manipulated to increase density.

8 References

1. Henriques, V.A.R., et al., Production of titanium alloys for advanced aerospace systems by powder metallurgy. Materials Research, 2005. **8**(4): p. 443-446.
2. Aboulkhair, N.T. and N.M. Everitt, Maskery, Ian and Ashcroft, Ian and Tuck, Chris (2017) Selective laser melting of aluminium alloys. MRS Bulletin, 42 (4). pp. 311-319. ISSN 1938-1425.
3. Herzog, D., et al., Additive manufacturing of metals. Acta Materialia, 2016. **117**: p. 371-392.
4. Dutta, B. and F.H.S. Froes, The additive manufacturing (AM) of titanium alloys, in Titanium powder metallurgy. 2015, Elsevier. p. 447-468.
5. Pereira, T., J.V. Kennedy, and J. Potgieter, A comparison of traditional manufacturing vs additive manufacturing, the best method for the job. Procedia Manufacturing, 2019. **30**: p. 11-18.
6. Unger, A.S., R.J. Lewis, and T. Gruen, Evaluation of a porous tantalum uncemented acetabular cup in revision total hip arthroplasty: clinical and radiological results of 60 hips. The Journal of arthroplasty, 2005. **20**(8): p. 1002-1009.
7. Kalpakjian, S., Manufacturing engineering and technology. 2001: Pearson Education India.
8. Hopkinson, N. and P. Dicknes, Analysis of rapid manufacturing—using layer manufacturing processes for production. Proceedings of the Institution of Mechanical Engineers, Part C: Journal of Mechanical Engineering Science, 2003. **217**(1): p. 31-39.
9. Ruffo, M., C. Tuck, and R. Hague, Make or buy analysis for rapid manufacturing. Rapid Prototyping Journal, 2007.
10. Upadhyay, M., T. Sivarupan, and M. El Mansori, 3D printing for rapid sand casting—A review. Journal of Manufacturing Processes, 2017. **29**: p. 211-220.
11. Levy, G.N., R. Schindel, and J.-P. Kruth, Rapid manufacturing and rapid tooling with layer manufacturing (LM) technologies, state of the art and future perspectives. CIRP annals, 2003. **52**(2): p. 589-609.

12. Gao, W., et al., The status, challenges, and future of additive manufacturing in engineering. Computer-Aided Design, 2015. **69**: p. 65-89.
13. Newman, S.T., et al., Process planning for additive and subtractive manufacturing technologies. CIRP Annals, 2015. **64**(1): p. 467-470.
14. Jiao, L., et al., Femtosecond Laser Produced Hydrophobic Hierarchical Structures on Additive Manufacturing Parts. Nanomaterials (Basel), 2018. **8**(8).
15. Thijs, L., et al., A study of the microstructural evolution during selective laser melting of Ti– 6Al–4V. Acta materialia, 2010. **58**(9): p. 3303-3312.
16. Vrancken, B., et al., Heat treatment of Ti6Al4V produced by Selective Laser Melting: Microstructure and mechanical properties. Journal of Alloys and Compounds, 2012. **541**: p. 177-185.
17. Facchini, L., et al., Ductility of a Ti-6Al-4V alloy produced by selective laser melting of prealloyed powders. Rapid Prototyping Journal, 2010.
18. Welsch, G., R. Boyer, and E. Collings, Materials properties handbook: titanium alloys. 1993: ASM international.
19. Leyens, C. and M. Peters, Titanium and titanium alloys: fundamentals and applications. 2003: John Wiley & Sons.
20. Henriques, V., et al., Microstructural evolution during hot pressing of the blended elemental Ti–6% Al–7% Nb alloy. Materials Science and Engineering: A, 2003. **347**(1-2): p. 315-324.
21. Lütjering, G. and J.C. Williams, Titanium. 2007: Springer Science & Business Media.
22. Donachie, M.J., Titanium: a technical guide. 2000: ASM international.
23. Shipley, H., et al., Optimisation of process parameters to address fundamental challenges during selective laser melting of Ti-6Al-4V: A review. 2018.
24. He, B., et al., Microstructural characteristic and mechanical property of Ti6Al4V alloy fabricated by selective laser melting. Vacuum, 2018. **150**: p. 79-83.
25. Malinov, S., et al., Differential scanning calorimetry study and computer modeling of β⇒ α phase transformation in a Ti-6Al-4V alloy. Metallurgical and materials transactions A, 2001. **32**(4): p. 879-887.
26. Elmer, J., et al., In situ observations of lattice expansion and transformation rates of α and β phases in Ti–6Al–4V. Materials Science and Engineering: A, 2005. **391**(1-2): p. 104-113.

27. Kelly, S.M., Thermal and microstructure modeling of metal deposition processes with application to titanium aluminum vanadium. 2004, Virginia Polytechnic Institute and State University.
28. Ahmed, T. and H. Rack, Phase transformations during cooling in α+ β titanium alloys. Materials Science and Engineering: A, 1998. **243**(1-2): p. 206-211.
29. Lütjering, G., J. Williams, and A. Gysler, Microstructure and mechanical properties of titanium alloys, in Microstructure And Properties Of Materials: (Volume 2). 2000. p. 1-77.
30. Lee, Y. and G. Welsch, Young's modulus and damping of Ti 6Al 4V alloy as a function of heat treatment and oxygen concentration. Materials Science and Engineering: A, 1990. **128**(1): p. 77-89.
31. Rack, H. and J. Qazi, Titanium alloys fbr biomedical applications [J i. Materials Seience and Engineering, 2006. **26**: p. 1.
32. Lütjering, G., Influence of processing on microstructure and mechanical properties of (α+ β) titanium alloys. Materials Science and Engineering: A, 1998. **243**(1-2): p. 32-45.
33. Peters, M., G. Lütjering, and G. Ziegler, Control of microstructures of (α+ β)-titanium alloys.
Zeitschrift für Metallkunde, 1983. **74**(5): p. 274-282.
34. Pook, L.P., Linear elastic fracture mechanics for engineers: theory and applications. 2000: WIT press.
35. Mecholsky Jr, J.J., Fracture mechanics principles. Dental Materials, 1995. **11**(2): p. 111-112.
36. Hosseini, Z.S., et al., On the theoretical modeling of fatigue crack growth. Journal of the Mechanics and Physics of Solids, 2018. **121**: p. 341-362.
37. Ritchie, R., et al., High-cycle fatigue of Ti-6Al-4V. Fatigue and Fracture of Engineering Materials and Structures, 1999. **22**(7): p. 621-632.
38. Totten, G., Fatigue Crack Propagation-A fatigue crack typically propagates in three stages: I (short cracks), II (long cracks), and III (final fracture). The article is from the ASM reference book," Failure. Advanced Materials and Processes, 2008. **166**(5): p. 39-44.
39. Suo, Z., et al., Fracture mechanics for piezoelectric ceramics. Journal of the Mechanics and Physics of Solids, 1992. **40**(4): p. 739-765.
40. Anderson, T.L., Fracture mechanics: fundamentals and applications. 2017: CRC press.

41. Ohta, A., M. Kosuge, and E. Sasaki, Fatigue crack closure over the range of stress ratios from− 1 to 0.8 down to stress intensity threshold level in HT80 steel and SUS304 stainless steel.

International Journal of Fracture, 1978. **14**(3): p. 251-264.

42. Tanaka, K. and S. Matsuoka, A tentative explanation for two parameters, C and m, in Paris equation of fatigue crack growth. International Journal of Fracture, 1977. **13**(5): p. 563-583.

43. Fatemi, A., Fundamentals of LEFM and applications to fatigue crack growth. University of Toledo, 2010: p. 133.

44. Dhansay, N.M., Fracture mechanics based fatigue and fracture toughness evaluation of SLM Ti-6Al-4V. 2015, University of Cape Town.

45. Pal, S., et al., Tensile properties of selective laser melting products affected by building orientation and energy density. Materials Science and Engineering: A, 2019. **743**: p. 637-647.

46. Cain, V., et al., Crack propagation and fracture toughness of Ti6Al4V alloy produced by selective laser melting. Additive Manufacturing, 2015. **5**: p. 68-76.

47. Van Hooreweder, B., et al., Analysis of fracture toughness and crack propagation of Ti6Al4V produced by selective laser melting. Advanced Engineering Materials, 2012. **14**(1-2): p. 92-97.

48. Leuders, S., et al., On the mechanical behaviour of titanium alloy TiAl6V4 manufactured by selective laser melting: Fatigue resistance and crack growth performance. International Journal of Fatigue, 2013. **48**: p. 300-307.
49. Do, D.K. and P. Li, The effect of laser energy input on the microstructure, physical and mechanical properties of Ti-6Al-4V alloys by selective laser melting. Virtual and Physical Prototyping, 2016. **11**(1): p. 41-47.
50. Simchi, A., Direct laser sintering of metal powders: Mechanism, kinetics and microstructural
features. Materials Science and Engineering: A, 2006. **428**(1-2): p. 148-158.
51. Campanelli, S.L., et al., Capabilities and performances of the selective laser melting process.
New Trends in Technologies: Devices, Computer, Communication and Industrial Systems,
2010. **1**(1): p. 233-252.
52. Kruth, J.-P., et al. Part and material properties in selective laser melting of metals. in Proceedings of the 16th International Symposium on Electromachining (ISEM XVI). 2010.
SHANGHAI JIAO TONG UNIV PRESS.
53. Semiatin, S., et al., Microstructure evolution during alpha-beta heat treatment of Ti-6Al-4V.
Metallurgical and Materials Transactions A, 2003. **34**(10): p. 2377-2386.
54. Simonelli, M., Y.Y. Tse, and C. Tuck, Effect of the build orientation on the mechanical properties and fracture modes of SLM Ti–6Al–4V. Materials Science and Engineering: A, 2014. **616**: p. 1-11.
55. Davis, J.R., Tensile testing. 2004: ASM international.
56. Tait, R., Tiny tots guide to the operation of the E.S.H universal servo hydraulic testing fascility.
"Tiny tots guide to the operation of the E.S.H universal servo hydraulic testing fascility," operation manual., Department of Mechanical Engineering., University of Cape Town, Cape Town, South Africa.
57. Mohazzab, P., Archimedes' principle revisited. Journal of Applied Mathematics and Physics, 2017. **5**(04): p. 836.
58. Clinning, N., Thermomechanical propcessing of blended elemental powder Ti-6Al-4V Alloy.

2012.

59. Shunmugavel, M., A. Polishetty, and G. Littlefair, Microstructure and Mechanical Properties of Wrought and Additive Manufactured Ti-6Al-4V Cylindrical Bars. Procedia Technology, 2015. **20**: p. 231-236.
60. Zhou, B., et al., A study of the microstructures and mechanical properties of Ti6Al4V fabricated by SLM under vacuum. Materials Science and Engineering: A, 2018. **724**: p. 1-10.
61. Chlebus, E., et al., Microstructure and mechanical behaviour of Ti—6Al—7Nb alloy produced by selective laser melting. Materials Characterization, 2011. **62**(5): p. 488-495.
62. Xu, Z., A. Liu, and X. Wang, The influence of building direction on the fatigue crack propagation behavior of Ti6Al4V alloy produced by selective laser melting. Materials Science and Engineering: A, 2019. **767**: p. 138409.
63. Van Hooreweder, B., et al., Microstructural characterization of SLS-PA12 specimens under dynamic tension/compression excitation. Polymer testing, 2010. **29**(3): p. 319-326.
64. Han, J., et al., Microstructure and mechanical property of selective laser melted Ti6Al4V dependence on laser energy density. Rapid Prototyping Journal, 2017. **23**(2): p. 217-226.
65. ASTM E8/E8M, "Standard Test Method for Tension Testing of Metallic Materials," Am. Soc. Test. Mater., pp. 1-28, 2013.
66. ASTM E647, "Standard Test Method for Measurement of Fatigue Crack Growth Rates," Am. Soc. Test. Mater., pp. 1-49, 2015.
67. ASTM B962, " Standard test Methods for Density of Compacted or Sintered Powder Metallurgy (PM) Products Using Archimedes' Principle;" Am. Soc. Test. Mater., pp. 1-7, 2015.
68. ASTM E399, "Standard test Method for Linear-Elastic Plane-Strain Fracture Toughness K_{IC} of Metallic Materials," Am. Soc. Test. Mater., pp. 1-34, 2017.

9 Bibliography

The bibliography section lists the sources from the internet that are not reviewed and therefore not included in the references section. These sources were accessed for images and relevant information pertaining to this project.

a) "3D printing machine SLM500." [Online]. Available:

https://alpha-products.com.sg/slm-500/. [Accessed 04-May-2021].

b) "Bohn Ford." [Online]. Available: https://www.bohnford.com/what-is-a-brake-caliper-harvey-la.html. Accessed 28-June-2021].

c) "Tiremaxx service centers." [Online]. Available: http://tiremaxx.com/services/brakes/. Accessed 28-June-2021.

d) "3D Printing Media Network." [Online]. Available: https://www.3dprintingmedia.network/bugattis-new-titanium-brake-caliper-largest-functional-component-3d-printed-date/. [Accessed 28-June-2021].

e) "Aeroswift." [Online]. Available: http://aeroswift.com.www27.cpt3.host-h.net/technology/ . Accessed 20-Sepetember-2021

10 Appendices

10.1 Fatigue crack growth rate testing parameters

This section lists the important parameters used for each of the FCGR tests which are “B”, “W”, the initial and terminal values of ΔK, R and “a^n ”, the loading variable ΔP. The stress ratio “R” used is 0.1and ΔP = 1170N. all specimens were tested to failure.

Table 39: Fatigue crack growth rate parameters

Speed [m/s]	Specimen	B [mm]	W [mm]	a_n [mm]	Starting ΔK [MPa.m$^{0.5}$]	Ending ΔK [MPa.m$^{0.5}$]
5.75	1	6.25	25	8.75	7,79	18,25
	2	6.25	25	8.75	8,13	21,83
6.0	1	6.25	25	8.75	8,62	30,03
	2	6.25	25	8.75	8,09	18,1
	3	6.25	25	8.75	8.13	17.67
6.25	1	6.25	25	8.75	8.32	72.54
	2	6.25	25	8.75	7.74	33.56
6.5	1	6.25	25	8.75	7.78	37.39
	2	6.25	25	8.75	8.18	51.11
	3	6.25	25	8.75	7.85	43..41

10.2 Fatigue crack images

This section shows the final fatigue crack oaths for each specimen tested.

10.2.1 5.75 m/s

Figure 98: Fatigue crack for 5.5 m/s specimen 1

Figure 99: Fatigue crack for 5.75 m/s specimen

10.2.2 6.0 m/s

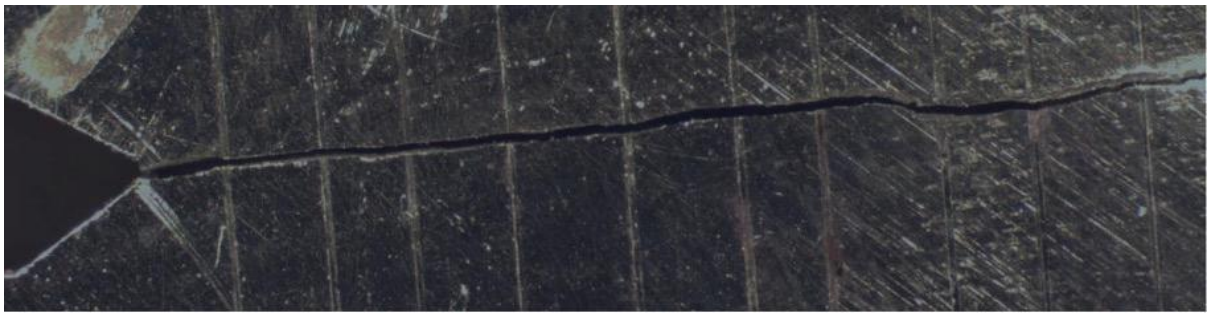

Figure 100: Fatigue crack for 6.0 m/s specimen 1

Figure 101: Fatigue crack for 6.0 m/s specimen 2

Figure 102: Fatigue crack for 6.0 m/s specimen 3

10.2.3 6.25 m/s

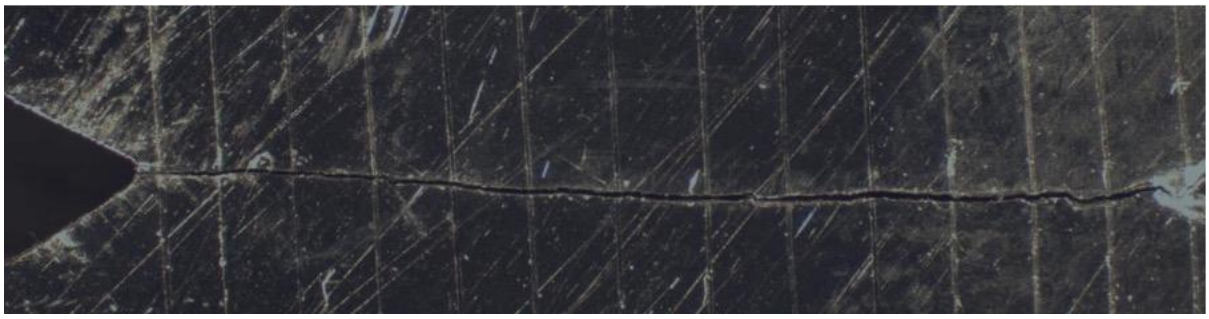

Figure 103: Fatigue crack for 6.25 m/s specimen 1

Figure 104: Fatigue crack for 6.25 m/s specimen 2

10.2.4 6.5 m/s

Figure 105: Fatigue crack for 6.5 m/s specimen 1

Figure 106: Fatigue crack for 6.5 m/s specimen 2

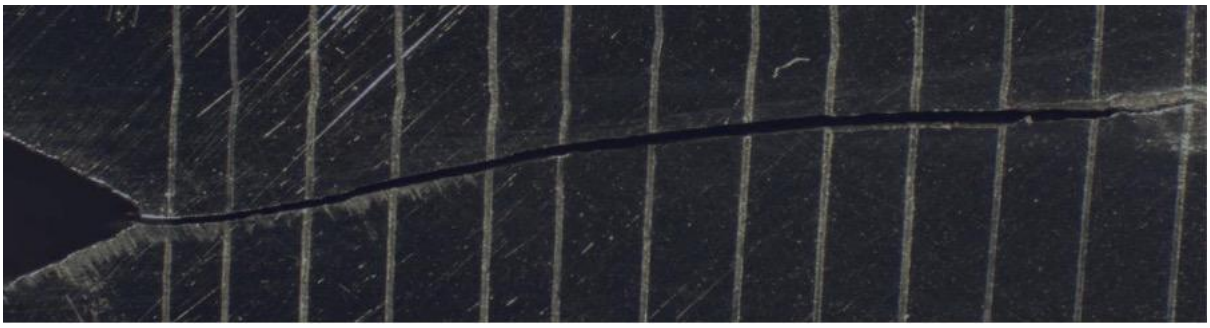

Figure 107: Fatigue crack for 6.5 m/s specimen

10.3 Fracture toughness testing parameters

This section lists the important parameters used for each of the fracture toughness tests which are “B”, “W”, ΔK, and the number of cycles for final 2.5% of overall crack size. The stress ratio “R” used is 0.1.

Table 40: Fracture toughness parameters

Speed [m/s]	**Specimen**	**B [mm]**	**W [mm]**	**ΔK [MPa.m$^{0.5}$]**	**Number of cycles for the final 2.5% of overall crack size**
5.75	1	12.5	25	45.30	226 933
	2	12.5	25	44.63	231 281
	3	12.5	25	47.76	277 027
6.0	1	12.5	25	43.47	223 222
	2	12.5	25	45.25	238 075
	3	12.5	25	44.73	267 822
6.25	1	12.5	25	49.35	235 975
	2	12.5	25	46.48	218 996
	3	12.5	25	47.63	263 173
6.5	1	12.5	25	48.62	224 689
	2	12.5	25	47.52	319 902
	3	12.5	25	48.02	255 422

Table 41: Fracture toughness parameters

Speed	Specimen	Number of cycles for the final 2.5% of overall crack size	Pmax [N]	PQ [N]	Pmax/ PQ [N]	Average crack length [mm]	K_{max} in fatigue precracking [MPa.m$^{0.5}$]	K_Q [MPa.m$^{0.5}$]
5.75	1	36298	8000	8000	1	14.38	50.33	50.33
	2	35830	9300	9100	1.02	13.19	49.58	48.52
	3	35123	9200	9000	1.02	13.77	53.07	51.92
6.0	1	34125	8800	8600	1.02	13.41	48.30	47.20
	2	34078	7800	7200	1.08	14.55	50.28	46.41
	3	34150	8200	780	1.05	14.13	49.71	47.28
6.25	1	34693	8300	8000	1.04	14.71	54.83	52.85
	2	34479	8200	7800	1.05	14.39	51.64	49.12
	3	35086	8800	8200	1.07	14.40	55.53	51.74
6.5	1	36723	7800	7600	1.02	15.02	54.03	52.64
	2	37163	7000	6800	1.03	15.54	52.80	51.29
	3	36580	7800	7400	1.05	14.94	53.36	50.62

10.4 Fracture toughness Load vs Displacement curves

10.4.1 5.75 m/s

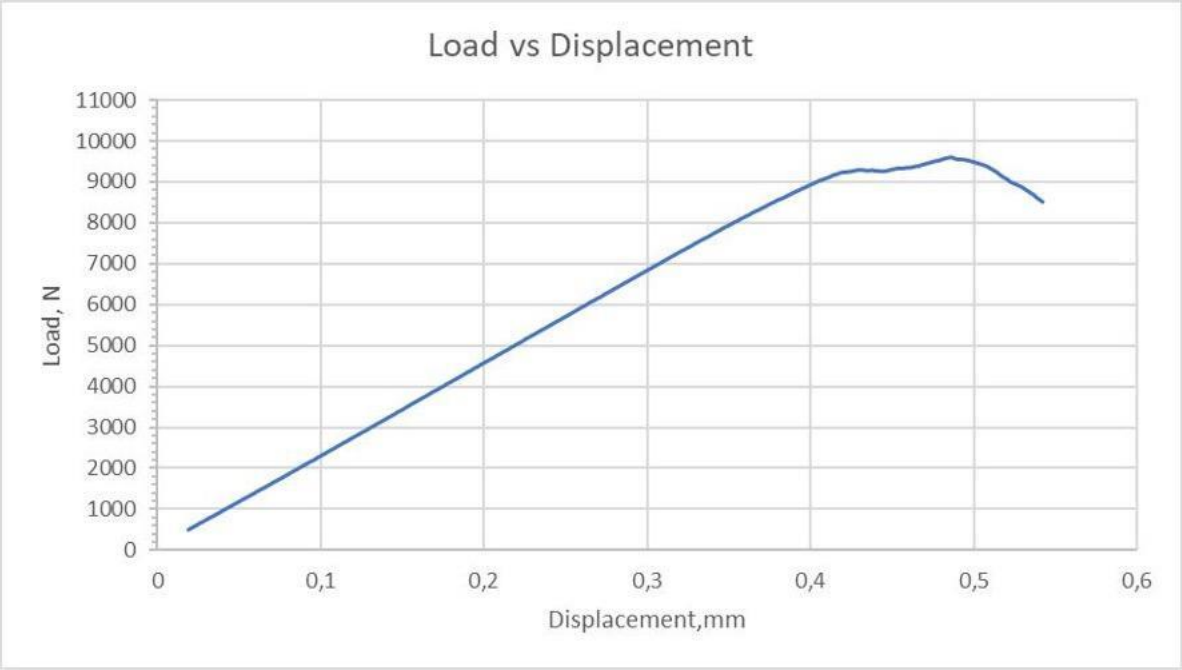

Figure 108: Load vs Displacement curve for 5.75 m/s 1

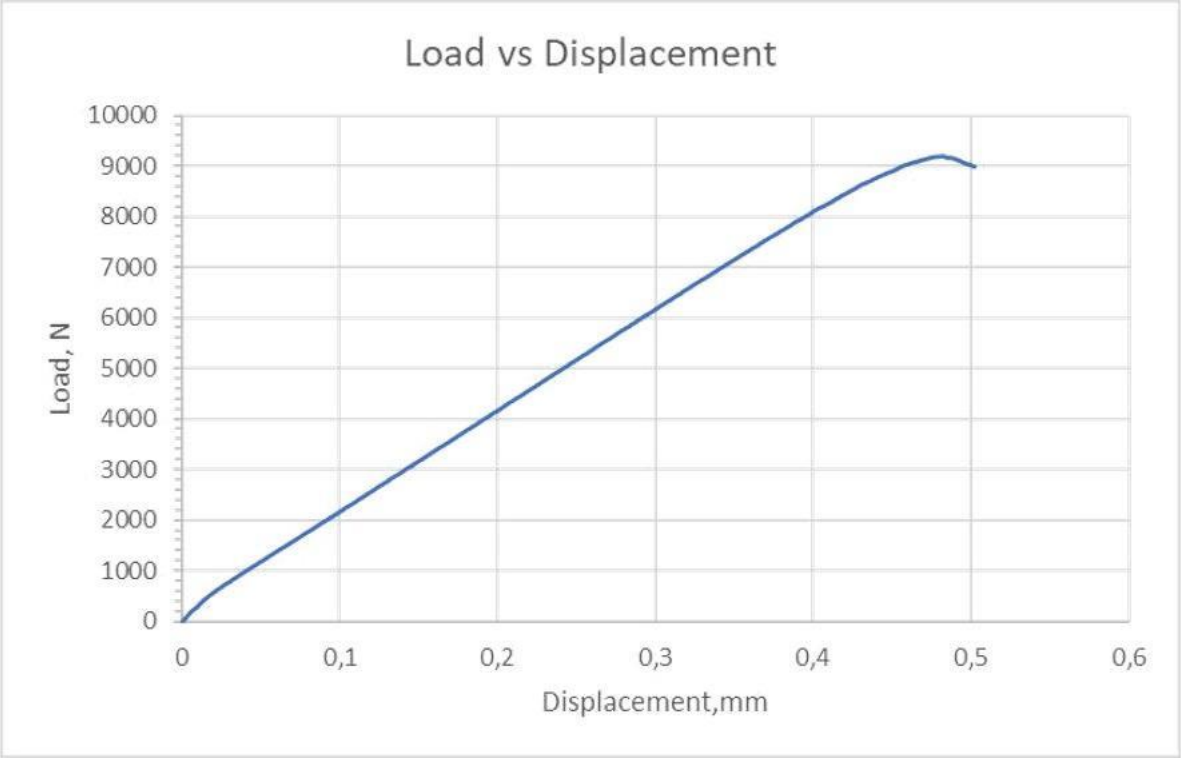

Figure 109: Load vs Displacement curve for 5.75 m/s 2

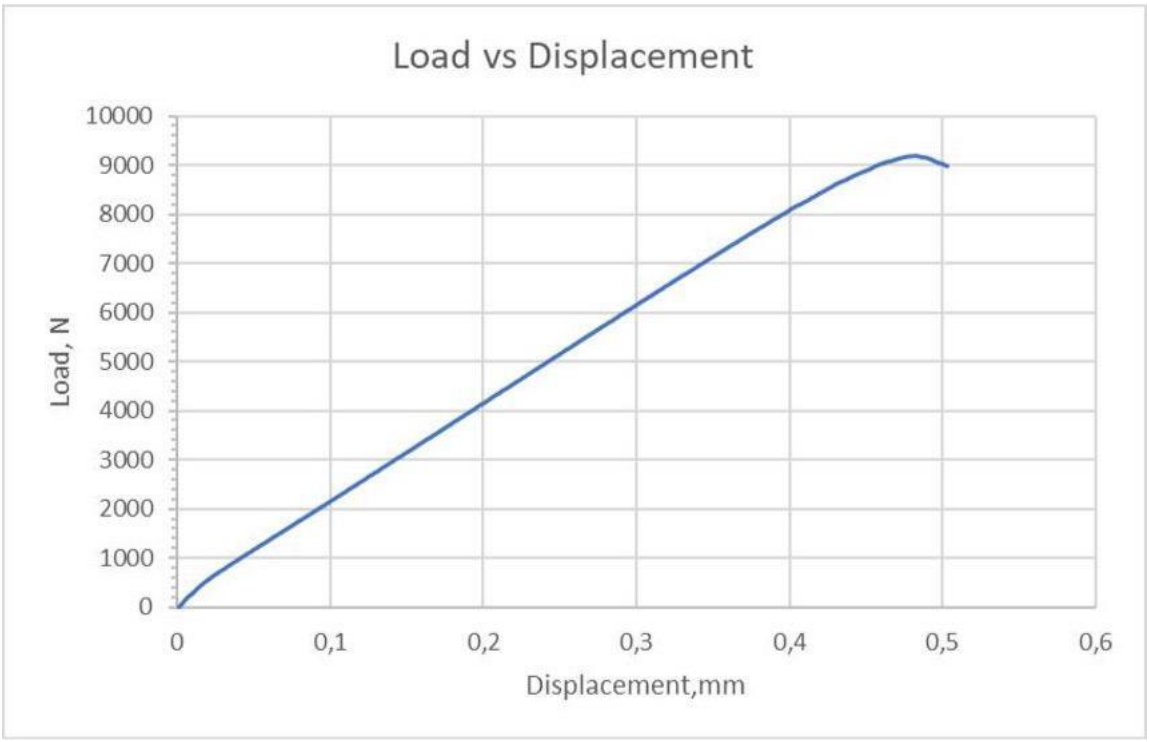

Figure 110: Load vs Displacement curve for 5.75 m/s 3

10.4.2 6.0 m/s

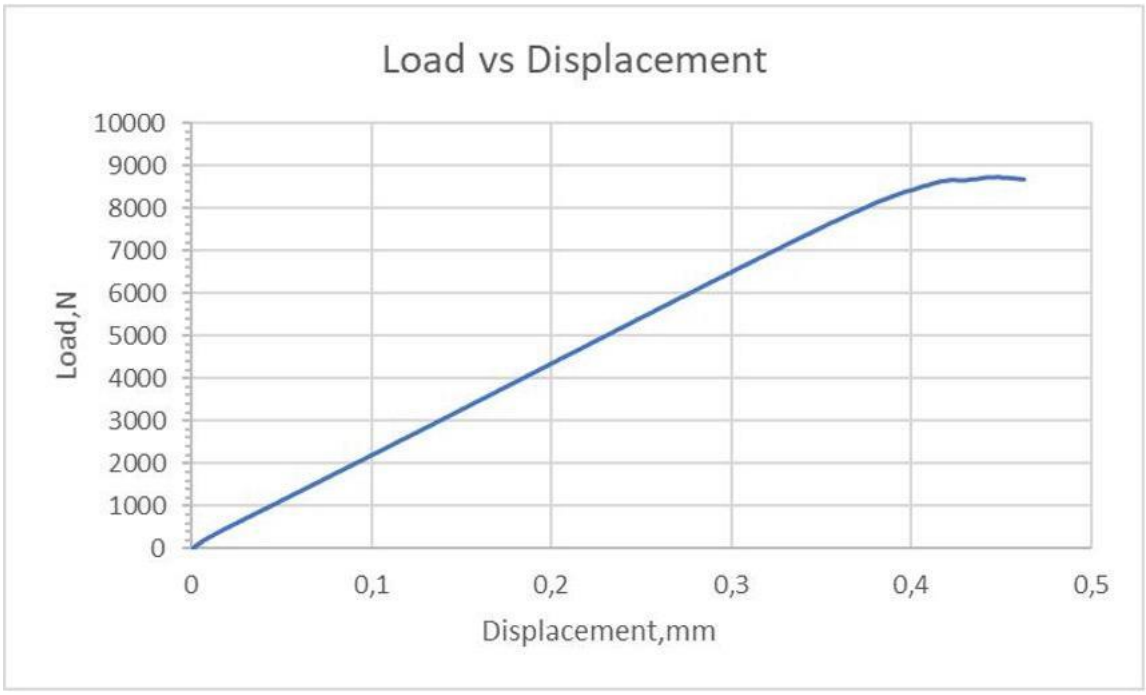

Figure 111: Load vs Displacement curve for 6.0 m/s 1

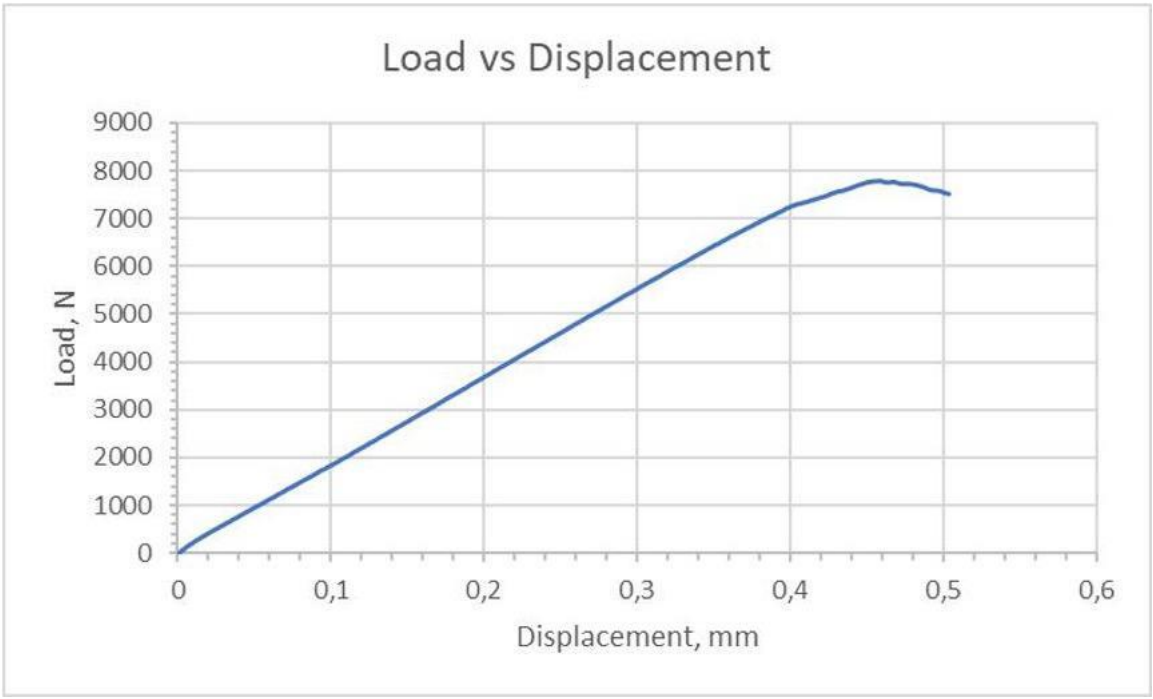

Figure 112: Load vs Displacement curve for 6.0 m/s 2

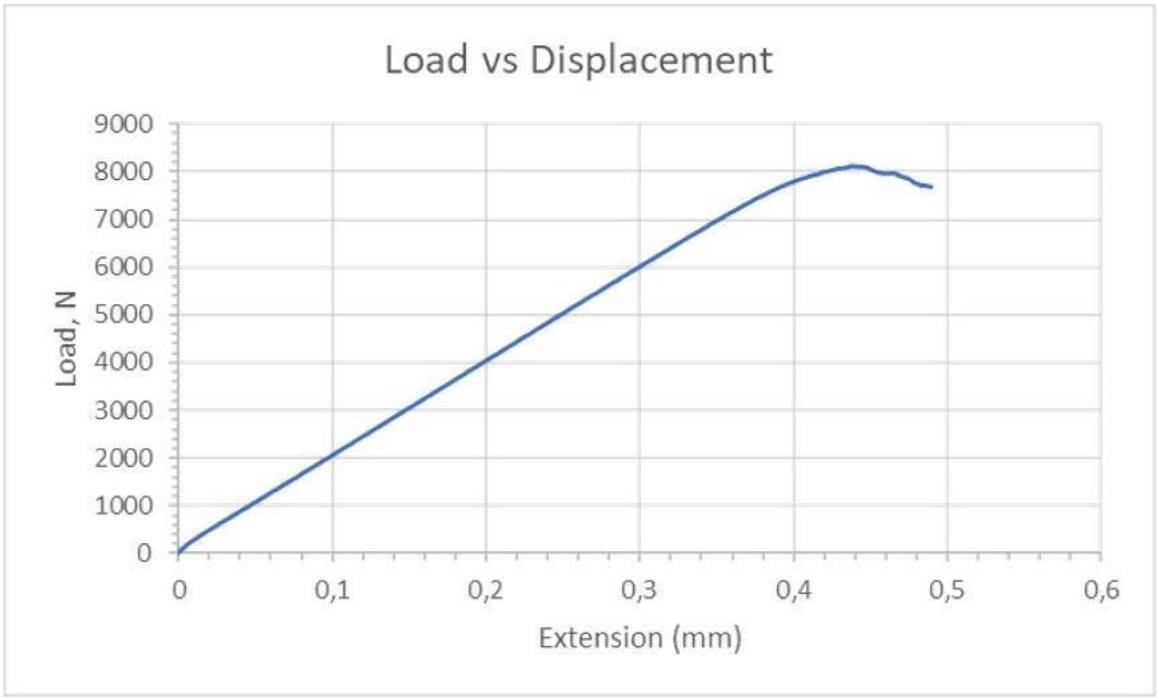

Figure 113: Load vs Displacement curve for 6.0 m/s 3

Figure 114: Load vs Displacement curve for 6.25 m/s 1

Figure 115: Load vs Displacement curve for 6.25 m/s 2

Figure 116: Load vs Displacement curve for 6.25 m/s 3

Figure 117: Load vs Displacement curve for 6.5 m/s 1

Figure 118: Load vs Displacement curve for 6.5 m/s 2

Figure 119: Load vs Displacement curve for 6.5 m/s 3

10.5 Fracture toughness crack measurements

10.5.1 5.75 m/s

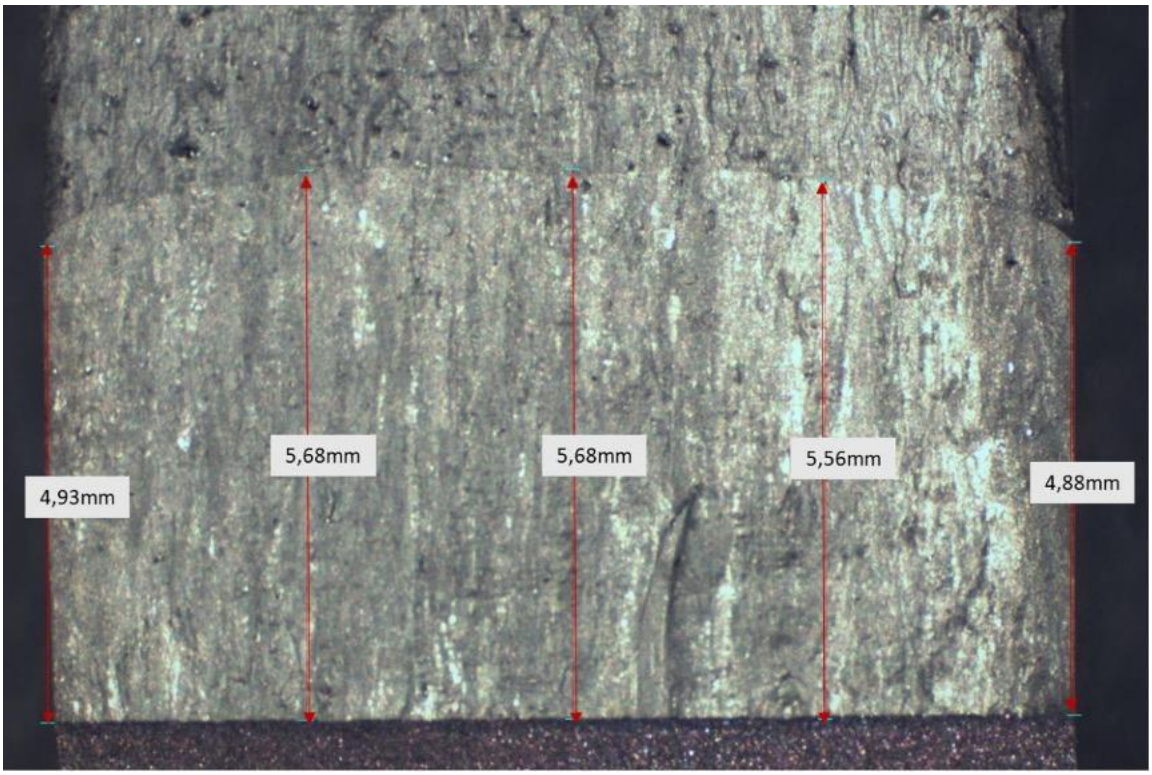

Figure 120: Fracture toughness crack measurement for 5.75 m/s 1

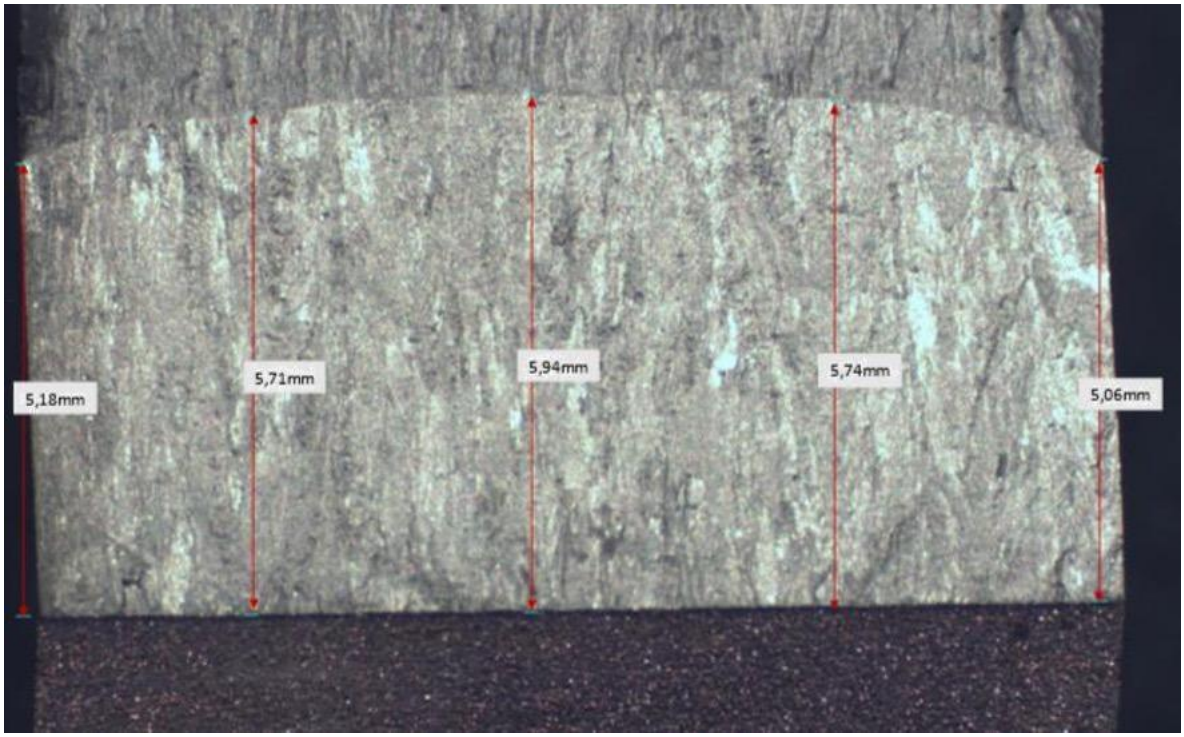

Figure 121: Fracture toughness crack measurement for 5.75 m/s 2

10.5.2 6.0 m/s

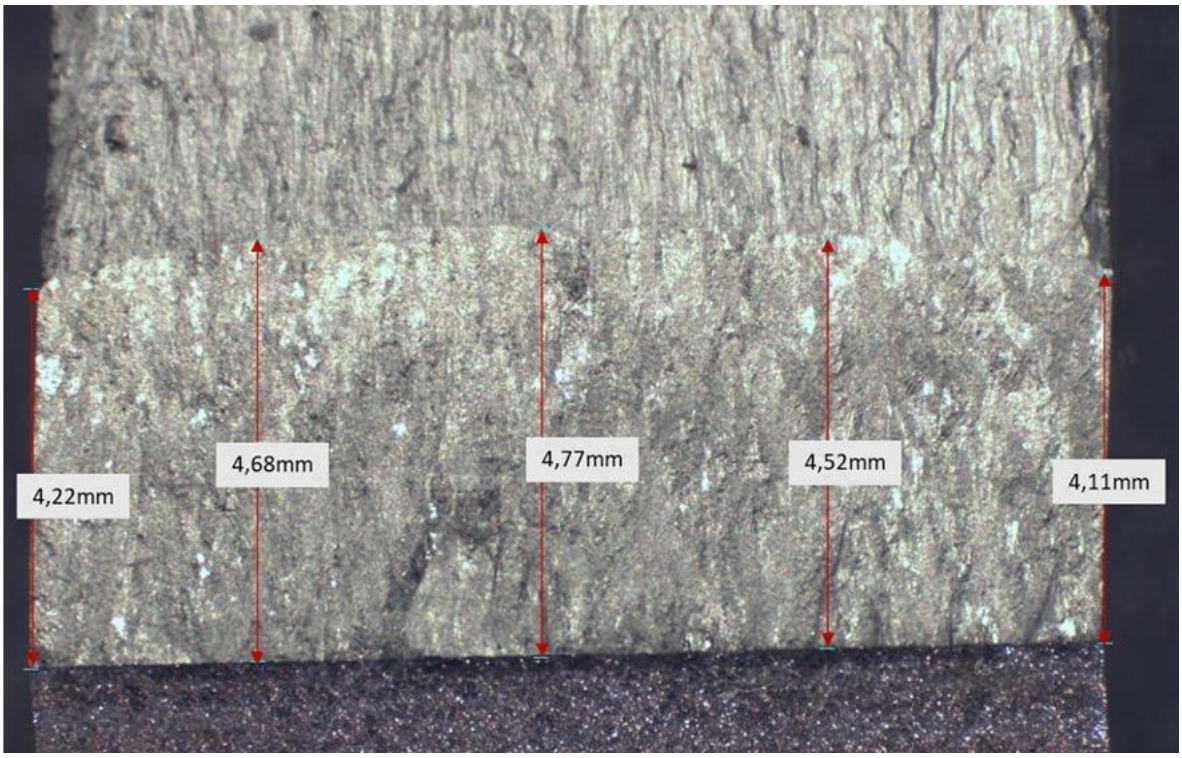

Figure 122: Fracture toughness crack measurement for 6.0 m/s 1

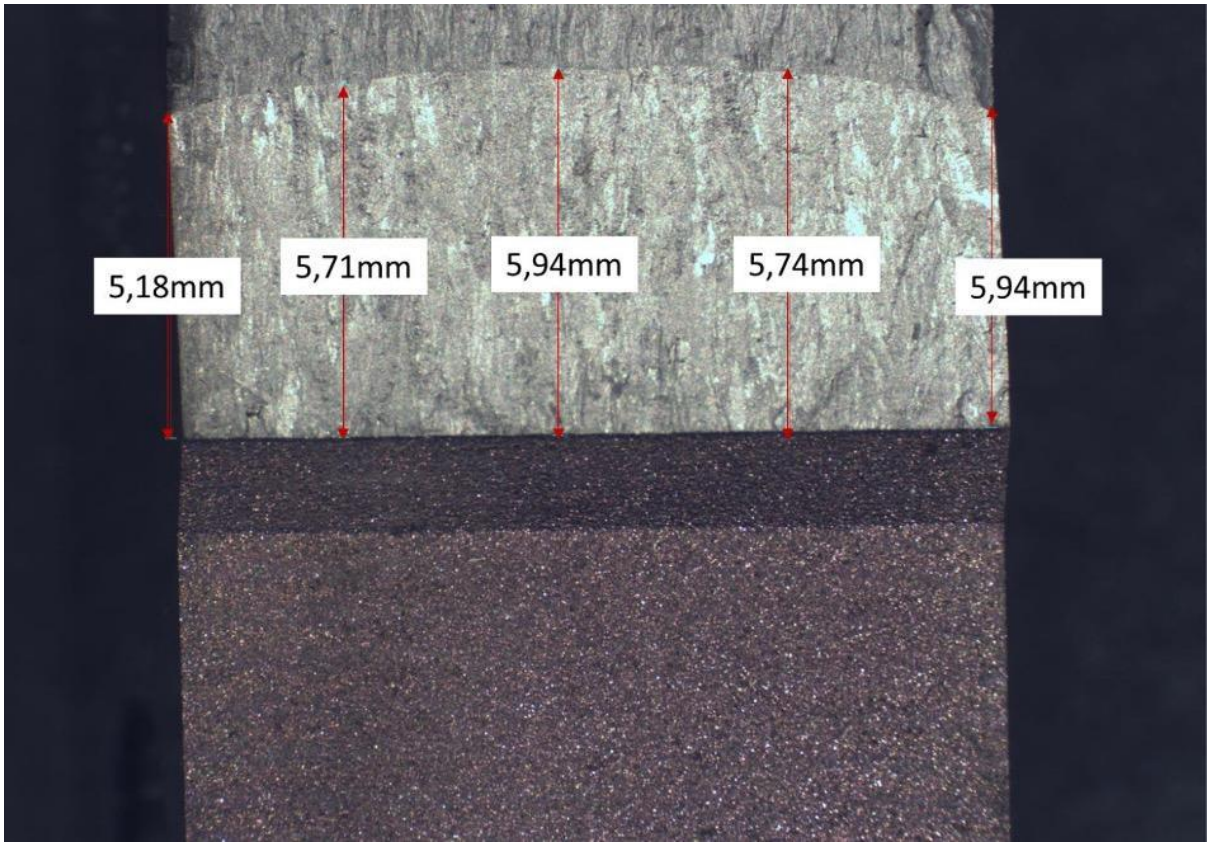

Figure 123: Fracture toughness crack measurement for 6.0 m/s 2

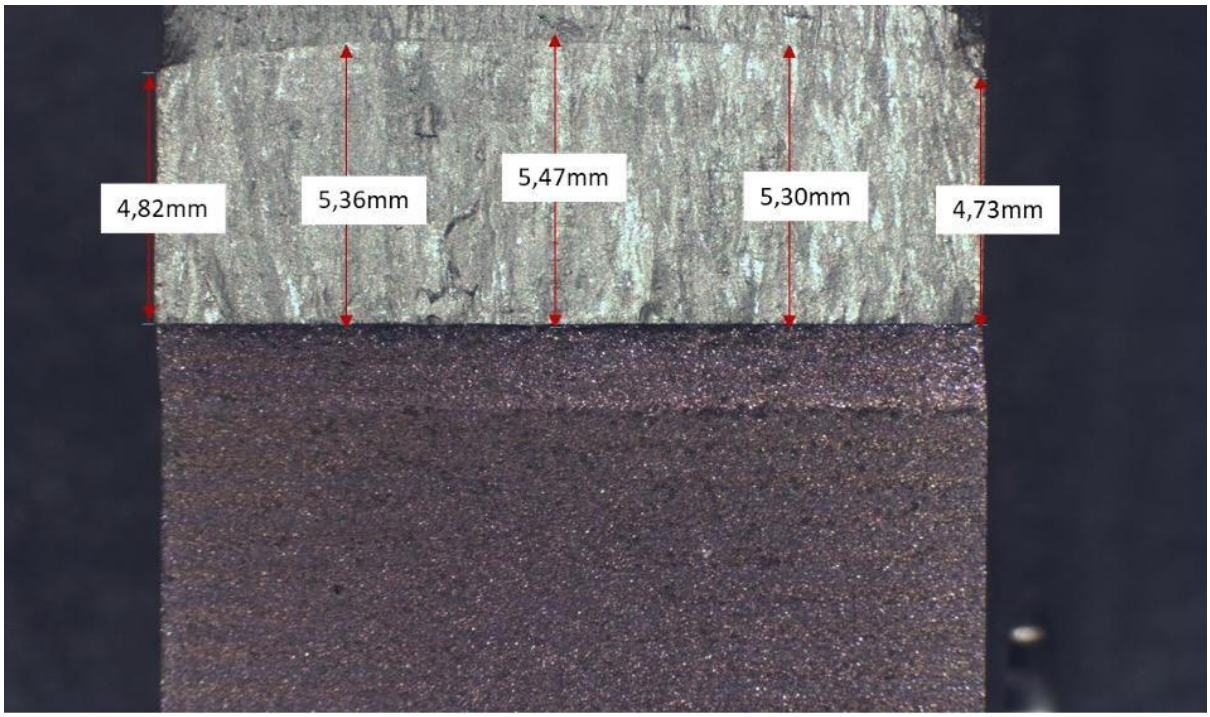

Figure 124: Fracture toughness crack measurement for 6.0 m/s 3

10.5.3 6.25 m/s

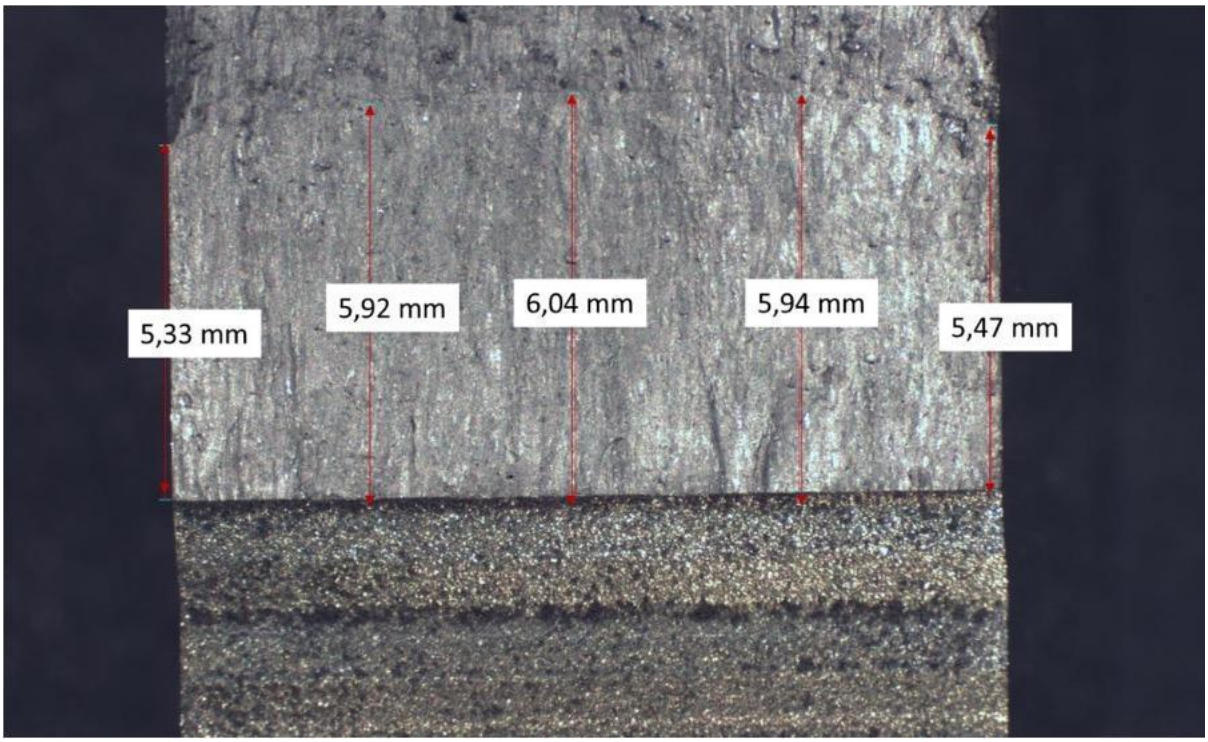

Figure 125: Fracture toughness crack measurement for 6.25 m/s 1

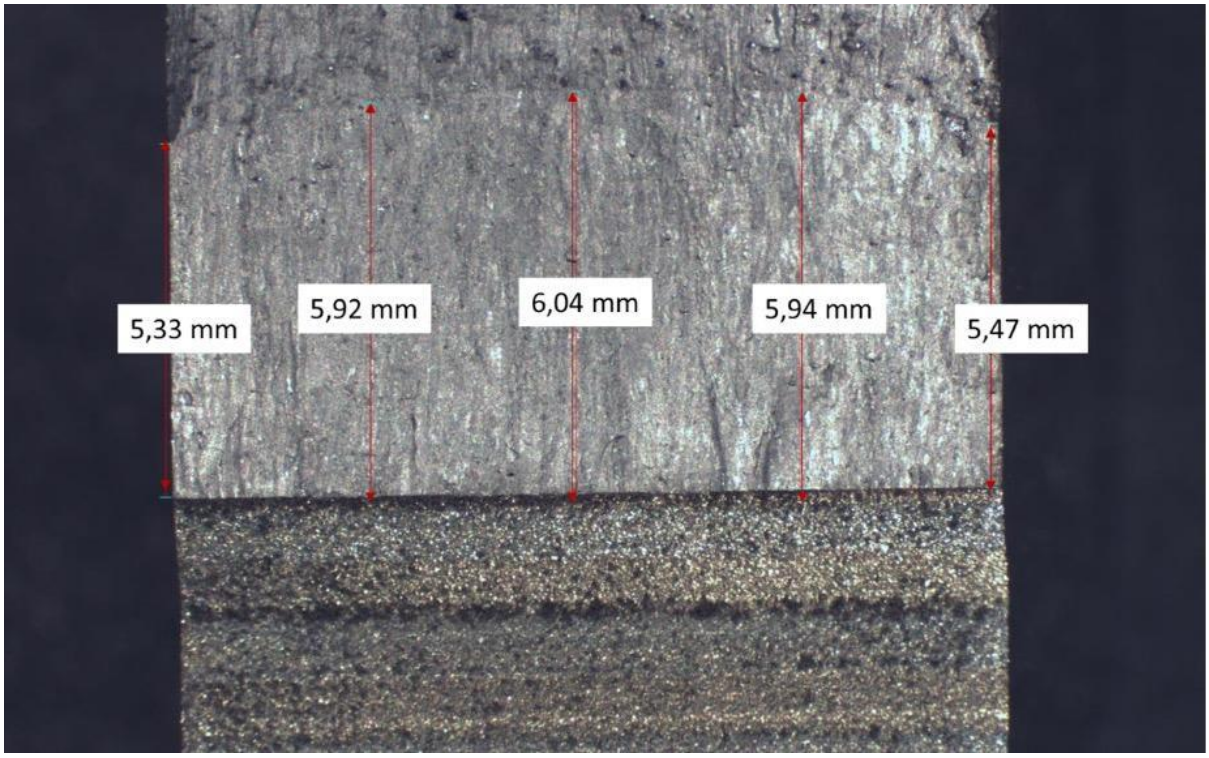

Figure 126: Fracture toughness crack measurement for 6.25 m/s 2

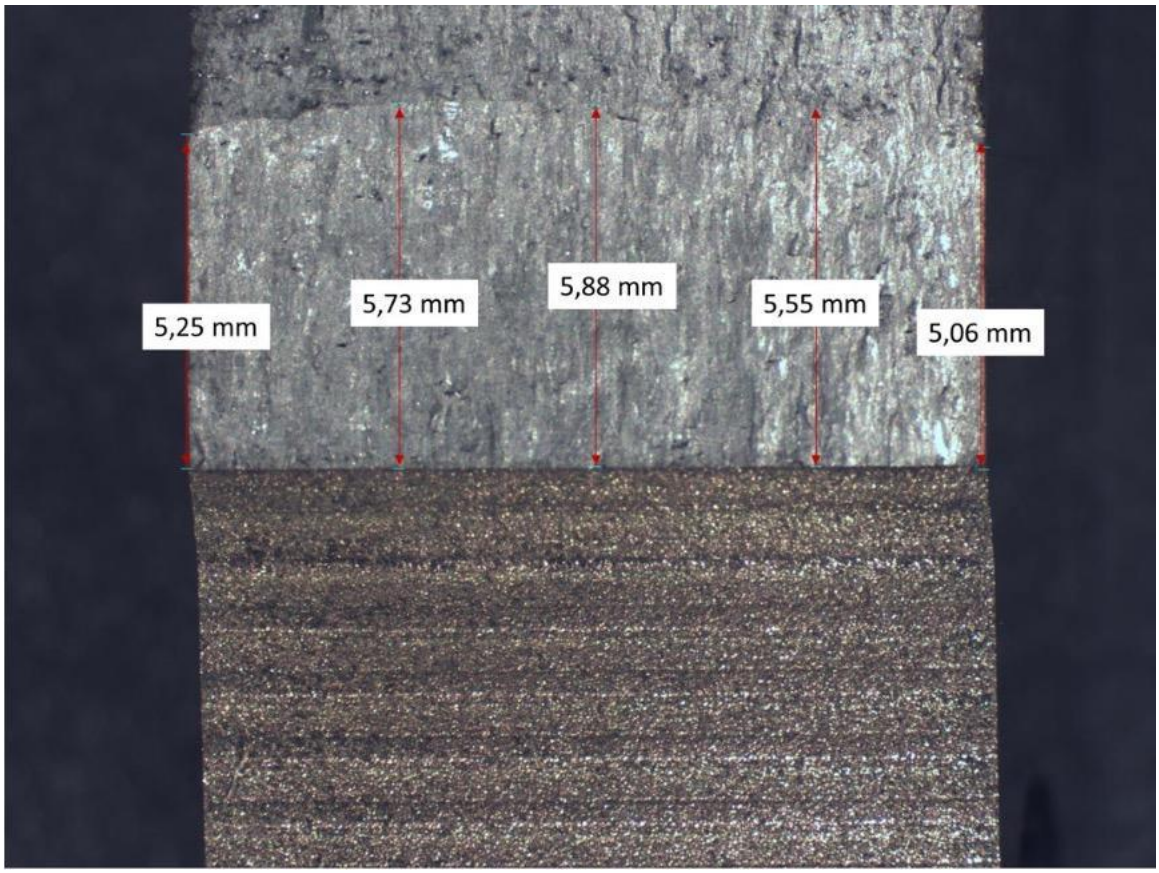

Figure 127: Fracture toughness crack measurement for 6.25 m/s 3

10.5.4 6.5 m/s

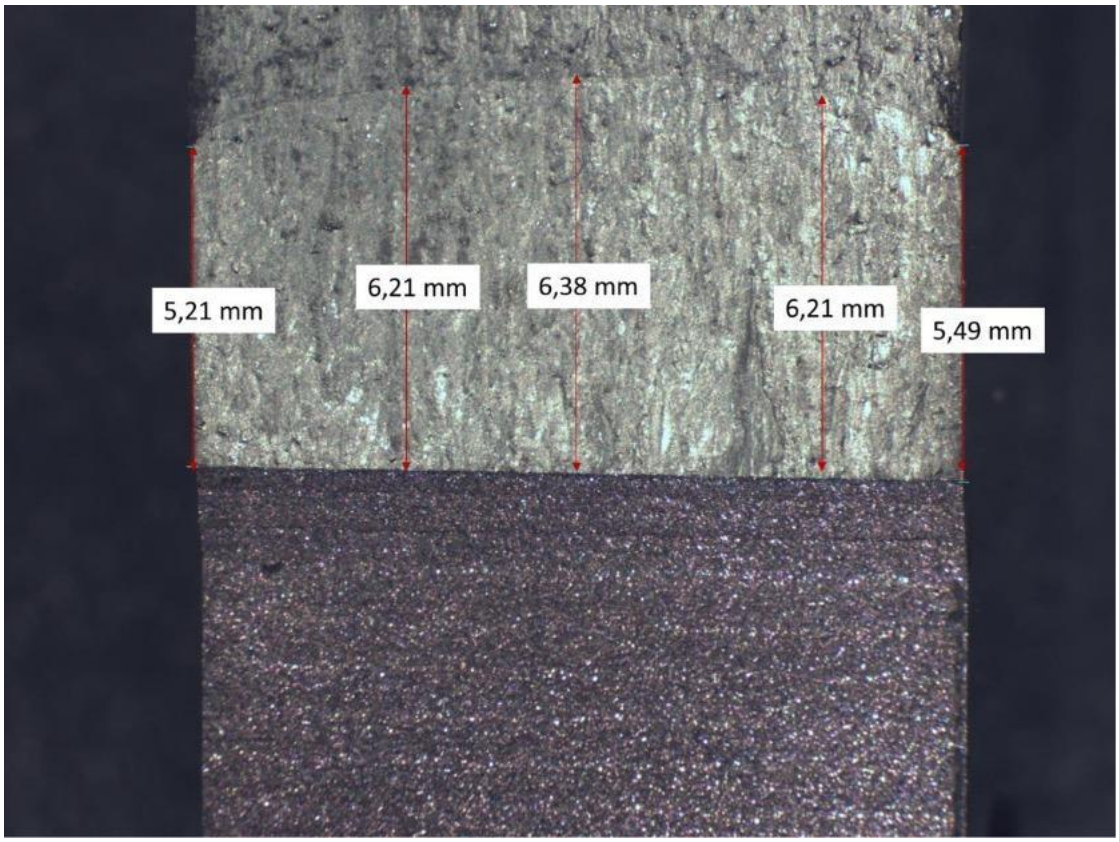

Figure 128: Fracture toughness crack measurement for 6.5 m/s 1

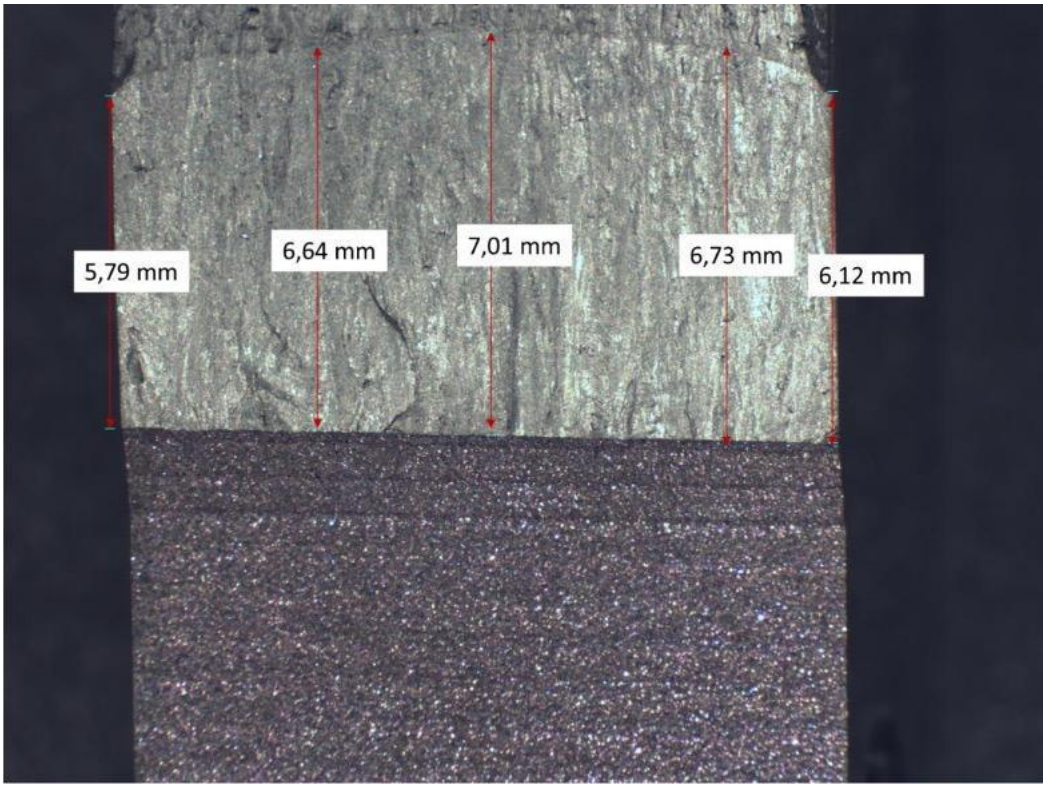

Figure 129: Fracture toughness crack measurement for 6.5 m/s 2

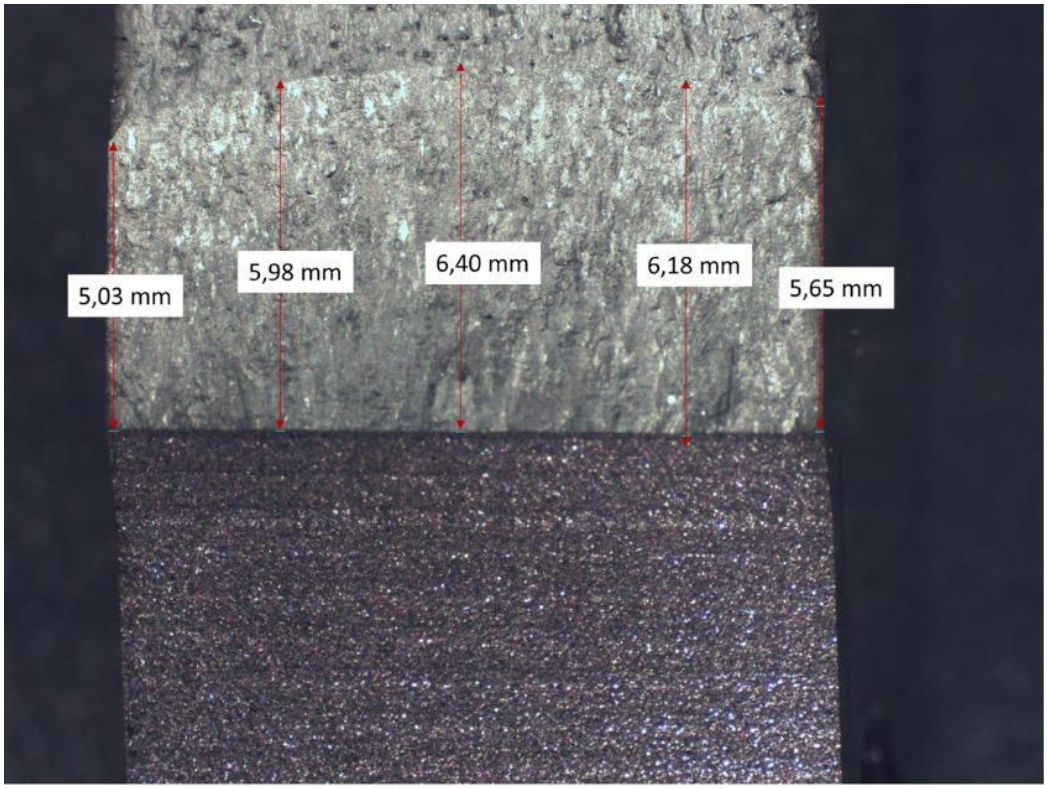

Figure 130: Fracture toughness crack measurement for 6.5 m/s

10.6 Density tables

Table 42: Density results for specimens built at 5.75 and 6.0 m/s

Scan speed [m/s]	Sample build orientation	Mass in air [g[	Mass in water [g]	Density [gcm^{-3}]	Density [%]	Porosity	Average relative density [gcm^{-3}]	Average Density [%]	Average Porosity [%]
5.75	X-TA 1	5.648	4,374	4,424414	99,89647	0,103534823			
		5.650	4,359	4,367699	98,61593	1,38407185			
		5.651	4,356	4,354979	98,32872	1,671276799	4,382	98,90	1.1
	X-TA 2	6,437	4,949	4,320193	97,54330	2,4567			
		6,439	4,958	4,345235	98,08617	1,91383			
		6,440	4,960	4,345587	98, 11663	1,88337	4,337	97,91	2,09
	X-TA 3	6,440	4,961	4,345585	98,11661	1,883385536			
		6,438	4,959	4,344235	98,08614	1,913856534			
		6,437	4,950	4,320192	97,54329	2,456709561	4,346	98,12	1,88
	Y-TA 1	6,505	5,001	4,316483	97,45953	2,540467086			
		6,517	5,012	4,321572	97,57444	2,425556717			
		6,517	5,013	4,324445	97,63932	2,360680092	4,316	97,46	2,54
	Y-TA 2	5,489	4,220	4,316802	97,46675	2,53325341			
		5,495	4,218	4,294448	96,96202	3,037978667			
		5,504	4,219	4,274702	96,51619	3,483812474	4,317	97,47	2,53
	Z-TA 1	5,544	4,261	4,31248	97,36916	2,630839361			
		5,552	4,268	4,31534	97,43372	2,566277628			
		5,547	4,289	4,400561	99,3579	0,642104126	4,312	97,37	2,63
	Z-TA 2	6,600	5,073	4,313556	97,39345	2,606547931			
		6,605	5,082	4,328162	97,72322	2,276777527			
		6,607	5,083	4,326631	97,68867	2,311329113	4,314	97,39	2,61
	Z-TA 3	6,490	4,996	4,335355	97,88563	2,114365492			
		6,499	4,995	4,312501	97,36964	2,630360583			
		6,497	5,002	4,337128	97,92567	2,07433372	4,335	97,89	2,11
6.0	X-TA 1	6,570	5,058	4,336996	97,9227	2,077298395			
		6,599	5,078	4,32992	97,76293	2,2370711			
		6,602	5,076	4,317258	97,47704	2,522960933	4,328	97,72	2,28
	X-TA 2	6,607	5,084	4,328604	97,73322	2,266776589			
		6,625	5,085	4,292484	96,91767	3,082326344			
		6,624	5,087	4,300213	97,09219	2,907814806	4,307	97,73	2,75
	X-TA 3	6,632	5,08	4,263795	96,26992	3,730078			
		6,604	5,079	4,320965	97,56073	2,439270235			
		6,616	5,065	4,256251	96,09959	3,900413706	4,264	96,27	3,36
	Y-TA 1	7,862	6,039	4,303184	97,15926	2,840741847			
		7,846	6,045	4,346884	98,14596	1,854043857			
		7,856	6,046	4,330783	97,78241	2,217593984	4,303	97,16	2,84
	Y-TA 2	6,093	4,679	4,299572	97,07772	2,922275487			
		6,107	4,695	4,315556	97,4386	2,561398381			
		6,122	4,699	4,292714	96,92287	3,077134716	4,300	97,08	2,92
	Y-TA 3	4,815	3,713	4,36059	98,4554	1,544596147			
		4,816	3,714	4,361495	98,47585	1,524148503			
		4,821	3,704	4,307393	97,2543	2,745698419	4,361	98,46	1,54
	Z-TA 1	4,094	3,139	4,27748	96,57891	3,42109301			
		4,13	3,145	4,183669	94,4608	5,539195405			
		4,121	3,151	4,239107	95,71251	4,2874913	4,277	96,58	3,42
	Z-TA 2	6,179	4,757	4,336598	97,9137	2,086300527			
		6,18	4,758	4,3373	97,92955	2,070454322			
		6,177	4,758	4,344359	98,08895	1,911054233	4,337	97,91	2,09
	Z-TA 3	7,035	5,418	4,341948	98,0345	1,96549894			
		7,04	5,422	4,342349	98,04354	1,956455667			
		7,036	5,414	4,329179	97,74619	2,253809176	4,342	98,03	1,97

Table 43: Density results for specimens built at 5.75 and 6.0 m/s

Scan speed [m/s]	Sample build orientation	Mass in air [g[	Mass in water [g]	Density [gcm^{-3}]	Density [%]	Porosity	Average relative density [gcm^{-3}]	Average Density [%]	Average Porosity [%]
6.25	X-TA 1	5,981	4,593	4,300029	97,08803	2,91197231	4,300	97,09	2,91
		5,996	4,6	4,286109	96,77375	3,226254932			
		5,987	4,592	4,282744	96,69776	3,302244655			
	X-TA 2	6,963	5,354	4,318878	97,5136	2,486395039	4,319	97,51	2,49
		6,955	5,352	4,330062	97,76614	2,233859042			
		6,955	5,35	4,324667	97,64431	2,355686009			
	X-TA 3	6,225	4,792	4,334911	97,87562	2,124384154	4,334	97,88	2,12
		6,233	4,787	4,30146	97,12034	2,87966399			
		6,220	4,792	4,346595	98,13943	1,860572633			
	Y-TA 1	6,394	4,925	4,34348	98,0691	1,930902534	4,343	98,07	1,93
		6,393	4,918	4,325135	97,6549	2,345102962			
		6,406	4,922	4,307646	97,26002	2,739975255			
	Y-TA 2	6,312	4,857	4,3290342	97,742927	2,257073226	4,329	97,74	2,26
		6,311	4,854	4,3224069	97,593293	2,406707337			
		6,309	4,855	4,3299526	97,763663	2,236337469			
	Z-TA 1	6,602	5,076	4,316825	97,46727	2,53272915	4,317	97,47	2,53
		6,594	5,074	4,328614	97,73344	2,266562489			
		6,592	5,074	4,333002	97,83252	2,167478629			
	Z-TA 2	5,466	4,203	4,319135	97,51943	2,480573675	4,297	97,52	2,48
		5,486	4,205	4,274027	96,50094	3,499062051			
		5,465	4,196	4,297928	97,04058	2,959415173			
	Z-TA 3	6,994	5,367	4,2901119	96,86412	3,135880282	4,290	96,86	3,14
		6,99	5,376	4,3221933	97,588469	2,411530627			
		6,987	5,373	4,3203383	97,546586	2,45341409			
6.5	X-TA 1	6,991	5,378	4,325058	97,65315	2,346845462	4,325	97,65	2,35
		7,001	5,379	4,307212	97,25021	2,749785004			
		7,006	5,38	4,299685	97,08026	2,919739267			
	X-TA 2	5,727	4,392	4,282166	96,68471	3,315289169	4,282	96,68	3,32
		5,727	4,396	4,295035	96,97527	3,024726552			
		5,729	4,392	4,277253	96,5738	3,42620449			
	X-TA 3	1,913	1,48	4,4100614	99,572396	0,427603706	4,410	99,57	0,43
		1,913	1,48	4,4100614	99,572396	0,427603706			
		1,912	1,479	4,4077561	99,520346	0,479654096			
	Y-TA 1	6,352	4,888	4,330988	97,78704	2,21296053	4,331	97,79	2,21
		6,361	4,884	4,298951	97,06369	2,936312691			
		6,359	4,894	4,332801	97,82798	2,172020125			
	Y-TA 2	7,189	5,529	4,3229276	97,605048	2,394951674	4,323	97,61	2,39
		7,186	5,527	4,3237283	97,623126	2,37687356			
		7,187	5,529	4,3269381	97,6956	2,304400131			
	Y-TA 3	6,384	4,897	4,28548	96,75954	3,240459993	4,285	96,76	3,24
		6,391	4,91	4,30756	97,25807	2,74193064			
		6,385	4,905	4,306424	97,23241	2,767585264			
	Z-TA 1	2,411	1,863	4,3917157	99,158178	0,84182223	4,392	99,16	0,84
		2,416	1,863	4,3610329	98,465408	1,534592202			
		2,412	1,864	4,3935372	99,199305	0,800694823			
	Z-TA 2	6,691	5,139	4,303451	97,1653	2,834699485	4,303	97,17	2,83
		6,688	5,138	4,307072	97,24705	2,752946489			
		6,698	5,145	4,305179	97,20432	2,795678602			
	Z-TA 3	6,781	5,215	4,3223462	97,591922	2,408077841	4,322	97,59	2,41
		6,798	5,22	4,3002304	97,092581	2,90741887			
		6,794	5,224	4,3195992	97,529899	2,470100798			